CORROSION INVESTIGATIONS ON AS-PREPARED AND ION-IMPLANTED Zr-BASED BULK AMORPHOUS ALLOYS

Ph.D. Thesis

POONAM SHARMA

(ID No. 2013RPH9023)

DEPARTMENT OF PHYSICS

MALAVIYA NATIONAL INSTITUTE OF TECHNOLOGY JAIPUR

December 2018

Corrosion Investigations on As-prepared and Ion-implanted Zr-based Bulk Amorphous Alloys

Submitted in

fulfill of the requirements for the degree of

Doctor of Philosophy

by

POONAM SHARMA

(ID: 2013RPH9023)

Under the supervision of

Prof. S. K. Sharma and Prof. Anil Dhawan

DEPARTMENT OF PHYSICS

MALAVIYA NATIONAL INSTITUTE OF TECHNOLOGY JAIPUR

December 2018

In Dedication to My Loving Sister

Late Ms. Sonam Sharma

DECLARATION

I, **Poonam Sharma** declare that this thesis titled **"Corrosion Investigations on As-prepared and Ion-implanted Zr-based Bulk Amorphous Alloys"** and the work presented in it, are my own. I confirm that:

- This work was done wholly or mainly while in candidature for a research degree at this university.
- Where any part of this thesis has previously been submitted for a degree or any other qualification at this university or any other institution, this has been clearly stated.
- Where I have consulted the published work of others, this is clearly attributed.
- Where I have quoted from the works of others, the source is always given. With the exception of such quotations, this thesis is entirely my own work.
- I have acknowledged all main sources of help.
- Where the thesis is based on work done by myself, jointly with others, I have made clear exactly what was done by others and what I have contributed myself.

Date: **Poonam Sharma**

(2013RPH9023)

CERTIFICATE

This is to certify that the thesis entitled **"Corrosion Investigations on As-prepared and Ion-implanted Zr-based Bulk Amorphous Alloys"** being submitted by **Poonam Sharma** (ID: 2013RPH9023) is a bonafide research work carried out under our supervision and guidance in fulfillment of the requirement for the award of the degree of **Doctor of Philosophy** in the Department of Physics, Malaviya National Institute of Technology, Jaipur, India. The matter embodied in this thesis is original and has not submitted to any other University or Institute for the award of any other degree.

(Prof. Anil Dhawan)

Professor
Department of Physics
ANAND ICE Jaipur (India)

(Prof. S. K. Sharma)

Professor
Department of Physics
MNIT Jaipur (India)

Place: Jaipur

Date:

ACKNOWLEDGEMENT

It is a pleasant aspect for me to express my deep and sincere gratitude to the people due to whom it has been possible for me to accomplish my Ph.D. thesis. It is very simple to list them all but very difficult to express the thanks for their innumerable supports.

First of all, I would like to express my sincere gratitude to my thesis supervisors, Prof. S. K. Sharma, Head of Department of Physics, Malaviya National Institute of Technology (MNIT), Jaipur and Prof. Anil Dhawan, Head of Department of Physics, Anand International College of Engineering, Jaipur for bringing me to this amazing field and providing endless support to my research. My Ph. D. period under their supervision has been an extraordinary period of my life. I have found them very good teacher as well as very good guardian. They have always given me time to discuss scientific things in spite of their busy schedule. I am really very fortunate to have Prof. S. K. Sharma and Prof. Anil Dhawan as my supervisors in my life. I am extremely thankful to them and I will always be indebted to them for their great and invaluable support.

The financial support for this work from the Board of Research in Nuclear Sciences (BRNS) and Department of Atomic Energy (DAE), Government of India under the BRNS/DAE Research Project sanction no. 2011/36/44-BRNS/1974 is gratefully acknowledged. I have learn a lot while working in this BRNS/DAE Research project and got opportunity to work at Corrosion Science & Technology Group (CSTG), Indira Gandhi Centre for Atomic Research (IGCAR), Kalpakkam.

I would like to express my heartful thanks to Dr. U. Kamachi Mudali, former Associate Director, CSTG, IGCAR, Kalpakkam for his guidance, unconditional support, enthusiastic supervision and providing me the facilities for casting the amorphous alloys at CSTG, IGCAR, Kalpakkam and performing experimental studies on these developed alloys. Apart from being an eminent scientist, Dr. U. Kamachi Mudali's exceptionally motivating attitude has been the source of inspiration for me.

I would like to express my profound gratitude and deep regards to Dr. J. Jayaraj, Scientific Officer (E), CSTG, IGCAR, Kalpakkam, for his guidance, enthusiastic supervision, technical discussions, positive approach, kindness and patience throughout my research work at IGCAR, Kalpakkam.

I pay my sincere gratitude to Mr. P. Magudapathy, Scientific Officer (F), Materials Physics Division (MPD), IGCAR, Kalpakkam for providing the ion implantation facilities and D. Nanda Gopala Krishna, CSTG, IGCAR, Kalpakkam for recording XPS spectra. I am also thankful to Dr. R. K. Duchaniya, Department of Metallurgical & Material Engineering, MNIT Jaipur and Dr. Pawan Kulariya, IUAC Delhi for their guidance and support.

It is very pleasant opportunity for me to express my sincere thanks to Head of Department of Physics, MNIT Jaipur for providing the administrative support and necessary facilities in the Department for accomplishment of my research work. I also thank the faculty members of the Department and DREC members with whom I had an opportunity to discuss academics at various stages of my work. In addition, I acknowledge the support provided by non-teaching staff members of Department of Physics, MNIT Jaipur.

I would also like to express my heartful thanks to management, faculty and staff members of Anand International College of Engineering, Jaipur for their constant encouragement throughout my Ph. D. work.

I convey my sincere thanks to Materials Research Centre (MRC) administration, scientific and technical staff for their help at various stages of my work. I am extremely thankful to MRC for making available the equipment's and facilities without which I would not have completed my research work.

I acknowledge the support provided by my colleagues Mr. Dinesh Saini, Mrs. Parul Sharma, Mrs. Indu Vashistha, Mr. Satyavir Singh, Dr. Vikas Sharma, Ms. Neeru Sharma, Mr. Veeresh Vishnoi, other lab mates, project students and all seniors for moral support and discussion. I am highly thankful to my other friends Mr. Keshav Sharma, Mrs. Garima Sharma, Mr. Ravindra Budania, Mr. Ronit Panda, Mr. Bhupendra Singh, Er. Rajveer Sihag and Mrs. Suman Sharma for their continuous motivation and entertainment.

The acknowledgement would remain incomplete without mentioning my father, husband Mr. Anubhav Sharma and other family members for their faith, kind support, love, patience and constant encouragement. Their endless love, guidance, teaching, training and invaluable support at each and every moment showed me the way to proceed in life.

December, 2018 Poonam Sharma

ABSTRACT

In the present investigation, the corrosion behavior of some Zr-based bulk amorphous alloys in oxidizing media has been examined for various engineering applications. The present research work reports the synthesis of $Zr_{55}Cu_{30}Ni_5Al_{10}$ amorphous alloy in strip and ribbon shape using copper mold suction casting and melt spinning method, respectively. Furthermore, the corrosion behavior of $Zr_{55}Cu_{30}Ni_5Al_{10}$, $Zr_{60}Nb_2Cu_{20}Ni_8Al_{10}$, $Zr_{59}Nb_3Cu_{20}Ni_8Al_{10}$, $Zr_{57}Nb_5Cu_{20}Ni_8Al_{10}$ $Zr_{57}Nb_5Cu_{15.4}Ni_{12.6}Al_{10}$, $Zr_{59}Ti_3Cu_{20}Ni_8Al_{10}$ and $Zr_{60}Pd_5Cu_{15}Ni_{10}Al_{10}$ amorphous alloys in different concentration of nitric acid has been examined using potentiodynamic polarization and weight loss analysis method. The amorphous nature of these alloys has been examined by XRD and the surface morphology of corroded surface was analyzed by FE-SEM. The FE-SEM micrographs and XPS results reveal the formation of ZrO_2 on the surface of Zr-based amorphous alloys after immersion in aqueous nitric acid which protects the alloy from corrosion attack.

Furthermore, to improve the corrosion resistance of Zr-based bulk amorphous alloys, oxygen ion beam of 100 KeV energy was implanted on $Zr_{55}Cu_{30}Ni_5Al_{10}$ bulk amorphous alloy at various fluences such as 1 x 10^{16}, 1 x 10^{17} and 3 x 10^{17} ions/cm^2. The corrosion behavior of O^+ ion implanted amorphous alloy has been examined in 0.5 M H_2SO_4, 0.5 M H_2SO_4 + 0.1 M NaCl, and 1 M HNO_3 media. GIXRD results reveal the formation of ZrO_2 and $Cu_{10}Zr_7$ crystalline phases on the surface of O^+ ion implanted samples. FE-SEM and XPS results confirmed the presence of predominant ZrO_2 layer on the surface of implanted sample at higher fluences. Potentiodynamic polarization results revealed that the alloy exhibits improved corrosion resistance in 0.5 M H_2SO_4 and 0.5 M H_2SO_4 + 0.1 M NaCl solutions after O^+ ion implantation due to the formation of a ZrO_2 layer on the surface of implanted alloy. However, no improvement in the corrosion resistance of the alloy was observed in the case of HNO_3 solution.

Nitrogen ion beam of 100 KeV energy was also implanted on $Zr_{55}Cu_{30}Ni_5Al_{10}$ amorphous alloy at various fluences such as 1 x 10^{16}, 5 x 10^{16} and 1 x 10^{17} ions/cm^2 and the corrosion behavior of N^+ ion implanted amorphous alloy has been investigated in 1 M HNO_3 medium. GIXRD and XPS results reveal the formation of ZrN on the surface of implanted samples along with the presence of ZrO_2 and Al_2O_3. Potentiodynamic polarization results revealed that the nitrogen ion implanted $Zr_{55}Cu_{30}Ni_5Al_{10}$ amorphous alloy exhibits better corrosion resistance in 1 M HNO_3 medium at lower fluences. The FE-SEM and XPS measurements have been carried out to further elucidate the changes in the surface of the treated samples.

CONTENTS

Chapter 2

Chapter 3

Chapter 4

Chapter 5

Chapter 6

LIST OF TABLES

LIST OF FIGURES

LIST OF ABBREVIATIONS

AFM: Atomic Force Microscopy

BMG: Bulk metallic glasses

E: Young's modulus

E_{corr} : Corrosion Potential

EDS: Energy Dispersive Spectroscopy

e/a: Ratio of Concentration of Conduction Electron and the Atomic Size Factor

FCC: Face Centered Cubic Packing

FE-SEM: Field Emission Scanning Electron Microscopy

GFA: Glass Forming Ability

HCP: Hexagonal Closed Packing

H_v: Vicker's Hardness

IGC: Inter Granular Corrosion

I_{corr}: Corrosion Current Density

I_{pass}: Passive Current Density

MEMS: Micro Electro Mechanical System

OCP: Open Circuit Potential

PDF: Pair Distribution Functions

R_c: Critical Cooling Rate

R_P Projected Range

SCC: Stress Corrosion Cracking Process

SEM: Scanning Electron Microscopy

S_n: Nuclear Energy Loss

S_e: Electronic Energy Loss

T_g: Glass Transition Temperature

T_l: Liquidus Temperature

T_m: Melting Temperature

T_n: Nose Temperature

T_{rg}: Reduced Glass Transition Temperature

T_0: Equilibrium temperature

TTT: Time Temperature Transformation

XPS: X-ray Photoelectron Spectroscopy

XRD: X-Ray Diffraction

ΔC_p^{l-s}: Specific Heat Capacity

ΔH: Enthalpy of Mixing

ΔH_f: Enthalpy of Fusion

$\Delta G_{l\text{-}s}$: Gibbs Free Energy Difference

ΔS_f : Entropy of Fusion

Δr : Difference in the Atomic Size

σ_f : Tensile Fracture Strength

dE/dx: Rate of Energy Loss

CHAPTER-1

Introduction

The chapter includes a basic understanding of each factor vital to complete the present research work. The present research work deals with the corrosion investigation on as-prepared and ion-implanted Zr-based bulk amorphous alloys. Before starting the research work on above mentioned research problem, it is important and mandatory to understand about the amorphous alloys; formation, structure, development, properties and applications of amorphous alloys; basic mechanism of corrosion and process of ion implantation. All these topics are covered in this introduction chapter. The last section of this chapter deals with the social impact of this present research problem as well as motivation behind the present research work.

1.1 Bulk amorphous alloys

1.1.1 Introduction

Amorphous alloys, also referred as metallic glasses, are prepared by rapid quenching of metallic liquid resulting into a disordered atomic configuration which has absence of crystalline structure. The metallic glasses are formed at a rapid cooling rate of the order of 10^5-10^6 K/s and enable the formation of small size and shape specimen such as ribbons, wires, powder or foils. Some metallic glasses are formed at a relatively lower cooling rate of 1-100 K/s known as bulk metallic glasses (BMG) or bulk amorphous alloys, which have wide supercooled liquid region of about 100 K. These bulk amorphous alloys possess specialized features of high strength, amorphous nature, corrosion resistance and are used for various engineering applications.

1.1.2 Formation of bulk amorphous alloys

The formation of glassy alloys requires the rapid cooling of metallic liquid in order to freeze the atoms in their liquid configuration. Rapid cooling instantly reduces the mobility of atoms before the atoms can arrange themselves into a lattice pattern and form crystalline structure [1]. The crystallization kinetics of BMGs can be studied by time–temperature–transformation (TTT) curve. Figure 1.1 shows the schematic representation of a typical TTT diagram which relates the time needed to form a crystalline phase in an undercooled liquid as a function of temperature. The typical ‘‘C’’ shape, which is also called “nose” shape in TTT diagram, reveals the fact that the increasing undercooling reduces the atomic mobility in the liquid and increases the thermodynamic driving force for crystallization. The ability to form a glass from a melt liquid, which is called glass forming ability (GFA), can be measured by the critical cooling rate (R_c) for glass formation. The critical cooling rate for glass formation is a slowest cooling rate at which

the melt liquid is cooled from its liquidus temperature (T_l) to below the glass transition temperature (T_g) with no noticeable crystallization [2]. A glass can be formed from the liquid melt if cooling rate is greater than the critical cooling rate. According to 'Nose Method', the critical cooling rate (R_c) can be determined from following expression, which is basically a slope of straight line from T_m (melting temperature) to T_n (nose temperature), the nose temperature (T_n) is the temperature where melt liquid transforms in crystallize phase in a shortest possible time (t_n) which is called the nose time [3]:

$$R_c = \frac{T_m - T_n}{t_n} \tag{1.1}$$

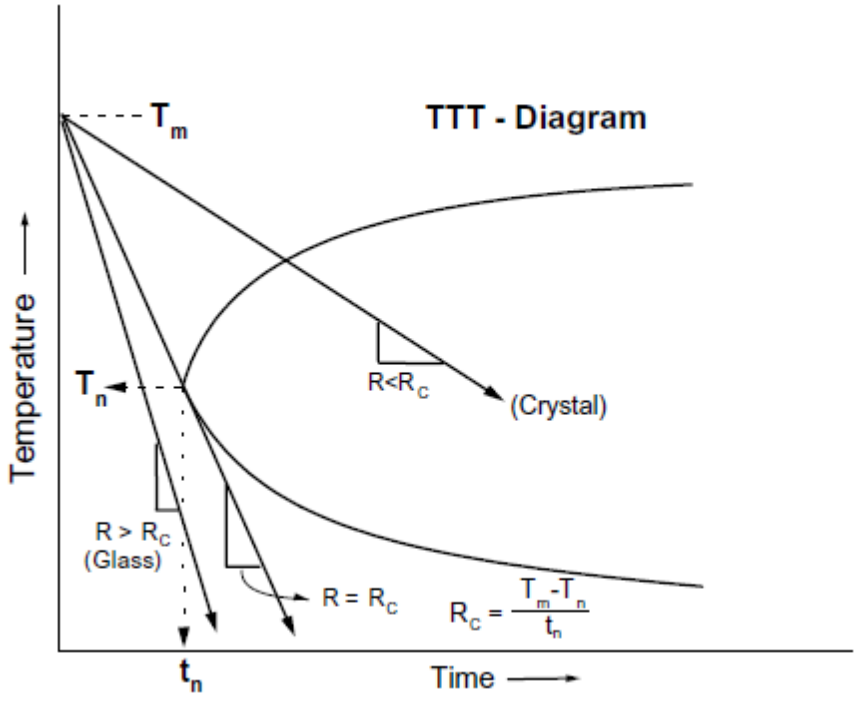

Figure 1.1: Schematic TTT diagram for the onset of crystallization [3]

Generally, both thermodynamic and kinetic aspects influence the glass forming ability (GFA). So, the basic understanding of these two perspectives is helpful in achieving high GFA of bulk amorphous alloys.

1.1.2.1 Thermodynamic aspect of glass formation

The high glass forming ability of bulk amorphous alloys is achieved by low driving force for crystallization, which favours low nucleation rate and enhances the stability of supercooled liquid. According to thermodynamic considerations, the Gibbs free energy difference ($\Delta G_{l\text{-}s}$) between the supercooled liquid and corresponding crystalline states basically acts as a driving force for crystallization [4,5]. The expression for Gibbs free energy difference ($\Delta G_{l\text{-}s}$) is given by following equation 1.2.

$$\Delta G_{l-s}(T) = \Delta H_f - \Delta S_f T_0 - \int_T^{T_0} \Delta C_p^{l-s}(T)dT + T_0 \int_T^{T_0} \frac{\Delta C_p^{l-s}(T)}{T} dT \qquad (1.2)$$

The ΔH_f is enthalpy of fusion; ΔS_f is entropy of fusion; ΔC_p^{l-s} is the specific heat capacity difference between supercooled liquid and corresponding crystalline states and T_0 is the equilibrium temperature of the liquid and crystalline states. So, a glassy system will possess high GFA if it exhibits low value of Gibbs free energy difference.

For example, the Gibbs free energy difference calculated for $Zr_{41.2}Ti_{13.8}Cu_{12.5}Ni_{10}Be_{22.5}$ (Vitreloy 1) [6], $Zr_{52.5}Cu_{17.9}Ni_{14.6}Al_{10}Ti_5$ [7] and $Zr_{57}Cu_{15.4}Ni1_{2.6}Al_{10}Nb_5$ [8] alloys was 1.5 kJ/mol, 2.11 kJ/mol and 2.18 kJ/mol, respectively. Hence, Viteraloy 1 possesses highest glass forming ability and very low critical cooling rate of the order of 1 K/s [9] because it exhibits lowest value of the Gibbs free energy difference among these three alloys.

1.1.2.2 Kinetic aspect of glass formation

Apart from thermodynamic aspect of glass formation, kinetic consideration of glass formation is a key parameter in deciding the GFA of glassy alloys. From kinetic point of view, the viscosity has a greater influence on glass forming ability of a glassy system and it governs the nucleation and growth of crystalline phases [10]. The large value of viscosity at the melting point of the crystalline phase favors the formation of glass [9]. The value of viscosity (η) can be determined from the Vogel-Fulcher-Tamman (VFT) equation 1.3 [11]:

$$\eta = \eta_0 \exp\left(\frac{DT_0}{T - T_0}\right) \tag{1.3}$$

Where η_0 is a constant, D is used to identify the property of liquid and called the fragility parameter and T_0 is the VFT temperature at which viscosity of liquid will be infinite.

The large value of fragility parameter gives the higher viscosity which retards the nucleation and crystal growth. Hence, the glassy alloy system exhibits high glass forming ability if fragility parameter has a large value.

1.1.3 Criteria for evaluation of glass forming ability

1.1.3.1 Reduced glass transition temperature criterion

Several criteria were proposed for evaluation of glass forming ability. In 1969, Turnbull has proposed the reduced glass transition temperature criterion to evaluate GFA [12]. The ratio of the glass transition temperature T_g and the melting temperature T_m is defined as reduced glass transition temperature (T_{rg}). Turnbull has reported that the homogeneous nucleation of the crystalline phase is suppressed when ($T_{rg}= T_g/T_m$) $\geq 2/3$, hence formation of glass takes place.

Lately, Lu et al. [13] have modified this criterion by replacing the melting temperature T_m from the liquidus temperature T_l. The T_{rg} plays key role in determining the glass forming ability of alloys. Chen et al. [14] have studied the glass forming ability of different composition of Zr-Cu-Ni-Al glassy alloys by calculating the value of T_g/T_m and T_g/T_l which resulted in the range of 0.584 - 0.610 and 0.525 - 0.582, respectively.

1.1.3.2 Three empirical rules

Inoue has proposed a very important and basic thumb rule for the formation of bulk amorphous alloys [15]. It is divided into three sub-rules:

(i) A multi-component system containing at least three elements is favorable for the formation of bulk metallic glass. The degree of random packing of atoms is increases as the number of elements increases in the system resulting into an increased entropy of the fusion which leads to the decrease in the Gibbs free energy.

(ii) All the components of the system must have difference in their atomic sizes. This difference in the atomic size (Δr) should be nearly 12% ($\Delta r \sim 12\%$) which increases the density of randomly packed atoms resulting in enhanced viscosity of melt. Hence, this second sub-rule is favorable for the glass formation.

(iii) The enthalpy of mixing (ΔH) between the elements of the glass forming system should be negative. It helps in stabilization of undercooled liquid and formation of a homogeneous glass state.

This empirical rule is useful in choosing the elements for a glassy system. The identification of a proper composition to form an amorphous structure cannot be decided by this empirical rule. It requires continuous efforts and rigorous experiments.

1.1.3.3 e/a criterion

To evaluate the glass forming ability, a new criterion is proposed based on the mechanism of 'The Nagel- Tauc rule' [16]. This criterion deals with the concentration of conduction electrons and the atomic size factor. It provides a facility to determine the composition range in a specified system. According to The Nagel- Tauc rule, stability of metallic glasses can be achieved only if the system satisfies following equation:

$$K_p = 2K_f \tag{1.4}$$

Here; $K_p = \frac{4\pi \sin\theta}{\lambda}$ K_p is the peak position and can be determined from XRD pattern;

$K_f = (3\pi^2 N)^{1/3}$ $2K_f$ is the diameter of Fermi sphere;

$N = \frac{e}{a}\frac{n}{V_{cell}}$ N stands for number of the valence electrons per unit volume;

Here n represents the number of atoms in the unit cell and V_{cell} is the volume of unit cell. The value of e/a, which is the ratio of concentration of conduction electron and the atomic size factor, can be determined using above mentioned calculation.

In 1992, it has been reported that the composition of glass forming system exhibits 'ideal amorphous state' at a specific e/a value of 1.8 [17]. Hence, the stability of metallic glass can be explained by the electronic structure viewpoint and the glass forming ability of bulk amorphous alloys is associated with the ratio of concentration of conduction electron and the atomic size factor (e/a). In last few years, e/a criterion has become the empirical criterion for determining the glass forming ability of amorphous alloys, for example, Shek et al. [18] have studied $Zr_{65}Al_{7.5}Ni_{10}Cu_{17.5}$ alloy, Chen et al. [14] have studied Zr-Al-Ni, Zr-Al-Cu, and Zr-Al-Ni-Cu

systems and Wang et al. [19] have studied Zr-Al-Ni(Co) alloys on the basis of e/a criterion and found the highest glass forming composition among the given compositions.

1.1.4 Structure of bulk amorphous alloys

Despite intense research in the field of amorphous alloys, structural description of amorphous alloys has always been an interesting research topic due to the absence of unit cells in the amorphous alloys. In general terms the structure of amorphous alloy is described as a disordered atomic scale structure. Two type of disorder i.e. topological and chemical could explain the amorphous structure of material. The topological disorder arises due to the dispersion of distances in atomic arrangements, whereas the chemical disorder is a result of different local environment of each atom. The pinpoint description of amorphous structure can be made on statistical basis. The pair distribution functions (PDFs) are the most common statistical measurement for glass structure analysis, which finds the probability of an atom separated from another atom by a specific distance.

The pair distribution function (PDF) is obtained from scattering powder diffraction pattern using following equation [20]:

$$G(r) = 4\pi r[\rho(r) - \rho_0] \tag{1.5}$$

Here $\rho(r)$ is the number of atoms per unit volume at a distance r and ρ_0 is the number of atoms per unit volume in the sample.

Only statistical information of atomic distances can be extracted from the PDFs, but it is inefficient to specify the structure. The structure models are in good agreement for solution of this issue.

In 1964, Bernal has proposed the first structural model of 'dense random packing' of hard spheres having same diameter, to explain the structure of pure metallic liquids [21, 22]. This model was applicable only for monatomic metals and failed to explain the avoidance of metalloid–metalloid nearest neighbor atoms in metal-metalloid glassy system. Furthermore, in 1979, Gaskell has developed a new model of 'local coordination model' to explain the avoidance of nearest neighbor atoms in metal-metalloid glasses and proposed that this nearest atom referred as local unit possessing similar structure as its corresponding crystalline compounds [23]. To overcome all drawbacks in structural models, a new structural model 'efficient cluster packing model' was proposed by Miracle [24]. This model proposed the efficient packing (face centered cubic packing (FCC) or hexagonal closed packing (HCP)) of solute-centered atomic clusters, which were treated as a sphere, to occupy the 3-D space. This model accurately explains the medium range order of solute atoms because of special arrangements of solute-centered clusters as well as amorphous nature of metallic glass due to disordered nature of solvents. Furthermore, Sheng et al. [25] have carried out a reality check on different atomic structural model by analyzing the different binary alloy models and suggested an alternative cluster packing scheme. They have suggested that short range order can be effectively explained by icosahedral fivefold cluster packing rather than the FCC or HCP packing. Furthermore in 2008, Yang et al. [26, 27] has introduced cluster line model, which describes an approach for designing and predicting the best glass forming composition in the Al rich Al-TM-RE glasses, where the rare earth (RE) and transition metal (TM) coexist as a centered cluster. According to cluster line model, the composition at the intersection, where the desirable atomic composition ratios are satisfied and all Al solvent atoms are shared by both the TM and RE solutes, possess efficient atomic packing

and high glass forming ability. Despites intense and devoted research from all over the world, no model can perfectly enable the prediction of metallic glass formation.

1.1.5 Historical background

The formation of first metallic glass was reported by Klement et al. [28] in 1960 at Caltech, USA. They have developed an amorphous foil of $Au_{75}Si_{25}$ alloy (10μm thickness) by direct quenching of metallic liquid at very high cooling rates of 10^5–10^6 K/s to avoid crystallization. The unique properties and attractive benefits of amorphous alloys had attracted the attention of researchers. However, rapid quenching technique at high cooling rate was able to produce very thin μm sized alloys which limited the commercial applications of these amorphous alloys. In order to produce the amorphous alloys in bulk size, in 1974, a successful attempt has been made by Chen [29]. He has reported the development of first bulk metallic glass, Pd–Cu–Si ternary alloy, using suction-casting methods at a significantly lower cooling rate of 10^3 K/s. Two years later in 1976, Liebermann et al. [30] have developed a new method of synthesizing thin amorphous ribbons on a supercooled spinning wheel rotating with very high speed. They have developed commercial Fe-Ni-B amorphous alloy which is also referred as "Metaglas" and used in low-loss power distribution transformers (amorphous metal transformer). In 1984, Kui et al. [31] have prepared the $Pd_{40}Ni_{40}P_{20}$ ternary bulk metallic glass at relatively low cooling rate of 10 K/s using boron oxide fluxing method. Due to high cost of Pd, the use of Pd-based alloys was limited to academic and research field and researchers have shifted their interest on other glass forming systems. In 1989, Inoue group have developed La-Al-Cu, La-Al-Cu-Ni and La-Al-Cu-Ni-Co bulk glass forming systems owing to high glass forming ability [32]. Afterwards in 1991, Mg–Cu–Y and Mg–Ni–Y bulk amorphous systems were developed and $Mg_{65}Cu_{25}Y_{10}$ alloy was reported to exhibit the highest glass-forming ability [33]. At the same time, the Inoue group has

developed a new family of Zr–Al–Ni–Cu bulk amorphous alloys exhibiting high glass-forming ability with the sample thickness about 15 mm [34]. Detailed literature regarding development of Zr-based bulk amorphous alloys has been given in chapter 2 'Literature Review' of the thesis. A new epoch of the research in the field of bulk amorphous alloys has begun after the development of Zr-based bulk amorphous alloys possessing wide range of beneficial properties for various engineering applications.

1.1.6 Properties of bulk amorphous alloys

During the past five decades, extensive research has been carried out on multi-component bulk amorphous alloys due to distinctive properties of these alloys. Metallic glass exhibits unique properties that are superior to the conventional crystalline alloys, such as high strength, high elastic strain limit, high hardness, good soft magnetic properties and good corrosion resistance. So, lately the development of amorphous alloys has not only been focused to improve the critical casting thickness, but also intended towards improvement in these certain properties of metallic glasses.

It has been reported that the bulk amorphous alloys exhibits around 60% higher tensile strength, higher hardness and lower young modulus in comparison to tensile strength and young modulus of conventional crystalline alloys. This larger difference in mechanical properties is attributed to the different deformation mechanism and fracture mechanism of bulk amorphous alloys [35]. Inoue group has determined the values of tensile fracture strength (σ_f), Young's modulus (E) and Vicker's hardness (H_v) for different glassy alloys such as Mg-based, La-based, Zr-based, Pd-based and Ti-based bulk metallic glasses (as shown in figure 1.2) and reported that the bulk amorphous alloys have high tensile fracture strength in the range of 840-2100 MPa [36].

Furthermore, it has been reported that Ti-based, Cu-based and Ni-based metallic glasses exhibit the tensile strength greater than 2000 MPa, which is impossible to obtain in the case of crystalline alloys [37]. The high yield stress of glassy alloys is attributed to the absence of dislocation-mediated slip [35]. The soft magnetic property of bulk amorphous alloys is attributed to the absence of a magneto-crystalline anisotropy. Due to soft magnetic properties, glassy alloys have great demand for sensor applications and these glasses are used as core material of high frequency transformers [38]. Apart from mechanical and magnetic properties of bulk amorphous alloys, bulk metallic glasses possess high corrosion resistance when compared to the crystalline alloy. The high corrosion resistance of amorphous alloys is mainly due to the absence of defects such as grain boundaries, dislocations and stacking faults which are associated with the crystalline state. It has been reported that bulk amorphous alloys shows passivity even under severe corrosive environment [39]. Detailed corrosion investigations on Zr-based bulk amorphous alloys have been reviewed in Chapter 2 of the thesis.

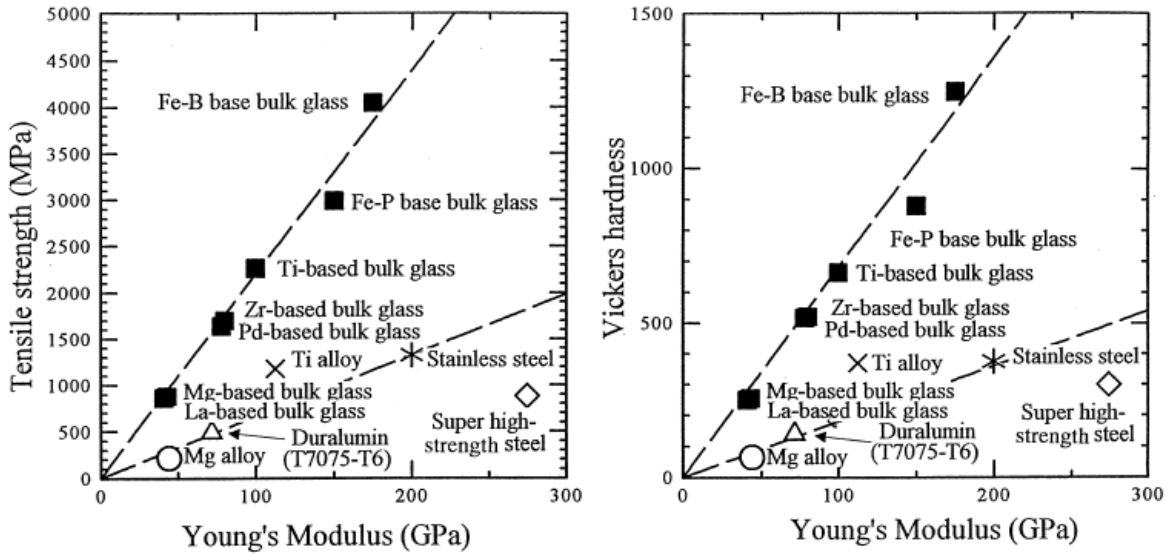

Figure 1.2: Relationship of (a) tensile fracture strength with Young's modulus and (b) Vicker's hardness with Young's modulus for different alloy system [36]

1.1.7 Applications of bulk amorphous alloys

With the exceptional and eccentric characteristics, bulk amorphous alloys are considered as a candidate material for various engineering application. Due to the high glass forming ability and critical thickness, Pd-based bulk amorphous alloys such as Pd–Cu–Ni–P BMG are used as die materials and Pd-Cu-Si-P BMG plays important role in fabrication of electrode materials. The Fe-based bulk amorphous alloys have immense applications in making of common mode choke coils due to soft magnetic property of these amorphous alloys. On the other hand, Zr-Al-Ni-Cu bulk amorphous alloys were firstly used in the sports application for making golf plate [40]. Furthermore, these amorphous alloys were used in other sporting goods such as tennis rackets, baseball bats, hunting bows, bicycle frames, and even in edged cutting tools such as axes. Apart from sporting field, bulk amorphous alloys have vast applications in micro-electro-mechanical system (MEMS) such as spring actuator [35]. The use of bulk amorphous alloys was also taken into account for the manufacturing of micro-springs, micro gears, micro-motors and other demanding engineering applications. Due to the superior mechanical properties of bulk amorphous alloys over conventional light alloys, these alloys are used in manufacturing of mobile phones and digital cameras cases. Apart from these engineering applications, bulk amorphous alloys also have a potential use in more serious applications such as in defence industry. Due to high mechanical strength and light weight of bulk amorphous alloys, these alloys are helpful in designing the military equipments with no compromise in the reliability. These alloys are used in fabrication of components of missile fins, aircraft fasteners, light weight armor case etc. [35]. Fabrication of BMG foam, which is a stronger and lighter material, is a great achievement in aerospace application [41]. Biomedical field is one another area, where glassy materials have wide applications. These metallic glasses are used to fabricate biomedical

devices and surgical implants. Titanium and Titanium alloys are widely used as biomedical devices and implant material because of their desirable properties such as high mechanical strength, corrosion resistance and biocompatibility [42]. A new emerging research field, reprocessing of spent nuclear fuel involves the use of high corrosion resistant material in nitric acid environment. The bulk amorphous alloys could be a candidate material in spent fuel reprocessing applications due to corrosion resistant properties of these alloys. Recently, Ni-based bulk amorphous alloys [43-44] and Ti-Zr-Al alloys [45] have been studied in HNO_3 medium aiming to its applications in spent fuel reprocessing.

1.2 Motivation and objective of the present research work

A novel engineering material namely, the bulk amorphous alloys exhibit outstanding mechanical properties and good corrosion resistance in different environments [15]. Among various bulk amorphous alloys, Zr-based bulk amorphous alloys possess high glass forming ability and interesting mechanical as well as corrosion resistant properties [40]. Also, Zr is a well known nuclear material, owing valuable application in engineering field as well as in nuclear industry [46]. Corrosion property of any material plays vital role in selecting the material for various engineering application depending upon the environmental conditions. Due to serious consequences of corrosion, that not only wastes the resources or harms the industries but also affects the mankind causing deadly accidents. So the prevention of corrosion is a strong need of industries as well society. Hence, to understand the corrosion properties of Zr-based amorphous alloys, several investigations were carried out in different media by many researchers. Li et al. [47] have found that $Zr_{56}Ni_{20}Al_{15}Nb_4Cu_5$ amorphous alloy exhibits excellent corrosion resistance in comparison to $Zr_{60}Ni_{25}Al_{15}$ and $Zr_{56}Ni_{25}Al_{15}Nb_4$ amorphous in 1 N H_2SO_4, 1 N HCl and 3% NaCl medium. The $Zr_{52.5}Cu_{17.9}Al_{10}Ni_{14.6}Ti_5$ alloy exhibited excellent corrosion resistance in

3.5% NaCl medium, good corrosion resistance in 1 N HNO_3 and 1 N H_2SO_4 and poor corrosion resistance in 1 N HCl medium as compared to 304L stainless steel (SS) [48]. Furthermore, the corrosion behavior of $Zr_{65}Cu_{17.5}Ni_{10}Al_{7.5}$ and $Zr_{46.75}Ti_{8.25}Cu_{7.5}Ni_{10.0}Be_{27.5}$ (Viteraloy-4) amorphous alloys was investigated in 0.5 M H_2SO_4, 0.5 M HNO_3, 0.5 M HCl and 0.5 M NaOH solutions and it was found that $Zr_{65}Cu_{17.5}Ni_{10}Al_{7.5}$ amorphous alloy exhibits better corrosion resistance in all aqueous solutions in comparison to Viteraloy-4 [49]. These investigations indicate that Zr-based bulk amorphous alloys are found to be a suitable candidate material for engineering applications as far as corrosion properties are concerned. Thus, to understand the fundamental corrosion behavior of Zr based bulk amorphous alloys in oxidizing environment i.e. nitric acid, the systematic corrosion investigations are proposed on Zr-based bulk amorphous alloys.

In addition to this, a new emerging area of research for these alloys is fuel reprocessing applications, which involves the use of highly concentrated boiling nitric acid and bulk amorphous alloys have been found to withstand in these severe conditions [50]. Hence, this application has also attracted the attention of researchers to carry out the detailed corrosion investigations on Zr-based bulk amorphous alloys in oxidizing media at higher temperature.

Since, O^+ ion implantation on Zr-based bulk amorphous alloys favors the formation of ZrO_2 which possesses corrosion resistant properties in oxidizing media [51] and N^+ ion implantation on Zr-based bulk amorphous alloys involves the formation of ZrN layer which is a highly corrosion resistant layer [52]. Hence, surface modification techniques such as O^+ and N^+ ion beam implantation are carried out to improve the corrosion resistance of Zr-based bulk amorphous alloys.

Therefore, the main objectives of this work are outlined as follows:

- To develop the $Zr_{55}Cu_{30}Ni_5Al_{10}$ amorphous alloys in strip and ribbon shape.
- To investigate the corrosion behavior of Zr-based bulk amorphous alloys in various concentrations of HNO_3 media at room and higher temperature.
- To study the influence of oxygen ion implantation on the corrosion behavior of bulk $Zr_{55}Cu_{30}Ni_5Al_{10}$ amorphous alloy in H_2SO_4, H_2SO_4 + NaCl and HNO_3 media.
- To study the influence of nitrogen ion implantation on the corrosion behavior of $Zr_{55}Cu_{30}Ni_5Al_{10}$ amorphous alloy in HNO_3 medium.

CHAPTER-2

Literature Review

The chapter includes a concise review of the literature available on the development in the field of amorphous alloys over last five decades. The development of Zr-based BMG system has been focused in this chapter with more attention given on the glass forming ability of Zr-based bulk amorphous alloys. Subsequent part of this section deals with the literature review carried out on the corrosion studies on Zr-based bulk amorphous alloys in different media. Furthermore, the effect of different ion beams on corrosion behaviour of various metallic glasses is profoundly discussed. Apart from this, the detailed literature review on oxygen and nitrogen ion implantation on bulk amorphous alloys is provided. The last section of this chapter deals with research gap and objective of the present research work.

2.1 Development of Zr-based bulk amorphous alloys

The development of first bulk metallic glass $Au_{75}Si_{25}$ in 1960 [28] has given new opportunity to researchers to work in the area of amorphous alloys and produced widespread scientific interest due to unique properties of these alloys. Many researchers have developed different families of amorphous alloys and investigated different properties of these alloys. In 1990, Inuoe group have developed a novel Zr-based ternary amorphous alloy system i.e. Zr–Al–M(M=Ni, Cu, Co, Fe or Mn) exhibiting wide supercooled liquid region [53]. Furthermore in 1991, Zhang et al. [34] have reported extremely wide supercooled liquid region of quaternary and pentad amorphous alloys in Zr-Al-TM (TM=Co,Ni,Cu) system. The amorphous $Zr_{65}Al_{7.5}Ni_{10}Cu_{17.5}$ alloy has shown the largest temperature span (ΔT_x) of 127 K in this system. In 1993, A. Peker and W. L. Johnson [54] developed a new family of Zr-based bulk amorphous alloys i.e. Zr-Ti-Cu-Ni-Be system and reported first commercial bulk amorphous $Zr_{41.2}Ti_{13.8}Cu_{12.5}Ni_{10}Be_{22.5}$ alloy which is commonly known as Vitreloy 1. It exhibits high glass forming ability with a critical casting thickness up to 14 mm. In 1995, Inoue group have introduced an additional element in Zr-Cu-Ni-Al glassy system in order to improve the glass forming ability of the glassy system and developed new amorphous Zr-Cu-Ni-Al-M(M=Ti, Hf, C, Nb, Cr, Mo, Fe, Co, Pd or Ag) alloys [55]. It has been found that only Ti, Nb and Pd element helps in improving the glass forming ability of amorphous Zr-Cu-Ni-Al system. In 2005, Jin et al. [56] have developed Fe containing new Ni free Zr-based bulk amorphous system $(Zr_xCu_{100-x})_{80}(Fe_{40}Al_{60})_{20}$ where x=68–77 and $Zr_{58}Cu_{22}Fe_8Al_{12}$ has been reported to be the best glass forming composition of this system. Furthermore, Zr– Cu–Al–Ag system was developed by Zhang et al. [57] in 2007 and bulk amorphous $Zr_{48}Cu_{36}Al_8Ag_8$ alloy of 25 mm diameter was synthesized. After developing various families of Zr-based bulk amorphous alloys, thickness and glass forming abilities of amorphous alloys has become concerned issue for

researchers. Several investigations were carried out to increase the thickness and glass forming ability of these amorphous alloys, so that it can be used in various engineering applications. Inoue et al. [58] have summarized the critical and standard diameter of Zr-based bulk amorphous alloys in their review article. The maximum diameter in the case of Zr-based amorphous alloys have been reported in the literature: $Zr_{50}Cu_{40}Al_{10}$- 22 mm [58], $Zr_{55}Cu_{30}Al_{10}Ni_5$- 30 mm [59], $Zr_{60}Cu_{20}Al_{10}Ni_{10}$- 20 mm [58], $Zr_{65}Cu_{17.5}Al_{7.5}Ni_{10}$- 16 mm [60], $Zr_{53}Cu_{18.7}Ni_{12}Al_{16.3}$- 6 mm [61], $Zr_{51.9}Cu_{23.3}Ni_{10.5}Al_{14.3}$- 10 mm [61], $Zr_{50.7}Cu_{28}Ni_9Al_{12.3}$- 14 mm [61], $Zr_{56}Ni_{20}Al_{15}Nb_4Cu_5$- 25 mm [47], $Zr_{41.2}Ti_{13.8}Cu_{12.5}Ni_{10}Be_{22.5}$ (VIT-1)- 10 cm [62], $Zr_{48}Cu_{36}Al_8Ag_8$- 25 mm [57] $Zr_{54.4}Cu_{25.6}Fe_8Al_{12}$- 5 mm [56], $Zr_{58}Cu_{22}Fe_8Al_{12}$- 13 mm [56] and $Zr_{61.6}Cu_{18.4}Fe_8Al_{12}$- 5mm [56]. Recently in 2017, Hua et al. [63] have reported the improvement in glass forming ability of amorphous $Zr_{65}Al_{10}Ni_{25}$ alloy with the addition of limited amount of Pd and synthesized amorphous $Zr_{65}Al_{10}Ni_{15}Pd_{10}$ alloy of 5 mm critical thickness.

2.2 Some important corrosion investigations on Zr-based amorphous alloys at room temperature

Zr-based bulk amorphous alloys possess high glass forming ability, interesting mechanical properties and corrosion resistant properties. Due to these outstanding properties, Zr-based amorphous alloys have various engineering applications. Corrosion property of any material plays vital role in selecting the material for various engineering application depending upon the environmental conditions. Hence, to understand the corrosion properties of Zr-based amorphous alloys, several investigations were carried out in different media by many researchers. Some important studies are summarized in tabular form.

Table 2.1: Corrosion studies on Zr-based amorphous alloys in different environments at room temperature

Alloy	**Experimental method**	**Medium**	**Results/ Major findings**	**Ref./ Year**
$Zr_{60}Ni_{25}Al_{15}$ $Zr_{56}Ni_{25}Al_{15}Nb_4$ $Zr_{56}Ni_{20}Al_{15}Nb_4Cu_5$ alloys	Electrochemical measurements	1 N H_2SO_4 1 N HCl 3% NaCl	It was reported that the Zr-Ni-Al-Nb-Cu alloy exhibits excellent corrosion resistance in comparison to Zr-Ni-Al and Zr-Ni-Al-Nb alloys	[47]/ 2014
$Zr_{55}Cu_{30}Al_{10}Ni_5$ alloy	Potentiodynamic polarization method	0.1 M Na_2SO_4	It was reported that alloy exhibits high corrosion resistance in comparison to its crystalline counterpart	[64]/ 1999
$Zr_{60-x}Nb_xAl_{10}Ni_{10}Cu_{20}$ (x=0, 5, 10, 15, 20 at%) alloys	Immersion test and electrochemical measurement	1 N HCl	It was found that the addition of Nb effectively improves the corrosion resistance of Zr-Cu-Ni-Al glassy alloys	[65]/ 2000
$Zr_{52.5}Cu_{17.9}Al_{10}Ni_{14.6}Ti_5$ alloy	Cyclic anodic-polarization tests	0.6 M NaCl 0.05M Na_2SO_4	Amorphous alloy exhibited passive behavior in both Na_2SO_4 and NaCl solutions	[66]/ 2002

Alloy	**Experimental method**	**Medium**	**Results/ Major findings**	**Ref./ Year**
$Zr_{55}Cu_{30}Al_{10}Ni_5$, $Zr_{62-x}Cu_{20}Al_{10}Ni_8Nb_x$ (x=2 & 3) $Zr_{57}Cu_{15.4}Al_{10}Ni_{12.6}Nb_5$ $Zr_{59}Cu_{20}Al_{10}Ni_8Ti_3$ $Zr_{52.5}Cu_{17.9}Al_{10}Ni_{14.6}Ti_5$ alloys	Potentiodynamic polarization method	0.1 M Na_2SO_4 0.01 M NaCl	It was reported that Ti and Nb containing Zr-Cu-Al-Ni system exhibit improved corrosion resistance in chloride solutions in comparison to Zr-Cu-Al-Ni system	[67]/ 2002
$Zr_{52.5}Cu_{17.9}Al_{10}Ni_{14.6}Ti_5$ Alloy	Immersion test and potentiodynamic polarization method	3.5% NaCl 1 N HNO_3 1 N H_2SO_4 1 N HCl	It was found that the alloy shows excellent corrosion resistance in NaCl; good corrosion resistance in HNO_3 and H_2SO_4 and poor corrosion resistance in HCl solution in comparison to 304L stainless steel (SS)	[48]/ 2003
$Zr_{55}Cu_{30}Al_{10}Ni_{5-x}Pd_x$(x = 0, 5at.%) alloys	Electrochemical measurement	0.6 M NaCl 1 M NaOH	Pd-free Zr-Cu-Ni-Al alloy exhibited passive region and better corrosion resistance than Pd-containing Zr-Cu-Ni-Al alloys in NaCl medium	[68]/ 2004

Alloy	**Experimental method**	**Medium**	**Results/ Major findings**	**Ref./ Year**
$Zr_{57}Ti_8Nb_{2.5}Cu_{13.9}Ni_{11.1}Al_{7.5}$ alloy	Potentiodynamic Polarization method	1 M H_2SO_4 1 M HNO_3	The amorphous alloy exhibited higher corrosion resistance in comparison to its crystalline, nano-crystalline and quasi-crystalline states	[69] / 2004
$Zr_{59}Ti_3Cu_{20}Al_{10}Ni_8$ alloy	Electrochemical measurement	1 N H_2SO_4 1 N H_2SO_4 + (0.01, 0.025, 0.02, 0.05, 0.1 0.2 N) NaCl	The alloy exhibited passive behavior in H_2SO_4 medium but shows susceptibility to pitting corrosion in the presence of chloride ions	[70]/ 2004
$Zr_{65}Cu_{17.5}Ni_{10}Al_{7.5}$ (Inoue alloy) $Zr_{46.75}Ti_{8.25}Cu_{7.5}Ni_{10.0}Be_{27.5}$ (Viteraloy-4)	Potentiodynamic polarization method	0.5 M H_2SO_4 0.5 M HNO_3 0.5 M HCl 0.5 M NaOH	The Inoue alloy exhibited better corrosion resistance in all aqueous solutions in comparison to Viteraloy-4	[49]/ 2005
$Zr_{55}Ti_{25}Ni_{20}$ $Zr_{58}Cu_{28}Al_{10}Ti_4$ $Zr_{65}Cu_{7.5}Al_{7.5}Ni_{10}Pd_{10}$ alloys	Potentiodynamic polarization method	0.5 M NaCl 0.5 M NaOH 0.25 M H_2SO_4	Ternary amorphous $Zr_{55}Ti_{25}Ni_{20}$ alloy showed better corrosion resistance than quaternary and quinary alloys in NaCl solution	[71]/ 2006

Alloy	**Experimental method**	**Medium**	**Results/ Major findings**	**Ref./ Year**
$Zr_{58.5}Cu_{15.6}Ni_{12.8}Al_{10.3}Nb_{2.8}$ alloy	Immersion test	1 M HCl 1 M HNO_3	The preferential dissolution of Cu and Al from the oxide film along with enrichment of Zr content in the film was reported	[72]/ 2008
$Zr_{59}Ti_3Cu_{20}Al_{10}Ni_8$ alloy	Electrochemical measurements and immersion test	1 M HNO_3 6 M HNO_3 11.5 M HNO_3 0.5 M NaCl 1 M NaCl	It was reported that the corrosion resistance and passive film stability depends upon concentration of nitric acid	[73]/ 2010
$Zr_{41.2}Ti_{13.8}Ni_{10}Cu_{12.5}Be_{22.5}$ alloy	Potentiodynamic polarization method and immersion test	3.5 % NaCl 1 N HNO_3 1 N H_2SO_4 1 N HCl	The amorphous alloy exhibited high corrosion resistance in all aqueous solutions in comparison to 316L stainless steel (SS)	[74]/ 2010
$Zr_{50}Cu_{40}Al_{10}$ $Zr_{70}Cu_6Al_8Ni_{16}$ alloys	Electrochemical measurements and immersion test	0.5 M NaCl	The amorphous $Zr_{70}Cu_6Al_8Ni_{16}$ alloy exhibited spontaneous passivation whereas $Zr_{50}Cu_{40}Al_{10}$ alloy is highly susceptible to pitting corrosion	[75]/ 2011

Alloy	**Experimental method**	**Medium**	**Results/ Major findings**	**Ref./ Year**
$Zr_{59}Ti_3Cu_{20}Al_{10}Ni_8$ $Zr_{59}Ti_3Cu_{20}Al_{10}Ni_8$-coated 304L stainless steel (SS)	Potentiodynamic polarization method	1 M HNO_3 6 M HNO_3 11.5 M HNO_3	Amorphous metallic glass coated 304L SS exhibited lower corrosion resistance than amorphous alloy	[76]/ 2011
$Zr_{67.5}Cu_{15}Ni_{10}Al_{7.5}$ alloy	Electrochemical measurement	0.1 M HCI + NaF	It was reported that the amorphous alloy forms homogeneous 3-D porous structures in HCl + NaF solution whereas the nano-crystalline sample undergoes selective dissolution	[77]/ 2015
$Zr_{58.5}Ti_{14.3}Nb_{5.2}Cu_{6.1}Ni_{4.9}Be_{11}$ alloy	Electrochemical measurements and immersion test	1 M NaCl 1 M HCl 0.5 M H_2SO_4 1 M NaOH	It was reported that the amorphous alloy shows poorest corrosion resistance in NaOH solution	[78]/ 2016
$(Zr_{58}Nb_3Cu_{16}Ni_{13}Al_{10})_{100-x}Y_x$ (x = 0, 0.5, 2.5 at.%) alloys	Electrochemical measurements	3.5wt.% NaCl	Yttrium free Zr-Nb-Cu-Ni-Al alloy showed better corrosion resistance than Yttrium containing Zr-Nb-Cu-Ni-Al alloy	[79]/ 2017

2.3 Some important corrosion investigations on different alloys at higher temperatures

Zr-based bulk amorphous alloys possess high corrosion resistance in various aqueous solutions at room temperature. Enough data are available in the literature regarding corrosion behavior of these alloys at room temperature but limited corrosion investigations have been carried out on amorphous alloys at high temperature. Few corrosion investigations carried out on various alloys at high temperature using immersion test are summarized in tabular form.

Table 2.2: Corrosion studies on different alloys at higher temperature in different environments

Alloy	**Medium**	**Results/ Major findings**	**Ref./ Year**
Ti-5% Ta alloy Ti-0.25% Pd alloy Zircaloy-2	Boiling 12 M HNO_3	The Zircaloy-2 exhibited lowest corrosion rate among all investigated alloys	[80]/ 1993
Commercially pure (CP) Ti Ti-5%Ta alloy	Boiling 12 M HNO_3	Ti-5%Ta alloy showed lower corrosion rate than CP Ti	[81]/ 1996
Zircaloy-4 Commercially pure (CP)-Ti Ti–5%Ta alloy Ti–5%Ta–1.8%Nb alloy	Boiling 11.5 M HNO_3.	It was reported that Zircaloy-4 exhibits excellent corrosion resistance than Ti based alloys	[82]/ 2007
$Ni_{60}Nb_{15}Zr_5Ti_{15}Ta_5$ alloy NAR-310Nb stainless steel (SS)	Boiling 6 N HNO_3 Boiling 6N HNO_3 + 5 g/l Cr^{+6}	It was found that $Ni_{60}Nb_{15}Zr_5Ti_{15}Ta_5$ glassy alloy exhibits better corrosion resistance than NAR-310Nb SS	[83]/ 2008
$Ni_{60}Nb_{20}Zr_{20}$ alloy $Ni_{57}Nb_{19}Zr_{19}Ta_5$ alloy NAR-310Nb stainless steel (SS)	Boiling 6 N HNO_3 Boiling 6N HNO_3 + 5 g/l Cr^{+6}	$Ni_{57}Nb_{19}Zr_{19}Ta_5$ glassy alloy exhibited superior corrosion resistance among all investigated alloys	[44]/ 2009

Alloy	**Medium**	**Results/ Major findings**	**Ref./ Year**
$Ni_{65}Cr_{15}P_{16}B_4$ $Ni_{65}Cr_{10}P_{16}B_4Ta_5$ $Ni_{60}Nb_{20}Zr_{20}$ $Ni_{57}Nb_{19}Zr_{19}Ta_5$ $Ni_{60}Nb_{15}Zr_5Ti_{15}Ta_5$ $Fe_{43}Cr_{16}Mo_{16}C_{15}B_{10}$ $Fe_{43}Cr_{11}Mo_{16}C_{15}B_{10}Ta_5$	Boiling 9 N HNO_3 Boiling 9N HNO_3 + 5 g/l Cr^{+6}	It was reported that Ni-based glassy alloys shows better corrosion resistance than Fe-based glassy alloys	[84]/ 2009
Ti–5%Ta–1.8%Nb alloy	Boiling 11.5 M HNO_3	It was reported that alloy possesses good corrosion resistance in 11.5 M HNO_3 acid	[85]/ 2010
Zirconium-702 Zr-4 Autoclaved Zr-4 Commercially pure (CP)-Ti	Boiling 11.5 M HNO_3	It was found that autoclaved Zr-4 exhibited lowest corrosion rate among all investigated alloys	[86]/ 2015
$Ni_{60}Nb_{40}$ glassy alloy $Ni_{60}Nb_{30}Ta_{10}$ glassy alloy	Boiling 11.5 M HNO_3 11.5 M HNO_3 + 0.05 M NaF	It was reported that $Ni_{60}Nb_{30}Ta_{10}$ exhibits high corrosion resistance in both solutions	[43]/ 2015
Zr-1Nb-xGe (x = 0, 0.05, 0.1 and 0.2,wt%) alloys	Deionized water at 360° C/18.6 MPa	Zr-1Nb-0.05Ge alloy showed the higher corrosion resistance in comparison to Zr-1Nb alloy	[87]/ 2016
Zircaloy-4 Commercially pure (CP)-Ti	Boiling 11.5 M HNO_3 + 0.05 M NaF (contains $Al(NO_3)_3$ and $ZrO(NO_3)_2$)	CP-Ti exhibited better corrosion resistance than Zircaloy-4 in boiling 11.5 M HNO_3 + 0.05 M NaF containing 0.15 M $ZrO(NO_3)_2$	[88]/ 2016

2.4 Effect of different ion beam irradiation/implantation on amorphous $Zr_{55}Cu_{30}Ni_5Al_{10}$ alloy

Many irradiation/implantation investigations have been performed on Zr-based glassy alloys using various ion beams of different energies to understand the influence of irradiation/implantation on mechanical, corrosion and thermal properties of amorphous alloys. Researchers have mainly focused on mechanical properties of Zr-based alloy after ion irradiation/implantation. Limited investigations have been carried out to understand the effect of irradiation/implantation on corrosion properties of Zr-based amorphous alloys. Some important investigations of ion beam interaction with amorphous $Zr_{55}Cu_{30}Ni_5Al_{10}$ alloy are listed in tabular form.

Table 2.3: Effect of ion beam irradiation/implantation on $Zr_{55}Cu_{30}Ni_5Al_{10}$ amorphous alloy

Alloy	**Ion beam**	**Energy**	**Crystallization (Yes/No)**	**Irradiation/ Implantation effect**	**Ref./ Year**
$Zr_{55}Cu_{30}Ni_5Al_{10}$ bulk	Ga^+ Ar^+	30 keV	No	Enhanced etch rate and decreased corrosion resistance	[89]/ 2006
$Zr_{55}Cu_{30}Ni_5Al_{10}$ ribbon	H^+ Cu^+ Au^+ Ag^+	150 keV 350 keV 500 keV 350 keV	No	Crystalline peaks occurred after heat treatment of irradiated samples due to increase of nucleation sites.	[90]/ 2007
$Zr_{55}Cu_{30}Ni_5Al_{10}$ ribbon	Ar^+	10 keV	Yes	Hardness and elastic modulus increased	[91]/ 2007
$Zr_{55}Cu_{30}Ni_5Al_{10}$ plate	Co^+	40 keV	No	Surface micro hardness increased	[92]/ 2009

Alloy	Ion beam	Energy	Crystallization (Yes/No)	Irradiation/ Implantation effect	Ref./ Year
$Zr_{55}Cu_{30}Ni_5Al_{10}$ plate	Co^+	40 keV	No	Enhancement in the thermodynamic stability and supercooled liquid region	[93]/ 2009
$Zr_{55}Cu_{30}Ni_5Al_{10}$ ribbon	Cu^+	1 MeV	Yes	Enhancement in the ductility of the alloy was reported	[94]/ 2009
$Zr_{55}Cu_{30}Ni_5Al_{10}$ bulk	Ar^+	1 keV	No	The improvement in bonding quality of the irradiated BMG with pure Al was reported and the joint tensile strength was improved after irradiation	[95]/ 2013
$Zr_{55}Cu_{30}Ni_5Al_{10}$ bulk	Ar^+	1 keV	No	The improvement in bonding quality of irradiated BMG with pure Cu was reported and the joint tensile strength was improved after irradiation	[96]/ 2014

2.5 Effect of oxygen ion implantation on corrosion behavior of various materials

Oxygen implantation studies have not been carried out on Zr-based bulk amorphous alloys till date. However, a limited studies have been reported in the literature regarding corrosion investigations of oxygen ion implantation on other alloys such as commercially pure (CP)-Ti, Ti-based alloys, which are shown in tabular form.

Table: 2.4: Effect of oxygen ion implantation on corrosion behavior of various materials

Material	**Ion beam / Energy**	**Fluence (ions/cm^2)**	**Investigations**	**Results/ Major findings**	**Ref./ Year**
OT-4-0 Titanium alloy ($Ti_{98}Fe_{0.09}N_{0.0059}$ - $V_{0.04}Al_{0.67}Co_{0.01}$ - $Cu_{0.002}Ni_{0.03}Cr_{0.01}$- $S_{0.001}Si_{0.01}Mn_{0.71}$- $C_{0.01}$) wt%	O^+ 50 keV	5×10^{16} 1×10^{17}	Potentiodynamic polarization studies in NaCl medium	It was reported that corrosion resistance improves after implantation	[97]/ 1997
Ti-5%Ta-2%Nb DOCTOR-Ti (double oxide coating on titanium for reconditioning)	O^{+5} 116 MeV	1×10^{17} 1×10^{18} 1×10^{19}	Electrochemical measurements in 11.5M HNO_3	Corrosion resistance of both alloys improved with increasing fluence of implantation and oxide layer stability is enhanced	[98]/ 2008
Commercially pure (CP)-Ti	O^{+5} 116 MeV	1×10^{13} 1×10^{14} 1×10^{15}	Electrochemical measurements in 11.5M HNO_3	It was reported that the corrosion resistance of CP-Ti is decreased after irradiation	[99]/ 2011

2.6 Effect of nitrogen ion implantation on corrosion behavior of various materials

Researchers have shown more interest in surface modification of amorphous alloys using nitrogen ion implantation methods to improve the corrosion resistance of alloys. The influence of nitrogen ion implantation on corrosion properties of various materials has been extensively

studied. Some of the important corrosion investigations on various materials after nitrogen implantation are mentioned in tabular form.

Table: 2.5: Effect of nitrogen ion implantation on corrosion behavior of various materials

Material	**Ion beam/ Energy**	**Fluence (ions/cm^2)**	**Investigation**	**Results/ Major findings**	**Ref./ Year**
Al	N_2^+ 30 keV	1 x 10^{17} 5 x 10^{17} 9.9 x 10^{17}	Electrochemical measurement in NaCl solution	Improvement in corrosion resistance	[100]/ 1987
Ti	N^+ 100 keV	5 x 10^{17}	Electrochemical measurement and Immersion test in HCl, H_2SO_4, HNO_3	Improvement in corrosion resistance after ion implantation	[101]/ 1988
Zircaloy-4	N^+ 100 keV 120 keV	1 x 10^{17} 3 x 10^{17} 1 x 10^{18}	Electrochemical measurement in NaCl solution	The alloy exhibited improvement in the corrosion resistance	[52]/ 1995
OT-4-0 Titanium alloy ($Ti_{98}Fe_{0.09}N_{0.0059}$ - $V_{0.04}Al_{0.67}Co_{0.01}$ - $Cu_{0.002}Ni_{0.03}Cr_{0.01}$- $S_{0.001}Si_{0.01}Mn_{0.71}$- $C_{0.01}$) wt%	N_2^+ 50 keV	1 x 10^{17} 6 x 10^{17}	Electrochemical study in NaCl and H_2SO_4 solutions	Improvement in corrosion resistance of the alloy after ion implantation	[102]/ 1996
Zircaloy-4	N^+ 120 keV	3 x 10^{17}	Electrochemical measurements in NaCl solution	Improvement in corrosion resistance of Zircaloy-4	[103]/ 1997

Material	**Ion beam/ Energy**	**Fluence (ions/cm^2)**	**Investigation**	**Results/ Major findings**	**Ref./ Year**
304 type stainless steel (SS)	N^+ 70 keV	1 x 10^{16} 1 x 10^{17}	Electrochemical measurement in NaCl and H_2SO_4 solutions	Improvement in corrosion resistance at high fluence of implantation	[104]/ 1999
Zircaloy-4	$N^+ + N_2^+$ 120 keV	2 x 10^{17} 5 x 10^{17} 1 x 10^{18}	Immersion test in high temp. water at 350º C	Improvement in corrosion resistance up to 5 x 10^{17} ions/cm^2 fluence	[105]/ 2000
304L stainless steel (SS)	N^+ 70 keV	1 x 10^{15} 1 x 10^{16} 1 x 10^{17} 2.5 x 10^{17}	Electrochemical measurement in 1 M HNO_3	Corrosion resistance of 304L SS was improved	[106]/ 2010
Ti	N^+ 30 keV	5 x 10^{16} 1 x 10^{17} 3 x 10^{17} 6 x 10^{17} 8 x 10^{17}	Electrochemical measurement in NaCl solution	Implanted Ti exhibited improvement in corrosion resistance up to 1x10^{17} ions/cm^2 fluence	[107]/ 2010
$Ti_{60}Ni_{40}$ alloy	N^+ 150 keV	1 x 10^{16}	Potentiodynamic polarization studies in 1M HNO_3	Improvement in corrosion resistance of the alloy	[108]/ 2011

2.7 Research gap

Based upon the literature survey, the following areas are identified as a research gap which needs to be investigated:

- ✓ Even though enough corrosion investigations have been carried out on Zr based bulk amorphous alloys in different aqueous environments, inspite of this Nb-containing Zr-based bulk amorphous alloy has not been studied in nitric acid environment.
- ✓ Few corrosion investigations on Ni-based bulk amorphous alloys and Ti-based amorphous alloys have been carried out in boiling nitric acid environment but corrosion behavior of Zr-based bulk amorphous alloy in boiling nitric acid medium has not been addressed till date.
- ✓ Surface modification of amorphous alloys using ion irradiation/ion implantation methods is well known technique to improve the corrosion resistance of alloy. But influence of O^+ and N^+ ion implantation on corrosion behavior of Zr-based bulk amorphous alloy has not been taken up so far by any of researcher and this could be an important finding in this area and able to generate database.

CHAPTER-3

Materials, Methods and Characterization Techniques

The chapter introduces to the composition of Zr-based amorphous alloys used for the investigation. This chapter comprises the details about the casting methods of amorphous alloys, experimental techniques used for testing the corrosion behavior and surface modification and characterization techniques. A detailed specific description about the various characterization techniques such as X-Ray Diffraction (XRD), Optical Microscopy, Scanning Electron Microscopy (SEM), Energy-dispersive spectroscopy (EDS), Atomic Force microscopy (AFM) and X-ray Photoelectron Spectroscopy (XPS); which have been used to accomplish the present research work.

3.1 Composition of Zr-based bulk amorphous alloys

The different compositions of Zr-based bulk amorphous alloys were used to achieve the objective of present research work. Besides the bulk amorphous $Zr_{55}Cu_{30}Ni_5Al_{10}$ alloy which is the main material of the present study, some other compositions of Zr-based bulk amorphous alloys such as $Zr_{60}Nb_2Cu_{20}Ni_8Al_{10}$, $Zr_{59}Nb_3Cu_{20}Ni_8Al_{10}$, $Zr_{57}Nb_5Cu_{20}Ni_8Al_{10}$ and $Zr_{60}Pd_5Cu_{15}Ni_{10}Al_{10}$ were also studied. The corrosion behavior of these Zr-based bulk amorphous alloys was tested in aqueous oxidizing medium. The chemical composition (at% and wt%) of these alloys are as given in Table 3.1.

Table 3.1: The chemical composition (at% and wt%) of Zr-based bulk amorphous alloys

Element	$Zr_{55}Cu_{30}Ni_5Al_{10}$ Alloy	$Zr_{60}Nb_2Cu_{20}Ni_8Al_{10}$ Alloy	$Zr_{59}Nb_3Cu_{20}Ni_8Al_{10}$ Alloy	$Zr_{57}Nb_5Cu_{20}Ni_8Al_{10}$ Alloy	$Zr_{57}Nb_5Cu_{15.4}Ni_{12.6}Al_{10}$ Alloy	$Zr_{60}Pd_5Cu_{15}Ni_{10}Al_{10}$ Alloy	$Zr_{59}Ti_3Cu_{20}Ni_8Al_{10}$ Alloy
	Content (wt%)	Content (wt%)	Content (wt%)	Content (wt%)	Content (wt%)	Content (wt%)	Content (wt%)
Zr	67.01	71.37	70.16	67.74	67.95	7.51	71.42
Cu	25.46	16.57	16.57	16.57	12.79	12.20	16.86
Ni	3.92	6.12	6.12	6.12	9.66	70.03	6.23
Al	3.61	3.52	3.52	3.52	3.53	3.45	3.58
Nb	0.0	2.42	3.63	6.05	6.07	0.0	0.0
Pd	0.0	0.0	0.0	0.0	0.0	6.81	0.0
Ti	0.0	0.0	0.0	0.0	0.0	0.0	1.91

3.2 Sample preparation

The bulk amorphous $Zr_{55}Cu_{30}Ni_5Al_{10}$ alloy was prepared in ribbon and strip shape. The casting of the samples was carried out at UGC-DAE, IGCAR Kalpakkam using Edmund Buhler GmbH system (shown in figure 3.1). The preparation of samples follows different steps as outlined below:

Figure 3.1: Overview of metallic glass casting system at IGCAR Kalpakkam

3.2.1 Materials

The following elemental materials are used to prepare the bulk amorphous $Zr_{55}Cu_{30}Ni_5Al_{10}$ alloy; Zr granules (Zr; 99.98% purity, Alfa Aesar), Cu granules (Cu; 99.99% purity, Alfa Aesar), Ni granules (Ni; 99.99% purity, Alfa Aesar), Al granules (Al; 99.99% purity, Alfa Aesar). All the elemental granules were taken in equal size of 5 mm.

3.2.2 Preparation of ingot by arc melting technique

The sample casting was carried out by preparing an ingot of bulk amorphous $Zr_{55}Cu_{30}Ni_5Al_{10}$ alloy using arc melting system (figure 3.2). The total mixtures of desired composition was

obtained by weighing a total quantity of 10 g. This mixure of elements were cleaned with ethenol and placed on the copper hearth which was connected to a chiller for rapid quenching. This entire chamber was evacuated and backfilled with high purity Ar gas to attain desired vacuum level. The ingots were remelted four times to ensure the chemical homogeneity. After preparing the ingot, mass of ingot was checked which was almost equal to 10 g. This ensures that no mass loss has taken place during arc melting process. The vacuum level of this entire chamber was kept at 3.5 x 10^{-4} mbar. Diffusion and turbo pump were used to reach such a high vacuum level.

Figure 3.2: Ingot of bulk amorphous $Zr_{55}Cu_{30}Ni_5Al_{10}$ alloy

3.2.3 Casting of ribbon sample by melt spinning method

The ingots were cut into many small pieces using diamond cutting machine. These small pieces were cleaned with ethanol and dried in air. Appropriate amount of cut pieces of ingot were placed in a quartz crucible which has a small nozzle. These ingot pieces were remelted and melt stream was impinged onto a rotating copper wheel through a nozzle by applying an over pressure of 300 mbar. This copper wheel was connected to a chiller for rapid quenching process and rotated with the speed of 20 m/s. Figure 3.3 (a) shows a schematic diagram of melt-spinning apparatus. Prepared glassy ribbons were collected in the collection chamber.

The whole chamber was evacuated and back-filled with high purity Ar gas. The evacuation is achieved by turbo pump and rotary vane pump. The resulting $Zr_{55}Cu_{30}Ni_5Al_{10}$ ribbon samples of thickness of about 30 μm and 7 mm width were obtained using melt spinning system as shown in figure 3.3 (b).

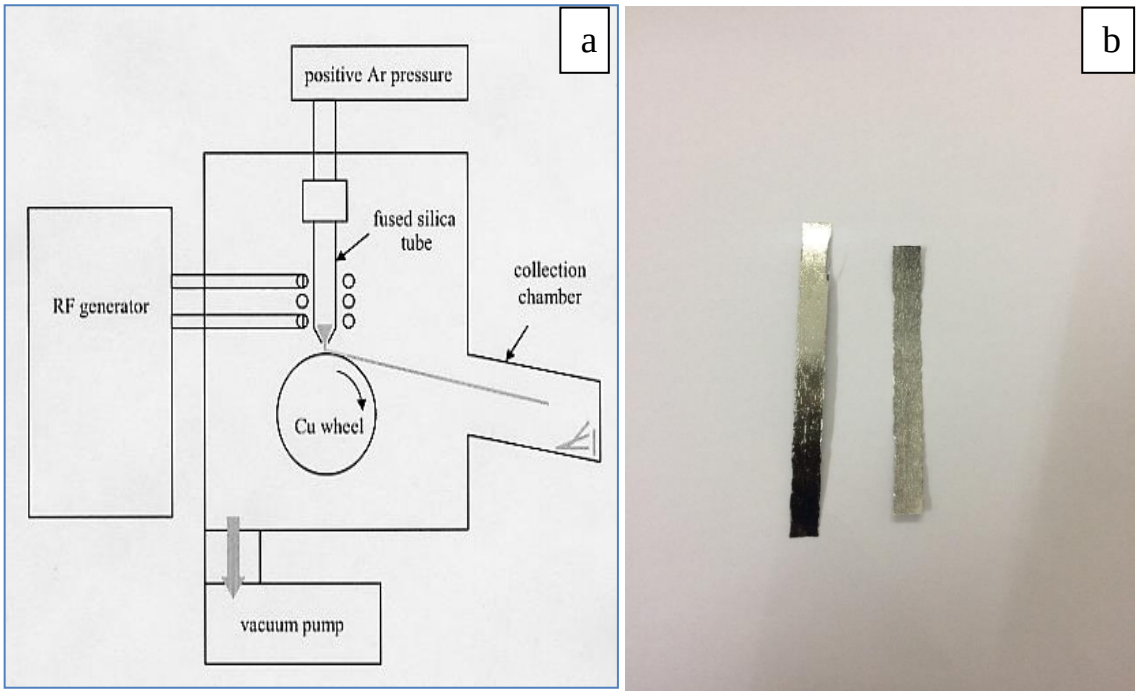

Figure 3.3: (a) Schematic diagram of melt spinning apparatus and (b) image of $Zr_{55}Cu_{30}Ni_5Al_{10}$ ribbon sample

3.2.4 Casting of rod/strip sample by suction casting method

The suction casting technique was used to cast bulk specimens in rod or strip shape. In this present work, strip shape of $Zr_{55}Cu_{30}Ni_5Al_{10}$ samples were prepared. Figure 3.4 (a) shows a schematic diagram of suction casting apparatus. The ingots were cut into small pieces using diamond cutter and appropriate amount of ingot pieces were placed on the copper mold. The ingot pieces were then remelted and cast into water-cooled copper mold of strip dimensions of 27 mm x 5 mm x 2 mm using suction casting method. The chamber was evacuated and back-filled with a high purity Ar gas. The vacuum level was mantained at 3.5 x 10^{-5} mbar

with the help of turbo and rotary pump. The strip shaped $Zr_{55}Cu_{30}Ni_5Al_{10}$ samples (shown in figure 3.4 (b)) were obtained.

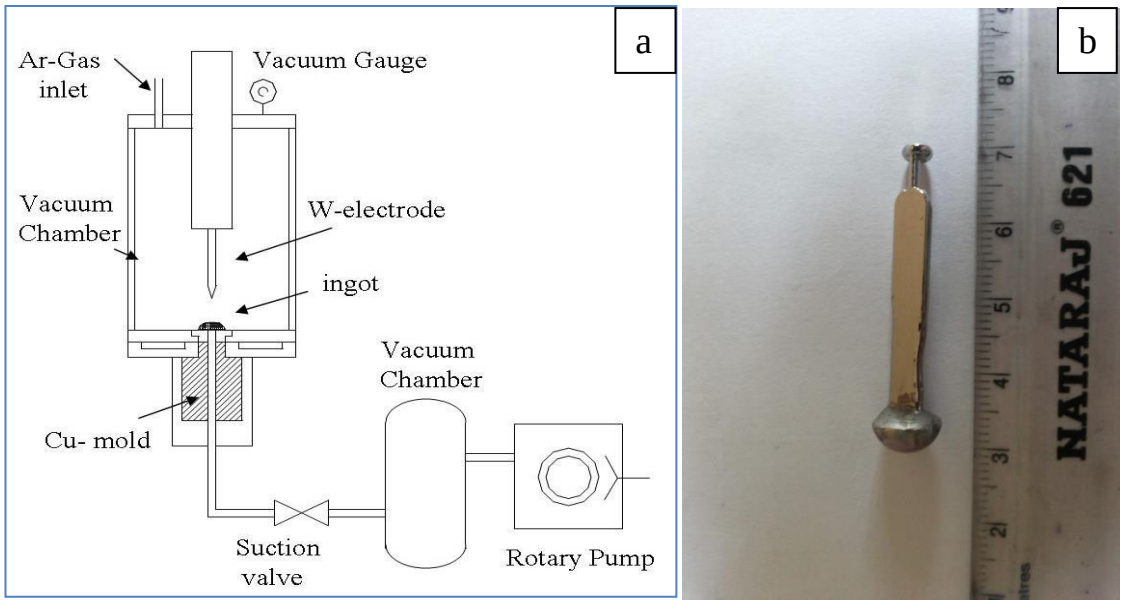

Figure 3.4: (a) Schematic diagram of suction casting apparatus (b) image of strip shaped $Zr_{55}Cu_{30}Ni_5Al_{10}$ samples.

3.3 Corrosion study

3.3.1 Definition of corrosion and classification

Corrosion is basically the destruction or deterioration of a metal surface by chemical or electrochemical reaction with its environment [109]. A general example of corrosion is rusting, which is basically the deterioration of iron due to oxidation of iron atoms. Corrosion can be a fast or slow process depending upon the nature of the environment. General categorization of corrosion is schematically represented in figure 3.5.

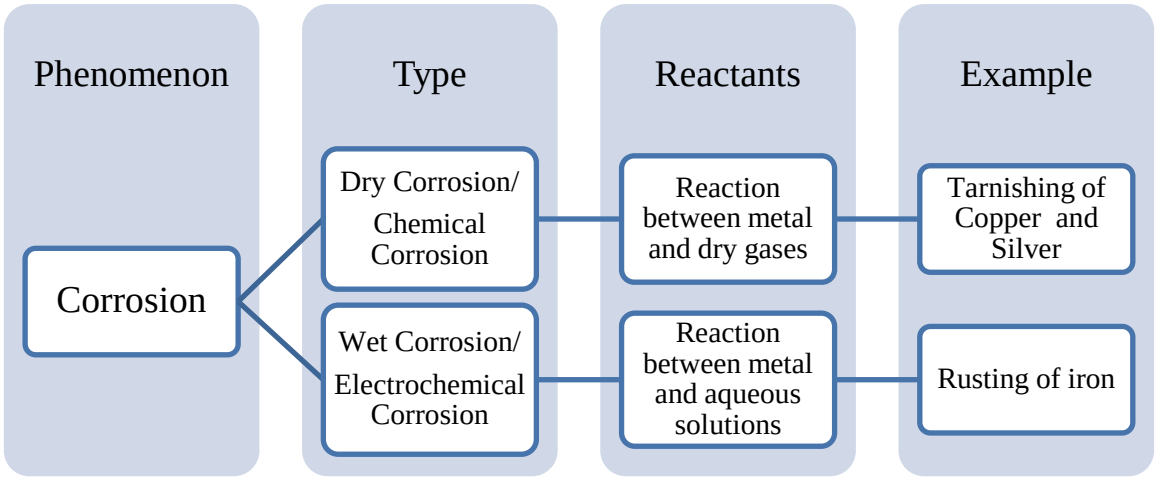

Figure 3.5: Flow chart of categories of corrosion

In general, most types of corrosion occur by electrochemical mechanisms. Electrochemical corrosion involves the flow of electrical current from one point to another point through some perceptible distance. This electric current arises due to the potential difference between different points on the surface of metal.

Corrosion can be further classified in eight forms on the basis of external appearance or changes in the physical properties of involved material. These forms of corrosion are as follows:

i. **Uniform corrosion:** It is also referred as "general" corrosion. In this type of corrosion, the reaction starts on the exposed surface of material and proceeds uniformly. The entire exposed surface experiences uniform thinning of metallic surface due to corrosion attack. Most prevalent example of uniform corrosion are rusting of iron or tarnishing of silver which can be observed in our daily life.

ii. **Galvanic corrosion:** Galvanic corrosion occurs between two coupled dissimilar materials in the presence of a common electrolyte due to electrochemical reaction. These two dissimilar metals possess different surface potential in the electrolyte, which causes the flow of galvanic current. In galvanic corrosion, the less noble or

more active material work as a anode and undergo accelerated corrosion, whereas another material which is more noble or less active, serves as a cathode and experiences reduced corrosion effects. The selection of noble or active material is based on the galvanic series.

iii. **Crevice corrosion:** Crevice corrosion is a form of localized corrosion which arises due to presence of small gap or space between two metal- metal joints or metal-non-metal contacts. For example, it usually occurs at washers, lap joints, under protective coatings, clamps and at threaded joints. Basic mechanism behind crevice corrosion is establishment of oxygen differential cells in the crevice region. In this process, oxygen is trapped within the crevice and this area becomes anodic relative to bulk area exposed to electrolyte. This complete process results into metal dissolution at a very high rate.

iv. **Pitting corrosion:** This type of corrosion involves aggressive localized corrosion attack producing microscopic defects in the form of pits or holes on a metal surface. The initiation of pitting corrosion takes place by breaking down of passivity at preferred minor site due to lack of oxygen in this area. This minor area behaves like an anode and rest passive area works as cathode leading to flow of current due to formation of the electrolytic cell. These pits propagate into depth of the material rather than spreading due to protective passive film surrounding the anode. This form of corrosion is highly dangerous, as it perforates the material with a rapid speed.

v. **Intergranular corrosion:** Intergranular corrosion is also called IGC involves the corrosion attack on or adjoining area of the grain boundaries of the metal. The boundaries of grains act as anode and the remainder large area of grains acting as cathode, forms an electrolytic cell. So, grain boundaries will have a tendency to undergo accelerated corrosion. The mechanism behind IGC corrosion is usually

related to chemical segregation of solute atoms or a precipitated phase at the grain boundary. This precipitation can produce very reactive zones in the immediate vicinity, which lead to a rapid intergranular corrosion. In this type of corrosion, the corrosion attack propagates along the trajectory of grain boundaries.

vi. **Selective leaching:** This process involves the preferential removal of electrochemically active element from an alloy. It is also known as “Dealloying” or “Parting corrosion”. This corrosion occurs due to the potential difference between the electrochemically active and the noble element. A well-known example of dealloying is “dezincification”. In the dezincification of brass, zinc undergoes preferential removal leaving behind a relatively weak layer of copper and oxides of copper.

vii. **Erosion corrosion:** In this type of corrosion, the removal of metal surface occurs due to mechanical force such as wall shear stress generated by flowing fluid. The velocity and direction of fluid has direct impact on severity of erosion corrosion. Erosion corrosion can be easily seen at turbines, pumps, elbows, oil or petroleum pipes and any other structural tools that are used to change the velocity or direction of flowing fluid.

viii. **Stress corrosion cracking:** This type of corrosion involves slow propagation of crack induced by mechanical stress of tensile nature under specific environmental conditions. Stress corrosion cracking process, generally referred as SCC, comprises three main stages i) initiation of crack in the direction normal to the tensile stress axis, ii) steady-state crack propagation and iii) crack propagation and final failure. The rate of crack growth can be influenced by environmental parameters such as pressure, temperature, pH and viscosity of the aqueous solution. Pure metals have a low tendency of showing stress corrosion cracking.

3.3.2 Basic mechanism of electrochemical corrosion

Electrochemical corrosion is a most common corrosion phenomenon which involves the release of ions into the electrolyte and the flow of electrons through the material. This process involves oxidation or anodic reaction and reduction or cathodic reaction. For example zinc metal dissolves in hydrochloric acid, forming zinc chloride solution, which can be expressed by following chemical reaction:

$$Zn + 2HCl \rightarrow ZnCl_2 + H_2 \tag{3.1}$$

The equation 3.1 is a generalized form of the chemical reaction of Zn in HCl aqueous solution. This reaction does not involve chloride ions; the simplified form of this reaction can be written as:

$$Zn + 2H^+ \rightarrow Zn^{+2} + H_2 \tag{3.2}$$

Abovementioned equation 3.2 involves two reactions; oxidation of Zn and reduction of hydrogen ions and can be written as:

$$Zn \rightarrow Zn^{+2} + 2e \tag{3.3}$$

$$2H^+ + 2e \rightarrow H_2 \tag{3.4}$$

Equation 3.3 is the oxidation or anodic reaction which shows the production of electrons and equation 3.4 is the reduction or cathodic reaction which involves the consumption of electrons. So, metallic corrosion would take place if rate of oxidation is equal to the rate of reduction. This is a basic principle of corrosion [109]. In general form, oxidation of a metal M to its ions M^{+n}, is a common anodic reaction in every metallic corrosion reaction and it can be written as:

$$M \rightarrow M^{+n} + ne \tag{3.5}$$

During corrosion, one or more than one oxidation and reduction reactions may occur.

3.3.3 Quantitative corrosion evaluation

The quantitative evaluation of corrosion reaction of any metallic material in aqueous solution can be done by using electrochemical cell and potentiostat. The electrochemical cell is an assembly which consist a container holding the electrodes and the electrolyte. The electrochemical cell consists of three electrodes:

i. Working electrode: The material, whose corrosion properties have to be determined, is known as a working electrode. The electrochemical reactions occur at working electrode (test electrode).
ii. Reference electrode: The potential of working electrode is measured using reference electrode. The most commonly used reference electrodes is (Ag/AgCl) electrode.
iii. Counter electrode: It is also known as auxiliary electrode, which is used as electronic conductor to complete the electrochemical cell circuit. A very noble metal platinum is used as a counter electrode

The electrolyte, filled in the electrochemical cell, is the environment in which corrosion property of the working electrode are being studied. The schematic representation of the electrochemical cell is shown in figure 3.6 [110]. It is not favorable to directly measure the potential of working electrode by placing the reference electrode near to working electrode. So, a luggin capillary is used to separate the reference and working electrode and the luggin probe tip is adjusted close to working electrode which minimizes the ohmic resistance interference. This electrochemical cell is connected to a potentiostat. The potentiostat is an electronic device, which is used to measure and control the potential of electrochemical cell by the means of changes in the resistance. In other words, potentiostat varies the potential of working electrode and records the corresponding currents. Polarization is one of the

mechanisms, which permits to study the corrosion reactions and kinetics of corrosion phenomenon. Basically polarization is a shift of electrode potential from equilibrium potential due to electrochemical reaction [110]. Potentiodynamic polarization is an important measurement technique, which involves the change in working electrode potential at a selected rate and observing the current as a function of potential. The plot between applied potential and current is called polarization curve and is effectively used to determine the corrosion resistance of metals.

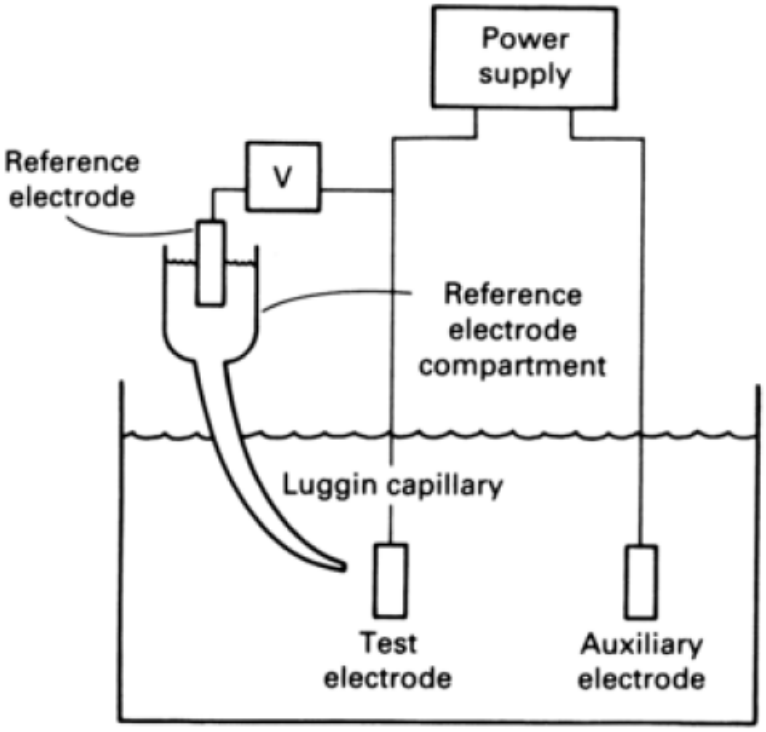

Figure 3.6: Schematic diagram of 3-electrode electrochemical cell [110]

The polarization curve consist anodic and cathodic arms due to anodic and cathodic reactions. These polarization curves generally plotted in the form of log i versus E by taking the logarithm of absolute current (log i) on horizontal axis and potential (E) on vertical axis. These types of curves are called Evans diagrams, which exhibit two linear portions that are known as Tafel regions. In order to determine the corrosion current from these curves, the current from anodic and cathodic Tafel regions is extrapolated to the corrosion potential

(E_{corr}) as shown in figure 3.7 [111]. At E_{corr}, the hydrogen evolution and metal dissolution, both processes take place at equal rate and at this point the value of current per unit area is termed as corrosion current density (I_{corr}). The corrosion current density is a key parameter to understand the corrosion behavior of a metal or alloy in respective environment.

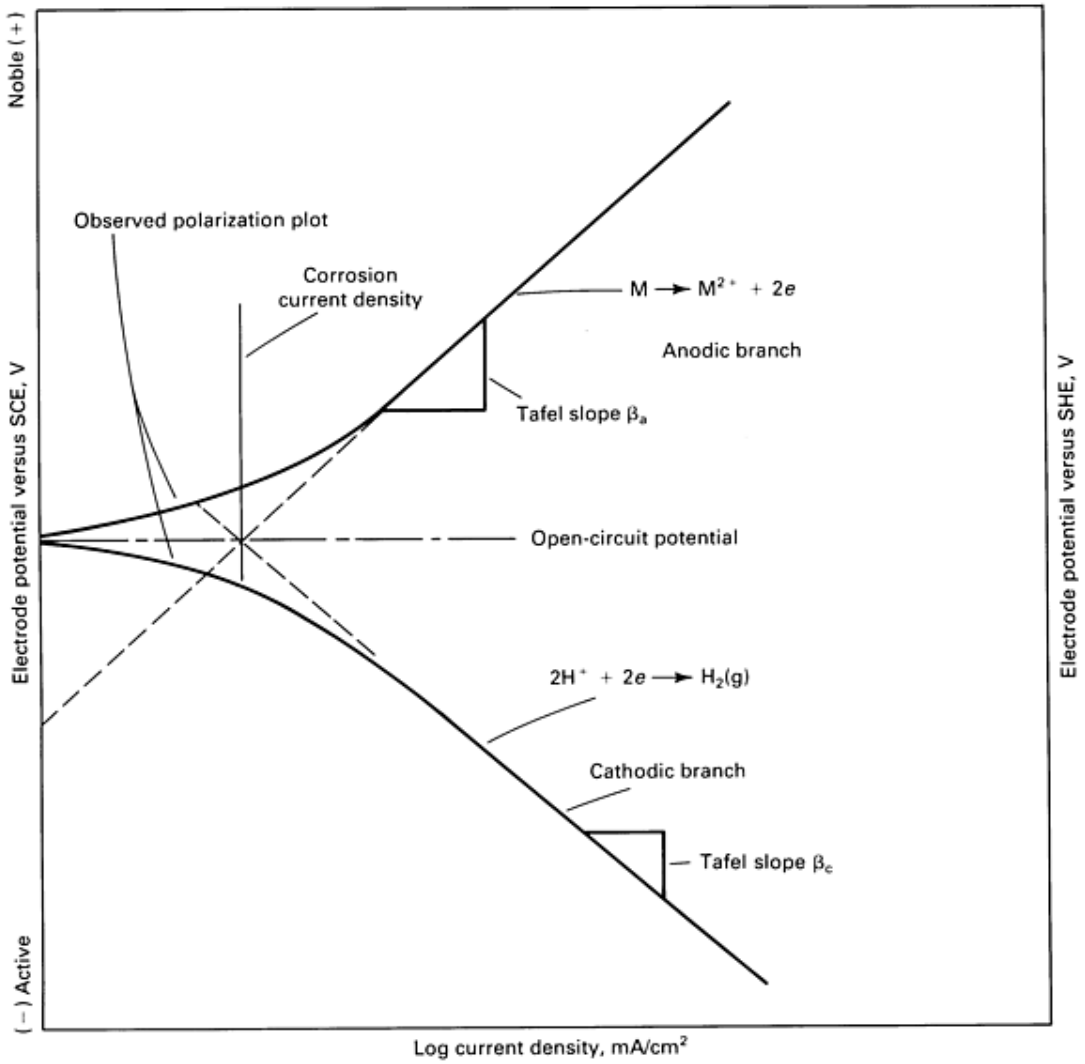

Figure 3.7: Classic Tafel Analysis [111]

An electrochemical reaction under kinetic control obeys the following Tafel equation:

$$I = I_0 e^{2.3\left(\frac{E-E_0}{\beta}\right)} \tag{3.6}$$

In the equation 3.6, I is the current caused by electrochemical reaction, I_0 is exchange current density which is equal to the rate of metal dissolution, the electrode potential is E, the equilibrium potential is E_0 and β is the reaction Tafel Constant. This Tafel equation is capable in explaining the behavior of one isolated reaction. In a corrosion system, there is an involvement of two opposing anodic and cathodic reactions. So, according to Butler-Volmer, the combined Tafel equations for a corrosion system will be:

$$I = I_{corr}\left[\left(e^{2.3\left(\frac{E-E_{corr}}{\beta_a}\right)}\right)-\left(e^{-2.3\left(\frac{E-E_{corr}}{\beta_c}\right)}\right)\right] \tag{3.7}$$

Where, I_{corr} is the corrosion current, E is the electrode potential, E_{corr} is the corrosion potential, β_a is the anodic Beta Tafel constant, β_c is the cathodic Beta Tafel constant. The value of I_{corr} can be determined from this equation 3.7, which is called Butler-Volmer equation. The value of I_{corr} is very beneficial for a corroding system to study the corrosion behavior of the system and the value of corrosion rate can also be determined with the help of I_{corr} value. The corrosion rate (CR) in mils per year (mpy) can be calculated from the corrosion current density (I_{corr}) in $\mu A/cm^2$ by the following equation:

$$CR = 0.129\frac{I_{corr}}{\rho}(EW) \tag{3.8}$$

where, ρ is the alloy density ($gram/cm^3$) and EW is the alloy equivalent weight (gram/equivalent).

3.3.4 Electrolytes for corrosion study

The electrolytes used in this study were 1 M aqueous HNO_3, 6 M aqueous HNO_3 and 11.5 M aqueous HNO_3, 1 M aqueous H_2SO_4 and mixture of 1 M H_2SO_4 and 0.5 M NaCl. All solutions used in this study were prepared with analytical grade reagents and double distilled

water. The nitric acid solutions were prepared from Ranbaxy make analytical grade chemical reagent of specific gravity 1.41, and maximum permissible impurity of sulphate and chloride was around 0.00005 %.

3.3.5 Corrosion testing at room temperature

3.3.5.1 Potentiodynamic polarization study

Potentiodynamic polarization study is a most effective method to understand the corrosion behavior of any metallic material and corrosion reactions happening on the surface of material in corrosive environment. It gives the potential-current relationship of the material in corrosive environment which characterizes the corrosion behavior of the material. It works on the mixed potential theory, according to which the total rates of oxidation and reduction must be equal. The potential at which both these reactions are equal is called corrosion potential (E_{corr}) and the corresponding current density is called corrosion current density (I_{corr}). The value of corrosion current density is determined by Tafel Extrapolation Method [112]. The potentiodynamic polarization study also provides essential information regarding the passive nature of the material in any medium.

In the present research work, polarization experiments were carried out for unimplanted Zr-based bulk amorphous $Zr_{55}Cu_{30}Ni_5Al_{10}$, $Zr_{60}Nb_2Cu_{20}Ni_8Al_{10}$, $Zr_{59}Nb_3Cu_{20}Ni_8Al_{10}$, $Zr_{57}Nb_5Cu_{20}Ni_8Al_{10}$, $Zr_{57}Nb_5Cu_{15.4}Ni_{12.6}Al_{10}$, $Zr_{59}Ti_3Cu_{20}Ni_8Al_{10}$ and $Zr_{60}Pd_5Cu_{15}Ni_{10}Al_{10}$ alloys in different concentration of nitric acid. The corrosion behavior of oxygen implanted bulk $Zr_{55}Cu_{30}Ni_5Al_{10}$ amorphous alloy in 1 M H_2SO_4, 1 M HNO_3 and in mixture of 1 M H_2SO_4 and 0.5 M NaCl aqueous media and nitrogen implanted $Zr_{55}Cu_{30}Ni_5Al_{10}$ amorphous alloy in 1 M HNO_3 medium at different fluences of implantation were investigated by potentiodynamic polarization method. The experiments were conducted using a potentiostat (Autolab-AUT84276) which is connected with a three electrode

electrochemical cell; saturated calomel reference electrode, Pt counter electrode and specimen as working electrode. A luggin probe is used to separate the reference electrode from the solution and is placed close to the working electrode to eliminate the effect of solution resistance. The potentiostat was interfaced with Nova (version 1.9) software for conducting the polarization experiments. Both sides of the samples were cleaned with acetone and distilled water. Only defined surface area of the sample was exposed to electrolyte and the unexposed area was covered with the teflon tape. The open circuit potential (OCP) was monitored for 30 minutes before each polarization experiment. The open circuit potential (OCP) is the potential of the working electrode measured with respect to a reference electrode in the absence of any potential or current on the corrosion system [113]. At OCP, the cathodic and anodic reaction rates are in equilibrium in a given corrosive surrounding, if zero potential is applied and thus net current is zero. In general, OCP of an electrode refers to the thermodynamic tendency of that electrode (metallic materials) to participate in the electrochemical corrosion reactions. The shift of potential in the anodic direction is termed as noble potential. The metallic materials which have nobler OCP are more thermodynamically stable as compared to the materials which have less nobler OCP. It also gives the brief idea about the formation of passive film on the surface of material in the corrosive environment. The potentiodynamic polarization curves were recorded at the scanning rate of 1 mV/s from 200 mV below OCP to 2200 mV. All the electrode potentials were measured against Ag/AgCl (saturated KCl) reference electrode and it was ascertained that all the polarization plots were almost reproducible using NOVA software. The other important corrosion parameters such as corrosion potential (E_{corr}) and corrosion current density (I_{corr}) were obtained using Tafel slops of potentiodynamic polarization plots.

3.3.5.2 Weight loss analysis at room temperature

Weight loss measurement is a common method for determining uniform corrosion rate of a metal and its alloys immersed in a solution. The rate of attack for each material must be expressed quantitatively. The known area of metallic sample is exposed to the corrosive environment for definite time period and metal loss due to corrosion is measured using micro balance. In the present investigation, semi microbalance XS 205 DU, Mettler Toledo is used to measure the accurate weight loss and the corrosion rate (mm/y) can be calculated by the formula given below [109]:

$$CR(mm/y) = \frac{87.6}{DAT}W \tag{3.9}$$

Where, W - Weight loss in mg,

D - Density of the material in g/cm^3,

A - Area of the sample exposed to the corrosive environment in cm^2,

T - Time in hours.

The corrosion rate can be expressed in number of ways such as percentage weight loss, mils per year, milligrams per square centimeter per day and grams per square inch per hour. The most desirable way is mils per year and can be easily obtained from equation 3.9 using the following relation.

1 mils/year = 0.0254 mm/year

In the present research work, the corrosion rates of virgin Zr-based bulk amorphous ribbon samples; $Zr_{55}Cu_{30}Ni_5Al_{10}$, $Zr_{60}Nb_2Cu_{20}Ni_8Al_{10}$, $Zr_{59}Nb_3Cu_{20}Ni_8Al_{10}$, $Zr_{57}Nb_5Cu_{20}Ni_8Al_{10}$, $Zr_{60}Pd_5Cu_{15}Ni_{10}Al_{10}$ and $Zr_{55}Cu_{30}Ni_5Al_{10}$ were determined in different concentrations of nitric acid.

3.3.6 Corrosion testing at a higher temperature

Corrosion rates of Zr-based bulk amorphous alloys at high temperature were examined by weight loss analysis method. Prior to the experiment, the specimens were cleaned with acetone and distilled water and dried in air. The specimens were weighed before immersing them into the test solution of concentrated nitric acid in boiling condition. The experimental setup (figure 3.8) used for the experiment is discussed in Mudali et al. [80], in which, a conical flask is filled with nitric acid and is corked with a cold finger condenser and placed on a temperature regulating hot plate. The cold finger condenser was used to reflux the vapors of nitric acid back into the solution. The specimen was suspended into boiling HNO_3 through the Teflon tape. The change in the weight of specimen was observed after the each test and corrosion rate of the glassy alloy was calculated for each concentration using the aforementioned corrosion rate formula.

Figure 3.8: The experimental setup for high temperature corrosion studies

In the present research work, the corrosion rates of as spun ribbon specimens of $Zr_{59}Nb_3Al_{10}Ni_8Cu_{20}$ and $Zr_{60}Pd_5Al_{10}Ni_{10}Cu_{15}$ glassy alloys at high temperature were examined in different concentration of nitric acid. In the preliminary study the experiment was carried out initially for 8 hours and the study was further extended to find the corrosion rate of glassy alloys with nominal composition $Zr_{55}Cu_{30}Ni_5Al_{10}$, $Zr_{60}Nb_2Cu_{20}Ni_8Al_{10}$ and $Zr_{59}Nb_3Cu_{20}Ni_8Al_{10}$ using weight loss experiment in the corrosive medium of 11.5 M HNO_3 at boiling temperature for 24 h, 48 h and 72 h using above mentioned process.

3.4 Ion implantation

3.4.1 Setup

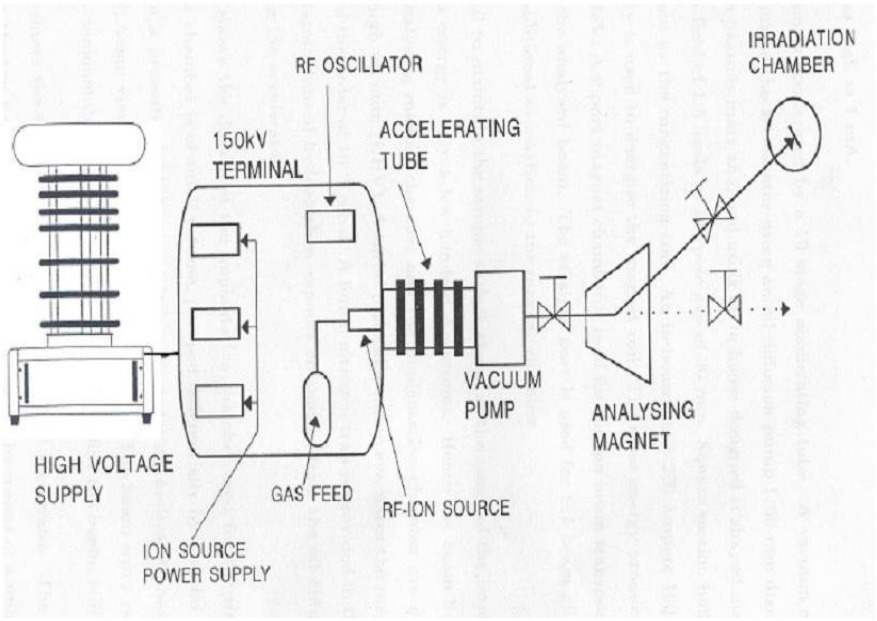

Figure 3.9: Layout of the low-energy ion accelerator at IGCAR, Kalpakkam.

The schematic layout of 100 keV ion accelerator is shown in figure 3.9. Ions are extracted at 5 keV from a RF (Radio Frequency, 100 MHz) ion source to produce positive gaseous ions. The positive ion beam is accelerated from a positive high voltage terminal to the target kept at ground potential. Cockroft –Walton voltage generator is used to produce the high voltage power (tunable from 10 to 150 kV). The beam is mass analysed by a 45^o bending mass

analyzing magnet. The accelerating tubes were maintained at high vacuum (~10^{-7} mbar) by the turbo molecular pump backed by the diffusion pump. The accelerated ion beam passes through an electrostatic quadrupole lens and a beam scanner to the target chamber. The target chamber was maintained at high vacuum i.e. below 2 x 10^{-7} torr and the sample holder was placed in this chamber where ion implantation takes place. The samples were stuck with copper tape on the sample holder and X-Y beam-rastering was used over 1 sq cm for uniform irradiations over samples. The beam current was kept below 2μA on the samples during the implantation to minimize the ion beam heating.

3.4.2 Surface modification by ion implantation

It has been well reported that surface treatments can alter the physical and chemical properties of any metallic surface and improve these properties. These treatments can be broadly classified into two categories: (i) covering the material surface with a coating (ii) altering the material surface by complete modification or slight modification in some specific region.

The first type of treatment involves organic coating such as lamination, paint or lubricant and inorganic coatings such as electrodeposition, thermal spraying, conversion coatings and hot dippings etc. This type of treatment has its own limitation depending on the nature of coating and is unable to make permanent changes on the surface of material. In the second type of treatment, various incident particles or ion beams are used, for example, shot peening, laser, flame, electron or ion irradiation/ implantation. Among these surface modification methods, ion implantation is an appealing method to improve the various properties of material, which involves the bombardment of energetic ions. In ion implantation process, the dense energy is deposited along the trajectory of ions which creates a non-equilibrium phase [114] and simultaneously introduces an additional element into the

material up to a limited depth. This additional element can interact with the constituent atoms and induce the changes in surface composition as well as can alter the chemical bond structure resulting into the formation of new metastable compounds [115].

3.4.3 Effect of irradiation/implantation

Irradiation is a process by which an object is exposed to radiation. The incident ions transfer its energy to the target object. The energy deposition takes place two processes: electronic excitations and nuclear collisions. At high energy of incident ions, the electronic energy losses dominates whereas, the nuclear stopping power predominates at low energies of ions [116]. Both the electronic and nuclear stopping depend on the atomic number and mass of the ion and target atoms, such that heavy ions penetrate to much shallower depths than light ions. Ion implantation is accomplished by bombarding the target with a beam of ions in the energy range from a few hundred keV to several MeV [117]. Irradiation is a complex process which may lead to generation of vacancies, ion sputtering, enhanced diffusivity, phase change, local heating, precipitate formation, etc.

Irradiation displaces an atom from its site, leaving a vacant site behind as vacancy and the displaced atom eventually comes to the rest in the interstices between lattice sites, becoming an interstitial atom [118]. A minimum amount of energy must be transferred to displace a lattice atom, creating a self interstitial and a vacancy. This displacement energy depends on the metal or alloy, the crystal structure, and direction of displacement. Irradiation also may cause sputtering which results from those nuclear collisions near the surface that give target atoms a sufficient momentum component in the direction away from the surface so that they exceed the surface binding energy. During irradiation, defects created (interstitials and vacancies) in non-equilibrium concentrations by the atomic displacement processes (e.g. cascades) may migrate by thermally activated diffusion at the ambient sample temperature. This is called radiation enhanced diffusion [119]. Typically only a few percent

of the interstitials and vacancies created escape the collision cascade for heavy ions, whereas a larger fraction are released for light ions.

3.4.4 Basics of ion implantation

In the ion implantation process, the energetic ions are bombarded on to the metallic substrate and these ions penetrate into the surface of substrate subsequently interacting with the substrate material. The depth of penetration depends on energy of projectile ions, which is generally in keV to MeV energy range. During this ion-substrate interaction, ions undergo collisions with target nuclei and loses their energy to the substrate via two processes [116] (i) kinetics energy of ions is directly transferred to target atoms by elastic collisions between target nuclei and projectile nucleus, this energy loss is commonly known as nuclear energy loss S_n (ii) transfer of energy to target electrons resulting in electronic excited atoms of target material, this process plays major contribution in energy loss of ions and called electronic energy loss S_e. The total distance travelled by the ion is called its Range (R) which depends on the rate of energy loss (dE/dx) and the value of R can be determined by following equation:

$$R = \int_{E_0}^{0} \frac{1}{-\left(\frac{dE}{dx}\right)} dE \tag{3.10}$$

Where, E_0 is the initial energy of incident ions. The total depth, normal to the surface, penetrated by the incident ion is called projected range and denoted by R_p. It is also known as penetration depth and depends on the energy of incident ions, mass of incident ions and substrate material.

Generally, ion irradiation/implantation leads to changes in the structure of crystalline metals and alloys by the formation of vacancies and interstitials but metallic glasses are not susceptible to this displacive irradiation/implantation due to their inherent disordered

structure. So, metallic glasses have widespread applications in irradiation environments, such as fusion, spallation sources, etc. In few cases, energetic ions displace the target atoms of metallic glasses from their initial sites and create some vacancy defects, which increase the free volume within the system, thus enhancing atomic mobility. This enhanced atomic mobility will lead to increased short-range order and subsequent nucleation resulting in crystal growth [120-121].

Hence, implantation or irradiation can induce the change in the composition of substrate and structure of the near surface region which results in the formation of new phases such as carbides, nitrides, oxides. These newly formed phases could be helpful in improving the corrosion behavior of metallic glasses.

3.4.5 Applications of ion implantation

Ion implantation has many intense engineering applications due to its ability of surface modification of the material. Ion implantation has also been greatly studied in the field of bulk amorphous alloys. It has been reported that ion implantation can significantly improve mechanical, corrosion and thermal properties of bulk amorphous alloys. Iqbal et al. [91] has found that Ar^+ ion implantation on $Zr_{55}Cu_{30}Al_{10}Ni_5$ bulk amorphous alloy reveals improvement in ductility and nanohardness. As far as corrosion properties are concerned, it has been found that nitrogen ion implantation is favorable to improve the corrosion resistance of bio implant materials i.e. Ti6Al4V alloy [122]. Sunderrajan et al. [123-124] have investigated the corrosion behavior of N^+ implanted stainless steel and Ti based alloys in Ringer's solution and reported the improvement in corrosion behavior after N^+ implantation. The corrosion behavior of ion implanted Zr-based bulk amorphous alloys, Zircaloy, Ti-based alloys, stainless steel and other materials in different environments has been investigated in various studies which is summarized in chapter 2 of the thesis.

3.4.6 Advantages of ion implantation

Ion implantation is one of the appealing methods for surface modification of a material without affecting its underlying bulk. The technique has following advantages among various surface modification techniques:

a) Ion implantation process serves flexibility in addition to inclusion any element into the substrate.
b) Ion implantation can initiate any chemical reaction or diffusion at normal temperature; it does not require elevated temperature to initiate a chemical reaction.
c) Ion implantation does not alter the dimensional integrity of material and shape of the specimen remains same.
d) Final finishing or polishing of the specimen is not required after the ion implantation.
e) There is no chance of separate interface failure because the ions penetrate into the surface of substrate.

In the present research work, O^+ ions of 100 keV energy were implanted on as-cast $Zr_{55}Cu_{30}Ni_5Al_{10}$ bulk amorphous alloy in target chamber of TAM SAMES 150 keV particle accelerator at Ion Beam Physics Section (IBPS), Materials Science Group (MSG), IGCAR, Kalpakkam. The fluences of implantation were taken as 1×10^{16}, 1×10^{17} and 3×10^{17} ions/cm^2. Furthermore, N^+ ion implantation on as spun $Zr_{55}Cu_{30}Ni_5Al_{10}$ ribbon samples was carried out using 100 keV energy ion beam at 1×10^{16}, 1×10^{17} and 3×10^{17} ions/cm^2 fluence.

3.5 Characterization technique

3.5.1 X-ray diffraction (XRD)

X-ray powder diffraction (XRD) is a non-destructive analytical technique which is used to study the structure, composition and physical properties of materials. In the research area of

amorphous alloys, XRD is a very important technique to evaluate the amorphicity of a sample. XRD is based on the constructive interference of monochromatic X-rays and a crystalline material samples (figure 3.10). X-rays, produced by X-ray tube, are allowed to fall on the smooth surface of a sample where it interacts with the sample. When the geometry of incident X-ray impinging the specimen satisfy the Bragg's equation ($n\lambda=2d\sin\theta$), constructive interference occurs and it reveals a peak in intensity. Bragg's law [125] correlates the wavelength of X-rays (λ) to the diffraction angle (θ) and atomic spacing (d) in the crystalline material. Diffracted X-rays are finally detected by a detector, processed and a diffraction pattern is generated.

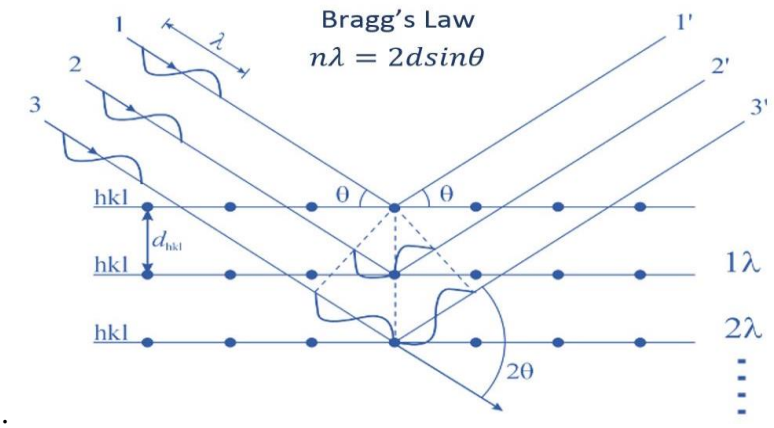

Figure 3.10: Diffraction of X-rays from atomic planes [125]

In the present work, characterization of the alloys (rod, strip and ribbon samples) was carried out by X-ray diffraction (XRD) technique with Inel- XRD (Equinox 2000) system using monochromatic Co radiation source (λ=1.78896 Å) and Xpert Pro- Pananalytical system using Cu-Kα radiation source (λ=1.54184 Å). XRD patterns were recorded over a range of diffraction angle (2θ) 20˚-80˚.

3.5.2 Glancing incidence X-ray diffraction (GIXRD)

Glancing incidence X-ray diffraction (GIXRD) is a non-destructive technique which is widely used to obtain the structural information from thin top most layer of the materials. The

structural changes occur in materials by the process of ion implantation within a depth of the order of 0.1 μm. The conventional XRD technique gives the information about the top layer of a thickness of the order of 5-10 μm, whereas, GIXRD is capable of analyzing very thin (100 Å) top layer [126]. Hence, GIXRD technique was used for characterization of implanted samples.

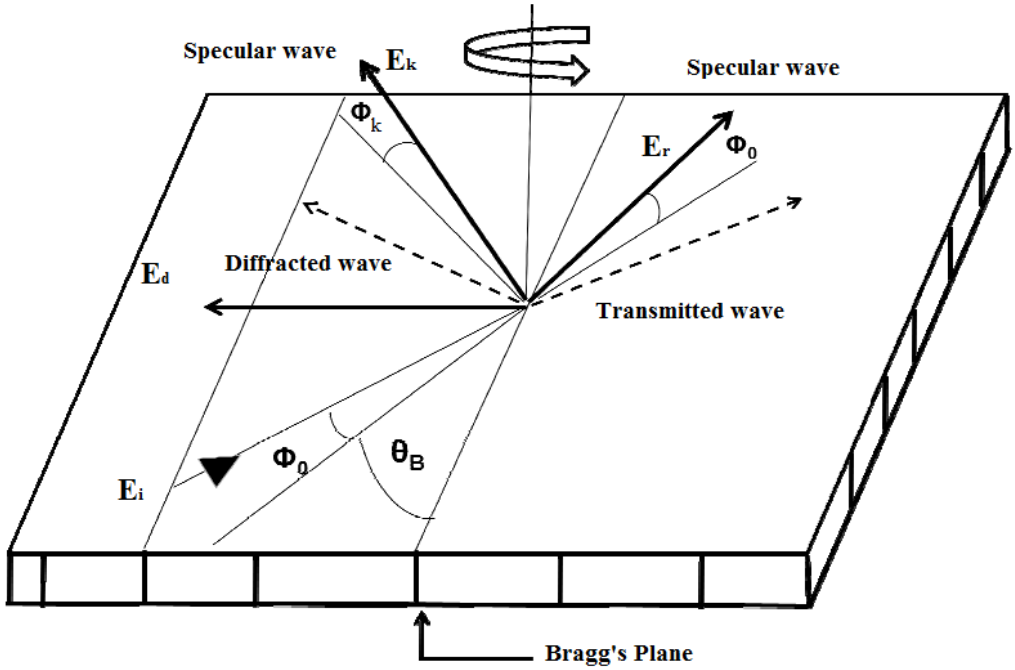

Figure 3.11: Schematic diagram of Glancing Incidence X-ray Diffraction

The schematic diagram of GIXRD is shown in figure 3.11. Glancing incidence is a scattering geometry i.e. a combination of Bragg's condition with the conditions for X-ray total external reflection from crystal surfaces. X-rays are made to fall on the specimen at a glancing angle (ϕ_0) which should be slightly greater than the critical angle of total reflection [127]. The incident wave E_i produces specularly reflected wave E_r and diffracted wave E_d. To obtain diffracted waves, incident wave E_i should fall on some lattice planes at Bragg's angle perpendicular to sample surface. This condition can be satisfied by rotating the specimen about a normal to the surface keeping the ϕ_0 angle constant. Since, diffracted wave E_d moves

inward to the plane so its specularly reflected wave E_k appears making an angle of ϕ_k with the surface of sample. E_k contains all the information about the structure of top thin layer. The GIXRD diffraction pattern is obtained by detecting these specularly reflected waves $E_{k.}$ The major limitation of GIXRD is that the sample surface must be very smooth and X-rays are wasted passing over the surface of sample due to small glancing angle.

In the present investigation GIXRD analysis was carried out by Inel- XRD (Equinox 2000) make diffractometer to study the structural modification occurring on $Zr_{55}Cu_{30}Ni_5Al_{10}$ glassy alloy with different fluences of oxygen and nitrogen ion implantation. The formation of certain phases on the surface of oxygen and nitrogen ion implanted specimens at 1×10^{16}, 1×10^{17} and 3×10^{17} ions/cm^2 fluences were analyzed. All the measurements were carried out at glancing angle of 1° for Co radiation source (λ=1.788965 Å) in the 2θ range from 20°-80°. The obtained diffraction patterns were analyzed using JCPDS data base and also compared with available literature data.

3.5.3 Optical microscope

The optical microscope also known as light microscope is a most common instrument for characterization of materials. It magnifies the images of small object by using a combination of lenses and visible light. Most commonly used optical microscope is a compound microscope. It consists of an objective lens, which is placed close to the object and eyepiece is placed near to the eyes. Both these lenses are separated through a tube. The objective lens focuses a real image of the object inside the microscope which is further magnified by eyepiece. The sample is placed on a flat platform, known as mechanical stage. The centre of the stage has a hole through which visible light passes and specimen is illuminated. A steady light source is used to illuminate the sample. This light beam is concentrated and focused onto the sample by the condenser which is equipped with diaphragm or filters to maintain the

intensity of illumination. The focus of specimen is controlled through the focus knob which actually moves the sample stage up and down. The coarse focusing is controlled through a large knurled wheel and a smaller knurled wheel controls the fine focusing. Thus, compound microscope provides a much higher magnified view of an object. Optical microscopy is widely used in metallurgy, microelectronics, histopathology, physics and pharmaceutical research, biotechnology and microbiology.

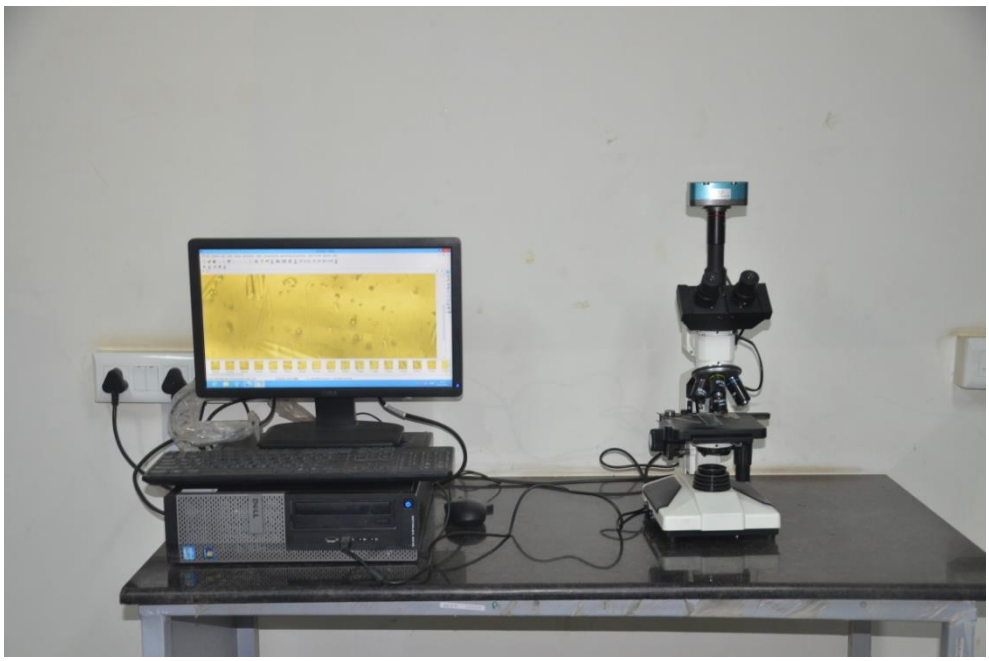

Figure 3.12: Image of metallurgical optical microscope

In the present investigation, Radical Universal Trinocular Metallurgical – RMM-8TCE optical microscope, shown in figure 3.12, was used to investigate the preliminary microstructure of Zr-based bulk amorphous after weight loss analysis in nitric acid.

3.5.4 Field emission scanning electron microscopy (FESEM)

Field emission scanning electron microscope makes use of the high energy electron beam instead of visible light to form an image. This electron beam is released from a field emission cathode by applying acceleration voltage ranging from 5-20 kV. These accelerated electron

beams with significant kinetic energy is made to fall on the sample surface using condenser and objective lens system. Interaction of the electron beam with sample surface dissipates kinetic energy and a variety of signals are produced i.e. secondary electrons, backscattered electrons, characteristic X-rays (photons), and visible light (cathodoluminescence) through different-different mechanisms as illustrated in figure 3.13 (a). These signals contain important information about the chemical composition, texture (external morphology), crystalline structure, orientation of grains and electrical conductivity of the material. Specialized detectors detect these signals and form an image of the sample which is further displayed on the screen. Secondary electrons and backscattered electrons are two different imaging modes. Secondary electrons provide information about the topography and morphology of the sample and backscattered electrons are used for phase discrimination in multiphase samples by varying the contrast. X-rays and Auger electrons are generated by shell-to-shell transition. These X-rays show the characteristic feature of the elements on the top surface of sample. The schematic diagram of SEM is shown in figure 3.13 (b).

In FE-SEM, field emission source is used in place of thermionic source which is used in conventional SEM. The FE-SEM involves a sharp pointed tungsten (W) filament placed in a large electrical potential gradient to produce concentrated electric field. Thus FE-SEM provides very high resolution which allows high level magnification of closely spaced samples and better image quality in comparison to SEM. It is also possible to analyze selected point locations of the sample for qualitative or semi-quantitative study (using EDX), crystal orientations (using EBSD) and surface morphology. SEM technique is a non-destructive technique because electronic interactions do not lead to volume loss of the sample. Therefore, same materials can be analyzed repeatedly [128]. FE-SEM technique also does not require any kind of sample preparation for conductive samples. All of these key benefits make the FE-SEM one of the most important techniques in the research field [129].

FE-SEM also has few limitations such as sample should be conductive, in a solid form, proper size and stable in vacuum.

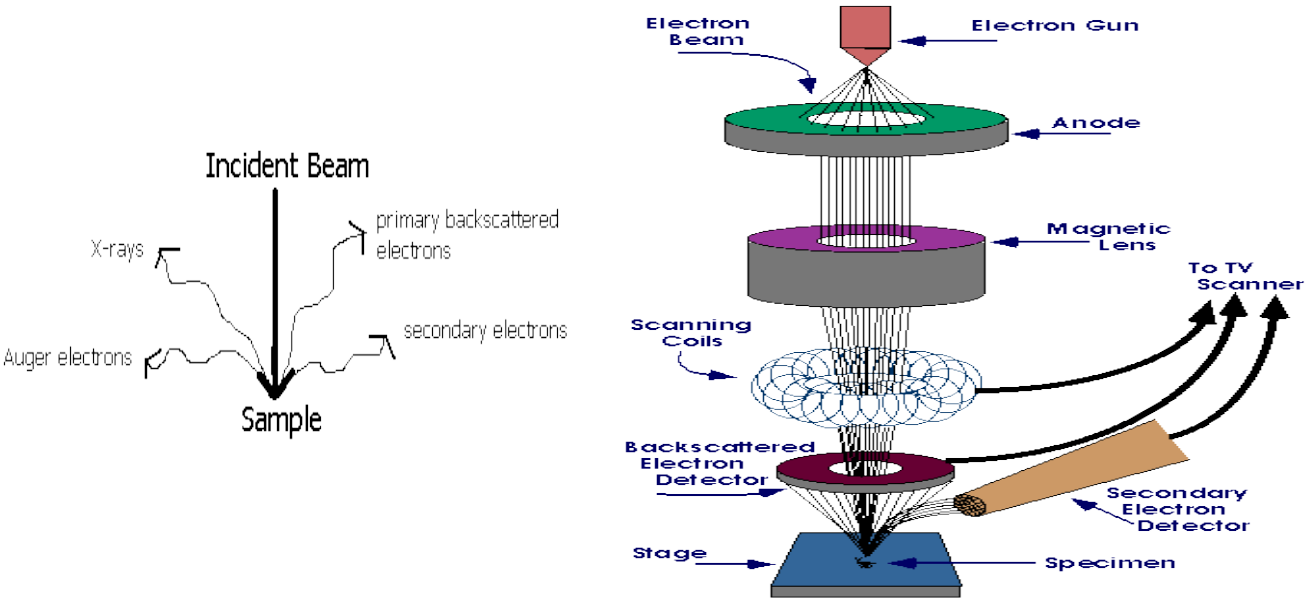

Figure 3.13: (a) Interaction of electron beam with sample and (b) Schematic diagram of SEM [129]

In present research work, the surface morphology of all Zr-based bulk amorphous alloys before and after corrosion testing and ion implantation was investigated by FE-SEM. FESEM characterizations were carried out using Nova Nano SEM450, FEI, North America (figure 3.14). FE-SEM images are taken in secondary electron mode. The elemental composition of the alloys was investigated by Energy dispersive X-ray spectroscopy (EDS) detector (Bruker, Germany) which is attached with FESEM.

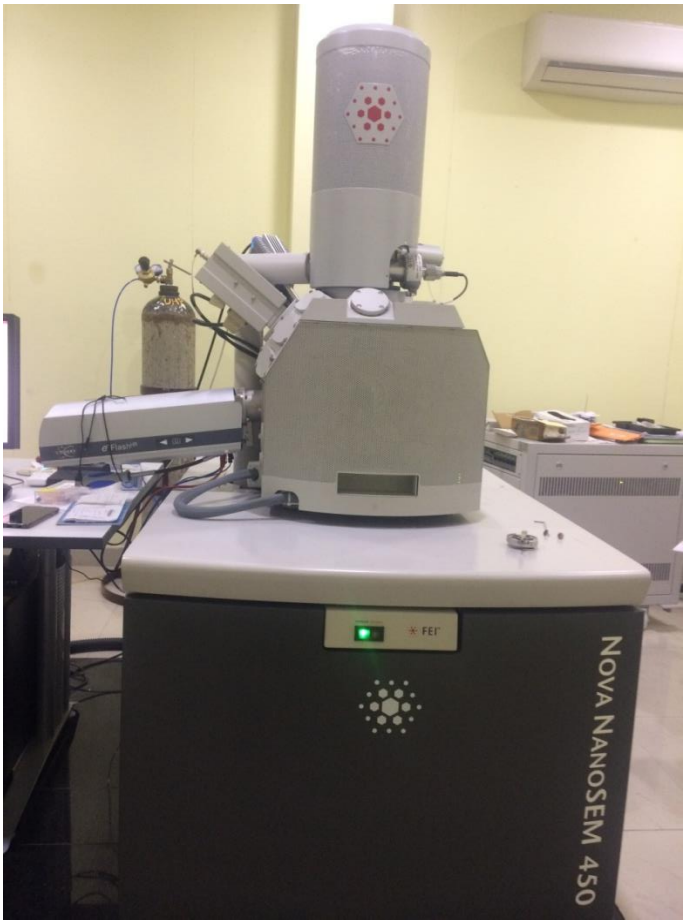

Figure 3.14: Image of FESEM Nova Nano SEM450 system at MRC, MNIT Jaipur

3.5.5 Atomic force microscopy (AFM)

Atomic force microscope (AFM) has major impact in the field of material science for surface investigation. AFM is a characterization tool for obtaining force and topographical maps of surfaces. AFM has an important advantage of imaging any kind of surface whether conducting, semi-conducting or insulating material [130]. Using AFM system, the materials can be analysed in various environments, such as in liquid media, under ultra high vacuum and at ambient conditions.

The AFM provides information about the surface of material on the basis of interaction of probe and sample surface. The schematic of an atomic force microscope is shown in figure 3.15 (a) [131]. The probe consists of a sharp tip, usually made from silicon or

silicon nitride is mounted on the end of a flexible cantilever. The tip having radius in nm order scans the surface of material in rastering pattern with the help of a scanner which is made up of piezo-ceramic elements and moves the tip in all the three dimentions i.e. X,Y and Z directions. When the tip comes very close (below 5nm) to the sample surface, it will experience repulsive force due to electrostatic repulsion of the electron clouds of the atoms of tip and sample [132]. It is called contact mode and this is the most common mode of AFM analysis. Second operating mode i.e. non-contact mode works at relatively large tip-sample distances where the tip experiences attractive force towards the sample due to long-range van der Waals forces. Tapping mode is another approach in which the tip oscillates in close proximity of the surface and changes in the amplitude of oscillation of the cantilever are measured during the scan. Due to these forces, three dimensional movement of the tip is detected with the help of laser light that is reflected from the backside of the cantilever and subsequently detected by a position sensitive detector made from an array of photodiodes. The signal of this detector is forwarded to a feed-back regulator which will dictate the movement of Z-piezo. AFM also does have some limitations such as: imaging a maximum height in the order of μm and a limited scan area. Furthermore, the tip of AFM is very sensitive so it deforms very easily if it encounters a substantial shear force during a scan.

In the present investigation, surface topography of $Zr_{60}Nb_2Cu_{20}Ni_8Al_{10}$, $Zr_{59}Nb_3Cu_{20}Ni_8Al_{10}$ alloys immersed in nitric acid was investigated using AFM (Bruker) at MRC, MNIT Jaipur (figure 3.15 (b)).

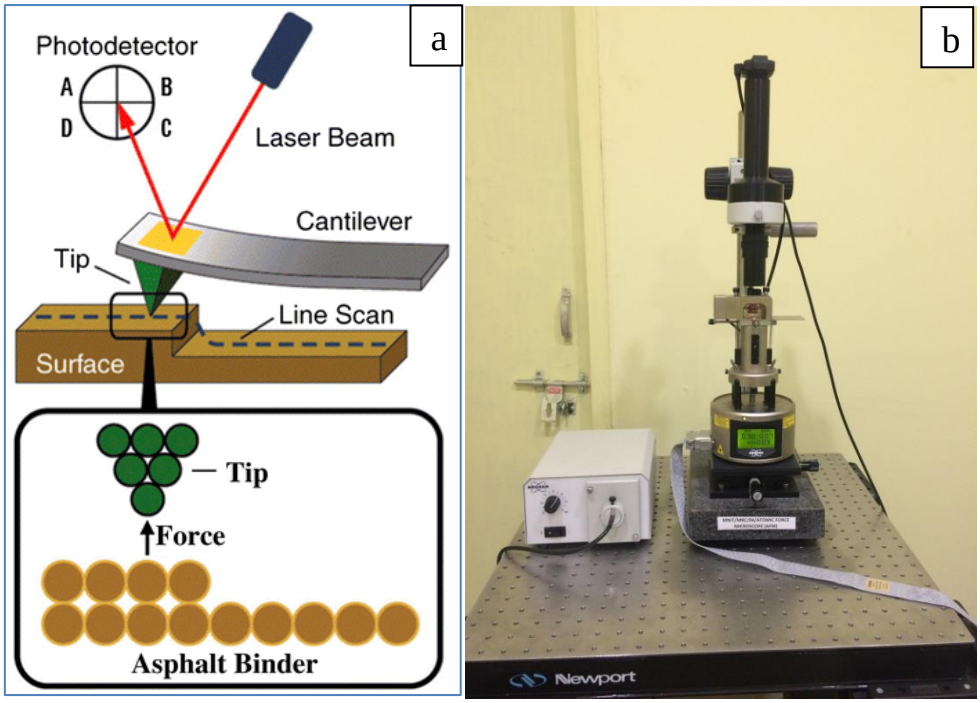

Figure 3.15: (a) Schematic diagram of AFM [131] and (b) image of AFM (Bruker) system at MRC, MNIT Jaipur

3.5.6 X-ray photoelectron spectroscopy (XPS)

X-ray photoelectron spectroscopy (XPS) also known as Electron Spectroscopy for Chemical Analysis (ESCA) is a surface analysis technique which is used to obtain the information regarding the bonding in different chemical states of elements [133]. It is a widely-used technique having versatile applications such as identification of chemical composition, oxidation state determination of elements, identification of the chemical state of the metal oxide films, elemental depth profiling and surface analysis of semi-conducting and insulating materials etc [134]. XPS plays an important role in understanding the corrosion mechanism so it is widely used in the field of corrosion science and the research areas of corrosion, where XPS is commonly used for understanding the (i) selective oxidation phenomenon, (ii) compositional analysis at interface, (iii) the phenomenon of passivity, (iv) assessment of mass transport process, and (v) the interaction of materials in different electrochemical environment [135].

XPS involves bombarding a sample with monochromatic X-rays and observing the energy of emitted photoelectrons. The main component of XPS instruments are (a) X-ray source, (b) ultra high-vacuum system, (c) electronic focusing system, (d) electron energy analyzer, (e) metal magnetic field shielding and (f) electron detector system. The schematic of X-ray photoelectron spectroscopy is shown in Figure 3.16.

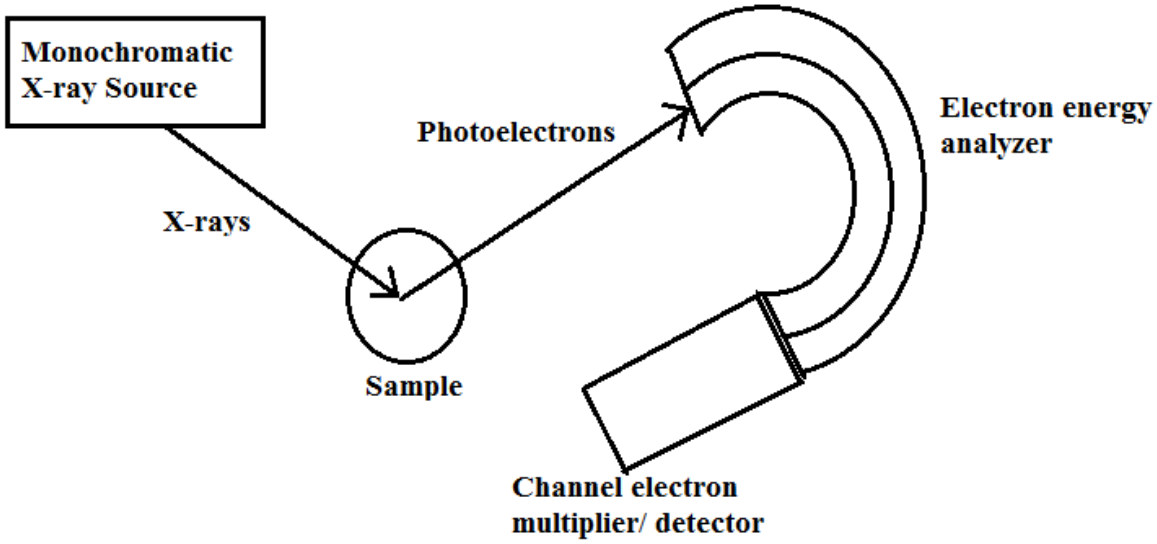

Figure 3.16: Schematic diagram of XPS system

For XPS studies, most commonly used photon energies are Al Kα (1486.6 eV) and Mg Kα (1253.6 eV). The monochromatized X-rays are focused on the specimen which led to the emission of photoelectrons based on the phenomenon of photoelectric effect. The kinetic energy of these emitted photoelectrons is analysed by an electron energy analyzer. Analyzer is used to separate out electrons in a desired band of energies from all other emitted electrons which enter into the analyzer with wide range of energies. In XPS, two types of electron energy analyzers are mainly used; (a) cylindrical mirror analyzer (CMA) and (b) concentric hemispherical analyzer (CHA). The CHA is most commonly used energy analyzer in laboratory XPS. The current induced due to energy analyzed electron at the exit slit of energy analyzer is very low so, electron multiplier (detector) is used to detect and count these photoelectrons of different kinetic energy. Most commonly used electron multiplier is

channel electron multiplier. Hence spectra of detected electron density versus their binding energy are obtained using detector.

The binding energies are characteristic of the individual elements and it can be determined with the help of kinetic energy of the released photoelectron [136]. The binding energy is related to the known energy of the X-ray photon and the kinetic energy of the released photoelectron by the means of following equation.

$$KE = h\upsilon - BE - \phi \tag{3.11}$$

where, KE is the kinetic energy of the photoelectron, hυ is energy of the incident X-ray, BE is binding energy of the photoelectron and ϕ is the work function of the material.

Figure 3.17: Image of XPS ESCA+ Omicron Nanotechnology system at MRC, MNIT, Jaipur

In present investigations, (Oxford Instrument, Germany) at MRC, MNIT, Jaipur (Figure 3.17) and SPECS Surface Nano Analysis GmbH, Germany spectrometer at CSTG, IGCAR Kalpakkam were used for recording data and the analysis was done using CASA software. The sytem is equipped with Al source for monochromatic Al Kα (1486.6 eV) X-ray generation. The XPS analysis was carried out to investigate the passive film developed on

$Zr_{59}Nb_3Cu_{20}Ni_8Al_{10}$ amorphous alloy in 11.5 M HNO_3 medium. Survey scans and high resolution spectra of major alloying elements in as spun $Zr_{59}Nb_3Cu_{20}Ni_8Al_{10}$ amorphous alloy were also acquired to compare the changes in the chemical state of the alloying elements in nitric acid. The passive film as formed on $Zr_{59}Nb_3Cu_{20}Ni_8Al_{10}$ amorphous alloy in boiling 11.5 M HNO_3 medium was also analysed by XPS to understand the changes in chemical composition of alloy in boiling conditions. Similarly, XPS analysis of oxygen ion and nitrogen ion implanted $Zr_{55}Cu_{30}Ni_5Al_{10}$ amorphous alloy was carried out to study the influence of ion implantation on chemical composition of alloying elements. XPS depth profiling for oxygen and nitrogen ion implanted specimens was carried out after different sputtering time interval. XPS analysis of potentiodynamic polarized nitrogen ion implanted $Zr_{55}Cu_{30}Ni_5Al_{10}$ alloy in nitric acid medium was also carried out to understand the corrosion mechanism of the ion implanted alloy in aforementioned medium.

CHAPTER-4

Corrosion Investigations on Zr-based Bulk Amorphous Alloys

This chapter reports the results of corrosion studies performed on the different compositions of Zr-based bulk amorphous alloys in 1 M, 6 M and 11.5 M HNO_3 aqueous solutions. This chapter is divided into two major sections.

4.1. Corrosion investigations at room temperature

4.2. Corrosion investigations at high temperature

First section includes the detailed experimental studies performed on different composition of Zr-based bulk amorphous alloys such as $Zr_{55}Cu_{30}Ni_5Al_{10}$, $Zr_{60}Nb_2Cu_{20}Ni_8Al_{10}$, $Zr_{59}Nb_3Cu_{20}Ni_8Al_{10}$, $Zr_{57}Nb_5Cu_{20}Ni_8Al_{10}$, $Zr_{57}Nb_5Cu_{15.4}Ni_{12.6}Al_{10}$, $Zr_{59}Ti_3Cu_{20}Ni_8Al_{10}$ and $Zr_{60}Pd_5Cu_{15}Ni_{10}Al_{10}$ at room temperature. Furthermore, the comparison between corrosion behavior of bulk and ribbon sample of $Zr_{59}Nb_3Cu_{20}Ni_8Al_{10}$ alloy was also carried out. The corrosion behavior was investigated using potentiodynamic polarization and weight loss analysis methods at room temperature. The characterization techniques such as XRD, FESEM and XPS techniques were used to investigate the corrosion behavior of the above mentioned alloys. The second section deals with the corrosion investigations on Zr-based amorphous alloys at high temperature. In this section the weight loss analysis has been performed to determine the corrosion resistance of $Zr_{59}Nb_3Cu_{20}Ni_8Al_{10}$ and $Zr_{60}Pd_5Cu_{15}Ni_{10}Al_{10}$ amorphous alloys in aqueous boiling 11.5 M HNO_3 media. Surface characterization was done using FESEM and XPS techniques for detailed corrosion studies.

4.1 CORROSION INVESTIGATIONS AT ROOM TEMPERATURE

4.1.1 Introduction

Bulk metallic glasses generally exhibit outstanding mechanical properties such as high mechanical strength, high fracture toughness and good corrosion resistance which cannot be obtained for conventional materials [15]. Among glass forming systems, Zr-based multi-component alloys have received more attention due to the easy castability and high thermal stability against crystallization together with interesting mechanical properties [38,137]. Among these alloys, the Zr-TM-Al alloys, where TM is transition metal, are particularly interesting because they exhibit an extremely large temperature interval of super-cooled liquid region exceeding 100 K [34]. Bulk amorphous Zr-Al-Ni-Cu alloys are known as best glass forming systems and can be cast at relatively low cooling rates in order to solidify as a glass [138]. Zr based bulk amorphous alloys are expected to be used as engineering materials in many potential applications [139-141]. Environmental degradation pertains to the study of oxidation and corrosion behavior of the amorphous alloy in terms of its utility and various engineering applications. In particular, electrochemical study is required to better understand the behavior of the amorphous alloys in corrosive environment and also suggest the possible corrosion rate in terms of corrosion current density with which that alloy will corrode in stipulated time interval. In order to investigate the performance of highly corrosion resistant amorphous alloy, electrochemical investigations were carried out by Dhawan et al. [142] on $Zr_{46.75}Ti_{8.25}Cu_{7.5}Ni_{10}Be_{27.5}$, $Zr_{65}Cu_{17.5}Ni_{10}Al_{7.5}$, $Zr_{67}Ni_{33}$ and $Ti_{60}Ni_{40}$ amorphous alloys that were exposed in aqueous HNO_3 solutions of varying concentrations. Raju et al. [67] have studied the corrosion properties of the Nb- and Ti- containing Zr-based bulk amorphous alloys such as Zr-Cu-Al-Ni-X (X=Nb, Ti up to 5 at%) in comparison to those of the bulk glass forming $Zr_{55}Cu_{30}Al_{10}Ni_5$ alloy in aqueous electrolytes of Na_2SO_4 and NaCl. It was found that Nb- and Ti- containing alloys exhibited increased corrosion resistance, especially

in chloride solutions, as compared to the $Zr_{55}Cu_{30}Al_{10}Ni_5$ alloy. Homozava et al. [72] have predicted the high corrosion resistance for $Zr_{58.5}Cu_{15.6}Ni_{12.8}Al_{10.3}Nb_{2.8}$ in 1M HCl and 1M HNO_3 acidic media due to change in elemental composition in oxide film. S. Pang et al [65] have studied the corrosion behavior of Zr-Nb-Al-Ni-Cu glassy alloys in HCl, NaCl and H_2SO_4 solutions using weight loss and electrochemical measurements and reported that the addition of Nb is effective in improving the corrosion resistance of the investigated Zr based glassy alloys in HCl solution. In a further investigation, it was found that the resistance to pitting corrosion in HCl solution can be improved by the addition of Nb in the $Zr_{65}Al_{7.5}Ni_{10}Cu_{17.5}$ alloy [143]. Pd containing Zr based alloys were also investigated in different corrosive environments by many researchers such as Qin et al. [141] have reported the poor corrosion resistance of Pd containing Zr-based amorphous alloy in NaCl medium because the surface film formed on the alloy surface is not resistant to the chloride containing solution. Pd containing Zr-based bulk amorphous $Zr_{55}Al_{10}Cu_{30}Ni_{5-x}Pd_x$ (x=0, 5 at.%) alloys have been studied in NaOH medium and these alloys were found to be exhibiting an excellent corrosion resistance in NaOH medium [68]. Hence, Nb, Ti, Pd containing Zr-based bulk amorphous alloys were widely studied in different aqueous oxidizing media but no studies are available in nitric acid environment so far.

The motivation for the present study was derived from the need of searching a high corrosion resistant glassy alloy in nitric acid environment for various engineering applications. The interest for the present investigation resulted primarily from the lack of sufficient data in the literature on the corrosion behaviour of the Zr-based bulk amorphous alloys in different concentration of nitric acid. Therefore the main motive of this work is to analyze the corrosion resistance of different Zr-based bulk amorphous alloys using potentiodynamic polarization and weigh loss analysis methods in lower (1 M HNO_3), moderate (6 M HNO_3) and higher (11.5 M HNO_3) concentration of nitric acid solution at room temperature. Detailed surface characterization has been carried out using XRD, FESEM and XPS techniques.

4.1.2 Experimental procedure

4.1.2.1 Alloys investigated

The following Zr-based bulk amorphous alloys of different compositions investigated in the present study were prepared by copper mold suction casting method:

S.No.	Composition (at %)	Shape	Dimension
1	$Zr_{55}Cu_{30}Ni_5Al_{10}$	Strip	27 mm x 5mm x 2 mm
2	$Zr_{60}Nb_2Cu_{20}Ni_8Al_{10}$	Rod	3 mm dia
3	$Zr_{59}Nb_3Cu_{20}Ni_8Al_{10}$	Rod	3 mm dia
4	$Zr_{57}Nb_5Cu_{20}Ni_8Al_{10}$	Rod	3 mm dia
5	$Zr_{57}Nb_5Cu_{15.4}Ni_{12.6}Al_{10}$	Rod	5 mm dia
6	$Zr_{59}Ti_3Cu_{20}Ni_8Al_{10}$	Rod	3 mm dia
7	$Zr_{60}Pd_5Cu_{15}Ni_{10}Al_{10}$	Rod	3 mm dia

The following Zr-based amorphous ribbon alloys of different compositions investigated in the present study were prepared by melt spinning technique:

S.No.	Composition (at %)	Shape	Dimension (width x thickness)
1	$Zr_{55}Cu_{30}Ni_5Al_{10}$	Ribbon	7 mm x 30 μm
2	$Zr_{60}Nb_2Cu_{20}Ni_8Al_{10}$	Ribbon	3 mm x 30 μm
3	$Zr_{59}Nb_3Cu_{20}Ni_8Al_{10}$	Ribbon	3 mm x 30 μm
4	$Zr_{57}Nb_5Cu_{20}Ni_8Al_{10}$	Ribbon	3 mm x 30 μm
5	$Zr_{60}Pd_5Cu_{15}Ni_{10}Al_{10}$	Ribbon	3 mm x 30 μm

4.1.2.2 Aqueous media

The oxidizing aqueous media of different concentration were used in the present study:

- 1 M HNO_3 aqueous solution
- 6 M HNO_3 aqueous solution
- 11.5 M HNO_3 aqueous solution

4.1.2.3 Micro-structural characterization

Amorphous nature of the Zr-based amorphous alloy was characterized by X-ray diffraction (XRD) technique with Xpert Pro- Pananalytical system using Cu-Kα radiations and Inel-XRD (Equinox 2000) system using monochromatic Co source.

4.1.2.4 Potentiodynamic polarization method

The corrosion behavior of the Zr-based amorphous alloys was evaluated using potentiodynamic polarization method. For polarization experiments, a potentiostat (Autolab-AUT84276) was connected to a three-electrode cell which contains a saturated calomel reference electrode, Pt counter electrode and working electrode (Zr-based amorphous alloys). The open circuit potential (OCP) was monitored for 1800 sec prior to all the tests. The potentiostat was interfaced with Nova (version 1.9) software for measuring the changes in the OCP with immersion time and to conduct the polarization experiments. Potentiodynamic polarization tests were conducted in required aqueous solutions at room temperature. In the case of bulk rod or strip samples, the samples are connected with the brass rod. A small amount of Ag-paste was applied at the interface between the specimen and the brass rod to enhance the conductivity. The brass rod was drilled and threaded for connecting to the working electrode. These samples were placed in a mounting cup carefully and then a mixture of two components epoxy and hardener (10:1) were properly mixed and poured. This mixture was allowed to solidify (curing) for connecting to the working electrode for about 8 hours. A lubricant is applied to the walls of the mounting cup before pouring the resin into it which helps in easy removal of the sample after curing process. The mounted specimens were

polished with 80, 120, 220, 320, 400, 600, 800, 1000 and1200 grit SiC papers. The polished samples were then washed with distilled water and cleaned with ethanol and dried in air prior inserting them in the corrosion cell. Teflon tape was also used to prevent the exposure of brass rod and connecting steel rod to the corrosive electrolyte in the cell. Before this, the amorphous ribbon samples were cleaned with acetone and distilled water prior insertion into the test solution. A specific area of the specimen was exposed to the electrolyte. The potentiodynamic polarization experiments were carried out at a scanning rate 1 mV/s from 200 mV below OCP to 2200 mV above it. The values of corrosion potential (E_{corr}) and corrosion current density (I_{corr}) were obtained by Tafel method. The electrochemical experiments were repeated for checking the reproducibility of the results. The electrochemical experiments were performed at CSTG, IGCAR Kalpakkam.

4.1.2.5 Weight loss analysis

As-spun ribbon specimens of Zr-based amorphous alloys were cut in same size and were cleaned with distilled water, acetone and dried in air. The surface area and initial mass of each sample were measured and the samples then were immersed into the required aqueous medium at room temperature. Each sample was weighed after immersion in the solution for 120 h, 240 h 360 h and 480 h. The microgram balance (Mettler Toledo) used to measure the actual weight loss of the samples has an accuracy of ±10 µg. The corrosion rates were determined by using equation 3.9 mentioned in the chapter 3 of the thesis.

4.1.2.6 Surface characterization

The surface morphology of the virgin and treated samples was investigated using optical microscope (Radical Universal Trinocular Metallurgical – RMM-8TCE), scanning electron microscopic (ZEISS-EVO 18). The surface topography of virgin and treated samples was investigated by atomic force microscope using AFM Bruker Multimode-8 with Nanoscope V

controller. Furthermore the origin of corrosion in these investigated samples in nitric acid was studied by XPS using ESCA+ Omicron Nanotechnology (Oxford Instrument, Germany) at MRC, MNIT Jaipur.

4.1.3 Results and discussion

4.1.3.1 Micro-structural characterization

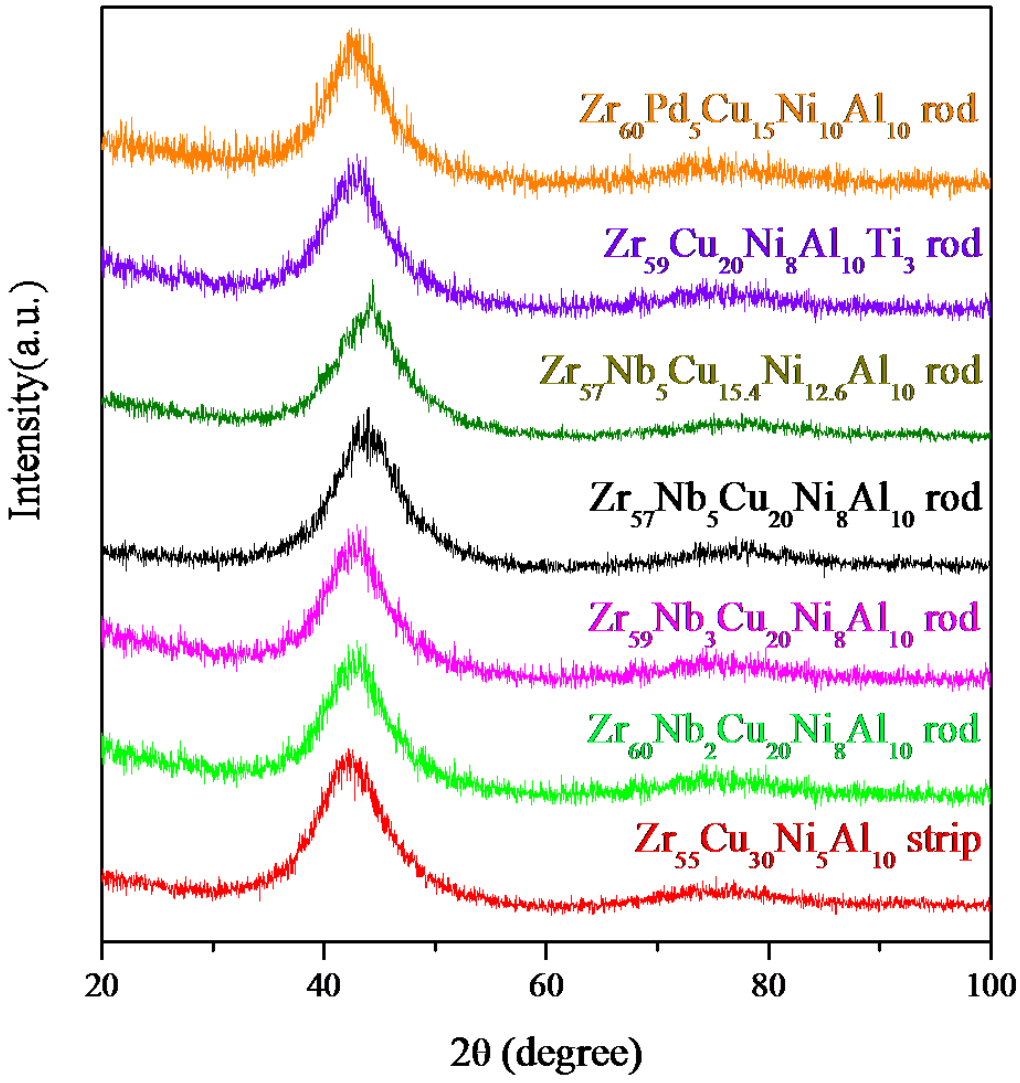

Figure 4.1: XRD pattern of different composition of Zr-based bulk amorphous alloys

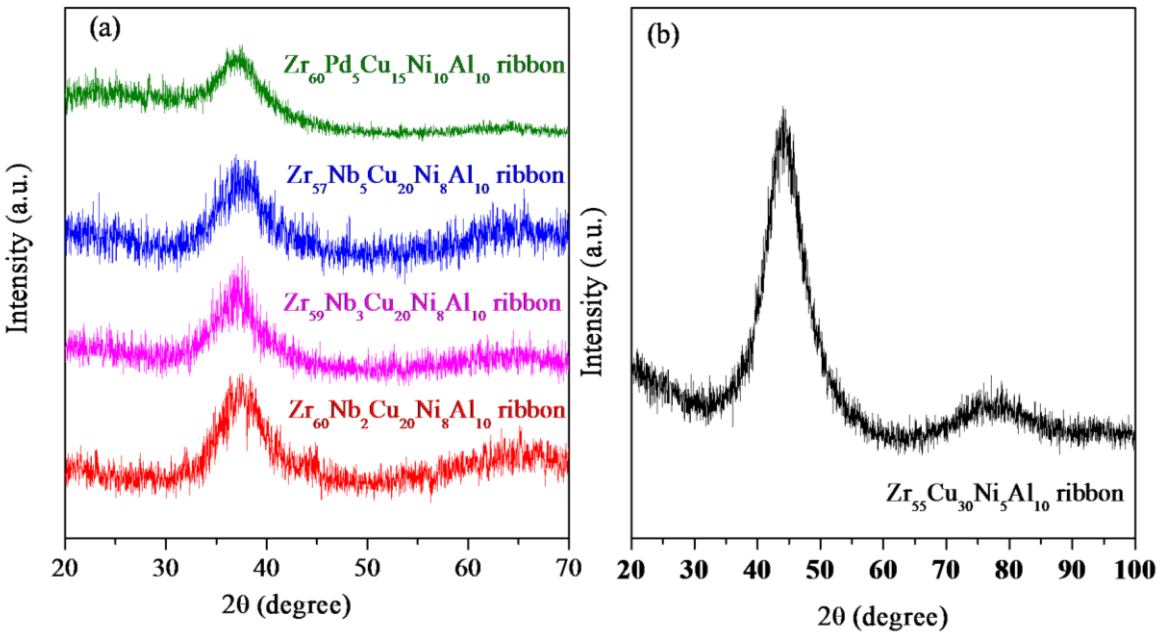

Figure 4.2: XRD pattern of (a) different composition of Zr-based ribbon alloys using Cu-Kα radiations; (b) $Zr_{55}Cu_{30}Ni_5Al_{10}$ amorphous ribbon using Co-Kα radiations

The XRD patterns recorded for different composition of Zr-based bulk amorphous alloys such as $Zr_{55}Cu_{30}Ni_5Al_{10}$, $Zr_{60}Nb_2Cu_{20}Ni_8Al_{10}$, $Zr_{59}Nb_3Cu_{20}Ni_8Al_{10}$, $Zr_{57}Nb_5Cu_{20}Ni_8Al_{10}$ $Zr_{57}Nb_5Cu_{15.4}Ni_{12.6}Al_{10}$, $Zr_{59}Ti_3Cu_{20}Ni_8Al_{10}$ and $Zr_{60}Pd_5Cu_{15}Ni_{10}Al_{10}$ are shown in figure 4.1. These XRD patterns were recorded by Inel-XRD (Equinox 2000) system using monochromatic Co source. Figure 4.1 indicates that the typical broad maxima were especially pronounced in the range from 36˚ to 50˚, suggesting that the Zr-based bulk amorphous alloys are predominantly amorphous. No significant peaks corresponding to crystalline phases were identified. The $Zr_{57}Nb_5Cu_{15.4}Ni_{12.6}Al_{10}$ bulk amorphous alloy shows relatively narrow hallow in comparison to other alloys which means it is not perfectly amorphous alloy. Sun et al. [144] have studied the effect of Nb element in GFA of Zr-based bulk amorphous alloys and reported that 5 at% Nb containing Zr based bulk amorphous alloy i.e. $Zr_{57}Nb_5Cu_{15.4}Ni_{12.6}Al_{10}$ shows presence of some dendrites. In the present study XRD patterns of all bulk samples revealed the amorphous nature of alloys. Figure 4.2 shows the XRD patterns of as-spun Zr-based ribbon alloys such as $Zr_{55}Cu_{30}Ni_5Al_{10}$, $Zr_{60}Nb_2Cu_{20}Ni_8Al_{10}$, $Zr_{59}Nb_3Cu_{20}Ni_8Al_{10}$,

$Zr_{57}Nb_5Cu_{20}Ni_8Al_{10}$ and $Zr_{60}Pd_5Cu_{15}Ni_{10}Al_{10}$ which also revealed the presence of broad hump indicating the amorphous nature of all ribbon samples. Figure 4.2 (a) is XRD pattern of $Zr_{60}Nb_2Cu_{20}Ni_8Al_{10}$, $Zr_{59}Nb_3Cu_{20}Ni_8Al_{10}$, $Zr_{57}Nb_5Cu_{20}Ni_8Al_{10}$ and $Zr_{60}Pd_5Cu_{15}Ni_{10}Al_{10}$ alloys which was recorded by Xpert Pro- Pananalytical system using Cu-Kα radiations whereas the XRD pattern of as-spun $Zr_{55}Cu_{30}Ni_5Al_{10}$ ribbon alloy was recorded by Inel-XRD (Equinox 2000) system using monochromatic Co source. These XRD patterns revealed the amorphous nature of the all samples except $Zr_{57}Nb_5Cu_{15.4}Ni_{12.6}Al_{10}$ rod sample which exhibits small diffraction peaks.

4.1.3.2 Potentiodynamic polarization behavior

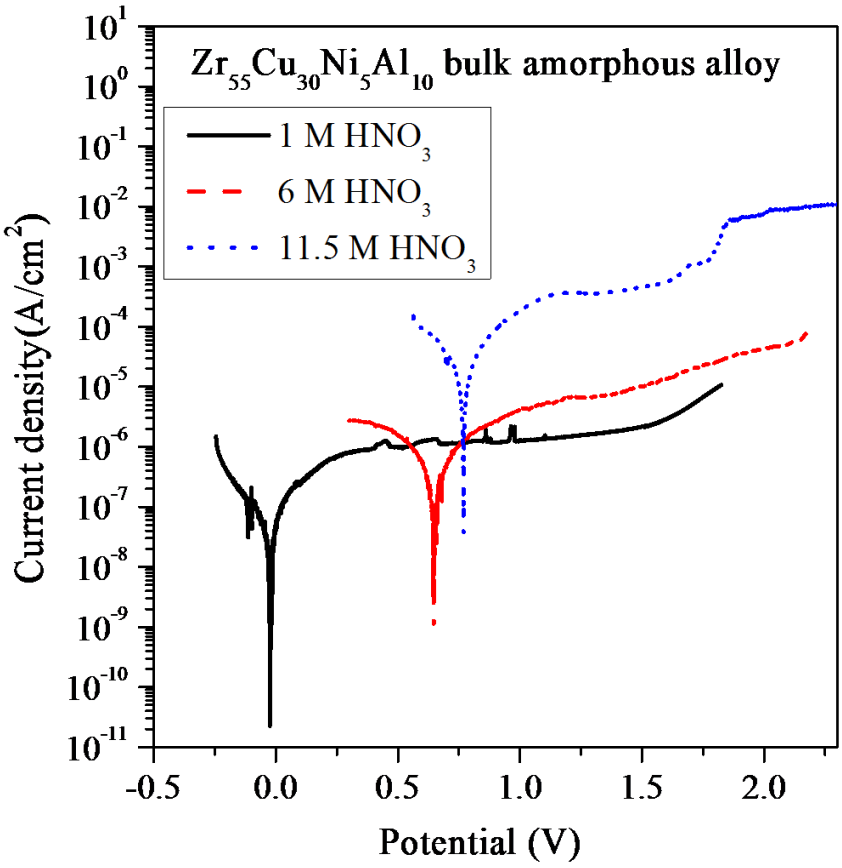

Figure 4.3: Potentiodynamic polarization curve of as-cast $Zr_{55}Cu_{30}Ni_5Al_{10}$ bulk amorphous alloy in different concentration of HNO_3

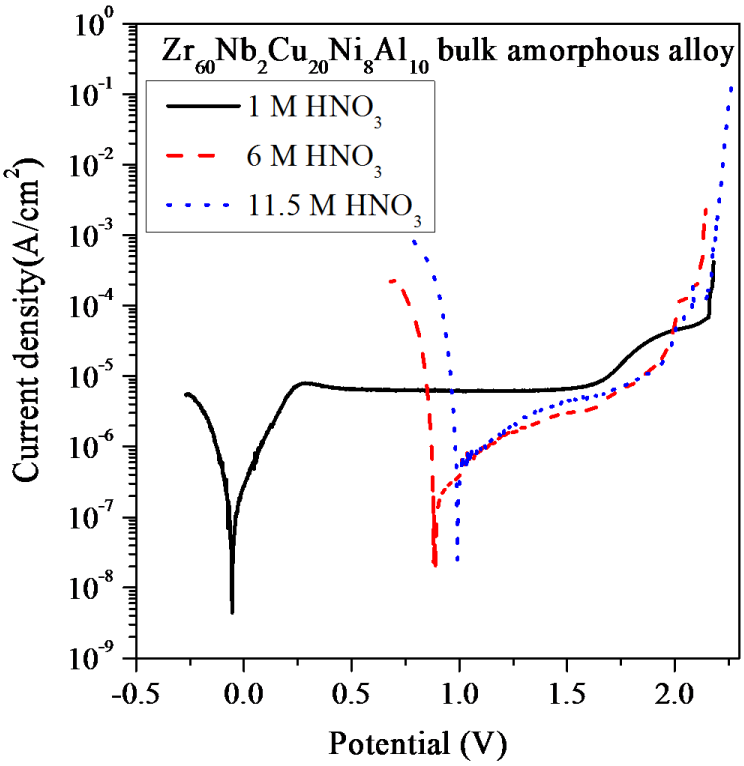

Figure 4.4: Potentiodynamic polarization curve of as-cast $Zr_{60}Nb_2Cu_{20}Ni_8Al_{10}$ bulk amorphous alloy in different concentration of HNO_3

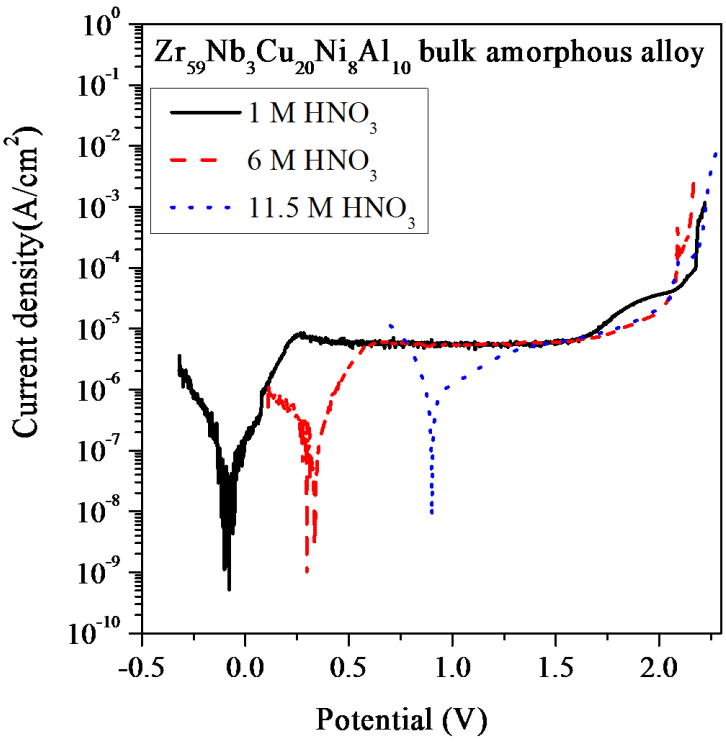

Figure 4.5: Potentiodynamic polarization curve of as-cast $Zr_{59}Nb_3Cu_{20}Ni_8Al_{10}$ bulk amorphous alloy in different concentration of HNO_3

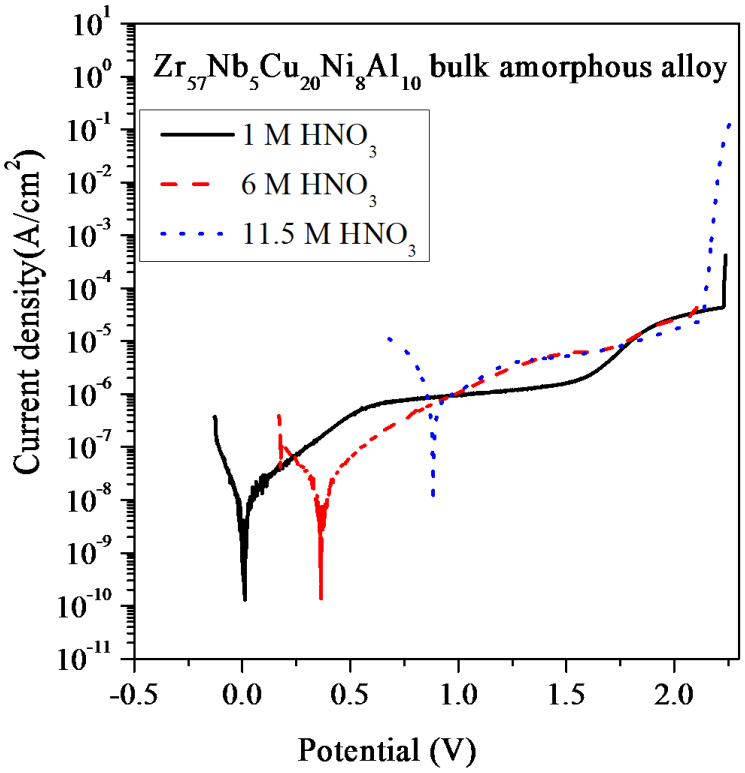

Figure 4.6: Potentiodynamic polarization curve of as-cast $Zr_{57}Nb_5Cu_{20}Ni_8Al_{10}$ bulk amorphous alloy in different concentration of HNO_3

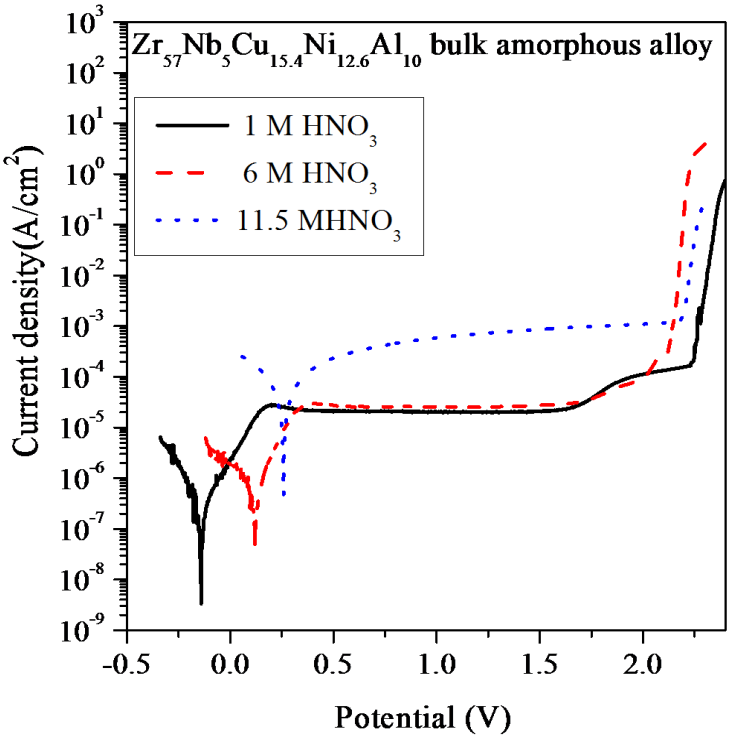

Figure 4.7: Potentiodynamic polarization curve of as-cast $Zr_{57}Nb_5Cu_{15.4}Ni_{12.6}Al_{10}$ bulk amorphous alloy in different concentration of HNO_3

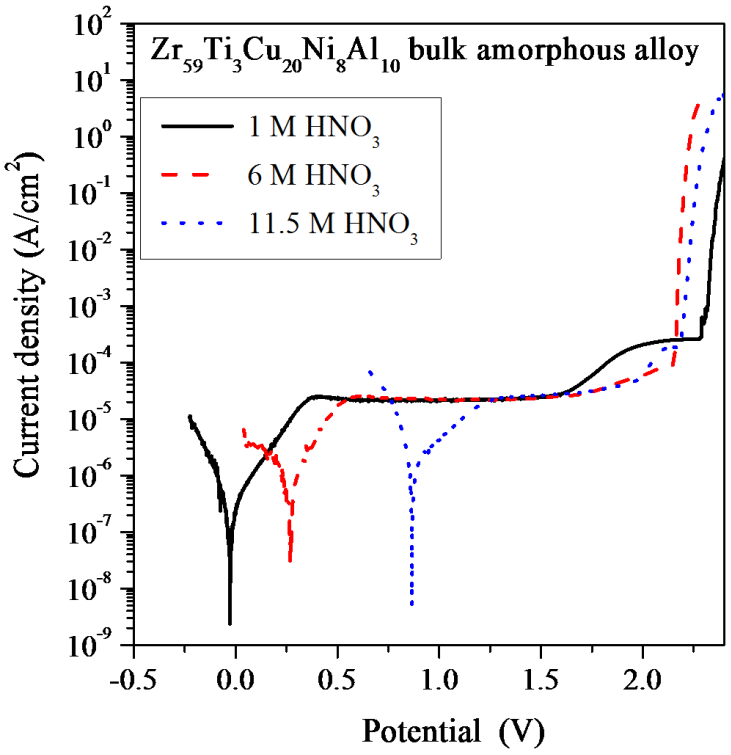

Figure 4.8: Potentiodynamic polarization curve of as-cast $Zr_{59}Ti_3Cu_{20}Ni_8Al_{10}$ bulk amorphous alloy in different concentration of HNO_3

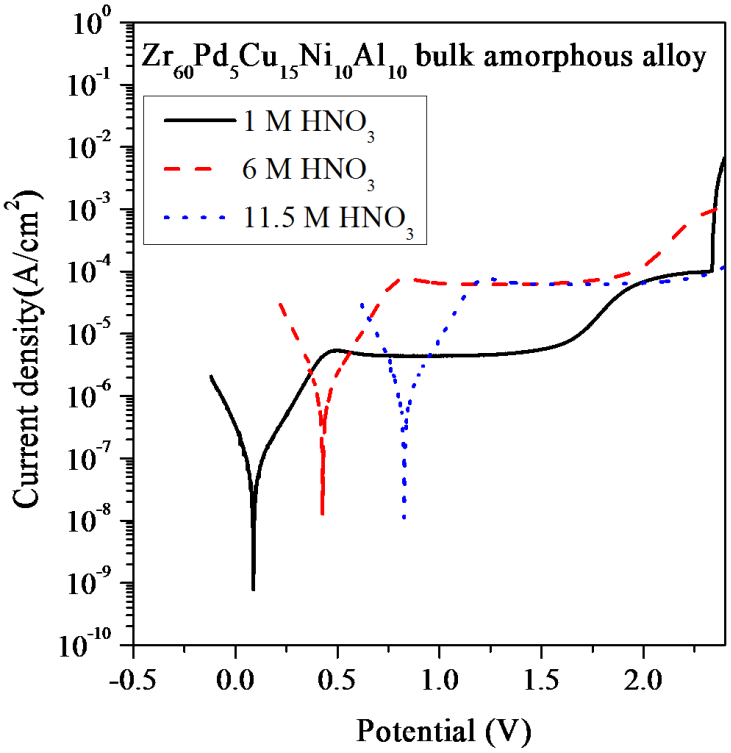

Figure 4.9: Potentiodynamic polarization curve of as-cast $Zr_{60}Pd_5Cu_{15}Ni_{10}Al_{10}$ bulk amorphous alloy in different concentration of HNO_3

The potentiodynamic polarization curves of as-cast $Zr_{55}Cu_{30}Ni_5Al_{10}$, $Zr_{60}Nb_2Cu_{20}Ni_8Al_{10}$, $Zr_{59}Nb_3Cu_{20}Ni_8Al_{10}$, $Zr_{57}Nb_5Cu_{20}Ni_8Al_{10}$ $Zr_{57}Nb_5Cu_{15.4}Ni_{12.6}Al_{10}$, $Zr_{59}Ti_3Cu_{20}Ni_8Al_{10}$ and $Zr_{60}Pd_5Cu_{15}Ni_{10}Al_{10}$ bulk amorphous alloys in lower (1 M HNO_3), moderate (6 M HNO_3) and higher (11.5 M HNO_3) concentration of nitric acid medium at room temperature are shown in figure 4.3, 4.4, 4.5, 4.6, 4.7, 4.8 and 4.9, respectively. The Corrosion parameters such as E_{corr} and corrosion current density I_{corr} for all these Zr-based bulk amorphous alloys are calculated and summarized in Table 4.1. The I_{corr} values were estimated by applying the Tafel slope method [145]. It is observed from all potentiodynamic polarization curves that the corrosion potential shifted towards more positive values with increasing concentration of nitric acid, which was due to the higher oxidizing nature of HNO_3 [146]. The value of corrosion current density was found to be increased with the increasing concentration of HNO_3 and all the samples have shown the similar trend. These results revealed that the corrosion rate of Zr-based bulk amorphous alloys is increased with the increasing concentration of nitric acid. All the potentiodynamic polarization curves exhibited the spontaneous passivation of Zr-based bulk amorphous alloys in various concentration of nitric acid. Judging from the polarization parameters as shown in Table 4.1, the as-cast bulk $Zr_{60}Nb_3Cu_{20}Ni_8Al_{10}$ and $Zr_{57}Nb_5Cu_{20}Ni_8Al_{10}$ amorphous alloys exhibit the lower value of corrosion current density among all tested Zr-based bulk amorphous alloys. In contrast the as-cast bulk $Zr_{55}Cu_{30}Ni_5Al_{10}$ amorphous alloy shows lower value of corrosion current density than $Zr_{60}Nb_3Cu_{20}Ni_8Al_{10}$ but higher as compared to the $Zr_{57}Nb_5Cu_{20}Ni_8Al_{10}$ bulk amorphous alloy in 1 M HNO_3 medium. Whereas in 6 M and 11.5 M HNO_3 medium, the $Zr_{55}Cu_{30}Ni_5Al_{10}$ bulk amorphous alloy shows higher corrosion current density than those value of other $Zr_{60}Nb_3Cu_{20}Ni_8Al_{10}$ and $Zr_{57}Nb_5Cu_{20}Ni_8Al_{10}$ bulk amorphous alloys. The bulk $Zr_{59}Nb_3Cu_{20}Ni_8Al_{10}$ amorphous alloy shows a clear and wide passive range in all concentration of HNO_3 medium whereas, the passive range of $Zr_{57}Nb_5Cu_{20}Ni_8Al_{10}$ amorphous alloy has been decreased with the increase in the concentration of nitric acid

which is attributed to the formation of nanocrystalline phases during the casting of the sample. XRD pattern of $Zr_{57}Nb_5Cu_{20}Ni_8Al_{10}$ amorphous alloy has exhibited the small diffraction peaks indicating the presence of nanocrystalline phases.

It is well known that amorphous alloys consist of structurally and chemically homogeneous single phase solid solutions, which do not contain crystalline defects, such as grain boundaries or dislocations, acting as nucleation sites for corrosion, and thus the amorphous state provides the formation of a uniform passive film without weak points with respect to corrosion [147]. In one of the study, Homozava et al. [72] have investigated the corrosion behavior of Nb containing Zr based amorphous $Zr_{58.5}Cu_{15.6}Ni_{12.8}Al_{10.3}Nb_{2.8}$ alloy in 1M HNO_3 and 1M HCl medium. In this study the detection limits of all elements potentially dissolved from $Zr_{58.5}Cu_{15.6}Ni_{12.8}Al_{10.3}Nb_{2.8}$ alloy were calculated based on a 3 σ method. It was found that the dissolution of Ni in nitric acid was below the detection limit and Zr and Nb was described by a very reduced dissolution rate as compared to Al and Cu. Padhy et al. [73] carried out electrochemical investigation on Zr based metallic glass $Zr_{59}Ti_3Cu_{20}Al_{10}Ni_8$ alloy in different concentration of nitric acid for reprocessing application of nuclear spent fuel. According to this study the decrease in OCP value with increase in nitric acid concentration indicates dependence of film stability upon nitric acid concentration and lower corrosion resistance of Ti containing Zr-based bulk metallic glasses at higher concentration of nitric acid.

Since, bulk $Zr_{59}Nb_3Cu_{20}Ni_8Al_{10}$ amorphous alloy exhibit highest corrosion resistance among all investigated Zr-based bulk amorphous alloys, so the corrosion behavior of $Zr_{59}Nb_3Cu_{20}Ni_8Al_{10}$ amorphous ribbon alloy was also investigated in lower (1 M HNO_3), moderate (6 M HNO_3) and higher (11.5 M HNO_3) concentration of nitric acid medium to compare the corrosion behavior of rod and ribbon sample. Figure 4.10 shows the potentiodynamic polarization curve of $Zr_{59}Nb_3Cu_{20}Ni_8Al_{10}$ amorphous ribbon alloy.

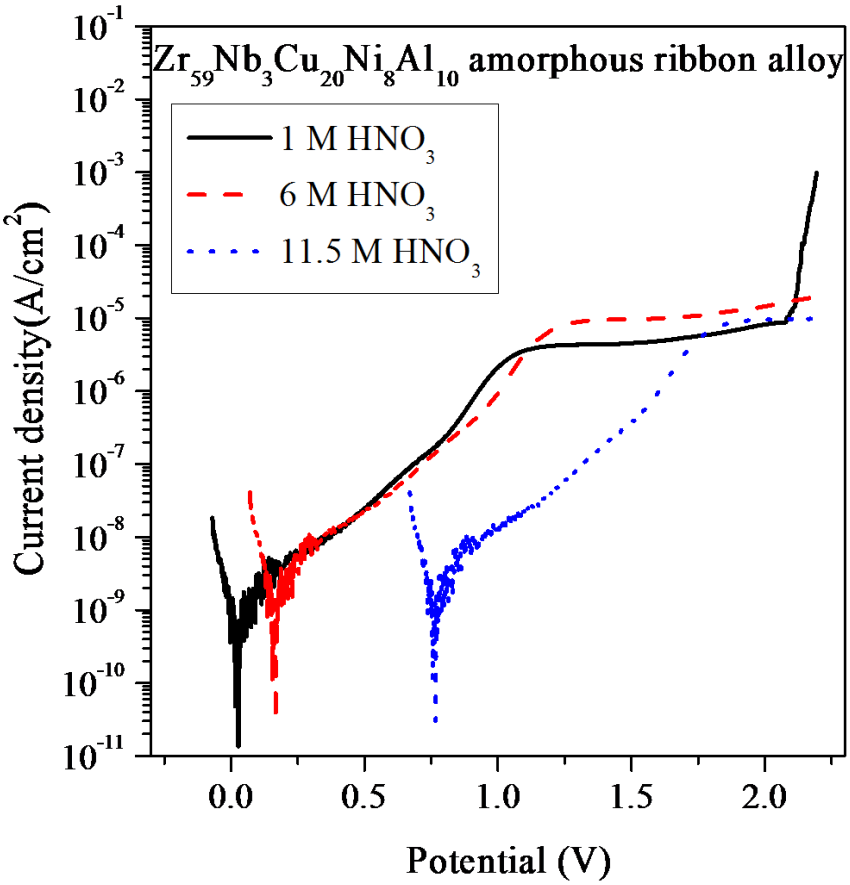

Figure 4.10: Potentiodynamic polarization curve of as-spun $Zr_{59}Nb_3Cu_{20}Ni_8Al_{10}$ amorphous ribbon in different concentration of HNO_3

The potentiodynamic polarization curve of $Zr_{59}Nb_3Cu_{20}Ni_8Al_{10}$ amorphous alloy (figure 4.10) revealed that the sample is passivated spontaneously with low passive current density in 1 M, 6 M and 11.5 M concentrations of HNO_3 at room temperature. Corrosion parameters such as E_{corr} and corrosion current density I_{corr} are calculated and summarized in Table 4.2. It is suggested that the alloy undergoes general corrosion and may tend to form a protective oxide film on the surface of the alloy in the aqueous HNO_3 medium. It was further observed that the corrosion potential shifted towards more positive values with increasing concentration of nitric acid due to the higher oxidizing power of the acid [146]. The increase in the I_{corr} values with the increase in the HNO_3 concentration is indicative of the severity of the environment but the passive current densities for 1 M, 6 M and 11.5 M concentration of HNO_3 were quite similar, as is evident from figure 4.10. It is revealed from the

potentiodynamic polarization curve (figure 4.10) that $Zr_{59}Nb_3Cu_{20}Ni_8Al_{10}$ amorphous alloy with a low open circuit potential, initially dissolved in 1 M HNO_3 solution and soon reached to a very stable condition with increasing applied potential. Similar behavior was observed for the same alloy in 6M HNO_3 solution, but at a comparatively higher concentration of 11.5 M HNO_3, the alloy showed a high corrosion current density with a protective passive layer film. Raju et al. [67] observed that thin passive layer films are formed on the bulk amorphous $Zr_{59}Nb_3Cu_{20}Ni_8Al_{10}$ alloy in Na_2SO_4 solution that are significantly more enriched in copper and nickel species close to the interface oxide/ alloy. In the present study, dissolution of Cu and Ni appears to occur, possibly due to the smaller Goldschmidt's radii of Cu and Ni amongst the other elements. For example the Goldschmidt's radii of Zr, Cu, Al, Ni and Nb are 0.160, 0.128, 0.143, 0.125, and 0.147 respectively, and therefore the mobility of these atoms is quite high. Thus, the Cu and Ni atoms that are underlying the native oxide film may reach the surface by a tunneling process due to applied potential during electrochemical corrosion and they are dissolved at the interface with the test environment [148]. Baunack et al. [149] have reported that the electrochemically treated Nb containing Zr-based alloys show a distinct enrichment of metallic copper at the oxide/metal interface. Aluminum has a strong chemical affinity with Zr, for which the mixing enthalpy is -44 kJ/mol, and this value is very similar to that of the Zr–Ni bimetallic, (i.e. -49 kJ/mol), whereas the mixing enthalpy of Zr-Cu is -23 kJ/mol. This means that the Zr-Cu bond is not stronger than the Zr-Al or Zr-Ni bonds [150], which may lead to the dissolution of Cu; this being weaker in bonding with the Zr. It has also been reported that the virgin surface of the $Zr_{65}Cu_{17.5}Ni_{10}Al_{7.5}$ had oxides of Zr and Al present on it, whereas Ni and Cu were present in the metallic form [151]. Hence, in the present work, the formation of passive film of ZrO_2, Al_2O_3 and Nb_2O_5 was expected which protects the alloy from corrosion in nitric acid environment.

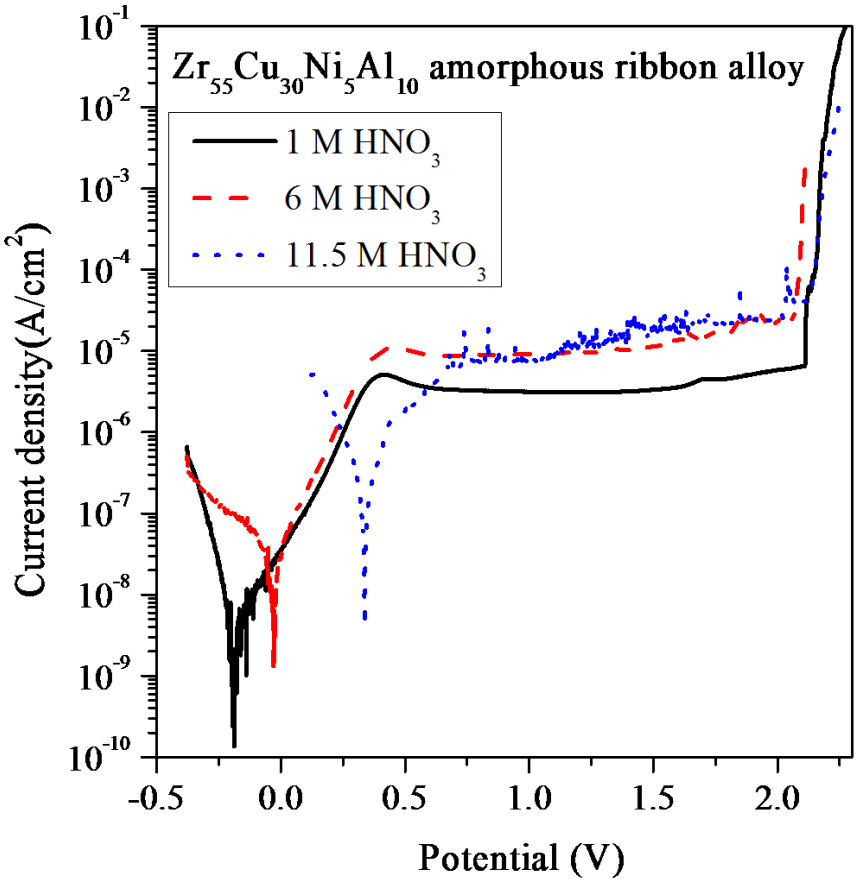

Figure 4.11: Potentiodynamic polarization curve of as-spun $Zr_{55}Cu_{30}Ni_5Al_{10}$ amorphous ribbon in different concentration of HNO_3

Since $Zr_{55}Cu_{30}Ni_5Al_{10}$ amorphous alloy possesses highest GFA among all investigated Zr-based bulk amorphous alloys so the corrosion behavior of as-spun $Zr_{55}Cu_{30}Ni_5Al_{10}$ amorphous ribbon was also investigated in different concentration of nitric acid to compare the corrosion behavior of strip and ribbon alloys. Figure 4.11 represents the potentiodynamic polarization curve of as-spun $Zr_{55}Cu_{30}Ni_5Al_{10}$ amorphous ribbon alloy in 1 M, 6 M and 11.5 M HNO_3 medium. Corrosion parameters such as E_{corr} and corrosion current density I_{corr} are calculated and summarized in Table 4.2. In 1 M and 6 M HNO_3 solution, the as-spun $Zr_{55}Cu_{30}Ni_5Al_{10}$ amorphous ribbon shows the active-passive transition and exhibited small active dissolution current peak. After that, the sample was passivated spontaneously. The formation of protective passive layer on the surface of sample is responsible for this spontaneous passivation. In 11.5 M HNO_3 solution, the as-spun $Zr_{55}Cu_{30}Ni_5Al_{10}$ amorphous

ribbon alloy exhibits many active dissolution current peak indicating the severe corrosion attack in this medium. The E_{corr} value was shifted towards nobler side with increasing concentration of nitric acid due to higher oxidizing nature of nitric acid. The value of corrosion current density was increased with increasing concentration of nitric acid. Dhawan et al. [49] have studied the corrosion behavior of Ti free $Zr_{65}Cu_{17.5}Ni_{10}Al_{7.5}$ glassy alloy in 0.5 M H_2SO_4 and 0.5 M HNO_3 solutions and found that the alloy possesses better corrosion resistance in H_2SO_4 solution. Jayaraj et al. [148] have also reported the presence of the active dissolution peak in the polarization curve recorded on $Zr_{48}Cu_{36}Ag_8Al_8$ amorphous alloy in 1 M H_2SO_4 solution due to active dissolution of Cu element. In the present study, Zr and Al elements tend to form oxides but Cu element profoundly dissolves in nitric acid solution.

Table 4.1: Polarization parameters for as-cast Zr-based bulk amorphous alloy in different concentration of nitric acid medium

Bulk samples	1 M HNO_3		6 M HNO_3		11.5 M HNO_3	
	E_{corr} (V)	I_{corr} ($\mu A/cm^2$)	E_{corr} (V)	I_{corr} ($\mu A/cm^2$)	E_{corr} (V)	I_{corr} ($\mu A/cm^2$)
$Zr_{55}Cu_{30}Ni_5Al_{10}$	-0.024	0.061	0.541	0.488	0.776	23.43
$Zr_{60}Nb_2Cu_{20}Ni_8Al_{10}$	-0.055	0.201	0.884	0.324	0.991	0.711
$Zr_{59}Nb_3Cu_{20}Ni_8Al_{10}$	-0.077	0.105	0.338	0.232	0.904	0.893
$Zr_{57}Nb_5Cu_{20}Ni_8Al_{10}$	0.014	0.015	0.326	0.025	0.884	0.971
$Zr_{57}Nb_5Cu_{15.4}Ni_{12.6}Al_{10}$	-0.145	0.344	0.122	0.882	0.255	39.24
$Zr_{59}Ti_3Cu_{20}Ni_8Al_{10}$	-0.031	0.424	0.269	0.831	0.862	2.331
$Zr_{60}Pd_5Cu_{15}Ni_{10}Al_{10}$	0.938	0.136	0.475	1.197	0.799	23.43

Table 4.2: Polarization parameters for as-spun Zr-based amorphous ribbon alloys in different concentration of nitric acid medium

Ribbon samples	1 M HNO_3		6 M HNO_3		11.5 M HNO_3	
	E_{corr} (V)	I_{corr} ($\mu A/cm^2$)	E_{corr} (V)	I_{corr} ($\mu A/cm^2$)	E_{corr} (V)	I_{corr} ($\mu A/cm^2$)
$Zr_{55}Cu_{30}Ni_5Al_{10}$	-0.190	7.713×10^{-3}	-0.022	34.67×10^{-3}	0.338	260.4×10^{-3}
$Zr_{59}Nb_3Cu_{20}Ni_8Al_{10}$	0.014	0.936×10^{-3}	0.162	6.942×10^{-3}	0.885	65.35×10^{-3}

4.1.3.3 Weight loss analysis at room temperature

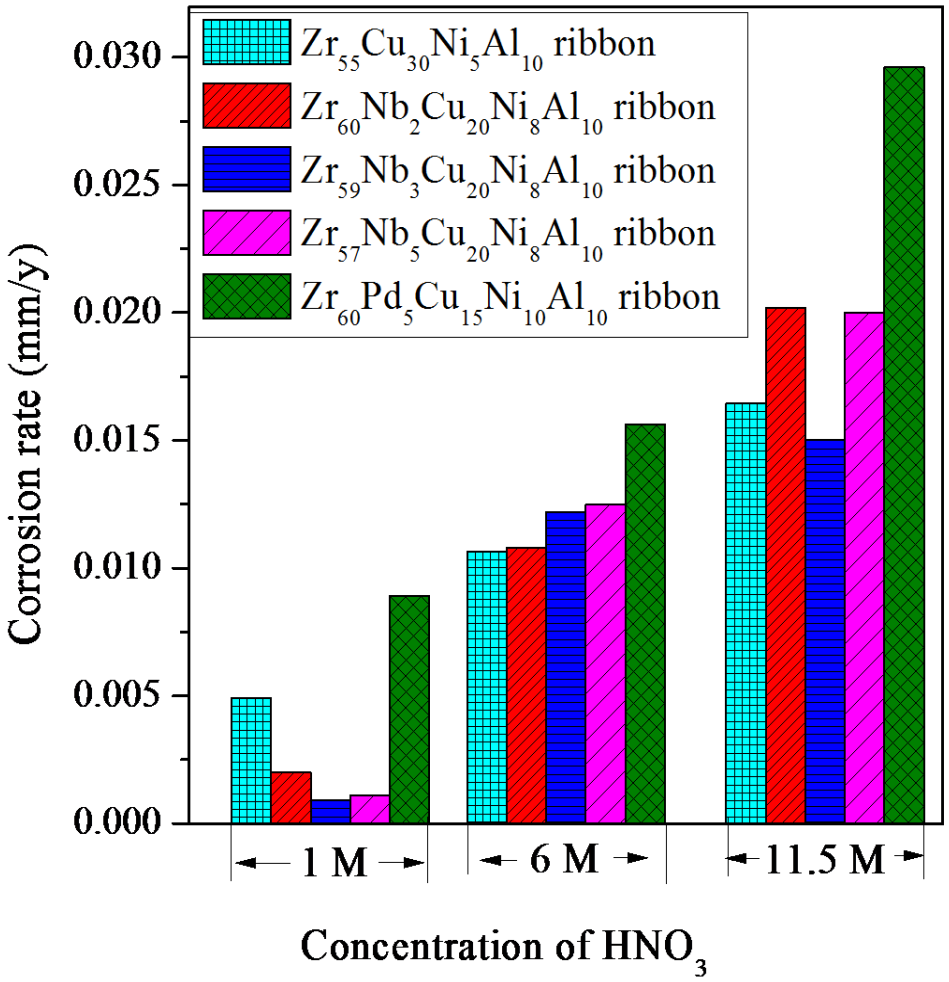

Figure 4.12: Corrosion rate versus concentration of HNO_3 plot of different as-spun Zr-based bulk amorphous ribbon alloys exposed in different concentration of nitric acid medium at room temperature for 480 h duration

Table 4.3: Corrosion rate values of different as-spun Zr-based bulk amorphous ribbon alloys exposed in different concentration of nitric medium at room temperature for 480 h duration

Concentration of HNO_3	**Corrosion rate (mm/y)**				
	$Zr_{55}Cu_{30}Ni_5Al_{10}$ amorphous ribbon alloy	**$Zr_{60}Nb_2Cu_{20}Ni_8Al_{10}$ amorphous ribbon alloy**	**$Zr_{59}Nb_3Cu_{20}Ni_8Al_{10}$ amorphous ribbon alloy**	**$Zr_{57}Nb_5Cu_{20}Ni_8Al_{10}$ amorphous ribbon alloy**	**$Zr_{60}Pd_5Cu_{15}Ni_{10}Al_{10}$ amorphous ribbon alloy**
1 M HNO_3	0.00492	0.0020	0.0009	0.0011	0.0089
6 M HNO_3	0.01066	0.0108	0.0122	0.0125	0.0156
11.5 M HNO_3	0.01645	0.0202	0.0150	0.0200	0.0296

The corrosion rate of as-spun $Zr_{55}Cu_{30}Ni_5Al_{10}$, $Zr_{60}Nb_2Cu_{20}Ni_8Al_{10}$, $Zr_{59}Nb_3Cu_{20}Ni_8Al_{10}$, $Zr_{57}Nb_5Cu_{20}Ni_8Al_{10}$ and $Zr_{60}Pd_5Cu_{15}Ni_{10}Al_{10}$ amorphous ribbon alloys, as shown in Table 4.3, was calculated using weight loss method in various concentration of nitric acid. The plot of the corrosion rates versus concentration of nitric acid of these Zr-based amorphous ribbon alloys at room temperature is shown in figure 4.12. The as-spun $Zr_{60}Pd_5Cu_{15}Ni_{10}Al_{10}$ amorphous alloy shows the highest corrosion rate in all concentrations of nitric acid among all the investigated Zr-based amorphous alloys. Figure 4.12 revealed that the corrosion rates of all investigated Zr-based amorphous alloys increase with the increase in concentration of HNO_3. It is noticeable from figure 4.12 that the Nb containing Zr-based amorphous alloy shows better corrosion resistance in all concentration of nitric acid than the Pd containing Zr-based amorphous alloy and other Zr-based $Zr_{55}Cu_{30}Ni_5Al_{10}$ amorphous alloy. In 11.5 M HNO_3 solution $Zr_{59}Nb_3Cu_{20}Ni_8Al_{10}$ amorphous alloy shows least value of corrosion rate

which is significantly less than other alloys. Infact $Zr_{59}Nb_3Cu_{20}Ni_8Al_{10}$ amorphous ribbon alloy exhibits better corrosion resistance in nitric acid environment among all investigated Zr-based amorphous alloys, so corrosion rate of this particular alloy was calculated for different duration in lower (1 M HNO_3), moderate (6 M HNO_3) and higher (11.5 M HNO_3) concentration of nitric acid medium at room temperature. These corrosion rate values are shown in Table 4.4. The corrosion rate versus concentration of nitric acid plot of $Zr_{59}Nb_3Cu_{20}Ni_8Al_{10}$ amorphous ribbon alloy for 120 h, 240 h, 360 h and 480 h is shown in figure 4.13. It was observed from figure 4.13 that the value of corrosion rate is very low in 1 M HNO_3 and 6 M HNO_3 medium in comparison to 11.5 M aqueous HNO_3 medium due to severity of the environment. The corrosion rate is slightly increased with the increase in time at lower concentration of nitric acid, but at 11.5 M HNO_3, the corrosion rate is found to be decreased with the increase in time. It has been reported that the passivation speed of Nb containing Zr based BMG sample is quickened with the increase of HNO_3 solution concentration in a certain range and its corrosion resistance becomes stronger as well [143]. In the present study, at higher concentration of HNO_3 medium, a significant decrease in corrosion rate has been observed due to the formation of passive layer of niobium oxide.

Table 4.4: Corrosion rate values of as-spun $Zr_{59}Nb_3Cu_{20}Ni_8Al_{10}$ amorphous alloy in different concentration of HNO_3 for 120 h, 240 h, 360 h and 480 h at room temperature

Exposure time	**Corrosion rate of $Zr_{59}Nb_3Cu_{20}Ni_8Al_{10}$ amorphous alloy (mm/y)**		
	1 M HNO_3	**6 M HNO_3**	**11.5 M HNO_3**
120	0.0007	0.0014	0.0327
240	0.0010	0.0017	0.0269
360	0.0023	0.0030	0.0291
480	0.0009	0.0122	0.0150

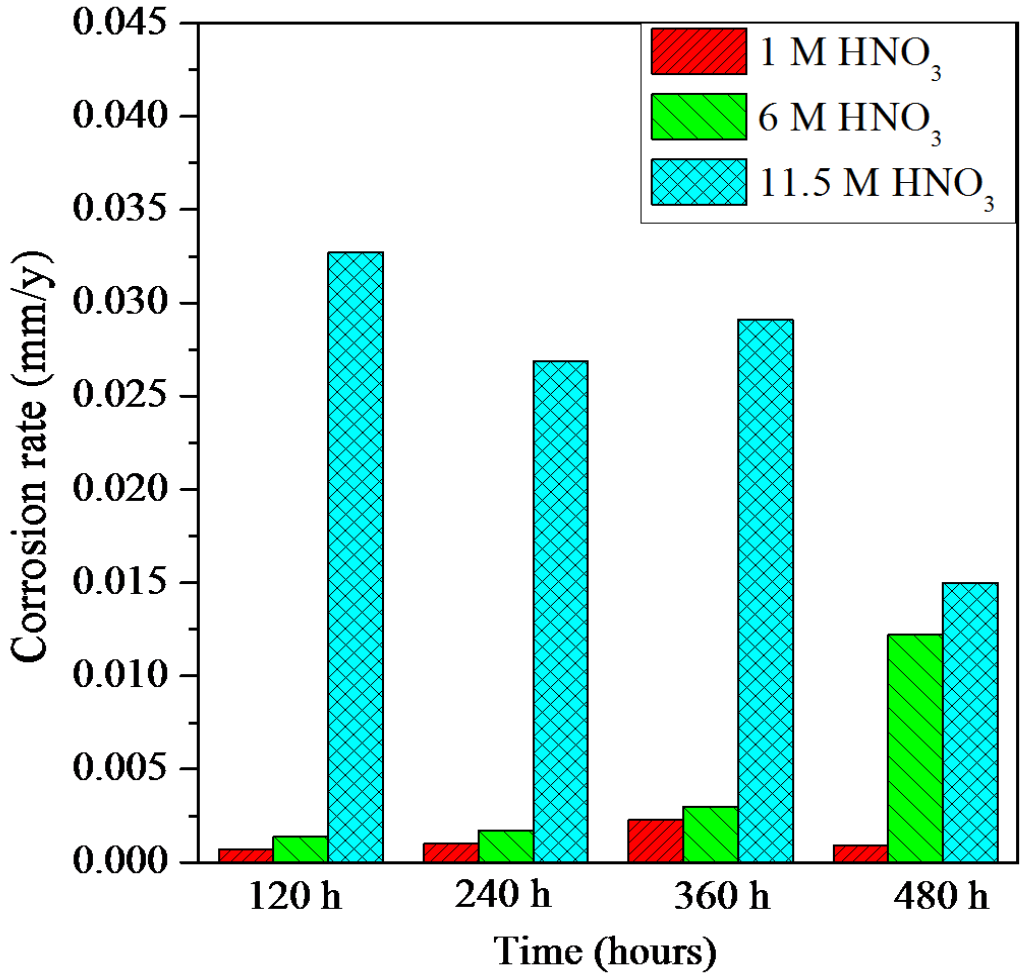

Figure 4.13: Corrosion rate versus exposure time plot of $Zr_{59}Nb_3Cu_{20}Ni_8Al_{10}$ amorphous alloy in different concentration of aqueous HNO_3 for 120 h, 240 h, 360 h and 480 h at room temperature

4.1.3.4 Surface morphology

The optical micrographs and SEM images of the $Zr_{59}Nb_3Cu_{20}Ni_8Al_{10}$ alloy after potentiodynamic polarization studies in lower (1 M HNO_3), moderate (6 M HNO_3) and higher (11.5 M HNO_3) concentration of nitric acid medium at room temperature are shown in figure 4.14 and 4.15, respectively. Optical micrographs and SEM results clearly show that as the concentration of HNO_3 increases, the oxidation layer formed on the surface of alloys improves. It can be seen from the SEM micrographs that the amorphous alloy have fine surface in oxidizing medium. The optical and SEM image of as-spun $Zr_{59}Nb_3Cu_{20}Ni_8Al_{10}$ amorphous alloy, as shown in figure 4.14 (a) and 4.15 (b), respectively indicates the smooth

and clean surface of sample. An oxide layer is formed on the surface of alloy after potentiodynamic polarization studies in 1 M HNO_3 medium, which can be observed from Fig. 4.15 (a) and 4.15 (b), on comparing the SEM micrographs of virgin and electrochemically treated $Zr_{59}Nb_3Cu_{20}Ni_8Al_{10}$ amorphous alloy specimen in 1 M HNO_3. But as the concentration of oxidizing acid increases the formation of the oxide layer also gets enhanced. Both optical and SEM micrographs (Fig. 4.14 and 4.15) revealed that the oxidation layer is formed on the surface of the alloy in nitric acid medium and also some dissolution of the oxidation layer has been observed at 11.5 M HNO_3 (figure 4.14 (d) and figure 4.15 (d)) due to the severity of the environment.

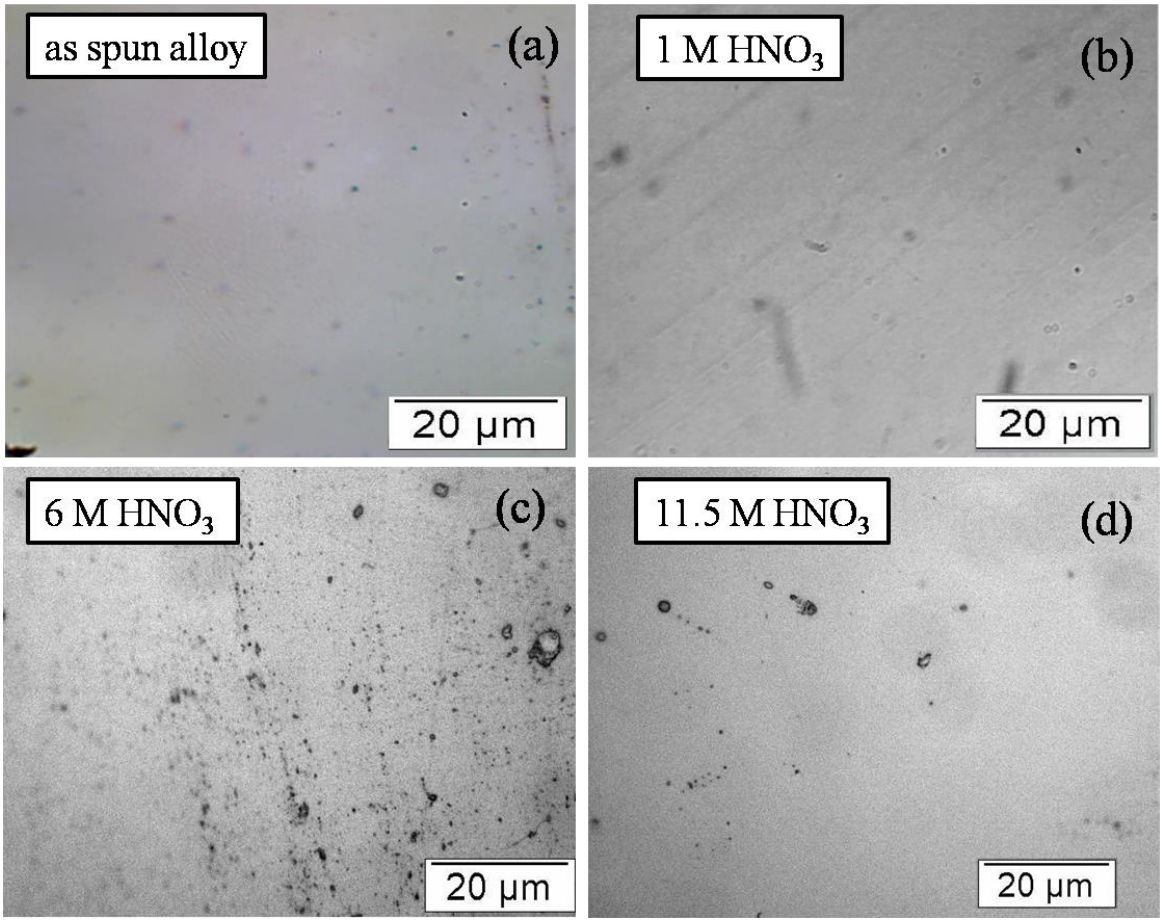

Figure 4.14: Optical micrographs of (a) as-spun $Zr_{59}Nb_3Cu_{20}Ni_8Al_{10}$ amorphous alloy and after potentiodynamic polarization studies in (b) 1 M aqueous HNO_3, (c) 6 M aqueous HNO_3 and (d) 11.5 M aqueous HNO_3 at room temperature

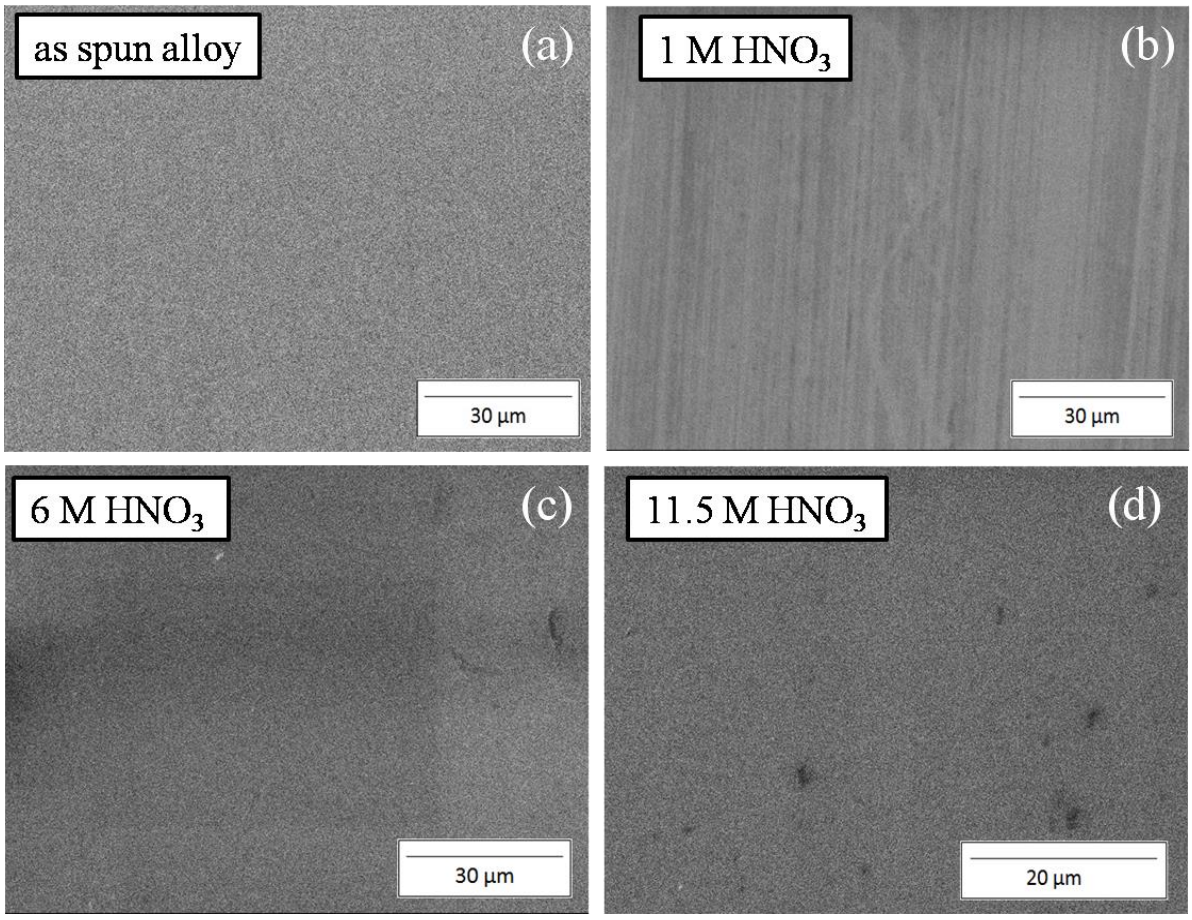

Figure 4.15: SEM micrographs of (a) as-spun $Zr_{59}Nb_3Cu_{20}Ni_8Al_{10}$ amorphous alloy and after potentiodynamic polarization studies in (b) 1 M aqueous HNO_3, (c) 6 M aqueous HNO_3 and (d) 11.5 M aqueous HNO_3

The optical microstructure of as-spun $Zr_{59}Nb_3Cu_{20}Ni_8Al_{10}$ amorphous alloy and after immersion in lower (1 M HNO_3), moderate (6 M HNO_3) and higher (11.5 M HNO_3) concentration of nitric acid medium at room temperature for 360 hours is shown in figure 4.16. The effect of aqueous HNO_3 medium on the surface of the alloy can be seen in the given microstructures. As the concentration of HNO_3 increases, the alloy $Zr_{59}Nb_3Cu_{20}Ni_8Al_{10}$ shows peeling of the surface at some places. The optical microstructure of $Zr_{59}Nb_3Cu_{20}Ni_8Al_{10}$ amorphous alloy after exposure in 11.5 M HNO_3 shows (figure 4.16 (d)) the significant changes on the surface of the alloy shown as small pockets and patches at various places on the surface than the other one at the lower concentrations which is further clarified by the SEM study.

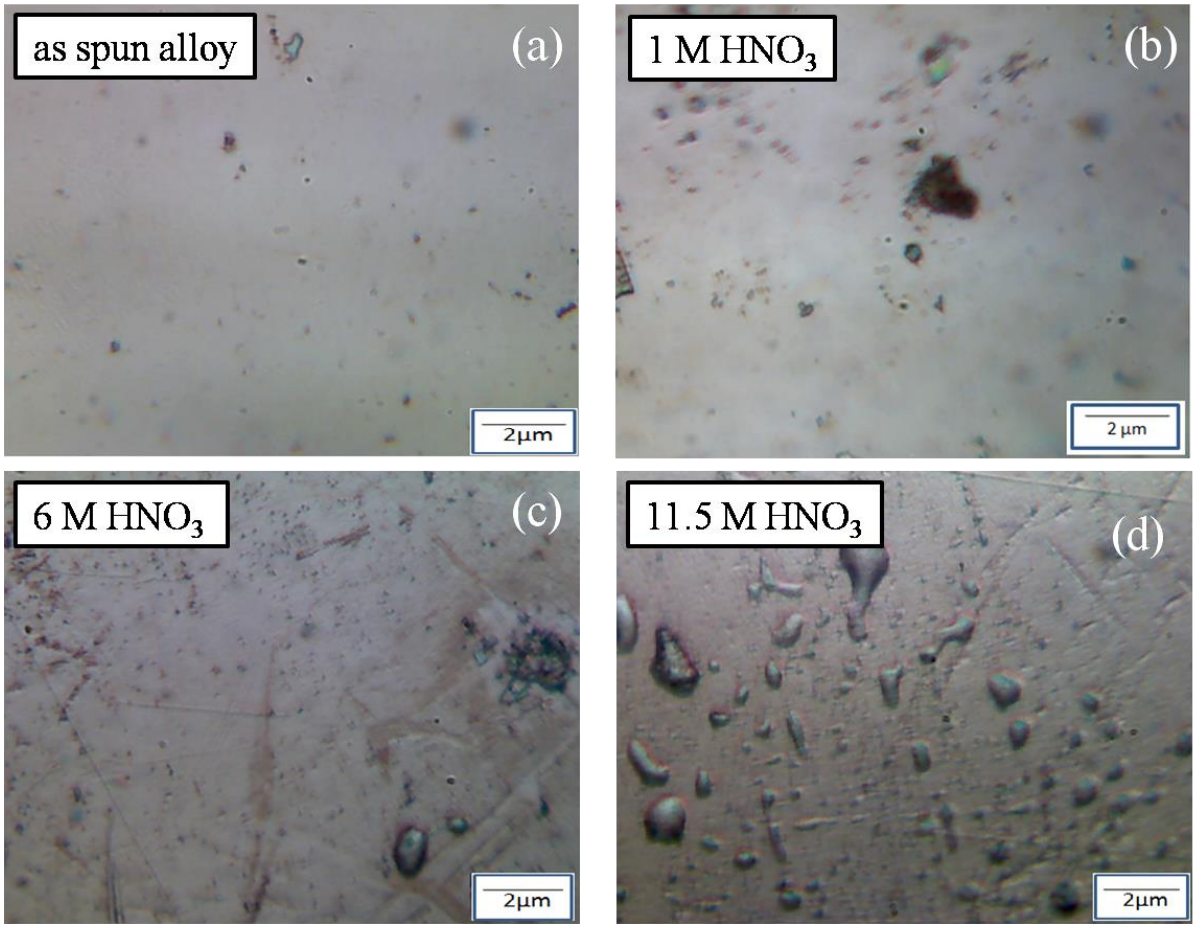

Figure 4.16: Optical Micrographs of $Zr_{59}Nb_3Cu_{20}Ni_8Al_{10}$ amorphous alloy (a) as spun ribbon and after exposure in (b) 1 M aqueous HNO_3, (c) 6 M aqueous HNO_3 and (d) 11.5 M aqueous HNO_3 for 360 hours

SEM was employed to better understand the corrosion behavior of the $Zr_{59}Nb_3Cu_{20}Ni_8Al_{10}$ amorphous alloy after immersion in lower (1 M HNO_3), moderate (6 M HNO_3) and higher (11.5 M HNO_3) concentration of nitric acid medium for 360 hours at room temperature. Figure 4.17 exhibits the SEM micrographs of $Zr_{59}Nb_3Cu_{20}Ni_8Al_{10}$ amorphous alloy. As concentration of nitric acid increases, the passive layer formation on the surface of alloy also increases. Figure 4.17 (c) shows that oxidation layer is not uniform in 6 M HNO_3 and in 11.5 M HNO_3 some granular inhomogeneous distribution of oxide layer has been noticed, as illustrated in figure 4.17 (d). It is suggested here that the passive layer of niobium oxide protects the alloy from corrosion because the Nb_2O_5 exhibits the good corrosion resistance [85]. The $Zr_{59}Nb_3Cu_{20}Ni_8Al_{10}$ alloy has already been studied in Na_2SO_4 solution by Raju et.

al. [67]. In this study niobium species were detected in the oxide layer region by AES analysis and this oxidized species of niobium, which as a valve metal in its pure state tends to form spontaneously very thin barrier type oxide layer when exposed to air or humid environments. This also participates in the passive layer formation on the amorphous alloys. In the present study possibly this could be a reason of passive layer formation on surface of $Zr_{59}Nb_3Cu_{20}Ni_8Al_{10}$ alloy in nitric acid media.

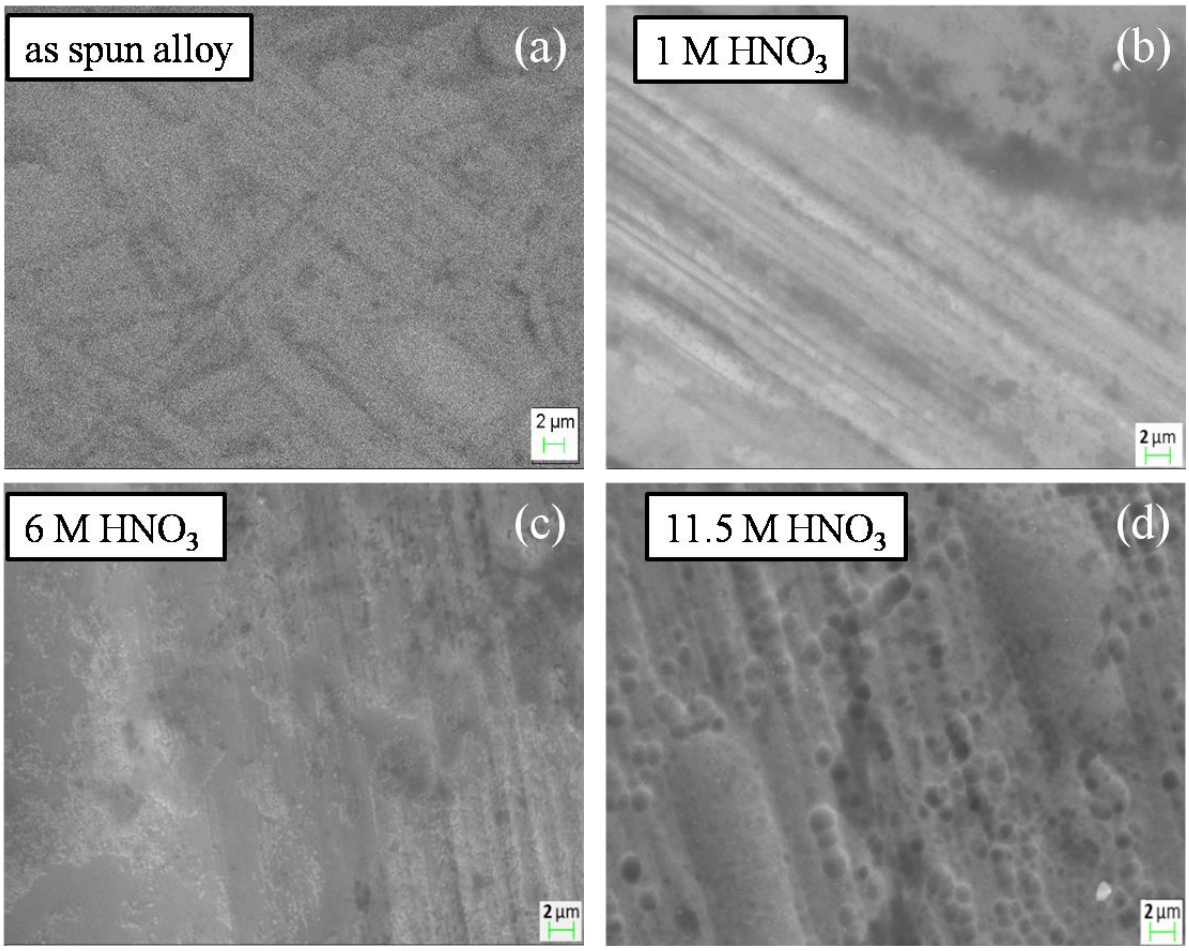

Figure 4.17: SEM Micrographs of $Zr_{59}Nb_3Cu_{20}Ni_8Al_{10}$ amorphous alloy (a) as spun ribbon and after exposure in (b) 1 M aqueous HNO_3, (c) 6 M aqueous HNO_3 and (d) 11.5 M aqueous HNO_3 medium for 360 hours

The surface morphology of the as-spun $Zr_{55}Cu_{30}Ni_5Al_{10}$, $Zr_{60}Nb_2Cu_{20}Ni_8Al_{10}$, $Zr_{59}Nb_3Cu_{20}Ni_8Al_{10}$, $Zr_{57}Nb_5Cu_{20}Ni_8Al_{10}$ and $Zr_{60}Pd_5Cu_{15}Ni_{10}Al_{10}$ amorphous ribbon alloys after immersion in nitric acid medium were examined by optical microscopy. Figure 4.18 shows the optical micrographs of $Zr_{55}Cu_{30}Ni_5Al_{10}$, $Zr_{60}Nb_2Cu_{20}Ni_8Al_{10}$, $Zr_{59}Nb_3Cu_{20}Ni_8Al_{10}$,

$Zr_{57}Nb_5Cu_{20}Ni_8Al_{10}$ and $Zr_{60}Pd_5Cu_{15}Ni_{10}Al_{10}$ amorphous ribbon alloys after immersion in 1 M and 11.5 M aqueous HNO_3 medium for 480 h at room temperature. Figure 4.18 revealed that $Zr_{59}Nb_3Cu_{20}Ni_8Al_{10}$ amorphous alloy possesses better corrosion resistance among all investigated Zr-based bulk amorphous alloys. The optical micrograph of $Zr_{60}Nb_2Cu_{20}Ni_8Al_{10}$, $Zr_{59}Nb_3Cu_{20}Ni_8Al_{10}$ amorphous alloys exhibit the presence of passive layer on the surface of immersed sample in 1 M and 11.5 M HNO_3 solution, as shown in the figures 4.18 (c), 4.18 (d), 4.18 (e) and 4.18 (f). These results revealed that the surface of $Zr_{57}Nb_5Cu_{20}Ni_8Al_{10}$ amorphous alloy immersed in 1 M HNO_3 (figure 4.18 (g)) and 11.5 M HNO_3 (figure 4.18 (h)) was profoundly corroded than the surface of $Zr_{60}Nb_2Cu_{20}Ni_8Al_{10}$ and $Zr_{59}Nb_3Cu_{20}Ni_8Al_{10}$ amorphous alloys. On the other hand, Pd containing $Zr_{60}Pd_5Cu_{15}Ni_{10}Al_{10}$ amorphous alloy was severly corroded among all investigated Zr-based bulk amorphous alloys as shown in optical micrographs (figure 4.18 (i) and 4.18 (j)). Further, SEM was employed to investigate the surface morphologies of these samples after immersion in 1 M aqueous HNO_3 and 11.5 M aqueous HNO_3 medium for 480 hours at room temperature. Figure 4.19 exhibits the SEM micrographs of $Zr_{55}Cu_{30}Ni_5Al_{10}$, $Zr_{60}Nb_2Cu_{20}Ni_8Al_{10}$, $Zr_{59}Nb_3Cu_{20}Ni_8Al_{10}$, $Zr_{57}Nb_5Cu_{20}Ni_8Al_{10}$ and $Zr_{60}Pd_5Cu_{15}Ni_{10}Al_{10}$ amorphous ribbon alloys after immersion in 1 M aqueous HNO_3 and 11.5 M aqueous HNO_3 medium for 480 h. The SEM micrographs revealed that the $Zr_{59}Nb_3Cu_{20}Ni_8Al_{10}$ glassy alloy shows clean surface (figure 4.18 (e) and (f)) as compared to all other investigated alloys in 1 M and 11.5 M HNO_3 medium. The formation of oxide pockets were observed on the surface of $Zr_{59}Nb_3Cu_{20}Ni_8Al_{10}$ amorphous alloy after immersion in 11.5 M HNO_3 medium as shown in figure 4.18 (f). SEM results exhibit that the $Zr_{55}Cu_{30}Ni_5Al_{10}$ (figure 4.18 (a) and (b)) and $Zr_{60}Pd_5Cu_{15}Ni_{10}Al_{10}$ (figure 4.18 (i) and (j)) amorphous alloys were severely corroded in nitric acid medium. SEM results indicate the possibility of pilling off of the passive film formed on the $Zr_{60}Nb_2Cu_{20}Ni_8Al_{10}$ alloy at 11.5 M HNO_3, as shown in figure 4.18 (d). These optical and SEM results were in good agreement with results of weight loss analysis.

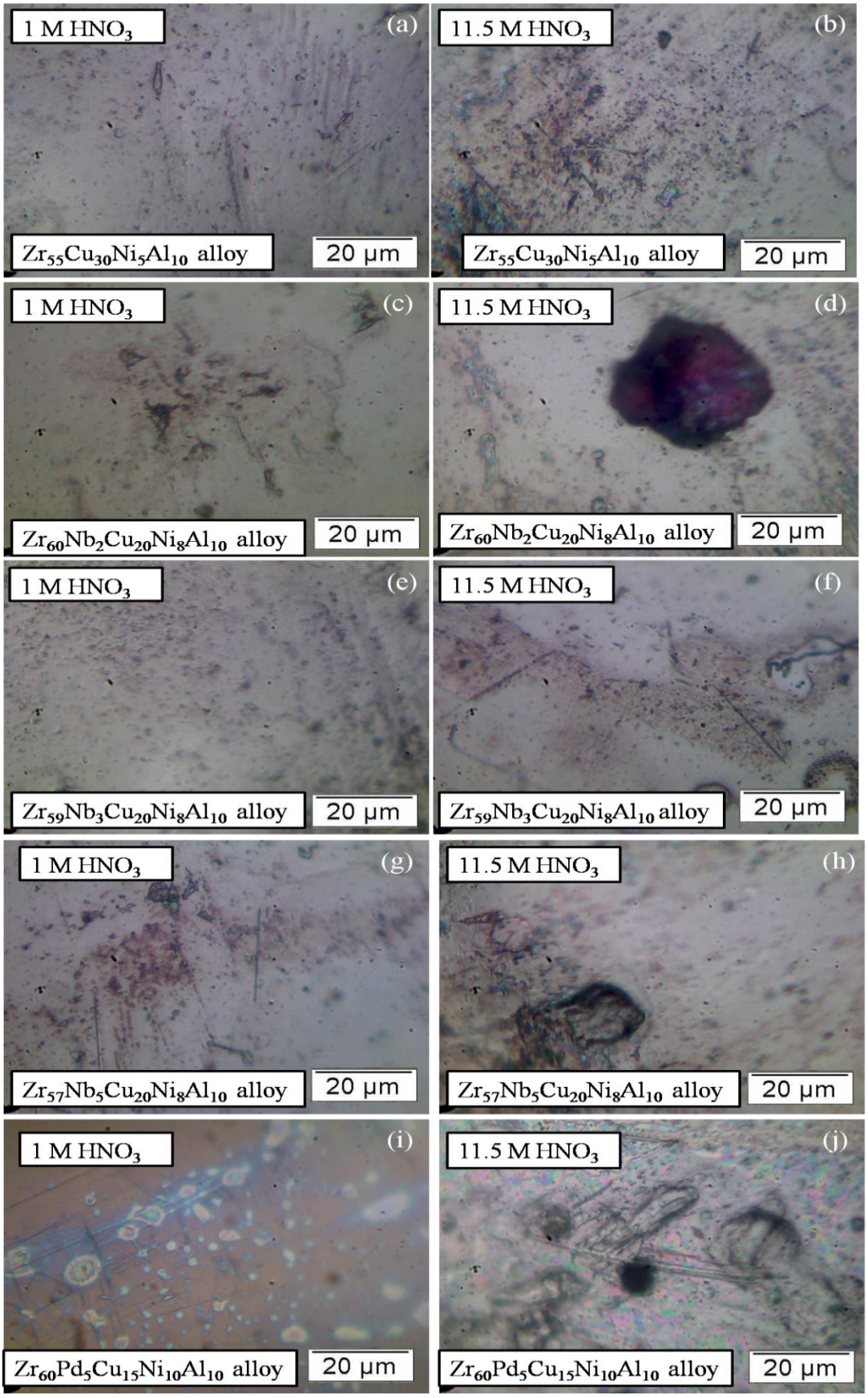

Figure 4.18: Optical micrographs of Zr-based bulk amorphous alloys after immersion in different concentration of nitric acid medium for 480 h at room temperature

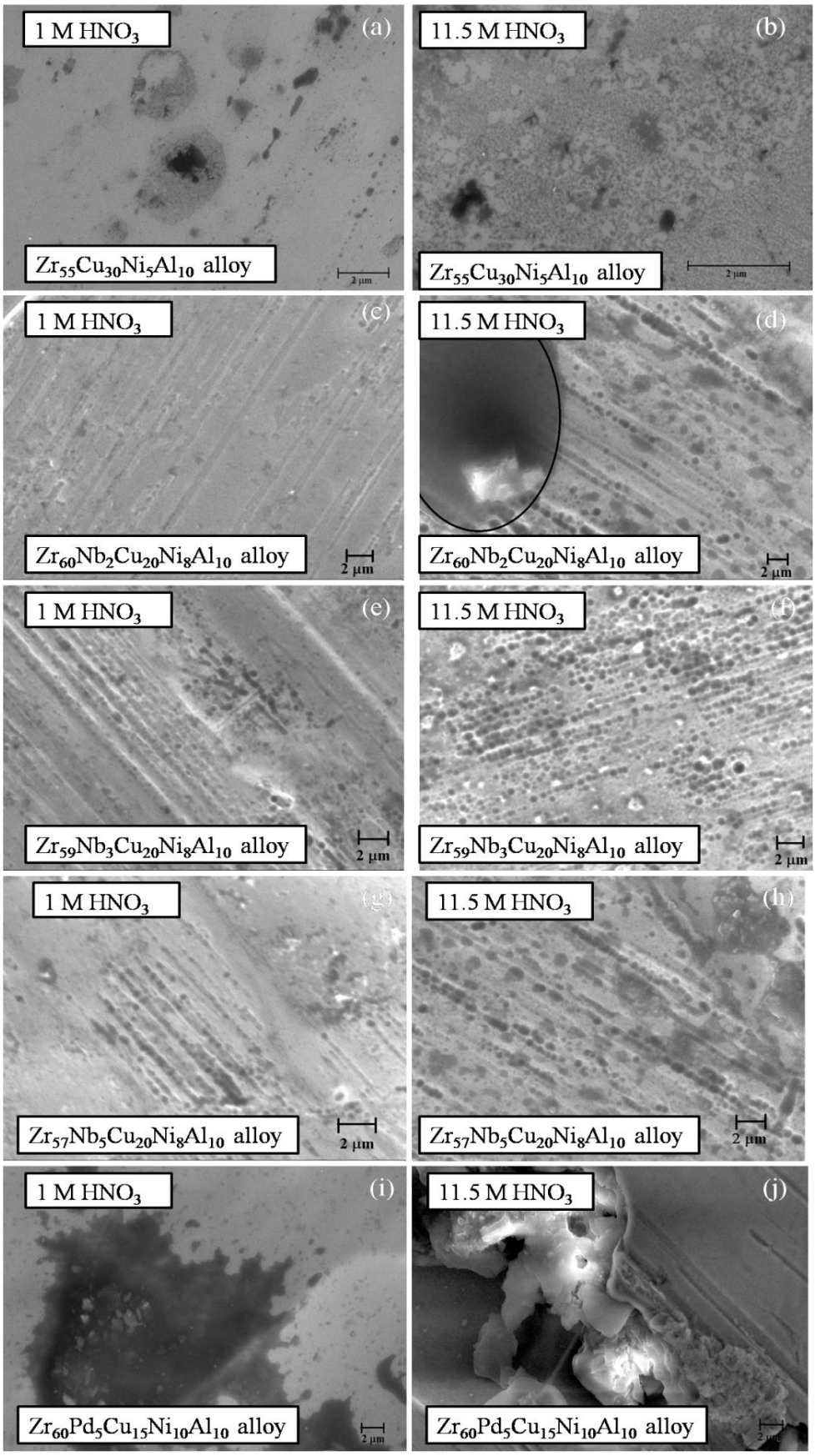

Figure 4.19: SEM micrographs of Zr-based bulk amorphous alloys after immersion in different concentration of nitric acid medium for 480 h at room temperature

Since, Nb containing Zr-based bulk amorphous alloys has exhibited better corrosion resistance in nitric acid environment so in order to further elucidate the surface topography of these Nb containing Zr-based bulk amorphous alloys such as $Zr_{60}Nb_2Cu_{20}Ni_8Al_{10}$, $Zr_{59}Nb_3Cu_{20}Ni_8Al_{10}$ and $Zr_{57}Nb_5Cu_{20}Ni_8Al_{10}$ amorphous alloys, AFM studies were carried out. Figure 4.20 show the AFM micrographs of $Zr_{60}Nb_2Cu_{20}Ni_8Al_{10}$, $Zr_{59}Nb_3Cu_{20}Ni_8Al_{10}$ and $Zr_{57}Nb_5Cu_{20}Ni_8Al_{10}$ amorphous alloys after immersion in 1 M aqueous HNO_3 and 11.5 M aqueous HNO_3 medium for 480 h at room temperature. The $Zr_{60}Nb_2Cu_{20}Ni_8Al_{10}$ glassy alloy in 1 M HNO_3 (figure 4.20 (a)) shows more rough surface than in 11.5 M HNO_3 (figure 4.20 (b)) whereas, the appearance of trench like structure in figure 4.20 (d) is due to the aggressive dissolution of $Zr_{59}Nb_3Cu_{20}Ni_8Al_{10}$ alloy in 11.5 M HNO_3 medium than 1 M HNO_3 medium (figure 4.20 (c)). On the other hand AFM micrographs of $Zr_{57}Nb_5Cu_{20}Ni_8Al_{10}$ amorphous alloy (figure 4.20 (e) and (f)) represent the presence of many trench like structures indicating the roughness of the surface in both the concentration of nitric acid. It can be suggested that the oxide film formed on the surface of $Zr_{60}Nb_2Cu_{20}Ni_8Al_{10}$ and $Zr_{59}Nb_3Cu_{20}Ni_8Al_{10}$ glassy alloys consist the oxides of Zr and Nb element, which play an important role in improving the corrosion resistance of the alloy in aqueous nitric acid medium. The oxide film present on the surface of $Zr_{59}Nb_3Cu_{20}Ni_8Al_{10}$ glassy alloy has a greater amount of Nb_2O_5 as compare to $Zr_{60}Nb_2Cu_{20}Ni_8Al_{10}$ glassy alloy due to the greater atomic percentage of Nb in $Zr_{59}Nb_3Cu_{20}Ni_8Al_{10}$ alloy and this leads to the better corrosion resistance of $Zr_{59}Nb_3Cu_{20}Ni_8Al_{10}$ glassy alloy in aqueous HNO_3. However, poor corrosion resistance of $Zr_{57}Nb_5Cu_{20}Ni_8Al_{10}$ amorphous is attributed to the presence of crystalline phases, as shown in XRD of this sample (figure 4.2 (a)).

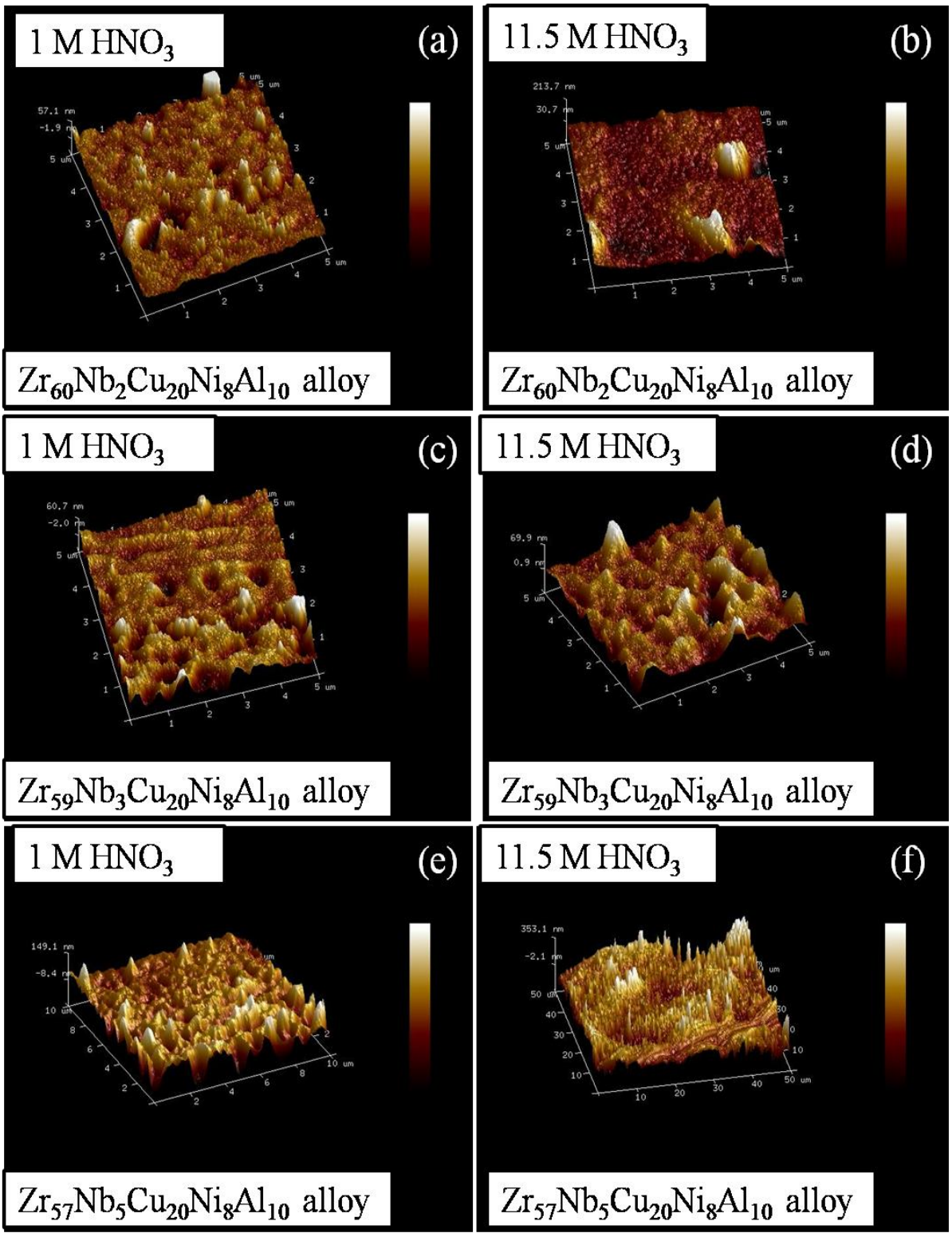

Figure 4.20: AFM micrographs of Zr-based amorphous alloys after immersion in different concentration of nitric acid medium for 480 h at room temperature.

4.1.3.5 XPS study

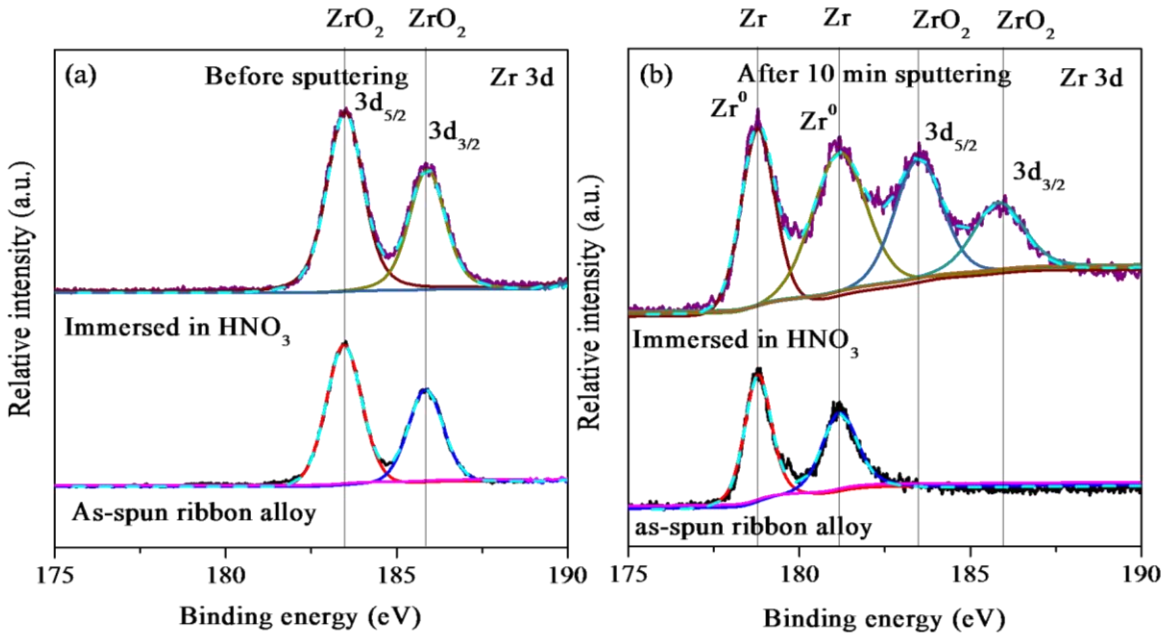

Figure 4.21: High resolution XPS spectra of Zr for as-spun and immersed $Zr_{59}Nb_3Cu_{20}Ni_8Al_{10}$ amorphous alloy in 11.5 M HNO_3 medium for 480 hours (a) before sputtering and (b) after 10 min sputtering

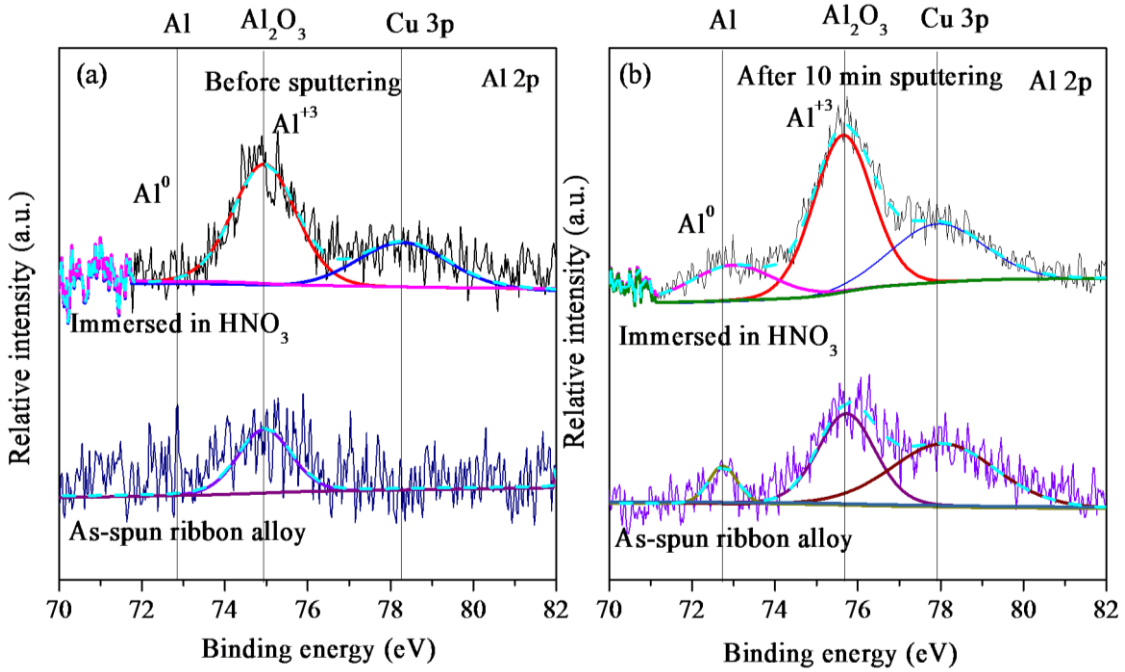

Figure 4.22: High resolution XPS spectra of Al for as-spun and immersed $Zr_{59}Nb_3Cu_{20}Ni_8Al_{10}$ amorphous alloy in 11.5 M HNO_3 medium for 480 hours (a) before sputtering and (b) after 10 min sputtering

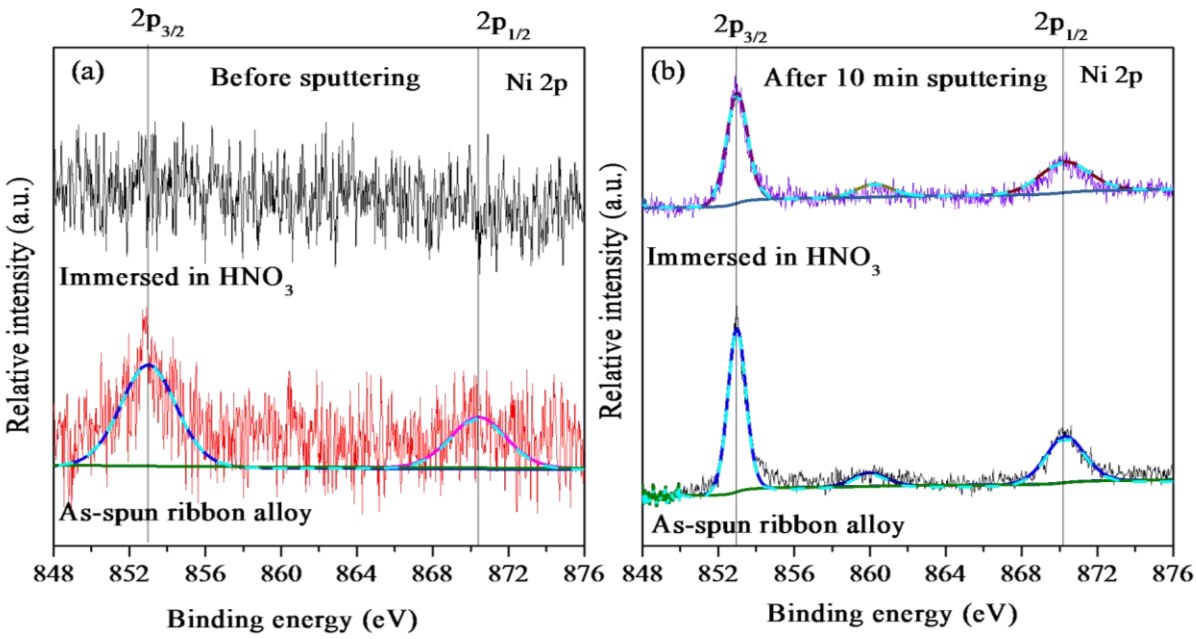

Figure 4.23: High resolution XPS spectra of Ni for as-spun and immersed $Zr_{59}Nb_3Cu_{20}Ni_8Al_{10}$ amorphous alloy in 11.5 M HNO_3 medium for 480 hours (a) before sputtering and (b) after 10 min sputtering

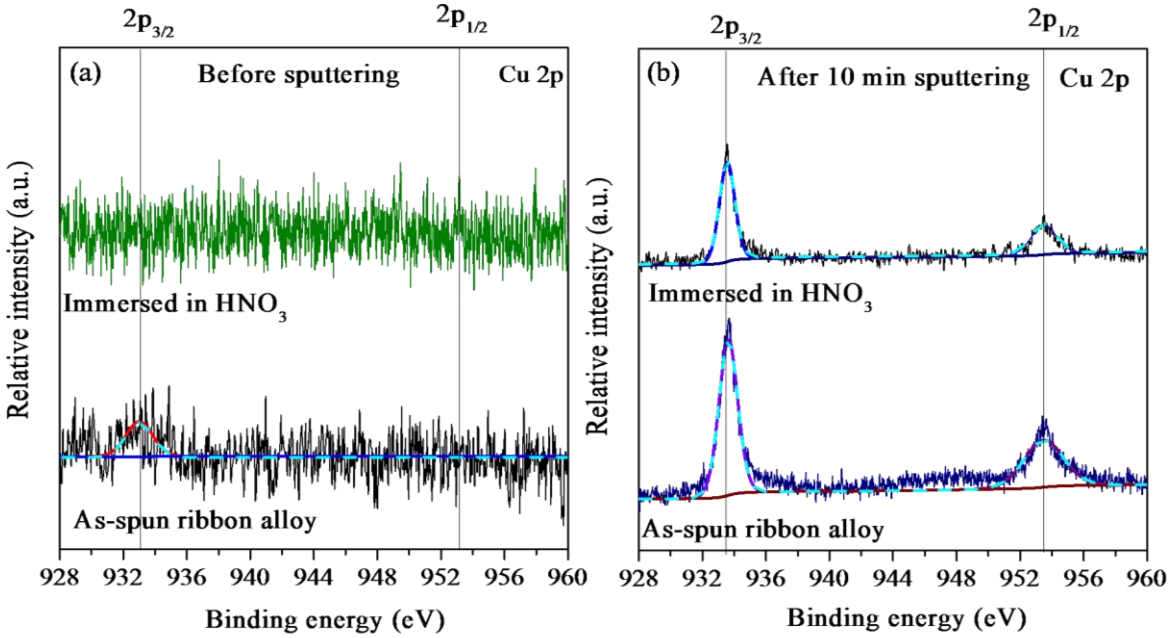

Figure 4.24: High resolution XPS spectra of Cu for as-spun and immersed $Zr_{59}Nb_3Cu_{20}Ni_8Al_{10}$ amorphous alloy in 11.5 M HNO_3 medium for 480 hours (a) before sputtering and (b) after 10 min sputtering

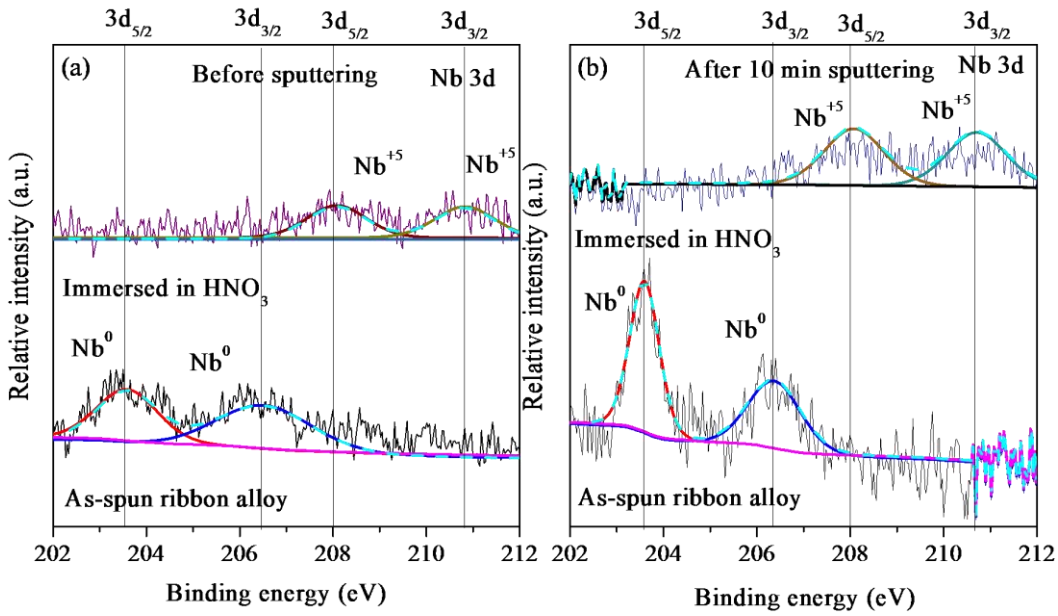

Figure 4.25: High resolution XPS spectra of Nb for as-spun and immersed $Zr_{59}Nb_3Cu_{20}Ni_8Al_{10}$ amorphous alloy in 11.5 M HNO_3 medium for 480 hours (a) before sputtering and (b) after 10 min sputtering

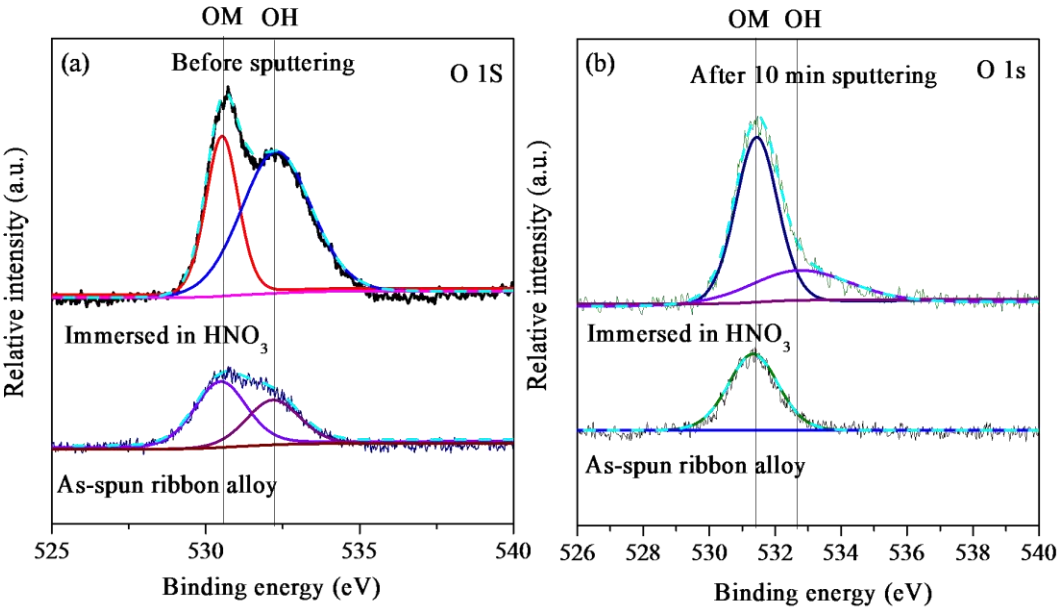

Figure 4.26: High resolution XPS spectra of O for as-spun and immersed $Zr_{59}Nb_3Cu_{20}Ni_8Al_{10}$ amorphous alloy in 11.5 M HNO_3 medium for 480 hours (a) before sputtering and (b) after 10 min sputtering

To understand the compositional changes on the surface of $Zr_{59}Nb_3Cu_{20}Ni_8Al_{10}$ amorphous alloy after immersion in 11.5 M HNO_3 medium, XPS studies were carried out on as-spun and immersed sample. The high-resolution XPS spectra of each element Zr, Al, Ni, Cu, Nb and O for as-spun and immersed $Zr_{59}Nb_3Cu_{20}Ni_8Al_{10}$ amorphous alloy in 11.5 M HNO_3 for 480 hours, before and after sputtering of 10 minutes, are shown in figure 4.21, 4.22, 4.23, 4.24, 4.25 and 4.26, respectively. The figure 4.21 (a) represents the Zr 3d spectra of as-spun and immersed $Zr_{59}Nb_3Cu_{20}Ni_8Al_{10}$ amorphous alloy before sputtering and figure 4.21 (b) shows the Zr 3d spectra of as-spun and immersed $Zr_{59}Nb_3Cu_{20}Ni_8Al_{10}$ amorphous alloy after 10 minutes sputtering. The deconvolution of Zr 3d spectra was done in the terms of metal Zr^0 and oxide ZrO_2 based on the literature values of their binding energies. The peaks of ZrO_2 were observed at the binding energies 183.3 eV and 185.7 eV corresponding to the peaks of Zr $3d_{5/2}$ and Zr $3d_{3/2,}$ respectively [151,152]. These peaks corresponding to ZrO_2 were observed before sputtering of the sample in both the conditions of sample i.e. surface of as-spun alloy and after immersion in nitric acid medium. The intensity of XPS peaks corresponding to ZrO_2 was high in the case of immersed sample. The peaks at 179.3 eV and 181.7 eV corresponding to metallic Zr [153] were observed after 10 min of sputtering along with peak corresponding to Zr^{4+} for as-spun alloy. However, the immersed sample has shown the presence of ZrO_2 along with metallic Zr after 10 min sputtering of the sample. The presence of ZrO_2 on the surface of as-cast sample was due to the formation of native oxide, which could not be observed after 10 min of sputtering. The XPS peak at 75.4 eV (figure 4.22 (a)) was assigned to Al 2p indicating Al_2O_3 [154] on the surface of as-spun sample as well as immersed sample. A very small intensity of XPS peak obtained at 72.9 eV indicated the presence of the metallic form of Al on the surface of as-spun alloy [154], which was not observed on the surface of immersed alloy. Figure 4.22 (b) exhibits the presence of Al_2O_3 along with metallic Al after 10 min sputtering of the sample. The XPS peak of Ni $2p_{3/2}$ at 853.3 eV and Ni $2p_{1/2}$ at 870.5 eV corresponding to metallic Ni were appeared on the surface

of as-spun sample (figure 4.23 (a)). No Ni XPS peaks could be observed on the surface of immersed sample as shown in figure 4,23 (a). After sputtering for 10 min, XPS peaks corresponding to metallic Ni were observed for both the samples [151]. The Cu 2p peak (figure 4.24 (a)) was also not observed on the surface of the as- spun sample, whereas the surface of immersed sample exhibited the presence of Cu $2p_{3/2}$ peaks referred to a metallic form of Cu at 933.3 eV, as shown in figure 4.24 (a) [151]. The as spun and immersed sample exhibited the presence of metallic Cu after 10 min of sputtering. It revealed that both Ni and Cu are present in metallic form in both the samples. Figure 4.25 represents the Nb 3d spectra of the surface of as-spun and immersed samples. The surface of as-spun sample exhibited the presence of Nb^0 peak corresponding to metallic Nb at 203.6 eV and 206.4 eV binding energy, as shown in figure 4.25 (a) [84], but the surface of immersed sample clearly exhibited the presence of XPS peaks corresponding to the Nb^{5+} state at 208.0 and 210.7 eV (figure 4.25 (a)), respectively which are assigned to Nb_2O_5 [84]. No peak corresponding to metallic Nb could be observed on the surface of $Zr_{59}Nb_3Cu_{20}Ni_8Al_{10}$ amorphous alloy after immersion in 11.5 M HNO_3 medium. Figure 4.25 (b) revealed that the as-spun alloy shows the presence of metallic Nb after 10 min of sputtering, whereas the immersed sample exhibits the XPS peaks corresponding to Nb^{+5} state indicating the presence of Nb_2O_5 after 10 min of sputtering. The O 1s spectra recorded from the surface of as-spun and immersed sample are shown in figure 4.26 (a). The O 1s spectrum was observed at 531.4 eV assigned to OM oxygen (metal-oxygen bond) [68] corresponds to O^{+2} ions in oxides [151] and a weaker peak at 532.7 eV , which is assigned to OH oxygen linked to bound water or hydrogen [155]. The as-spun sample exhibited the presence of OM oxygen along with OH oxygen on the surface of as-spun alloy due to formation of native oxide, whereas the immersed sample exhibited the presence of relatively high intensity XPS peaks corresponding to OM oxygen and OH oxygen (Figure 4.26 (a)). Figure 4.26 (b) represents the XPS peak recorded on as-spun and immersed samples after 10 min of sputtering of the sample. It revealed that the intensity of OH is

decreased to zero for as-spun alloy after 10 min of sputtering. The immersed sample has shown the presence of OM oxygen as well as OH oxygen due to immersion in aqueous HNO_3 medium after 10 min of sputtering.

These XPS results revealed the fact that the formation of passive film of ZrO_2, Al_2O_3 and Nb_2O_5 take place on the surface of $Zr_{59}Nb_3Cu_{20}Ni_8Al_{10}$ amorphous alloy after immersion in HNO_3 medium. Since ZrO_2 layer has a strong passivation ability and high corrosion resistance in H^+-containing solutions [51] thus, it protects the alloy from corrosion. Also, Nb_2O_5 possesses corrosion resistant properties [85] hence it is useful in protecting the alloy from corrosion attack in aqueous solutions.

4.1.4 Conclusion

The corrosion behavior of Zr-based amorphous alloys such as $Zr_{55}Cu_{30}Ni_5Al_{10}$, $Zr_{60}Nb_2Cu_{20}Ni_8Al_{10}$, $Zr_{59}Nb_3Cu_{20}Ni_8Al_{10}$, $Zr_{57}Nb_5Cu_{20}Ni_8Al_{10}$ $Zr_{57}Nb_5Cu_{15.4}Ni_{12.6}Al_{10}$, $Zr_{59}Ti_3Cu_{20}Ni_8Al_{10}$ and $Zr_{60}Pd_5Cu_{15}Ni_{10}Al_{10}$ alloys in lower (1 M HNO_3), moderate (6 M HNO_3) and higher (11.5 M HNO_3) concentration of nitric acid medium has been investigated in the present research work. In order to study the corrosion properties of these Zr-based amorphous alloys, electrochemical measurements and weight loss analysis were carried out. It is concluded from above mentioned investigations that Nb-containing Zr-based amorphous alloys possesses better corrosion resistance among all investigated alloys. The better corrosion resistance of Nb-containing Zr-based bulk amorphous alloys was attributed to the formation of passive layer containing ZrO_2 and Nb_2O_5 which was confirmed by XPS study.

4.2 CORROSION INVESTIGATIONS AT HIGH TEMPERATURE

4.2.1. Introduction

Zirconium is known as a good corrosion resistant material in nitric acid environments [156]. Zircaloy-4 has been studied in HNO_3 medium and it possess good corrosion resistance condition in comparison to commercial CP-Ti, Ti–5%Ta, and Ti–5%Ta–1.8%Nb alloy in 11.5 M HNO_3 [82]. The Ti-5%Ta1.8%Nb alloy was found more corrosion resistant than conventional stainless steel 304L and 304L nitric acid grade (NAG) for fuel reprocessing applications [157]. The corrosion behavior of some Zr-based bulk amorphous alloys has already been investigated in the nitric acid environment at room temperature [73,142,158] but the corrosion behavior of Zr-based amorphous alloys in nitric acid at high temperature has not been investigated in the literature. Since, fuel reprocessing applications involves the use of boiling nitric acid [50] so it is important to investigate the corrosion behavior of Zr-based bulk amorphous alloys in boiling nitric acid environment. Although Nb containing Ni-based bulk amorphous alloys [44,84] and Nb containing Ti-based alloys [85] have been studied in nitric acid medium at boiling temperature but enough information related to corrosion behavior of Zr based bulk amorphous alloy in nitric acid medium at boiling temperature, is not available in the literature.

Thus, the aim of the present research work in this section is to report the results of investigations on the corrosion behavior of some Zr-based amorphous alloys such as $Zr_{60}Nb_2Cu_{20}Ni_8Al_{10}$ and $Zr_{59}Nb_3Cu_{20}Ni_8Al_{10}$ and $Zr_{60}Pd_5Cu_{15}Ni_{10}Al_{10}$ amorphous alloys using weight loss study in nitric acid environment at boiling temperature

4.2.2 Experimental

For preliminary studies, Pd containing and Nb containing Zr-based bulk amorphous alloys, $Zr_{59}Nb_3Cu_{20}Ni_8Al_{10}$ and $Zr_{60}Pd_5Cu_{15}Ni_{10}Al_{10}$ amorphous alloy were immersed in lower (1 M

HNO_3), moderate (6 M HNO_3) and higher (11.5 M HNO_3) concentration of HNO_3 at boiling temperature for a shorter duration i.e. 8 hours (h) and corrosion rate was calculated by weight loss analysis method. Furthermore the duration of experiment was extended up to 24 h, 48 h and 72 h for the sample which has shown better corrosion resistance for these Zr-based bulk amorphous alloys. The experimental setup used for this high temperature corrosion studies has been already discussed in chapter 3 of this thesis. The surface morphology of these treated samples was examined by FESEM using NOVA-NANO-FESEM 450 at MRC, MNIT Jaipur. Furthermore the origin of corrosion in these investigated samples in boiling nitric acid was studied by XPS using ESCA+ Omicron Nanotechnology (Oxford Instrument, Germany) at MRC, MNIT Jaipur.

4.2.3 Results and discussion

4.2.3.1 Weight loss analysis at high temperature

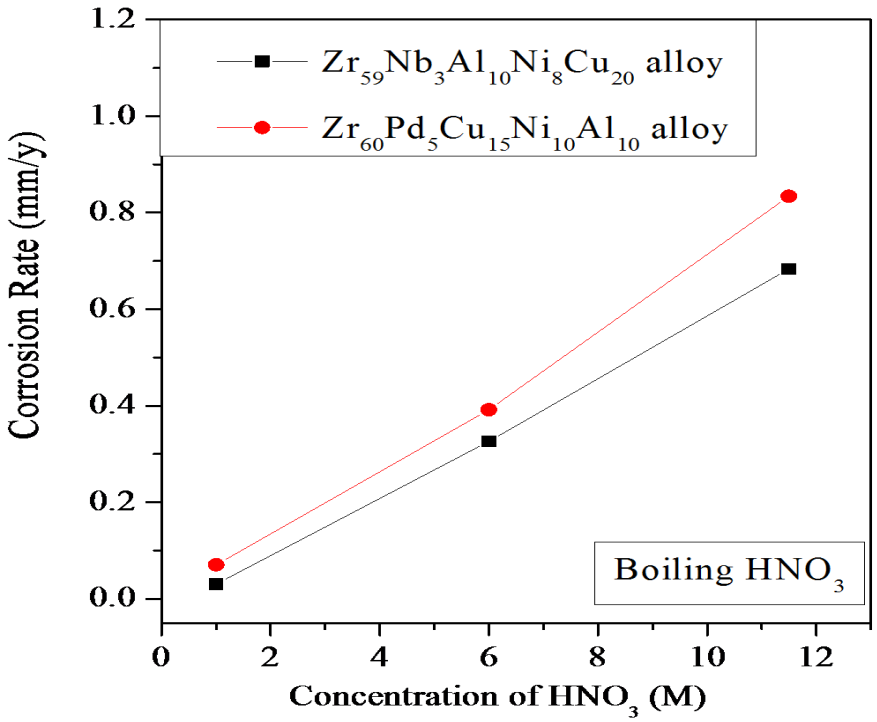

Figure 4.27: Corrosion rate versus concentration of aqueous HNO_3 plot of $Zr_{59}Nb_3Cu_{20}Ni_8Al_{10}$ and $Zr_{60}Pd_5Cu_{15}Ni_{10}Al_{10}$ amorphous alloys at boiling temperature.

Table 4.5: Corrosion rate values of $Zr_{59}Nb_3Cu_{20}Ni_8Al_{10}$ and $Zr_{60}Pd_5Cu_{15}Ni_{10}Al_{10}$ amorphous alloys exposed in different concentration of HNO_3 at boiling temperature for 8 hours.

Concentration of HNO_3	**Corrosion rate (mm/y)**	
	$Zr_{59}Nb_3Cu_{20}Ni_8Al_{10}$	**$Zr_{60}Pd_5Cu_{15}Ni_{10}Al_{10}$**
1 M HNO_3	0.0306	0.0704
6 M HNO_3	0.3264	0.392
11.5 M HNO_3	0.6834	0.8341

Table 4.5 shows the corrosion rate values obtained for the $Zr_{59}Nb_3Cu_{20}Ni_8Al_{10}$ and $Zr_{60}Pd_5Cu_{15}Ni_{10}Al_{10}$ amorphous alloys exposed in boiling 1 M, 6 M and 11.5 M aqueous HNO_3 for 8 hours. The corrosion rate versus concentration of aqueous boiling HNO_3 plot of $Zr_{59}Nb_3Cu_{20}Ni_8Al_{10}$ and $Zr_{60}Pd_5Cu_{15}Ni_{10}Al_{10}$ amorphous alloys is shown in figure 4.27. Both alloys show least value of corrosion rate in 1 M HNO_3 and the corrosion rate increases as the concentration of nitric acid increases. The alloys exhibit highest value of corrosion rate at 11.5 M concentration of HNO_3. At boiling temperature, the corrosion rate is low in 1 M HNO_3 and 6 M HNO_3 aqueous media in comparison to 11.5 M HNO_3, due to severity of environment for both amorphous alloys. The Goldschmidt's radii of Zr, Cu , Al, Ni, Nb and Pd are 0.160, 0.128, 0.143, 0.125, 0.147 and 0.146 nm, respectively. These data shows that Cu and Ni elements are smaller atoms among other elements therefore mobility of these atoms is quite high. So, it is quite possible that the dissolution of Cu takes place in aqueous nitric acid environment. Jayaraj et al. [148] has reported the dissolution of Cu and Ni atoms underlying the native layer is possible through tunneling process during the applied potential of electrochemical corrosion of $Zr_{48}Cu_{36}Ag_8Al_8$. Therefore, in the present study the alloys possess two simultaneous reactions, (1) active dissolution of Cu and Ni (2) passivation of elements like Zr, Al, Nb and Pd. In the present study, $Zr_{60}Pd_5Cu_{15}Ni_{10}Al_{10}$ amorphous alloy is

showing poor corrosion resistance than $Zr_{59}Nb_3Cu_{20}Ni_8Al_{10}$ amorphous alloy in HNO_3 medium, possibly due to the origination of passive layer of Nb_2O_5 on $Zr_{59}Nb_3Cu_{20}Ni_8Al_{10}$ alloy which is strong, protective and corrosion resistant in nitric acid medium [85]. Thus, the results of preliminary studies on $Zr_{60}Pd_5Cu_{15}Ni_{10}Al_{10}$ and $Zr_{59}Nb_3Cu_{20}Ni_8Al_{10}$ amorphous alloys revealed that Nb-containing Zr-based amorphous alloys shows better corrosion resistance in boiling nitric acid environment. Furthermore, these Nb-containing Zr-based amorphous alloys such as $Zr_{60}Nb_2Cu_{20}Ni_8Al_{10}$ and $Zr_{59}Nb_3Cu_{20}Ni_8Al_{10}$ amorphous alloys were chosen for extended studies in boiling nitric acid medium.

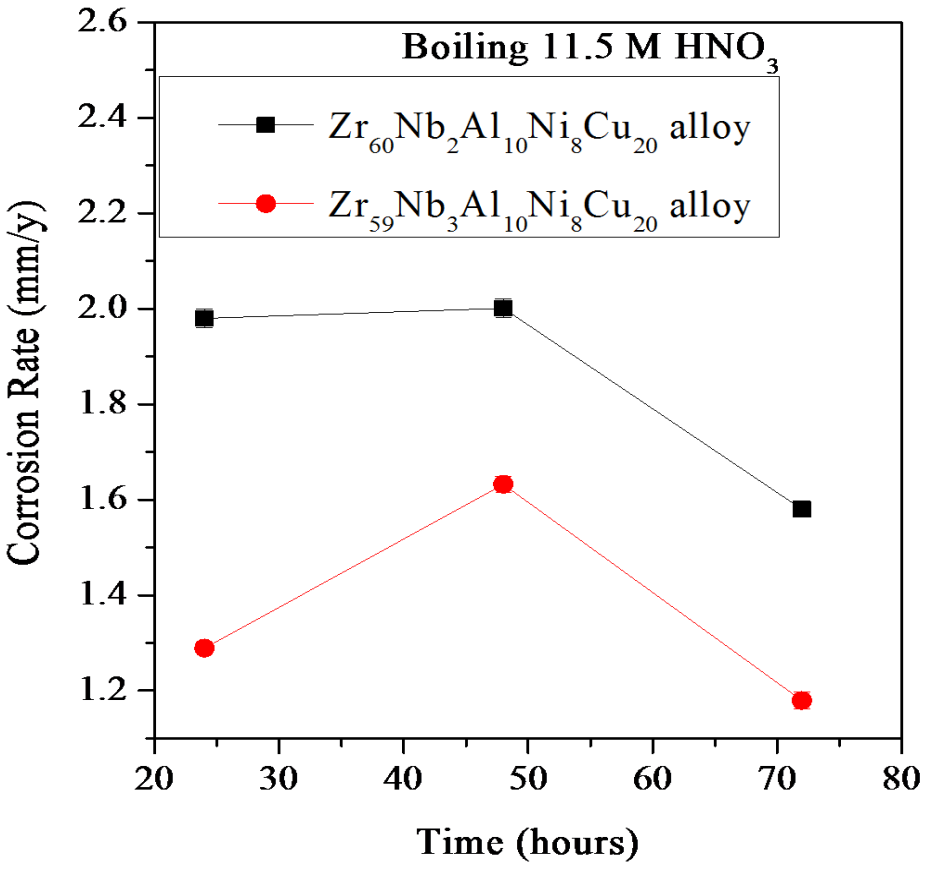

Figure 4.28: Corrosion rate versus exposure time plot of $Zr_{60}Nb_2Cu_{20}Ni_8Al_{10}$ and $Zr_{59}Nb_3Cu_{20}Ni_8Al_{10}$ amorphous alloys in 11.5 M HNO_3 at boiling temperature.

Table 4.6 shows the corrosion rate values obtained for the $Zr_{60}Nb_2Cu_{20}Ni_8Al_{10}$ and $Zr_{59}Nb_3Cu_{20}Ni_8Al_{10}$ amorphous alloys exposed in boiling 11.5 M HNO_3 for 24 h, 48 h and 72

hours. The corrosion rate versus exposure time plot of $Zr_{60}Nb_2Cu_{20}Ni_8Al_{10}$ and $Zr_{59}Nb_3Cu_{20}Ni_8Al_{10}$ amorphous alloys is shown in figure 4.28. The $Zr_{59}Nb_3Cu_{20}Ni_8Al_{10}$ alloy shows low corrosion rate in boiling nitric acid medium in comparison to $Zr_{60}Nb_2Cu_{20}Ni_8Al_{10}$ alloy. A slight decrease in corrosion rate has been observed after 48 hours for both the alloys. It has been reported that the passivation speed of Nb containing Zr based BMG sample is quickened with the increase in the concentration of HNO_3 solution concentration in a certain range and its corrosion resistance becomes stronger proportionally [143]. So, in the present study after 48 hours, alloy shows a decrease in value of corrosion rate due to better passivation in a certain range. These results were further confirmed by studying the surface morphology of these treated samples using FESEM.

Table 4.6: Corrosion rate values of $Zr_{60}Nb_2Cu_{20}Ni_8Al_{10}$ and $Zr_{59}Nb_3Cu_{20}Ni_8Al_{10}$ amorphous alloys exposed in boiling 11.5 M HNO_3 medium for 24 h, 48 h and 72 hours.

Concentration of HNO_3	**Corrosion rate (mm/y)**	
	$Zr_{60}Nb_2Cu_{20}Ni_8Al_{10}$ amorphous alloy	**$Zr_{59}Nb_3Cu_{20}Ni_8Al_{10}$ amorphous alloy**
24 h	1.980	1.289
48 h	2.001	1.632
72 h	1.580	1.179

4.2.3.2 Surface morphology

The surface morphology of $Zr_{59}Nb_3Cu_{20}Ni_8Al_{10}$ and $Zr_{60}Pd_5Cu_{15}Ni_{10}Al_{10}$ amorphous alloys immersed in lower (1 M HNO_3), moderate (6 M HNO_3) and higher (11.5 M HNO_3) concentration of nitric acid at boiling temperature was examined by SEM, as shown in figure 4.29 and 4.30, respectively. As per the results of weight loss analysis studies (figure 4.27), the corrosion rate increases as the concentration of boiling nitric acid increases. The SEM micrographs of these samples revealed the fact that the Nb containing $Zr_{59}Nb_3Cu_{20}Ni_8Al_{10}$

amorphous alloys show better uniformity on the surface than $Zr_{60}Pd_5Cu_{15}Ni_{10}Al_{10}$ amorphous alloys in the similar conditions. The surface of $Zr_{60}Pd_5Cu_{15}Ni_{10}Al_{10}$ amorphous alloy is relatively more corroded than that of $Zr_{59}Nb_3Cu_{20}Ni_8Al_{10}$ amorphous alloy in all concentration of nitric acid. The results obtained from SEM studies are in good agreement with results of weight loss analysis of these samples, which also indicates the better corrosion resistance of Nb containing $Zr_{59}Nb_3Cu_{20}Ni_8Al_{10}$ amorphous alloy in boiling aqueous HNO_3 media.

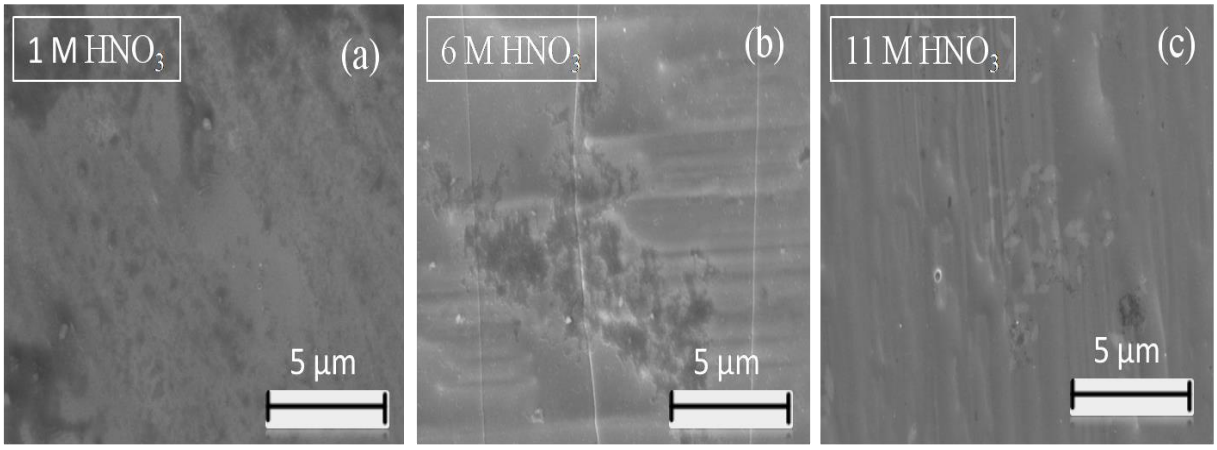

Figure 4.29: SEM micrographs of $Zr_{59}Nb_3Cu_{20}Ni_8Al_{10}$ amorphous alloy after immersion in boiling (a) 1 M HNO_3 (b) 6 M HNO_3 (c) 11.5 M HNO_3

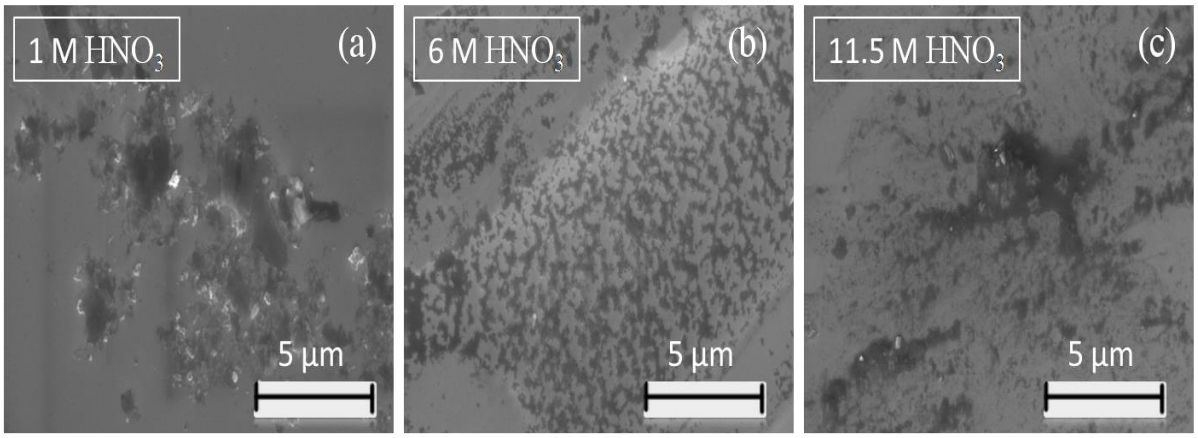

Figure 4.30: SEM micrographs of $Zr_{60}Pd_5Cu_{15}Ni_{10}Al_{10}$ amorphous alloy after immersion in boiling (a) 1 M HNO_3 (b) 6 M HNO_3 (c) 11.5 M HNO_3

Furthermore, the surface morphology of the $Zr_{60}Nb_2Cu_{20}Ni_8Al_{10}$ and $Zr_{59}Nb_3Cu_{20}Ni_8Al_{10}$ amorphous alloys immersed in boiling 11.5 M HNO_3 for 24 h, 48 h and 72 hours, was examined by SEM. Figure 4.31 and 4.32 represent the FESEM images of as-spun $Zr_{60}Nb_2Cu_{20}Ni_8Al_{10}$ and $Zr_{59}Nb_3Cu_{20}Ni_8Al_{10}$ amorphous alloys and after immersion in 11.5 M HNO_3 medium at boiling temperature for 24 h, 48 h and 72 hours, respectively.

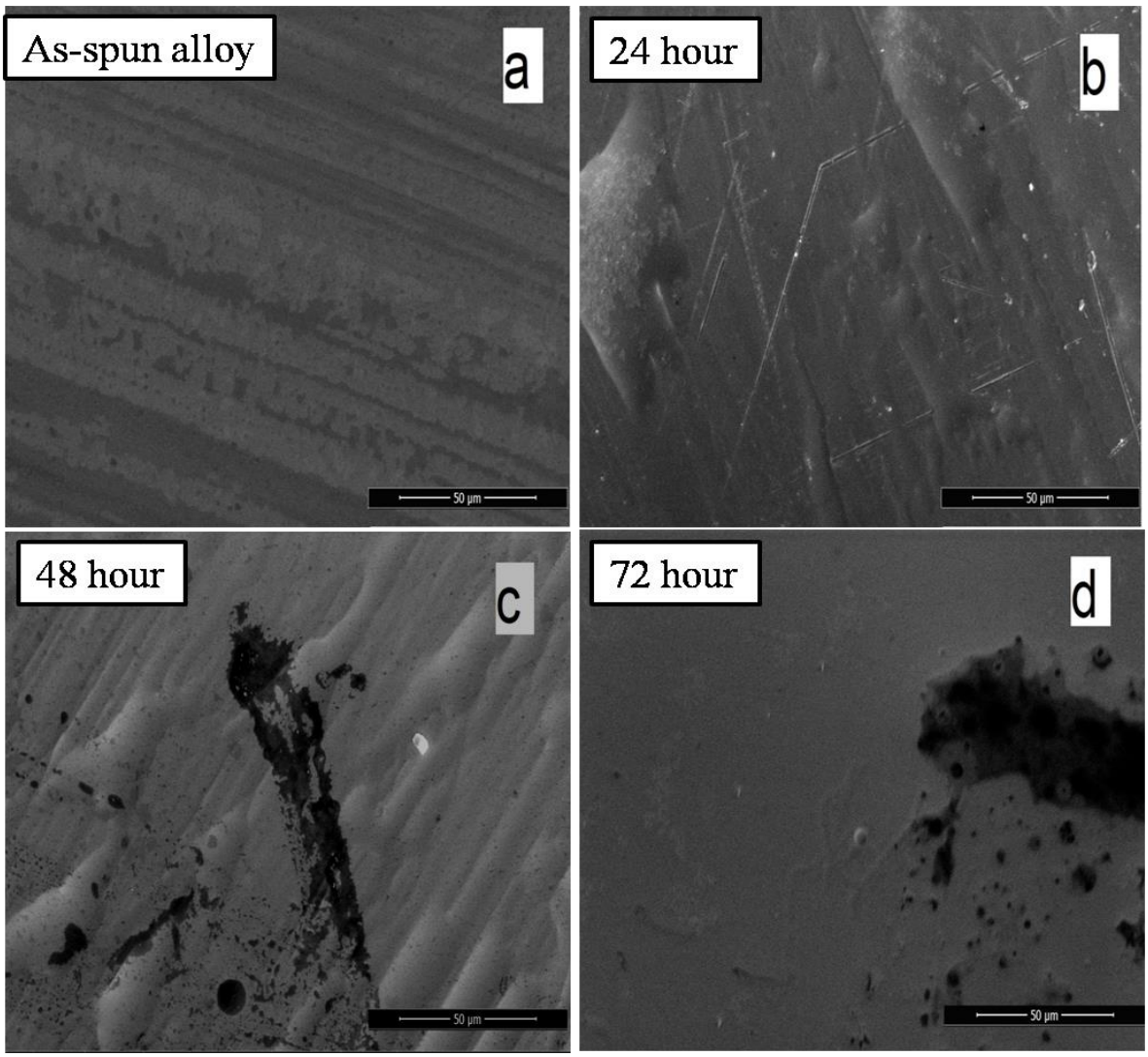

Figure 4.31: FESEM micrographs of (a) as-spun $Zr_{60}Nb_2Cu_{20}Ni_8Al_{10}$ amorphous alloy and after immersion in 11.5 M HNO_3 medium at boiling temperature for (b) 24 h (c) 48 h and (d) 72 h.

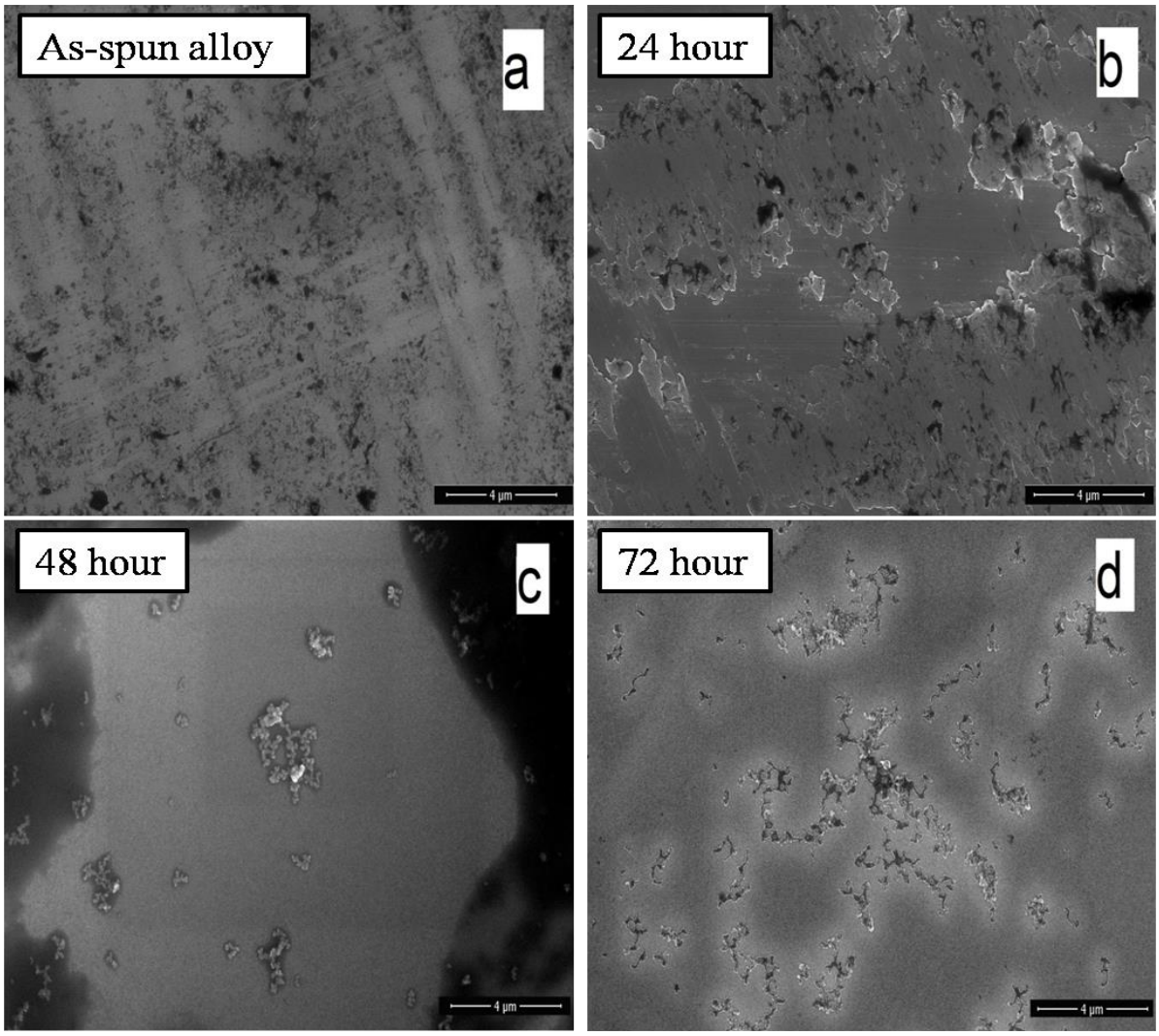

Figure 4.32: FESEM micrographs of (a) as-spun $Zr_{59}Nb_3Cu_{20}Ni_8Al_{10}$ amorphous alloy and after immersion in 11.5 M HNO_3 medium at boiling temperature for (b) 24 h (c) 48 h and (d) 72 h.

Figure 4.31 (b) and 4.31 (c) show typical air pocket morphology due to the entrapment of air at the wheel-melt interface [159]. Figure 4.31 (c) and 4.31 (d) shows that some dissolution has taken place on the surface of $Zr_{60}Nb_2Cu_{20}Ni_8Al_{10}$ amorphous alloy, whereas figure 4.32 shows no such dissolution except figure 4.32 (c). It means that $Zr_{60}Nb_2Cu_{20}Ni_8Al_{10}$ amorphous alloy shows poor corrosion resistance than $Zr_{59}Nb_3Cu_{20}Ni_8Al_{10}$ alloy and it confirms the results of weight loss analysis (figure 4.28). Also, figure 4.32 (c) shows that some dissolution has occurred on the surface of the $Zr_{59}Nb_3Cu_{20}Ni_8Al_{10}$ alloy due to which the value of corrosion rate is high after immersion in boiling nitric acid for 48 h as shown in

figure 4.28. Figure 4.32(b) is showing that the film formed on the surface of alloy after 24 hours is non-uniform. Figure 4.32 (c) and 4.32 (d) are the interesting micrographs in which some cluster structure formation has been observed. These structures were initiated in 48 hours duration and further grew up in 72 hours. The nanoscopic view of $Zr_{59}Nb_3Cu_{20}Ni_8Al_{10}$ amorphous alloy after immersion in boiling 11.5 M HNO_3 for 72 h has been shown in figure 4.33. This figure clearly shows a growth of cluster formation on surface of the alloy, which protects the alloy from further corrosion. It is well known that the oxide layer of Nb is more corrosion resistant in acidic medium [85] which may be the possible reason for better corrosion resistance of $Zr_{59}Nb_3Cu_{20}Ni_8Al_{10}$ alloy in nitric acid medium.

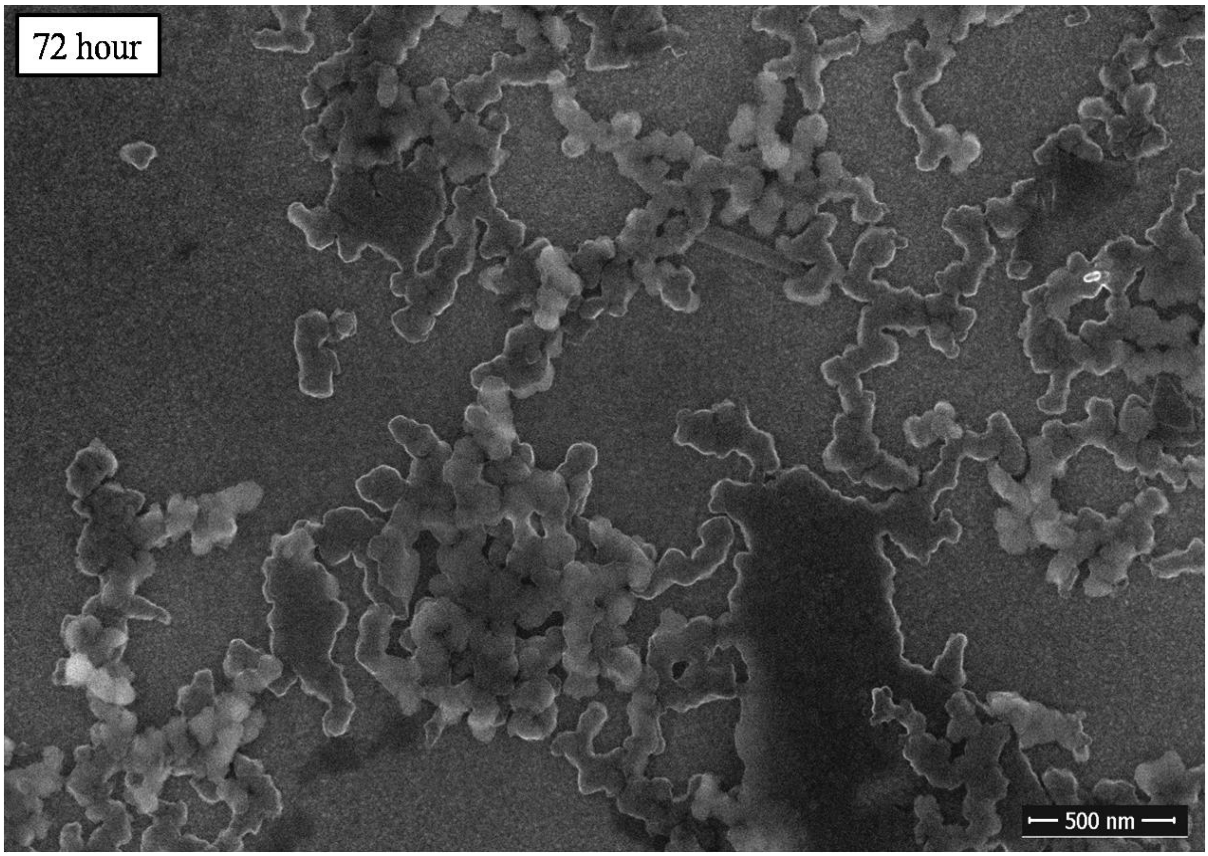

Figure 4.33: FESEM micrographs of $Zr_{59}Nb_3Cu_{20}Ni_8Al_{10}$ amorphous alloy after immersion in 11.5 M HNO_3 medium at boiling temperature for 72 h.

4.2.3.3 XPS study

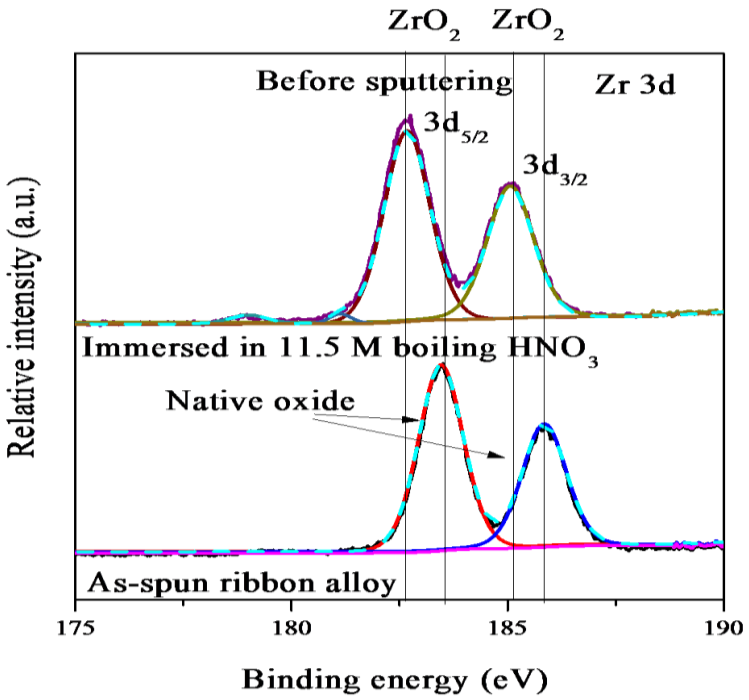

Figure 4.34: High resolution XPS peaks of Zr for $Zr_{59}Nb_3Cu_{20}Ni_8Al_{10}$ amorphous alloy immersed in 11.5 M HNO_3 medium at boiling temperature for 72 hours

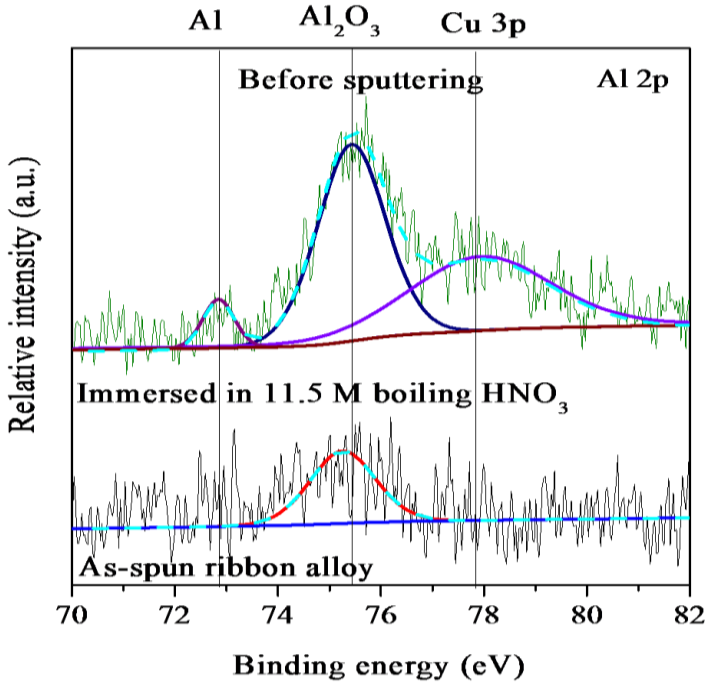

Figure 4.35: High resolution XPS peaks of Al for $Zr_{59}Nb_3Cu_{20}Ni_8Al_{10}$ amorphous alloy immersed 11.5 M HNO_3 medium at boiling temperature for 72 hours

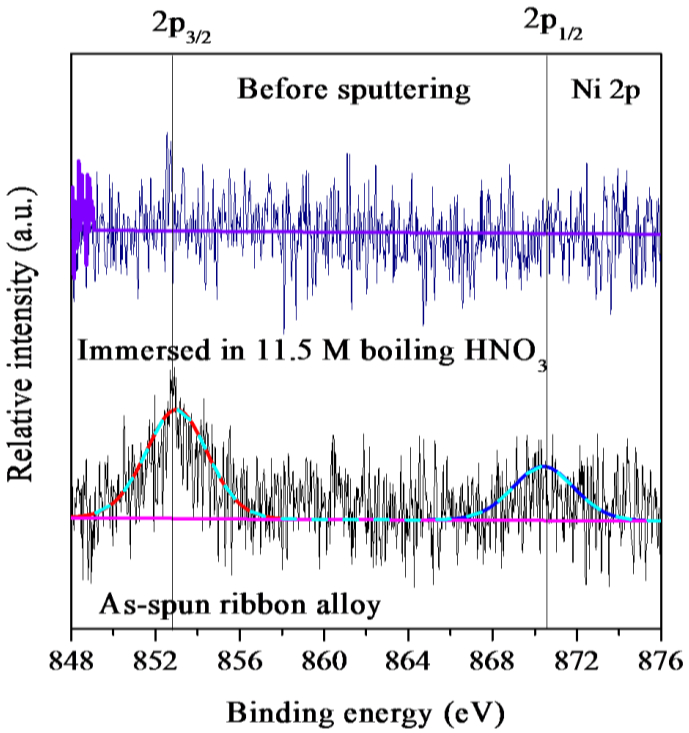

Figure 4.36: High resolution XPS peaks of Ni for $Zr_{59}Nb_3Cu_{20}Ni_8Al_{10}$ amorphous alloy immersed in 11.5 M HNO_3 medium at boiling temperature for 72 hours

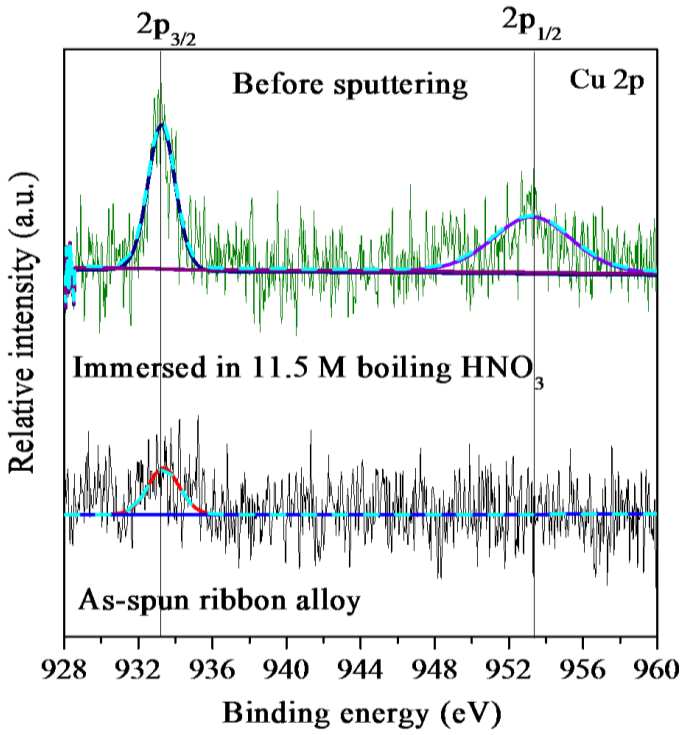

Figure 4.37: High resolution XPS peaks of Cu for $Zr_{59}Nb_3Cu_{20}Ni_8Al_{10}$ amorphous alloy immersed in 11.5 M HNO_3 medium at boiling temperature for 72 hours

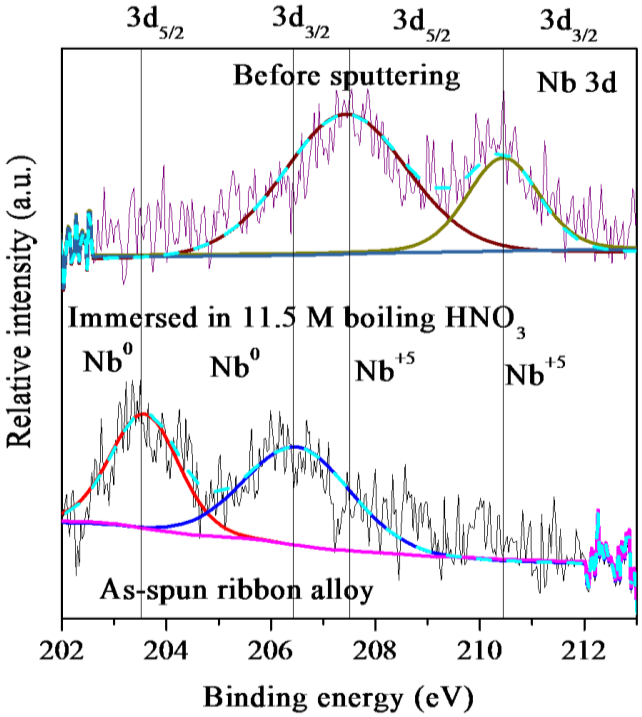

Figure 4.38: High resolution XPS peaks of Nb for $Zr_{59}Nb_3Cu_{20}Ni_8Al_{10}$ amorphous alloy immersed in 11.5 M HNO_3 medium at boiling temperature for 72 hours

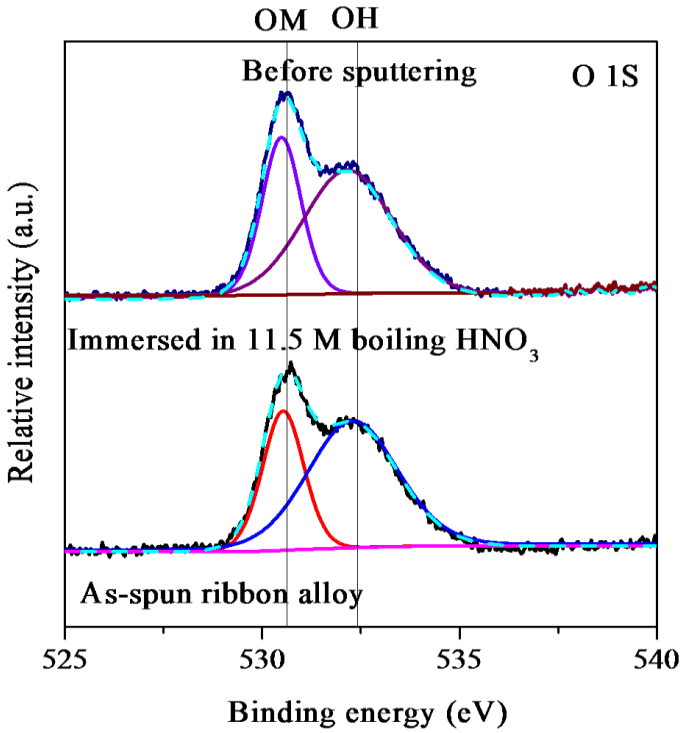

Figure 4.39: High resolution XPS peaks of O for $Zr_{59}Nb_3Cu_{20}Ni_8Al_{10}$ amorphous alloy immersed in 11.5 M HNO_3 medium at boiling temperature for 72 hours

To understand the compositional changes on the surface of $Zr_{59}Nb_3Cu_{20}Ni_8Al_{10}$ amorphous alloy after immersion in boiling 11.5 M HNO_3 medium for 72 hours, XPS spectra were recorded. The high-resolution XPS spectra of each element Zr, Al, Ni, Cu, Nb and O for as spun and immersed sample in boiling 11.5 M HNO_3 medium for 72 hours, are shown in figure 4.34, 4.35, 4.36, 4.37, 4.38 and 4.39, respectively. The figure 4.34 represents the Zr 3d spectra of the surface of as-spun and immersed $Zr_{59}Nb_3Cu_{20}Ni_8Al_{10}$ amorphous alloy. The peaks of ZrO_2 were observed at the binding energies 183.5 eV and 185.8 eV corresponding to the peaks of Zr $3d_{5/2}$ and Zr $3d_{3/2,}$ respectively on the surface of as-spun $Zr_{59}Nb_3Cu_{20}Ni_8Al_{10}$ amorphous alloy [151]. These peaks were observed due to the formation of native oxide layer on the surface of as-spun sample. The XPS peaks corresponding to ZrO_2 were observed at 182.6 eV and 185.1 eV [160] in the case of immersed sample in boiling HNO_3 medium. This shift in the peak position of XPS peak corresponding to ZrO_2 was obtained due to the formation of ZrO_2 after immersion in boiling nitric acid. The presence of metallic Zr was not observed on the surface of immersed sample. The XPS spectra recorded on the surface of as-spun sample as well as immersed sample was obtained at 75.4 eV (figure 4.35), which is assigned to Al 2p indicating Al_2O_3 [154]. A very small intensity of XPS peak obtained at 72.9 eV indicated the presence of the metallic form of Al on the surface of as-spun alloy [154], which was also observed on the surface of immersed alloy. The XPS peak of Ni $2p_{3/2}$ at 853.3 eV and Ni $2p_{1/2}$ at 870.5 eV corresponding to metallic Ni were obtained on the surface of as-spun sample (figure 4.36). On the other hand, a very small XPS peak belonging to Ni was observed on the surface of immersed sample as shown in the figure 4.36. Similarly a very small intensity Cu 2p doublet (figure 4.37) was observed at 933.3 eV for Cu $2p_{3/2}$ and 953.1 eV for Cu $2p_{1/2}$ corresponding to metallic Cu for the surface of the as- spun sample, whereas the surface of immersed sample exhibited the presence of relatively high intensity Cu 2p doublet referred to metallic Cu [75,161]. Figure 4.38 represents the Nb 3d spectra of the surface of as-spun and immersed samples in boiling 11.5 HNO_3 medium. The surface of as-

spun sample exhibited the presence of Nb^0 peak corresponding to metallic Nb at 203.6 eV and 206.4 eV binding energy, as shown in figure 4.38 [84], but the surface of immersed sample clearly exhibited the presence of XPS peaks corresponding to the Nb^{5+} state appeared at 208.0 and 210.7 eV (figure 4.38), which is assigned to Nb_2O_5 [84]. No peak corresponding to metallic Nb could be observed on the surface of $Zr_{59}Nb_3Cu_{20}Ni_8Al_{10}$ amorphous alloy after immersion in boiling 11.5 M HNO_3 medium for 72 hours. The O 1s spectra recorded for the surface of as-spun and immersed sample are shown in figure 4.39. The O 1s spectra were obtained at 531.4 eV assigned to OM oxygen and at 532.7 eV assigned to OH for both as-spun and immersed samples [155]. These XPS results revealed that a passive layer of ZrO_2, Al_2O_3 and Nb_2O_5 is formed on the surface of $Zr_{59}Nb_3Cu_{20}Ni_8Al_{10}$ amorphous alloy after immersion in boiling HNO_3 medium. The corrosion resistant properties of ZrO_2 and Nb_2O_5 are responsible factor for the high corrosion resistance of $Zr_{59}Nb_3Cu_{20}Ni_8Al_{10}$ amorphous alloy in boiling nitric acid medium.

4.2.4 Conclusion

The corrosion behavior of $Zr_{60}Nb_2Al_{10}Ni_8Cu_{20}$, $Zr_{59}Nb_3Cu_{20}Ni_8Al_{10}$ and $Zr_{60}Pd_5Cu_{15}Ni_{10}Al_{10}$ amorphous alloys in nitric acid medium at high temperature was studied by weight loss analysis method. The corrosion rates of these alloys were calculated and it was found that the $Zr_{59}Nb_3Cu_{20}Ni_8Al_{10}$ amorphous alloy shows better corrosion resistance among these samples. The better corrosion resistance of $Zr_{59}Nb_3Cu_{20}Ni_8Al_{10}$ amorphous alloy is attributed to the formation of ZrO_2 and Nb_2O_5 oxides which are corrosion resistant in aqueous HNO_3 medium.

CHAPTER-5

Surface Modification of $Zr_{55}Cu_{30}Ni_5Al_{10}$ Bulk Amorphous Alloy using Ion Beam Implantation

This chapter deals with the surface modification techniques which were used to improve the corrosion resistance of the Zr-based amorphous alloys. In order to improve the corrosion resistance of $Zr_{55}Cu_{30}Ni_5Al_{10}$ glassy alloy in different aqueous environments, an attempt has been made using ion beam implantation method. This chapter is divided into two major sections.

5.1. Oxygen ion implantation

5.2. Nitrogen ion implantation

First section deals with the influence of oxygen ion implantation at various fluences on the corrosion behavior of bulk $Zr_{55}Cu_{30}Ni_5Al_{10}$ amorphous alloy. The characterization techniques such as GIXRD, FESEM and XPS techniques were used for surface characterization of implanted alloys and potentiodynamic polarization experiments were used to investigate the changes in the corrosion behavior of the abovementioned alloy after oxygen ion implantation in various oxidizing media. The second section of this chapter deals with the nitrogen ion implantation on $Zr_{55}Cu_{30}Ni_5Al_{10}$ amorphous ribbon alloy at various fluences. The detailed surface characterization was carried out using GIXRD, FESEM, XPS techniques and corrosion behavior was investigated in nitric acid environment using potentiodynamic polarization studies.

5.1 OXYGEN ION IMPLANTATION

5.1.1 Introduction

The Zr-based bulk amorphous alloys are well known materials due to their high corrosion resistance property in various environments [156], but efforts can be made in further improving the corrosion resistance of these Zr-based bulk amorphous alloys by surface modification techniques. The ion implantation is an interesting surface modification technique, which can be used to improve the corrosion resistance of Zr-based bulk amorphous alloys. One of the practical advantages of this technique is that it can be processed at room temperature without distorting the sample [115]. Many investigations have been carried out to see the effect of ion implantation on the structural, mechanical and physical/chemical properties of different bulk amorphous alloys [162-164]. Researchers have mainly focused on the mechanical properties of the Zr-based alloys after ion implantation, such as Ar^+ implantation on $Zr_{55}Cu_{30}Ni_5Al_{10}$ alloy has resulted in the increased hardness and elastic modulus due to nucleation of fine crystalline phases in the amorphous matrix [91]. Carter et al. [94] have reported the formation of $Cu_{10}Zr_7$, $NiZr_2$, and $CuZr_2$ phases after Cu-ion irradiation on $Zr_{55}Cu_{30}Ni_5Al_{10}$ alloy. Improvement in the hardness of $Zr_{55}Cu_{30}Ni_5Al_{10}$ alloy has been reported by Tao et al. [165] after Co ion implantation. Furthermore, Kawasegi et al. [166] have studied the sub-micrometer scale rapid patterning on the surface of $Zr_{55}Cu_{30}Ni_5Al_{10}$ alloy using Ga^+ ion beam irradiation. On the other hand, researchers have also focused on the effect of ion implantation on corrosion behavior of the conventional engineering alloys. It has been reported that Ar^+ implantation improves the corrosion resistance of Zircaloy-4 in H_2SO_4 medium by decreasing the concentration of oxygen vacancies in its passive film [167] and reducing the grain size [168,169]. But, only limited corrosion investigations have been reported in the field of corrosion after ion implantation or irradiation [167-169]. Therefore, in the present study, an attempt has been made to improve

the corrosion resistance of the bulk $Zr_{55}Cu_{30}Al_{10}Ni_5$ amorphous alloy, which exhibits excellent GFA and wide supercooled liquid region with low cooling rate [58,170]. Thus, in this chapter detailed corrosion investigations has been carried out on the O^+ ion beam implanted bulk $Zr_{55}Cu_{30}Ni_5Al_{10}$ amorphous alloy in 0.5 M H_2SO_4, 1.0 M HNO_3 and in the mixture of 0.5 M H_2SO_4 and 0.1 M NaCl aqueous solutions at different ion fluences.

5.1.2 Experimental procedure

5.1.2.1 Materials

The ingots of $Zr_{55}Cu_{30}Ni_5Al_{10}$ (atomic %) alloy, weighing 10 g, were developed by arc melting system using a mixture of Zr, Cu, Ni and Al of 99.99% purity, under Ar atmosphere. Arc melting was repeated at least four times to get chemical homogeneity of the mixture. A strip of dimensions 27 mm x 5mm x 2 mm was prepared by copper mold suction casting method. The casting of the samples was carried out at UGC-DAE, IGCAR Kalpakkam using Edmund Buhler GmbH system. The $Zr_{55}Cu_{30}Ni_5Al_{10}$ alloy strip samples of 10 mm length were cut from the strip and polished up to 1200 grit SiC emery paper. Final polishing was done with 0.5 µm diamond paste. Samples were cleaned with acetone and distilled water and dried in air. Amorphous nature of the $Zr_{55}Cu_{30}Ni_5Al_{10}$ alloy was characterized by X-ray diffraction (XRD) technique with Inel-XRD (Equinox 2000) system using monochromatic Co source at Corrosion Science & Technology Group (CSTG), IGCAR Kalpakkam.

5.1.2.2 O^+ ion implantation

The O^+ ions of 100 keV energy were implanted on the polished surface of $Zr_{55}Cu_{30}Ni_5Al_{10}$ specimens (10 mm x 4 mm) in target chamber of TAM SAMES 150 keV particle accelerator at Ion Beam Physics Section (IBPS), Materials Science Group (MSG), IGCAR, Kalpakkam. The fluences for implantation were taken as 1×10^{16}, 1×10^{17} and 3×10^{17} ions/cm^2. The O^+ ion beam was impinged at normal incidence on the surface of alloy to achieve uniform

implantation. During the ion implantation, the beam current was kept low i.e. below 2 μA on the samples during the implantation to minimize the ion beam heating. During implantation, the vacuum at the target chamber was maintained below 2 x 10^{-7} torr.

5.1.2.3 Surface characterization

The O^+ ion implanted samples were characterized by glancing incidence X-ray diffraction (GIXRD). GIXRD pattern was acquired on an Inel-XRD (Equinox 2000) X-ray diffractometer using Co source (λ= 1.78901 Å). GIXRD measurement was carried out at an incidence angle of the X-ray beam of 1°. Surface morphology of the O^+ ion implanted samples at 3 x 10^{17} ions/cm^2 fluence was examined by FE-SEM using NOVA-Nano FE-SEM 450 system at MRC, Malaviya National Institute of Technology, Jaipur. The chemical state of the surface of O^+ ion implanted sample at 3 x 10^{17} ions/cm^2 fluence was examined by XPS, using Al-Kα excitation. The elemental depth profile information was obtained by sputtering the specimens using a SPECS Surface Nano Analysis GmbH, Germany spectrometer at CSTG, IGCAR Kalpakkam.

5.1.2.4 Electrochemical measurements

The electrochemical behavior of as-cast and O^+ ion implanted $Zr_{55}Cu_{30}Ni_5Al_{10}$ glassy alloy at a fluence of 3 x 10^{17} ions/cm^2 was investigated in 0.5 M H_2SO_4, 1.0 M HNO_3 and in the mixture of 0.5 M H_2SO_4 and 0.1 M NaCl aqueous solutions using a potentiostat (Autolab-AUT84276) consisting of a three-electrode cell. Samples were cleaned with ethanol and distilled water and dried in air before the experiment. These glassy samples were used as working electrodes; Ag/AgCl (3 M KCl) and platinum foil were used as reference and counter electrodes, respectively. An area of 1 cm x 0.3 cm of the sample was exposed to electrolyte and the open circuit potential (OCP) was monitored for 1 h. Further, potentiodynamic polarization tests were performed at the scanning rate of 0.001 V/s from -

0.2 V below OCP to 1.8 V. The values of corrosion potential (E_{corr}) and corrosion current density (I_{corr}) were obtained by Tafel method. The electrochemical experiments were repeated for checking the reproducibility of the results. The electrochemical experiments were performed at CSTG, IGCAR Kalpakkam.

5.1.2.5 Surface characterization after electrochemical measurements

After the electrochemical experiments in all aqueous media, to better understand the surface morphology of the corroded surface of as-cast and O^+ ion implanted Zr-based bulk amorphous alloys FE-SEM was carried out using FESEM Nova Nano SEM450, FEI, North America at MRC, MNIT Jaipur.

5.1.3 Results and discussion

5.1.3.1 Micro-structural characterization

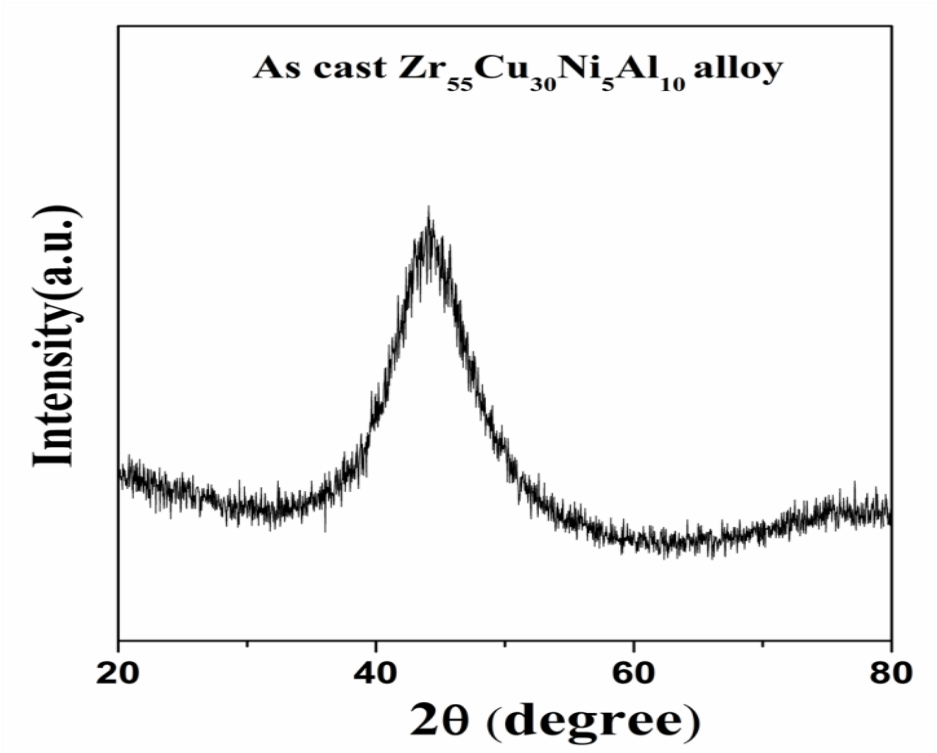

Figure 5.1: XRD pattern of as-cast $Zr_{55}Cu_{30}Ni_5Al_{10}$ amorphous alloy

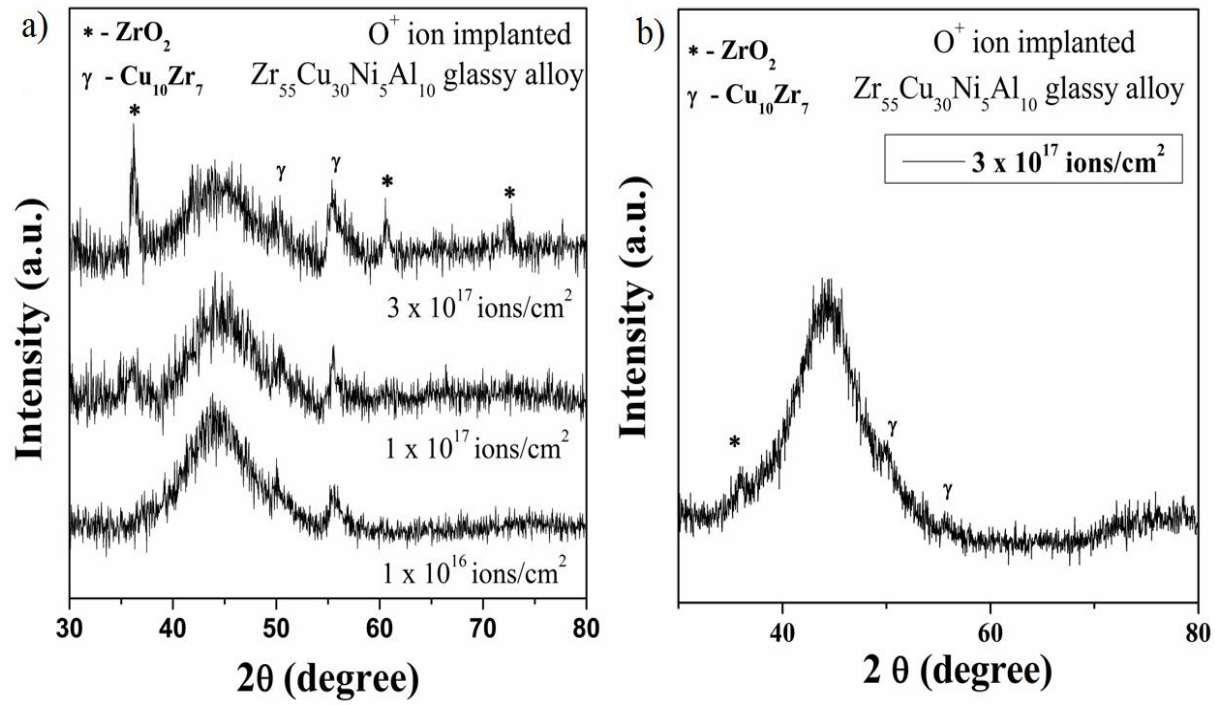

Figure 5.2: GIXRD pattern of O^+ ion implanted bulk $Zr_{55}Cu_{30}Ni_5Al_{10}$ amorphous alloys (a) ion fluences at 1 x 10^{16}, 1 x 10^{17} and 3 x 10^{17} ions/cm^2 and (b) XRD pattern of O^+ ion implanted sample at 3 x 10^{17} ions/cm^2 fluence

Figure 5.1 exhibits the X-ray diffraction pattern of the as-cast $Zr_{55}Cu_{30}Ni_5Al_{10}$ strip sample. It shows the presence of a broad halo peak, which indicates the amorphous nature of the bulk $Zr_{55}Cu_{30}Ni_5Al_{10}$ alloy. Since GIXRD is a technique which gives the structural information about the top most thin layer of the material and ion implantation induces the changes on the surface of material without altering the properties of bulk. Hence, GIXRD patterns of O^+ ion implanted bulk $Zr_{55}Cu_{30}Ni_5Al_{10}$ amorphous samples at 1 x 10^{16}, 1 x 10^{17}, 3 x 10^{17} ions/cm^2 fluences were recorded to understand the structural changes in the top surface of implanted samples as shown in figure 5.2 (a). The penetration depth of X-ray is estimated to be 0.368 μm at grazing incidence angle of 1º. The penetration depth is calculated with the help of mass attenuation coefficient which is 162.96 cm^2/g for $Zr_{55}Cu_{30}Ni_5Al_{10}$ amorphous alloy having 6.7067 g/cm^3 density. The GIXRD patterns exhibits the presence of low-intensity diffraction peaks along with the broad amorphous peak, indicating the formation of crystalline phases due to implantation on the top surface of the implanted samples. The presence of broad halo

peak along with small diffraction peaks ensures the amorphous nature of bulk material accompanying small crystalline phases occurred due to implantation. The samples implanted at higher fluences i.e. 1 x 10^{17} and 3 x 10^{17} ions/cm^2 exhibited the sharp diffraction peaks corresponding to $Cu_{10}Zr_7$ and ZrO_2 crystalline phases.

The XRD pattern of O^+ ion implanted sample at 3 x 10^{17} ions/cm^2 (figure 5.2 (b)) is also exhibiting the presence of low-intensity diffraction peaks as observed in the case of GIXRD of the similar alloy. It indicated that the crystalline phases have not only occurred on the surface of implanted alloy but are also present into bulk of the alloy at highest ion fluence. During ion implantation enhanced atomic mobility take place that could increase the nucleation and crystal growth which results in crystallization of amorphous materials [171]. It is also reported that the formation of nanocrystals is a result of thermal spike model [172]. According to thermal spike model, the energy is deposited by the projectile ions in the electronic sub-system of the material. It results in a large increase in the temperature along the vicinity of the ion path creating thermal spikes [173]. The quenching of thermal spikes is orders of magnitudes faster than the necessary critical cooling rate for metallic glass formation, thus the thermal spikes result in nano-crystal nucleation [174]. Therefore, crystallization can result from two effects: the first is a non-thermal process involving excessive free volume and the second is a thermal process from enhanced heating.

The formation of $Cu_{10}Zr_7$ phase was frequently observed in the heat treatment of the $Zr_{55}Cu_{30}Ni_5Al_{10}$ alloy under inert atmosphere [91] and oxidation process of the alloy [175]. Carter et al. [94] have also reported the formation of nano-crystalline $Cu_{10}Zr_7$ phase after Cu^+ irradiation on $Zr_{55}Cu_{30}Ni_5Al_{10}$ alloy. Apart from this, the formation of ZrO_2 was also observed in oxidation process of the $Zr_{55}Cu_{30}Ni_5Al_{10}$ alloy [176]. So, it is evident from GIXRD that ZrO_2 and $Cu_{10}Zr_7$ phases are present on the surface of O^+ ion implanted bulk $Zr_{55}Cu_{30}Ni_5Al_{10}$ amorphous alloy at higher ion fluences. Since the implanted sample at a

fluence of 3 x 10^{17} ions/cm^2 exhibited the sharp diffraction peaks of ZrO_2 and $Cu_{10}Zr_7$ crystalline phases, and so for the same reason this sample has been taken for further characterization and corrosion investigations.

5.1.3.2 O^+ ion implantation simulation by TRIM

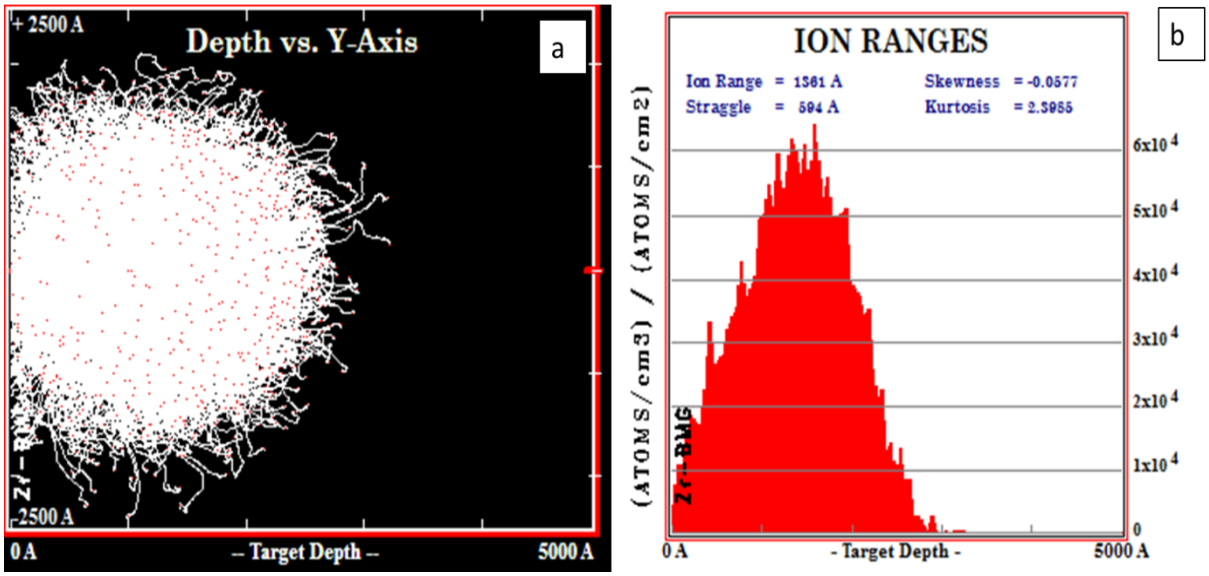

Figure 5.3: Structural simulation of $Zr_{55}Cu_{30}Ni_5Al_{10}$ amorphous alloy after O^+ ion implantation, (a) O^+ ion concentration distribution and (b) ion range profile.

The projected range of O^+ ions of 100 keV energy in $Zr_{55}Cu_{30}Ni_5Al_{10}$ amorphous alloy sample was calculated using computer code SRIM (stopping and ranges of ions in metals) [177]. The value of electronic energy loss (S_e), nuclear energy loss (S_n) and projected range are calculated to be 36.51 eV/Å, 12.87 eV/Å and 1309 Å, respectively. The ion range profile is also calculated using TRIM (transport of ions in matters), which is part of the SRIM software package. A pictorial presentation on the simulated trajectory of implant O^+ ions in the amorphous alloy substrate and ion range profile is shown in figure 5.3 (a) and 5.3 (b), respectively. The projected range calculated by SRIM is nearly equal to the projected range calculated from the ion range profile. In figure 5.3 (a), the distribution of O^+ ions after

implantation is shown with white color and red dots show the vacancies created due to the collision of ions to the target atom.

5.1.3.3 Surface morphology after O^+ ion implantation

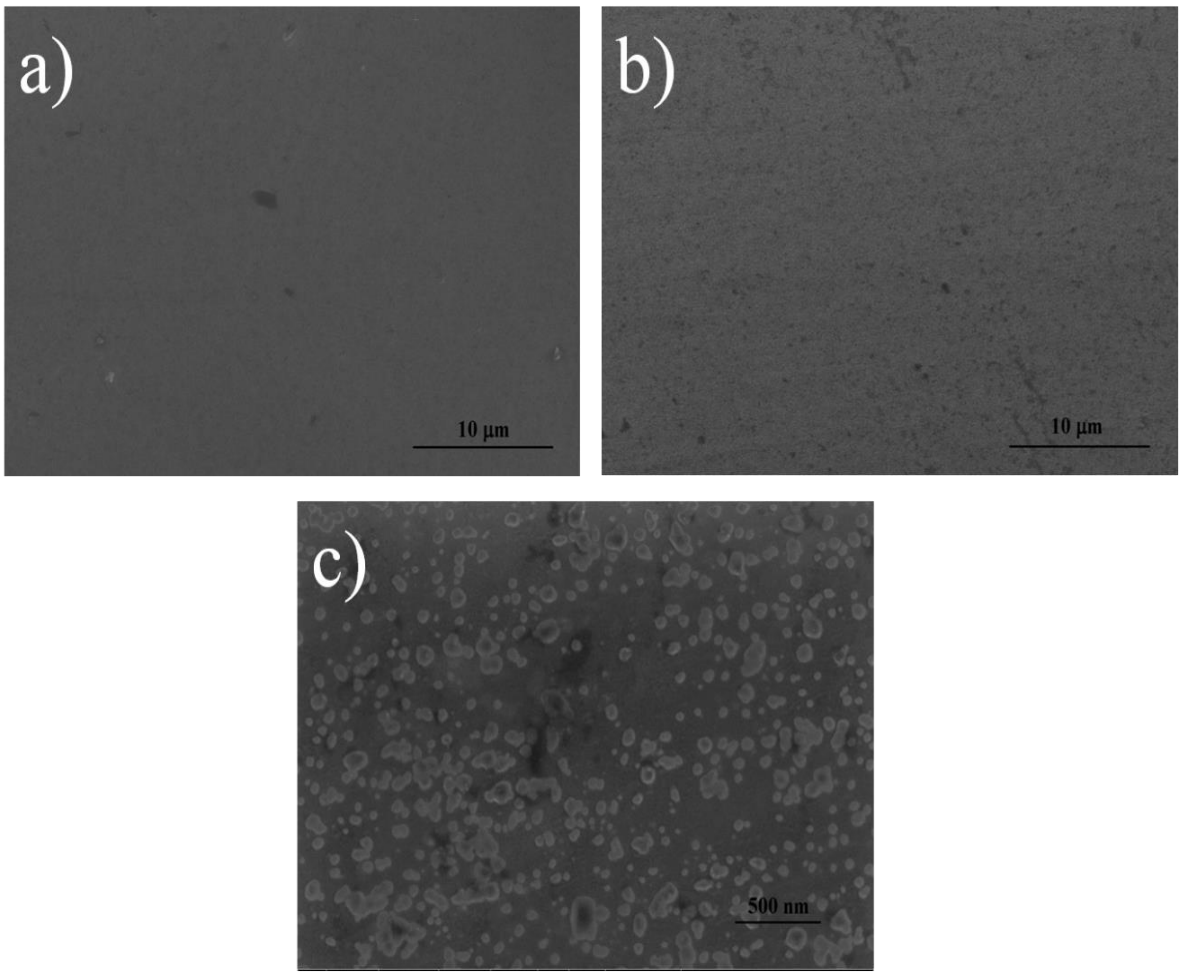

Figure 5.4: FE-SEM images of (a) as-cast and (b) O^+ ion implanted bulk $Zr_{55}Cu_{30}Ni_5Al_{10}$ amorphous alloy at 3 x 10^{17} ions/cm^2 fluence; (c) high magnification image of figure 5.3 (b)

Figure 5.4 shows the FE-SEM micrographs of as-cast and O^+ ion implanted bulk $Zr_{55}Cu_{30}Ni_5Al_{10}$ amorphous alloy at 3 x 10^{17} ions/cm^2 fluence. As shown in figure 5.4 (a) that surface of the as-cast bulk $Zr_{55}Cu_{30}Ni_5Al_{10}$ amorphous alloy is smooth, uniform and un-affected. Figure 5.4 (b) is the FE-SEM micrograph of ion implanted surface of the alloy. It exhibits the formation of a smooth oxide layer on the surface of glassy alloy due to O^+ ion

implantation. Higher magnification view of implanted surface is shown in figure 5.4 (c) and it reveals the formation of oxide pockets on the surface of implanted alloy. The density of these oxide pockets was relatively high and homogenous. FE-SEM results showed that the ZrO_2 crystalline phases were predominantly observed on the surface of implanted alloy which were also observed in the GIXRD pattern of O^+ ion implanted bulk $Zr_{55}Cu_{30}Ni_5Al_{10}$ amorphous alloy at 3 x 10^{17} ions/cm^2 fluence.

5.1.3.4 EDS study

To verify the quantitative composition of as-cast bulk $Zr_{55}Cu_{30}Ni_5Al_{10}$ amorphous alloy as well as oxide formation due to O^+ ion implantation, EDS study was carried out. The analysis of the EDS spectrum displayed in figure 5.5 (a) indicates that the composition of as-cast alloy is nearly equal to the targeted composition. The presence of oxygen peak in the EDS spectrum of as-cast alloy indicates the formation of native oxide layer on the surface of as-cast bulk $Zr_{55}Cu_{30}Ni_5Al_{10}$ amorphous alloy in the air. Other basic elements were present in their stoichiometric ratio as used during the casting of the sample. On the other hand EDS spectrum of O^+ ion implanted bulk $Zr_{55}Cu_{30}Ni_5Al_{10}$ amorphous alloy (figure 5.5 (b)) shows that the atomic concentration of Zr is significantly decreased in the implanted alloy as compared to the as-cast alloy, whereas the atomic concentration of oxygen is increased indicating the formation of ZrO_2 due to O^+ ion implantation. The atomic concentration of Al is also found to be decreased in EDS spectrum of O^+ ion implanted sample due to the formation of Al_2O_3 which could not be identified in FESEM images, though GIXRD pattern exhibited small diffraction peaks corresponding to Al_2O_3. These EDS results are in good agreement with GIXRD and FESEM findings.

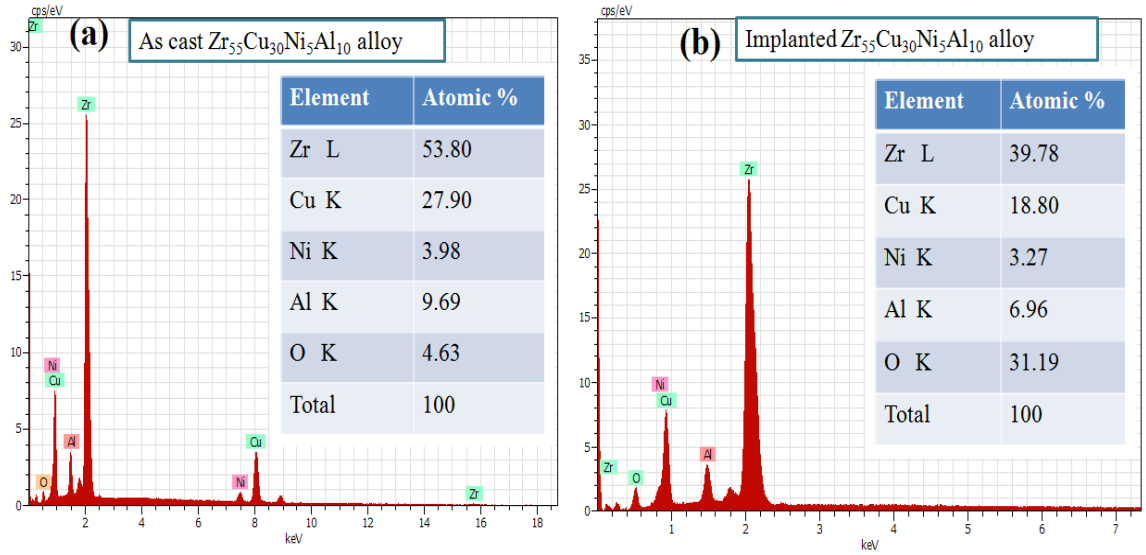

Figure 5.5: EDS spectrum of (a) as-cast bulk $Zr_{55}Cu_{30}Ni_5Al_{10}$ amorphous alloy (b) O^+ implanted bulk $Zr_{55}Cu_{30}Ni_5Al_{10}$ amorphous alloy at 3 x 10^{17} ions/cm^2 fluence

5.1.3.5 XPS study

XPS analysis was performed on the as-cast and O^+ ion implanted surface of the bulk $Zr_{55}Cu_{30}Ni_5Al_{10}$ amorphous alloy to investigate the surface chemistry and its distribution as a function of sputter depth. The wide scan survey over a wide binding energy region of the as-cast and O^+ ion-implanted sample for the surface and sputtered condition (1, 5 and 15 min) is shown in figure 5.6. The surface of as-cast sample and as-implanted sample show the presence of XPS peaks corresponding to Zr 3d, Al 2p, O 1s and C 1s. However, the Cu 2p and Ni 2p peaks were only observed after the sputtering condition of 5 and 10 min, respectively. The XPS peak of C 1s was obtained in XPS spectrum of as-cast bulk $Zr_{55}Cu_{30}Ni_5Al_{10}$ amorphous alloy at 284.8 eV (figure 5.6 (a)) resulting from a contaminant hydrocarbon layer which has covered the outermost surface of the sample [178]. Furthermore, this C 1s could not be observed after sputtering of the surface of as-cast sample. Similarly, the C 1s spectra at 284.8 eV (figure 5.6 (b)) were observed due to the contamination by residual gas and/or by outgassing from materials in the chamber during the ion implantation [179]. The carbon peak intensity was maximum on the surface of the as-implantedsample and it has dropped continuously with the depth as shown in figure 5.6 (b).

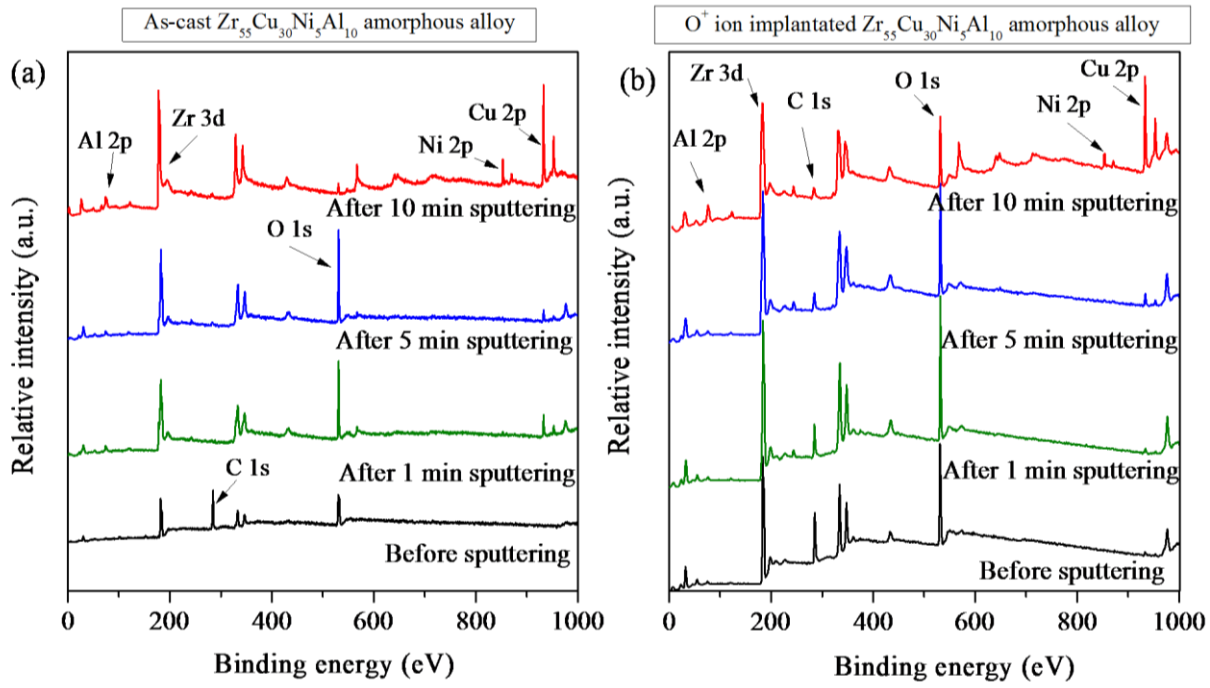

Figure 5.6: XPS survey scan of (a) as-cast and (b) O^+ implanted bulk $Zr_{55}Cu_{30}Ni_5Al_{10}$ amorphous alloy at 3 x 10^{17} ions/cm^2 fluence

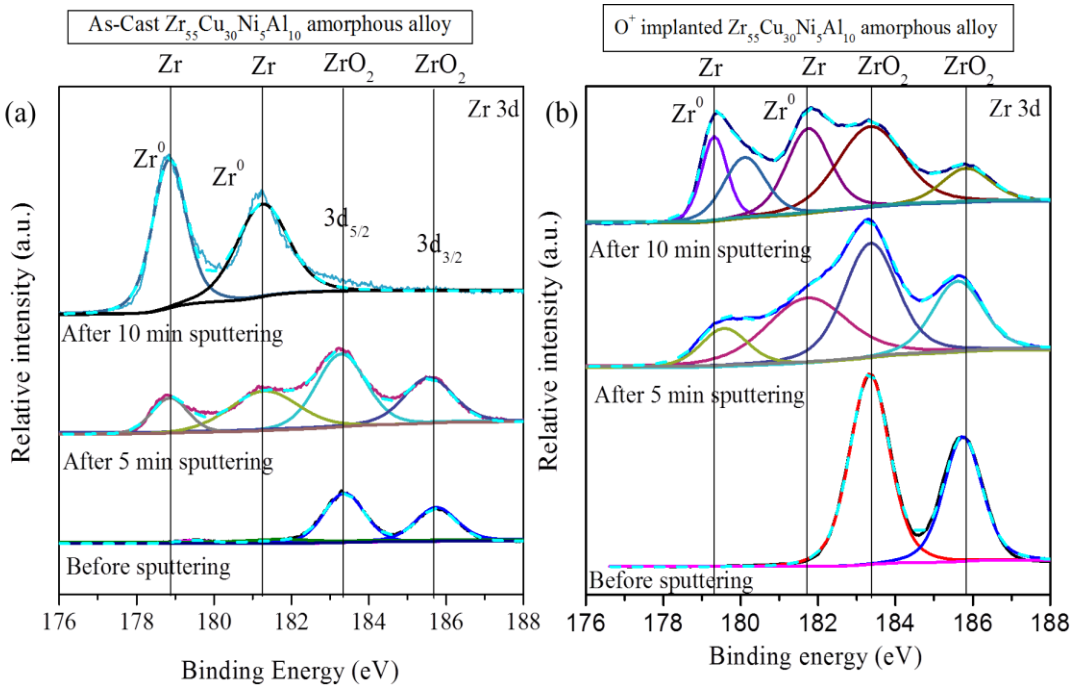

Figure 5.7: High resolution XPS peaks of (a) as-cast and (b) O^+ implanted bulk $Zr_{55}Cu_{30}Ni_5Al_{10}$ amorphous alloy for Zr

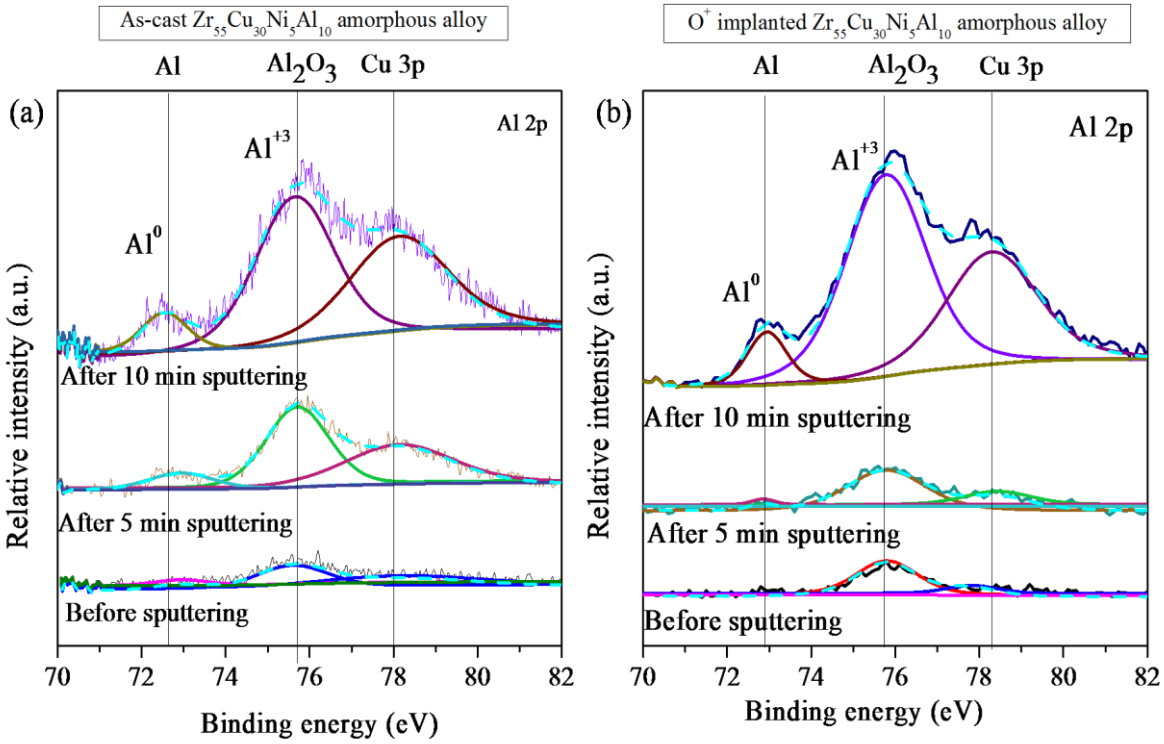

Figure 5.8: High resolution XPS peaks of (a) as-cast and (b) O^+ implanted bulk $Zr_{55}Cu_{30}Ni_5Al_{10}$ amorphous alloy for Al

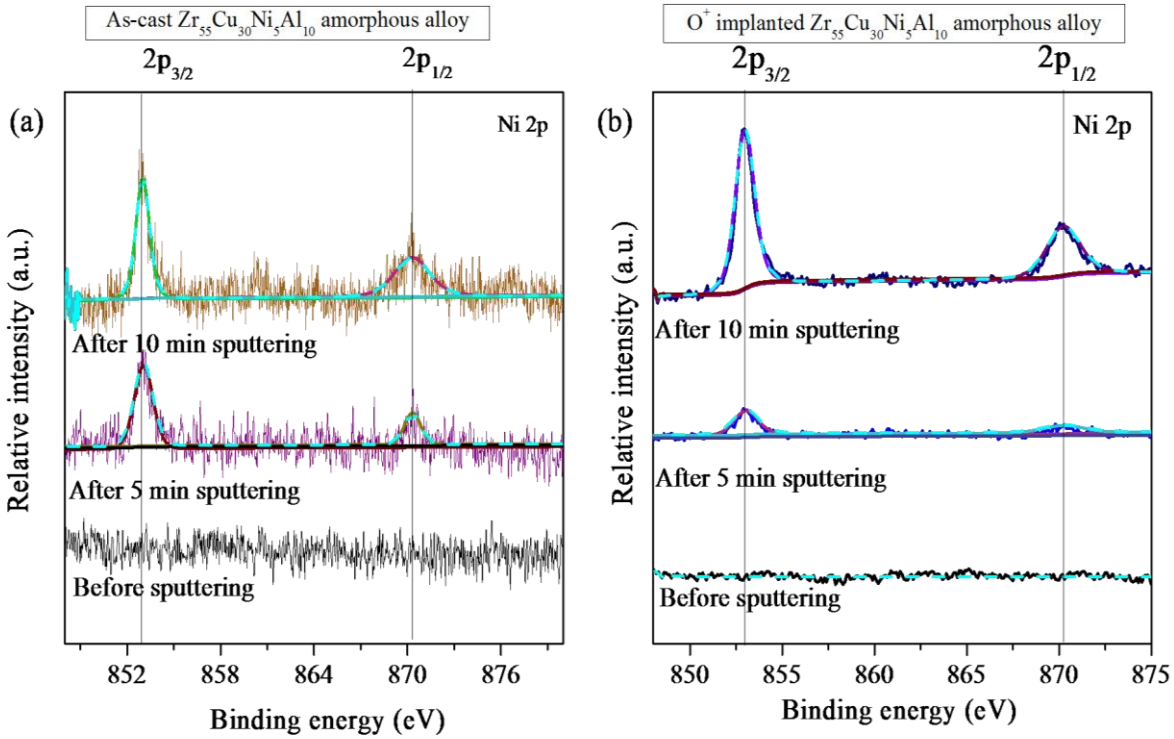

Figure 5.9: High resolution XPS peaks of (a) as-cast and (b) O^+ implanted bulk $Zr_{55}Cu_{30}Ni_5Al_{10}$ amorphous alloy for Ni

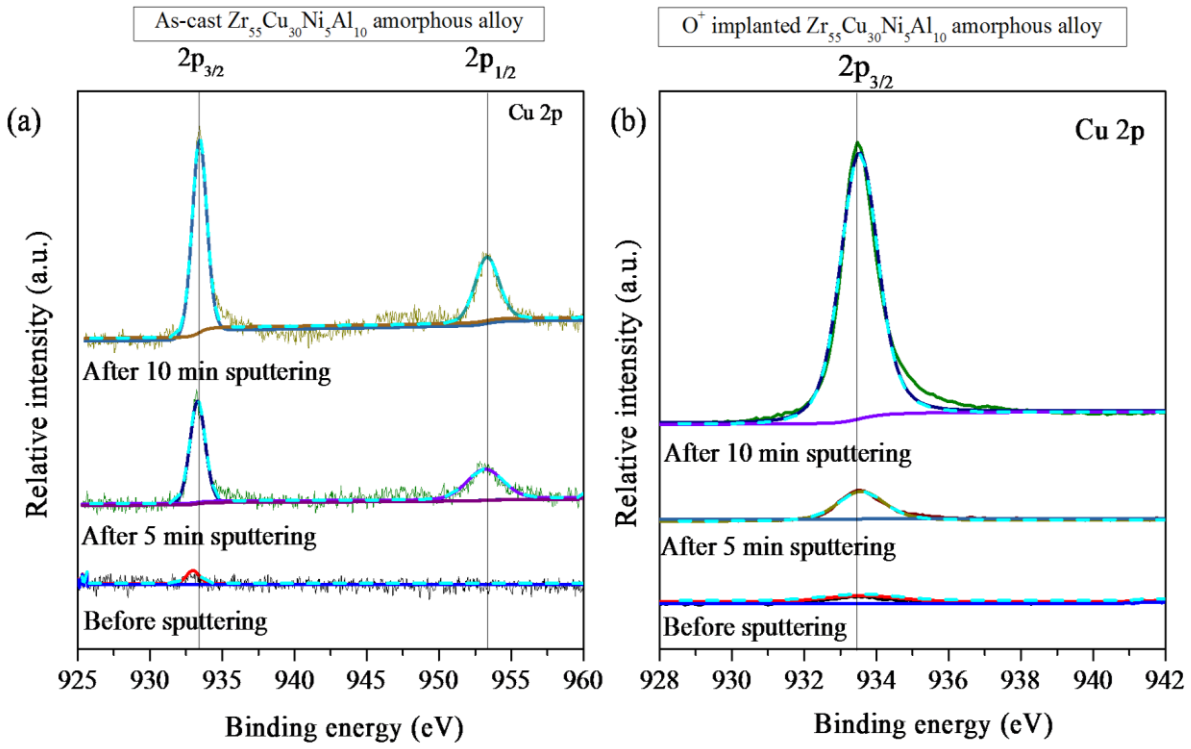

Figure 5.10: High resolution XPS peaks of (a) as-cast and (b) O^+ implanted bulk $Zr_{55}Cu_{30}Ni_5Al_{10}$ amorphous alloy for Cu

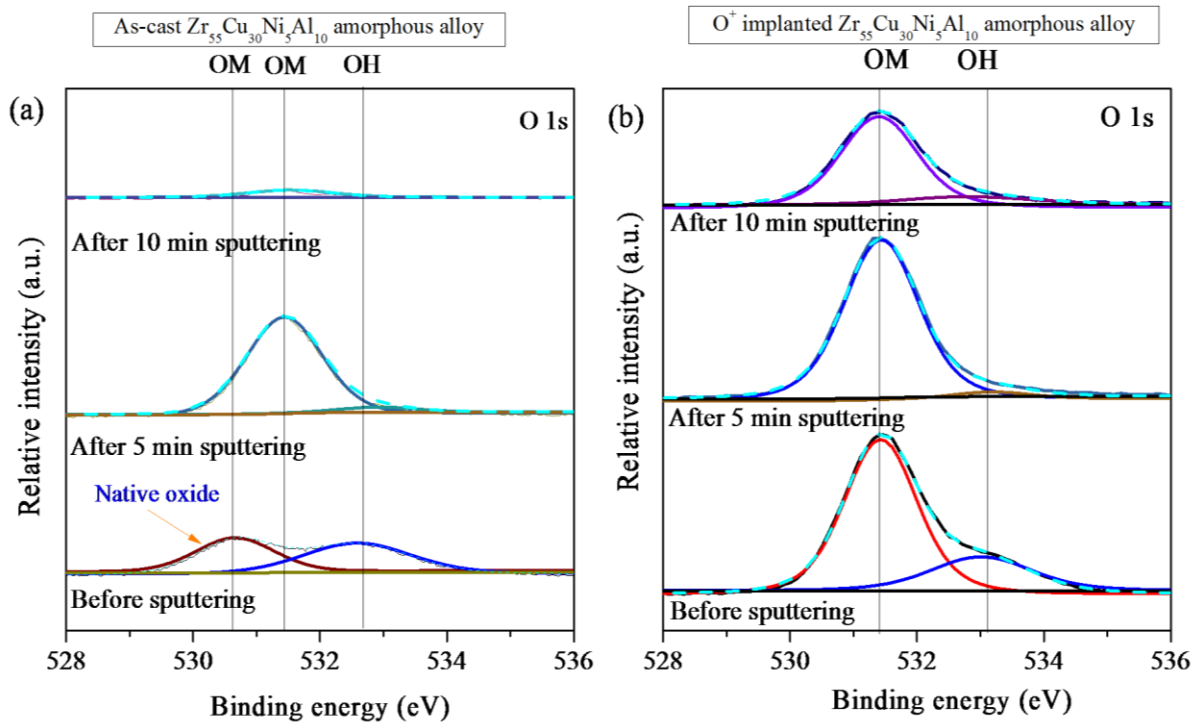

Figure 5.11: High resolution XPS peaks of (a) as-cast and (b) O^+ implanted bulk $Zr_{55}Cu_{30}Ni_5Al_{10}$ amorphous alloy for O

The high-resolution XPS spectra of each element Zr, Al, Ni, Cu and O for as-cast and O^+ implanted bulk $Zr_{55}Cu_{30}Ni_5Al_{10}$ amorphous alloy are shown in figure 5.7, 5.8, 5.9, 5.10 and 5.11, respectively. The figure 5.7 (a) represents the Zr 3d spectra of as-cast bulk $Zr_{55}Cu_{30}Ni_5Al_{10}$ amorphous alloy and figure 5.7 (b) shows the Zr 3d spectra of O^+ implanted bulk $Zr_{55}Cu_{30}Ni_5Al_{10}$ amorphous alloy. The deconvolution of Zr 3d spectra was carried out and Zr^0 (metal) and ZrO_2 (oxide) peaks were obtained based on the literature values of their binding energies. The peaks of ZrO_2 were observed at the binding energies 183.3 eV and 185.7 eV corresponding to the peaks of Zr $3d_{5/2}$ and Zr $3d_{3/2,}$ respectively [151,152]. The peaks at 179.3 eV and 181.7 eV corresponding to metallic Zr [153] were observed after 5 min of sputtering along with peaks corresponding to Zr^{4+} for both as-cast and O^+ implanted samples. The presence of ZrO_2 on the surface of as-cast sample was due to the formation of native oxide layer which was not observed after 10 min sputtering. On the other hand, the high-resolution spectra of Zr 3d for O^+ ion implanted sample shows the presence of ZrO_2 even after 10 min of sputtering along with metallic Zr. No metallic peak could be observed on the surface of O^+ implanted sample. The XPS peak at 75.4 eV (figure 5.8) was referred to Al 2p indicating Al_2O_3 [154] on the surface of as-cast sample as well as O^+ implanted sample. XPS peak obtained at 72.9 eV indicated the presence of the metallic form of Al [154] along with Al_2O_3 after 5 min of sputtering for both the samples. The intensity of XPS peaks corresponding to Al 2p was very low in comparison to the intensity of Zr 3d peaks. It shows that the concentration of Al_2O_3 was very less on the surface of as-cast alloy as well as on O^+ implanted alloy. Ni XPS peak could not be observed on the surface of both samples (as shown in figure 5.9). Only after sputtering for 5 min, the XPS peaks of Ni $2p_{3/2}$ at 853.3 eV and Ni $2p_{1/2}$ at 870.5eV corresponding to metallic Ni were appeared for both samples [151]. The Cu 2p peak (figure 5.10) was also not observed on the surface of the as-cast and O^+ implanted samples. The Cu $2p_{3/2}$ peaks referred to a metallic form of Cu at 933.3 eV [151] was observed only after 5 min sputtering. It is revealed that both Ni and Cu elements are

present in metallic form and appeared only after sputtering of O^+ implanted bulk $Zr_{55}Cu_{30}Ni_5Al_{10}$ amorphous alloy. Thus, the surface of implanted sample showed only the presence of ZrO_2 and Al_2O_3. The O 1s spectra recorded for as-cast and O^+ implanted sample are shown in figure 5.11 (a) and 5.11 (b), respectively. The O 1s spectra were observed at 531.4 eV assigned to OM oxygen (metal-oxygen bond) [68] corresponds to O^{+2} ions in oxides [151] and a weaker peak at 532.7 eV , which is assigned to OH oxygen linked to bound water or hydrogen [155]. The as-cast sample exhibited the presence of OM oxygen on the surface due to formation of native oxide, although the intensity of OM and OH oxygen peaks decreased to zero after 10 min of sputtering. Whereas, the O implanted sample has shown the presence of OM oxygen even after 10 min of sputtering. The concentration of ZrO_2 and Al_2O_3 on the surface of the as-implanted alloy was calculated from high-resolution spectra of Zr (figure 5.7 (b)) and Al (figure 5.8 (b)). The area under the deconvoluted peaks in figure 5.7 (b) and 5.8 (b) gives the concentration of ZrO_2 and Al_2O_3 state, after correcting the sensitivity factor of respective elements [153]. The calculated value of concentration was 90% and 10% for ZrO_2 and Al_2O_3, respectively. It can be noticed that concentration of ZrO_2 on the surface of the as-implanted sample is very high in comparison with Al_2O_3. So, it is confirmed by XPS that the surface of the as-implanted alloy mainly exhibits the presence of Zr^{4+} oxidation state, which revealed that the oxide layer mainly contains ZrO_2.

5.1.3.6 Potentiodynamic polarization study

Figure 5.12 shows the polarization curves, measured on the as-cast bulk $Zr_{55}Cu_{30}Ni_5Al_{10}$ amorphous alloy in 0.5 M H_2SO_4, 1.0 M HNO_3 and in the mixture of 0.5 M H_2SO_4 and 0.1 M NaCl aqueous solutions. Corrosion parameters such as E_{corr} and corrosion current density I_{corr} are calculated and summarized in Table 5.1. The I_{corr} values were estimated by applying the Tafel slope method [145]. As-cast glassy alloy exhibited nobler value of E_{corr} in 1 M HNO_3 solution (Table 5.1) than those for 0.5 M H_2SO_4, 0.5 M H_2SO_4 + 0.1 M NaCl solutions due to

higher oxidizing nature of nitric acid [146]. Whereas, the amorphous alloy exhibited an active value of E_{corr} in the mixture of 0.5 M H_2SO_4 and 0.1 M NaCl solution indicating an increase of free corrosion activity in Cl^- containing solution, it is observed from figure 5.12 that as-cast sample exhibited low I_{corr} value in H_2SO_4 solution than those for HNO_3 and H_2SO_4 + NaCl solutions. In 1 M HNO_3 solution, the alloy showed similar polarization behavior as H_2SO_4 solution i.e. spontaneously passivated with the wide passive region. However, it has exhibited a high value of I_{corr} in HNO_3 solution in comparison to H_2SO_4 solution. In contrast, the as-cast sample exhibited high I_{corr} value in H_2SO_4 + NaCl solution with no indication of passive behavior. The as-cast sample showed a steep rise in current density at E_{corr} value indicating the pitting corrosion behavior of the alloy. These results are similar to results obtained by Mudali et al. [180] on the $Zr_{59}Ti_3Cu_{20}Al_{10}Ni_8$ alloy in similar media and Dhawan et al. [49] on Ti free $Zr_{65}Cu_{17.5}Ni_{10}Al_{7.5}$ glassy alloy in 0.5 M H_2SO_4 and 0.5 M HNO_3 solutions. Mudali et al. [70] have reported that the $Zr_{59}Ti_3Cu_{20}Al_{10}Ni_8$ alloy shows excellent passivation behavior in 0.5 M H_2SO_4 medium due to strong passivation behavior of valve metals (Zr, Al, Ti). Whereas, it undergoes severe pitting corrosion in the mixture of 0.5 M H_2SO_4 and 0.1 M NaCl due to the presence of higher active sites available for chloride ion adsorption. On the other hand, Mudali et al. [180] have carried the Auger electron spectroscopy (AES) analysis on electrochemically treated $Zr_{59}Ti_3Cu_{20}Al_{10}Ni_8$ alloy in H_2SO_4 solution and reported the enrichment of Cu beneath the anodic passive film. Similar results were reported by Gebert et al. [64] for Na_2SO_4 solution. This Cu-enriched layer enhanced the diffusion of Cl ions across the passive film and favors the pitting corrosion of the alloy in H_2SO_4 + NaCl solution. Furthermore, it has been reported that the $Zr_{52.5}Cu_{17.9}Ni_{14.6}Al_{10}Ti_5$ alloy [48] and $Cu_{60}Zr_{30}Ti_{10}$alloys [181] exhibit better corrosion resistance in H_2SO_4 solution in comparison to HNO_3 solution. Similar results have been obtained in the present study.

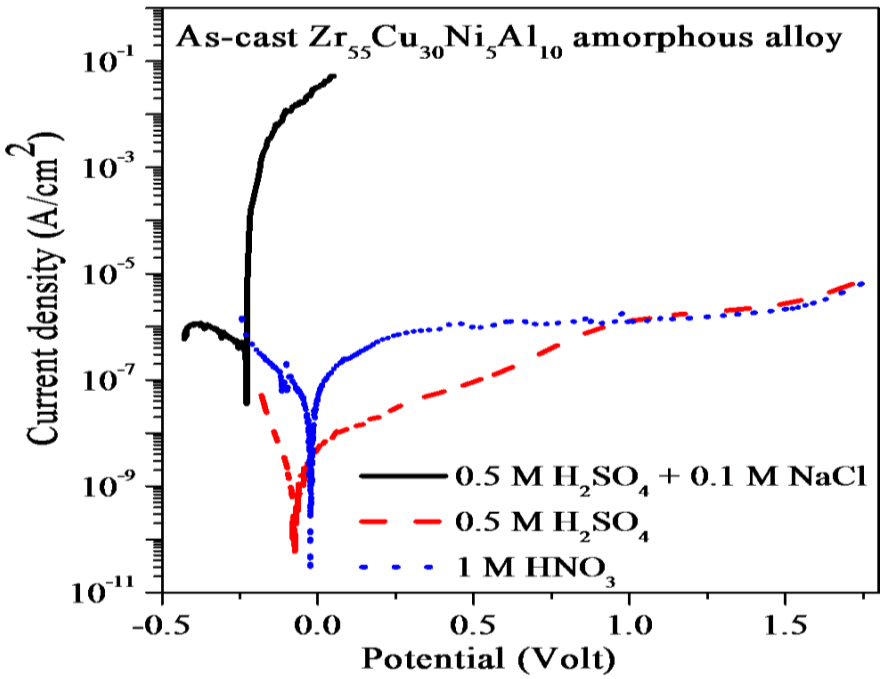

Figure 5.12: Potentiodynamic polarization curve of as-cast $Zr_{55}Cu_{30}Ni_5Al_{10}$ glassy alloy in 0.5 M H_2SO_4, 1.0 M HNO_3 and in the mixture of 0.5 M H_2SO_4 and 0.1 M NaCl aqueous solutions

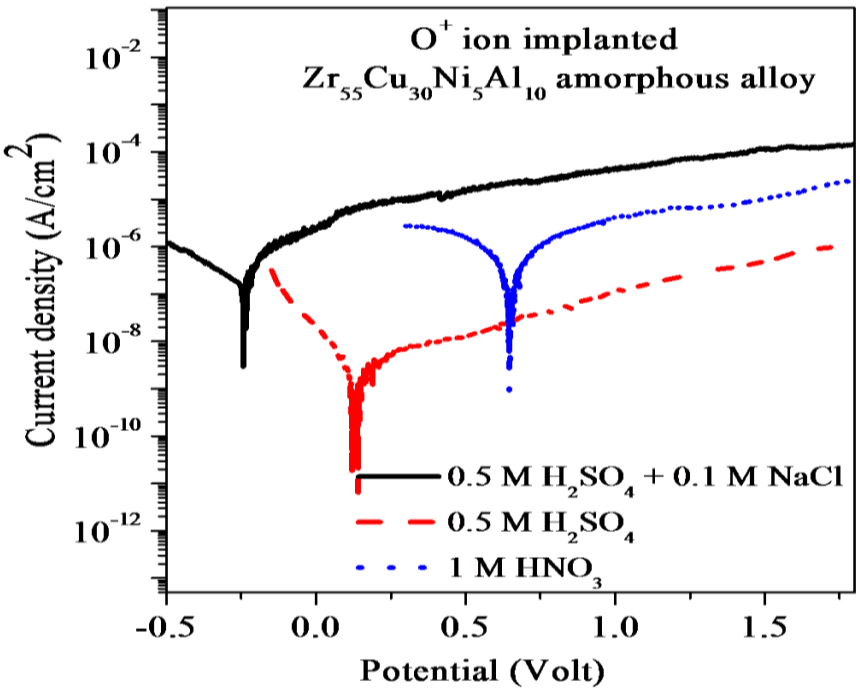

Figure 5.13: Potentiodynamic polarization curve of O^+ ion implanted $Zr_{55}Cu_{30}Ni_5Al_{10}$ alloy in 0.5 M H_2SO_4, 1.0 M HNO_3 and in the mixture of 0.5 M H_2SO_4 and 0.1 M NaCl aqueous solutions

The potentiodynamic polarization curves of O^+ ion implanted bulk $Zr_{55}Cu_{30}Ni_5Al_{10}$ amorphous alloy in 0.5 M H_2SO_4, 1.0 M HNO_3 and in the mixture of 0.5 M H_2SO_4 and 0.1 M NaCl aqueous solutions are shown in figure 5.13. The corrosion parameters such as E_{corr} and I_{corr}, obtained from figure 5.13 are summarized in Table 5.1. The comparison of both E_{corr} and I_{corr} values of as-cast and O^+ implanted samples revealed that the E_{corr} value of as-cast sample is shifted towards nobler side after O^+ ion implantation in all corrosive media. It is attributed to the presence of ZrO_2 film, formed due to the O^+ ion implantation, which is less susceptible for corrosion in the respective solutions. Li et al. [182] have reported the high E_{corr} value of annealed $Ti_{32.8}Zr_{30.2}Ni_{5.3}Cu_9Be_{22.7}$ metallic glass coating on 304 L stainless steel (SS) in comparison to as-deposited metallic glass coating on 304L SS in the nitric acid medium. It has been reported that the increase in E_{corr} values was due to the microstructure of coating i.e. substantial crystallinity led to the higher E_{corr} values. Mudali et al. [69] have also reported a shift in E_{corr} values towards more positive side for crystalline $Zr_{57}Ti_8Nb_{2.5}Cu_{13.9}Ni_{11.1}Al_{7.5}$ alloy in H_2SO_4 and H_2SO_4 + NaCl solutions due to the introduction of interfaces and the localization enrichment of alloy components in different adjacent phases. In the present study, as-cast bulk $Zr_{55}Cu_{30}Ni_5Al_{10}$ amorphous alloy was spontaneously passivated and exhibited low I_{corr} values after O^+ ion implantation in the mixture of 0.5 M H_2SO_4 + 0.1 M NaCl aqueous solutions and 0.5 M H_2SO_4. These results indicated that corrosion resistance of glassy alloy has increased after O^+ ion implantation in these media. It is worth mentioning here that O^+ implanted amorphous alloy exhibited passive behavior even in 0.5 M H_2SO_4 + 0.1 M NaCl as shown in figure 5.13. The high corrosion resistance of O^+ implanted alloy is attributed to the formation of stable ZrO_2 layer which is a protective passive layer in acidic, alkaline and chloride solutions [51]. Nie et al. [153] have reported that the $Zr_{64}Cu_{16}Ni_{10}Al_{10}$ glassy alloy exhibits improved corrosion resistance in 0.5 M H_2SO_4 and 0.5 M H_2SO_4 + 0.1 M NaCl solutions after thermal oxidation at 593 K for 5 h in the air. The better corrosion resistance of oxidized samples was attributed to the formation of the protective ZrO_2 layer

which has a strong passivation ability and high corrosion resistance in Cl^--, H^+- or both Cl^- and H^+-containing solutions. In the present study, the value of I_{corr} of the as-cast amorphous alloy was slightly increased in HNO_3 medium after O^+ implantation, possibly due to the presence of $Cu_{10}Zr_7$ phases, which were observed in GIXRD pattern of O^+ implanted sample. However, implanted alloy exhibited the passivation behavior in nitric acid medium due to the formation of ZrO_2 layer. Hence, potentiodynamic polarization results revealed that corrosion resistance of bulk $Zr_{55}Cu_{30}Ni_5Al_{10}$ amorphous alloy is improved in H_2SO_4 and H_2SO_4 + NaCl solution after O^+ ion implantation.

Table 5.1: Polarization parameters for as-cast and O^+ ion implanted bulk $Zr_{55}Cu_{30}Ni_5Al_{10}$ amorphous alloy in 0.5 M H_2SO_4, 1.0 M HNO_3 and in the mixture of 0.5 M H_2SO_4 and 0.1 M NaCl aqueous solutions

Medium	As-cast bulk $Zr_{55}Cu_{30}Ni_5Al_{10}$ amorphous alloy		O^+ ion implanted $Zr_{55}Cu_{30}Ni_5Al_{10}$ amorphous alloy	
	E_{corr} (V)	I_{corr} ($\mu A/cm^2$)	E_{corr} (V)	I_{corr} ($\mu A/cm^2$)
0.5 M H_2SO_4 + 0.1 M NaCl	-0.231	0.525	-0.223	0.256
0.5 M H_2SO_4	-0.076	0.005	0.131	0.002
1.0 M HNO_3	-0.024	0.061	0.642	0.392

5.1.3.7 Surface morphology after electrochemical measurements

Figure 5.14 (a-f) shows the surface morphology of polarized samples of as-cast and O^+ ion implanted bulk $Zr_{55}Cu_{30}Ni_5Al_{10}$ amorphous alloy in 0.5 M H_2SO_4, 1.0 M HNO_3 and in the mixture of 0.5 M H_2SO_4 and 0.1 M NaCl aqueous solutions. As shown in figure 5.14 (a) as-cast sample in H_2SO_4 medium exhibited smooth passive layer formation along with some corrosion product. The surface of the polarized sample was mainly covered with passive film. In contrast, the surface of O^+ ion implanted sample in H_2SO_4 medium exhibited only implanted layer i.e. ZrO_2 layer (figure 5.14 (b)). The ZrO_2 layer has protected the alloy from corrosion in this medium. Hence, no significant corroded area could be observed on the

surface of polarized implanted sample in H_2SO_4 medium. Figure 5.14 (c) shows the surface of the as-cast polarized sample in H_2SO_4 + NaCl medium. In this case, typical deep grown corrosion pit was observed which characterize the active nature of this alloy in H_2SO_4 + NaCl medium. Several pits with similar morphology were noticed throughout the samples, whereas, no such pit could be observed in the case of O^+ ion implanted sample in H_2SO_4 + NaCl medium (figure 5.14 (d)). However, implanted samples exhibited ZrO_2 layer along with some corrosion products. It revealed that ZrO_2 layer formed due to O^+ ion implantation has protected the alloy from pitting corrosion in H_2SO_4 containing Cl ions. Mudali et al. [70] have also observed such pits on $Zr_{59}Ti_3Cu_{20}Al_{10}Ni_8$ alloy in a similar medium. It has been reported that these pits were initiated due to adsorption and penetration of chloride ions by structural defects and crystalline inclusions present in glassy alloys. Moreover, pit growth was attributed to an enhanced local selective dissolution mainly of less noble metal (Zr, Ti, Al) at these structural defects due to an auto-catalytic reaction with chloride ions [70]. Furthermore, Mondal et al. [71] have also reported regarding the selective dissolution of base metal (Zr) and enrichment of Cu in the pit region formed on $Zr_{58}Cu_{28}Al_{10}Ti_4$ and $Zr_{65}Cu_{7.5}Al_{7.5}Ni_{10}Pd_{10}$ alloys in NaCl solution. Figure 5.14 (e) shows the surface morphology of corroded as-cast sample in HNO_3 medium. The micrograph exhibited large-scaled isolated oxide passive products on the surface of the sample along with polishing marks (indicated by arrow). However, as shown in figure 5.14 (f), the implanted sample has also exhibited corroded surface in HNO_3 solution, which means that oxide layer formed during implantation could not prevent the alloy from corrosion in this medium possibly due to presence of $Cu_{10}Zr_7$ crystalline phases. These FESEM results were in good agreement with the results of electrochemical studies.

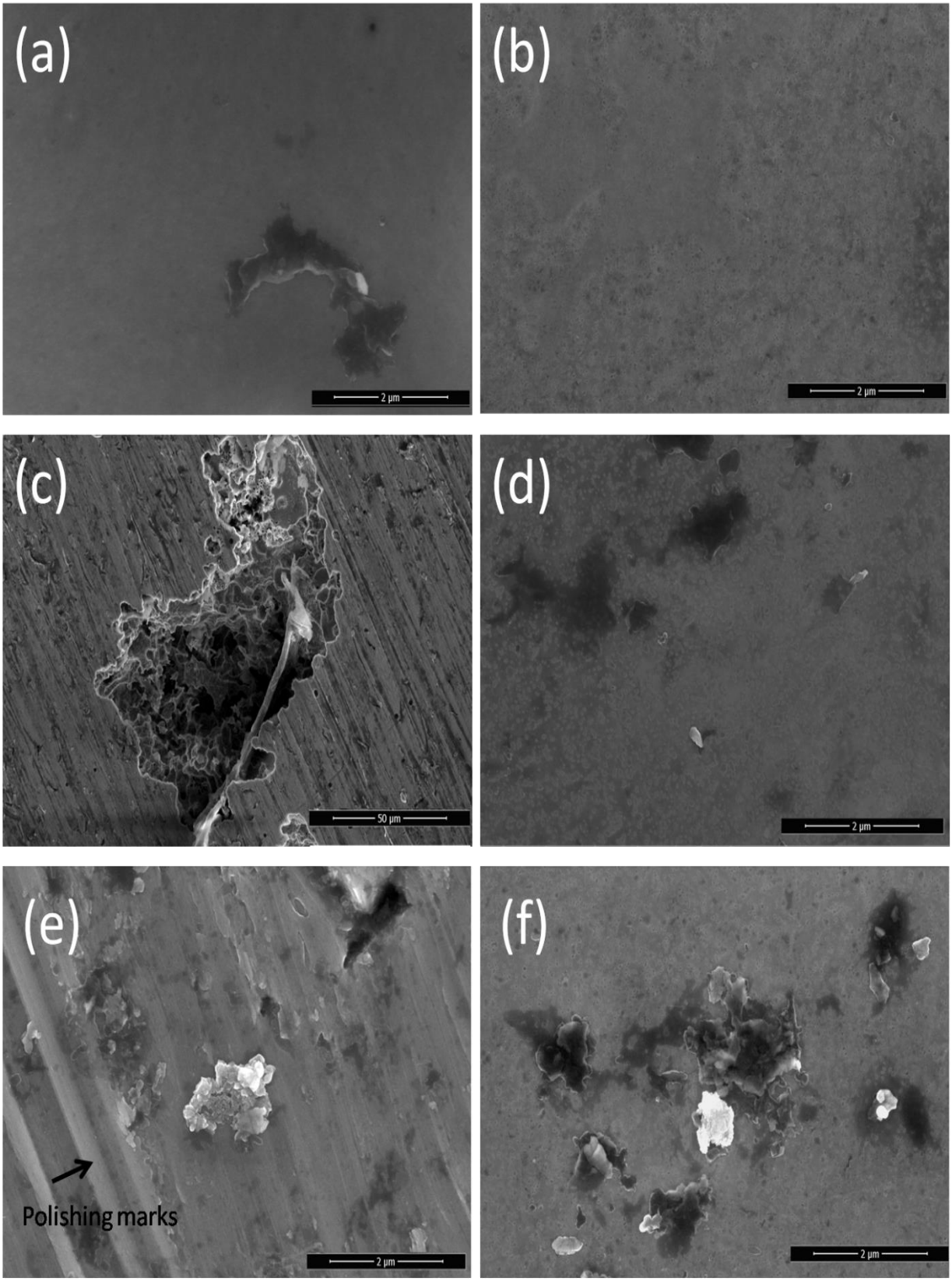

Figure 5.14: FESEM images of as-cast and O^+ ion implanted bulk $Zr_{55}Cu_{30}Ni_5Al_{10}$ amorphous alloys (a, b) in 0.5 M H_2SO_4; (c, d) in the mixture of 0.5 M H_2SO_4 and 0.1 M NaCl and (e, f) in 1 M HNO_3 medium, respectively

5.1.4 Conclusion

The influence of O^+ ion implantation at 1 x 10^{16}, 1 x 10^{17} and 3 x 10^{17} ions/cm^2 fluences on the corrosion behavior of the bulk $Zr_{55}Cu_{30}Ni_5Al_{10}$ amorphous alloy in 0.5 M H_2SO_4, 1.0 M HNO_3 and in the mixture of 0.5 M H_2SO_4 and 0.1 M NaCl aqueous solutions has been studied in the present research work. The GIXRD patterns showed the formation of $Cu_{10}Zr_7$ and ZrO_2 crystalline phases on the surface of O^+ implanted $Zr_{55}Cu_{30}Ni_5Al_{10}$ amorphous alloy. The formation of ZrO_2 layer on the surface of implanted alloy was confirmed by FE-SEM and XPS. The potentiodynamic polarization results revealed that corrosion resistance of the bulk $Zr_{55}Cu_{30}Ni_5Al_{10}$ amorphous alloy is improved in H_2SO_4 and H_2SO_4 + NaCl media after O^+ ion implantation due to the formation of the protective ZrO_2 layer. However, no improvement in corrosion resistance was observed in HNO_3 solution due the formation of $Cu_{10}Zr_7$ after O^+ ion implantation. Surface morphology of corroded surface has also indicated the improvement in corrosion resistance of the as-cast $Zr_{55}Cu_{30}Ni_5Al_{10}$ amorphous alloy in H_2SO_4 and H_2SO_4 + NaCl solution after O^+ ion implantation. It can be concluded that the pitting resistance of bulk $Zr_{55}Cu_{30}Ni_5Al_{10}$ amorphous alloy was increased in H_2SO_4 + NaCl medium after O^+ ion implantation.

5.2 NITROGEN ION IMPLANTATION

5.2.1 Introduction

The ion implantation is an effectual technology capable of improving the surface properties of material without distinctly changing dimensional integrity. Among various ion beams, used in ion implantation technique, nitrogen ion beam is widely used for surface modification of different materials. It has been reported that the implantation with nitrogen ions has improved the corrosion resistance of Ti, Ti- alloys, stainless steel (SS), Ti-modified SS alloys in simulated body fluid (SBF) and ringer's solution for bio-medical application due to the oxynitride formation along with oxide formation and titanium nitride precipitates [122-124,183-184]. Improved pitting corrosion resistance of N^+ implanted 304 Stainless steel in acidic chloride medium has been reported by Mudali et al. [104] due to the formation of inhibiting nitrates or nitrites, which provide the unfavorable condition for growth of pits.

It is found that O^+ ion implantation could not improve the corrosion resistance of bulk $Zr_{55}Cu_{30}Ni_5Al_{10}$ amorphous alloy in HNO_3 solution. Hence, an attempt was made to improve the corrosion resistance of Zr-based amorphous alloys by nitrogen ion implantation in nitric acid medium. Miyagawa et al. [185-186] have studied the changes in composition and thermal behavior of Zr metal due to nitrogen implantation and reported the ZrN formation on the surface of Zr metal. An improvement in corrosion resistance of N^+ implanted Zircaloy-4 has been reported in NaCl medium due to the formation of ZrN along with ZrO_2 [52,103,187]. The enhancement in corrosion resistance of the N-implanted Zr–Sn–Nb alloy in alkaline solution has been reported by Liu et al. [188] due to the formation of $ZrN + ZrO_2$. Since it is reported that N^+ implantation greatly affect the corrosion properties of Zr and Zircaloy-4 hence, it is imperative to understand the fundamental nature of the corrosion product formed on the $Zr_{55}Cu_{30}Al_{10}Ni_5$ amorphous alloy after N^+ implantation.

5.2.2 Experimental procedure

5.2.2.1 Materials and identification of phases

The ingots of $Zr_{55}Cu_{30}Ni_5Al_{10}$ (atomic %) alloy, weighing 10 g, were developed by arc melting system using a mixture of Zr, Cu, Ni and Al of 99.99% purity, under Ar atmosphere. Arc melting was repeated at least four times to get chemical homogeneity of the mixture using vacuum up to 3.6 x 10^{-4} mbar. Final casting of $Zr_{55}Cu_{30}Ni_5Al_{10}$ amorphous alloy was carried out using a melt spinning system. The ingot was then re-melted in a quartz crucible and ejected on the surface of Cu wheel, rotating with a velocity of 20 m/s. Fine quality ribbons of 7 mm width and 30 μm thickness were developed. The casting of the samples was carried out at UGC-DAE, IGCAR Kalpakkam using Edmund Buhler GmbH system. Samples were cleaned with acetone and distilled water and dried in air. The structure analysis of the $Zr_{55}Cu_{30}Ni_5Al_{10}$ amorphous alloy was carried out by X-ray diffraction (XRD) technique with Inel- XRD (Equinox 2000) system using monochromatic Co source at CSTG, IGCAR Kalpakkam.

5.2.2.2 N^+ ion implantation

Nitrogen ions were implanted on the shinning surface (air side) of the $Zr_{55}Cu_{30}Ni_5Al_{10}$ amorphous alloy in target chamber of TAM SAMES 150 keV particle accelerator at Ion Beam Physics Section (IBPS), Materials Science Group (MSG), IGCAR Kalpakkam. The as-spun $Zr_{55}Cu_{30}Ni_5Al_{10}$ ribbon samples were mounted on sample holder using double sided copper tape and further placed in irradiation chamber. The 100 keV N^+ ions were implanted on as-spun $Zr_{55}Cu_{30}Ni_5Al_{10}$ ribbon samples with 1 x 10^{16}, 5 x 10^{16}, 1 x 10^{17} ions/cm^2 fluences at room temperature at a vacuum of 2.1 x 10^{-7} torr. Mass analyzed N^+ ion beam impinged at normal incidence and scanned over the ribbon samples on an area ~0.6 cm^2 for uniform implantation. During the implantation, the beam current was kept low i.e. below 2 μA on the samples during the implantation to minimize the ion beam heating.

5.2.2.3 Surface characterization

Microstructure characterization of N^+ implanted specimens was performed using glancing incidence X-ray diffraction (GIXRD) measurement with Inel- XRD (Equinox 2000) system at CSTG, IGCAR Kalpakkam. All the measurements were carried out at a glancing angle of 1° using Co source. The chemical state of the surface of N^+ ion implanted $Zr_{55}Cu_{30}Ni_5Al_{10}$ ribbon sample at a fluence of 1 x 10^{16} ions/cm^2 was examined by XPS using SPECS Surface Nano Analysis GmbH, Germany spectrometer. All the spectra were collected using the PHOIBOS 150 MCD-9 analyzer.

5.2.2.4 Electrochemical measurements

The electrochemical behavior of as-spun and N^+ implanted $Zr_{55}Cu_{30}Ni_5Al_{10}$ ribbon samples in 1 M HNO_3 was investigated using a potentiostat (Autolab-AUT84276) consisting of a three electrode cell. Samples were cleaned with ethanol and distilled water and dried in air before experiment. These samples were used as working electrode; Ag/AgCl (3 M KCl) and platinum foil were used as reference and counter electrodes, respectively. An area of 0.18 cm^2 of the sample was exposed to electrolyte. Prior to each polarization experiment, the stable open circuit potential (OCP) was monitored for 1 h. Potentiodynamic polarization curves were recorded at the scanning rate of 0.001 V/s from -0.2 V below OCP to 2.6 V. The electrochemical experiments were repeated for checking the reproducibility of the results.

5.2.2.5 Surface characterization after electrochemical measurements

After the electrochemical experiments in nitric acid medium, the surface morphology of the corroded surface of as-cast and N^+ ion implanted samples was examined by FE-SEM using NOVA-Nano FE-SEM 450 system at MRC, MNIT Jaipur. The chemical composition of potentiodynamic polarized N^+ ion implanted samples at 1 x 10^{16} ions/cm^2 fluence were also evaluated by XPS.

5.2.3 Results and discussion

5.2.3.1 Micro-structural analysis

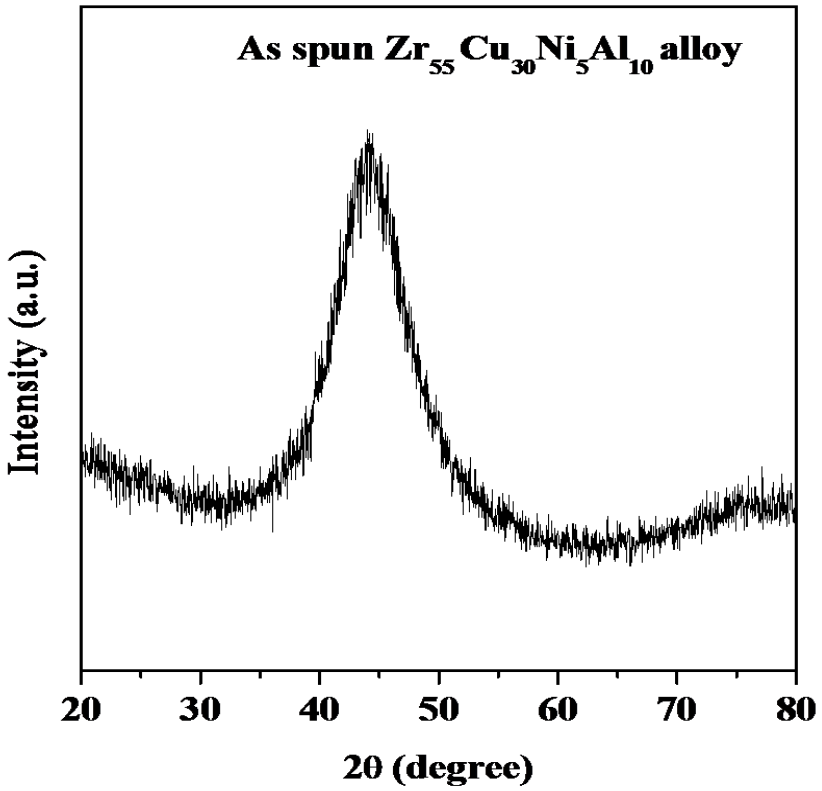

Figure 5.15: XRD pattern of as-spun $Zr_{55}Cu_{30}Ni_5Al_{10}$ amorphous alloy

Figure 5.15 presents the XRD pattern of the as-spun $Zr_{55}Cu_{30}Ni_5Al_{10}$ ribbon sample. The pattern consisted of a broad halo peak, indicating that the as-spun $Zr_{55}Cu_{30}Ni_5Al_{10}$ ribbon sample has amorphous nature. Figure 5.16 shows the GIXRD pattern of N^+ ion implanted $Zr_{55}Cu_{30}Ni_5Al_{10}$ amorphous alloy at 1 x 10^{16}, 5 x 10^{16} and 1 x 10^{17} ions/cm^2 fluences. It exhibited the presence of low intensity diffraction peaks corresponding to ZrO_2, Al_2O_3 and ZrN crystalline phases along with the broad amorphous peak. It is noticeable from figure 5.16 that the intensity of diffraction peaks becomes more prominent with increasing fluence of nitrogen ions. The formation of ZrO_2 and Al_2O_3 (figure 5.16) have been observed on the surface of implanted samples due to the presence of residual oxygen in vacuum chamber, which is activated during implantation. The intensity of GIXRD peak corresponding to Al_2O_3 was very small due to the very low atomic concentration of Al element in the sample. The

presence of ZrO_2 and Al_2O_3 was more significant at higher fluences during implantation. Kim et al. [52] have reported the formation of ZrN and ZrO_2 during nitrogen ion implantation of zircaloy. In one another study, GIXRD results showed the formation of ZrN on the surface of N-implanted Zr-Sn-Nb alloy at fluences above 1 x 10^{17} ions/cm^2 [188]. These crystalline phases were formed due to the enhanced atomic mobility during implantation, which led to the increased nucleation and crystal growth.

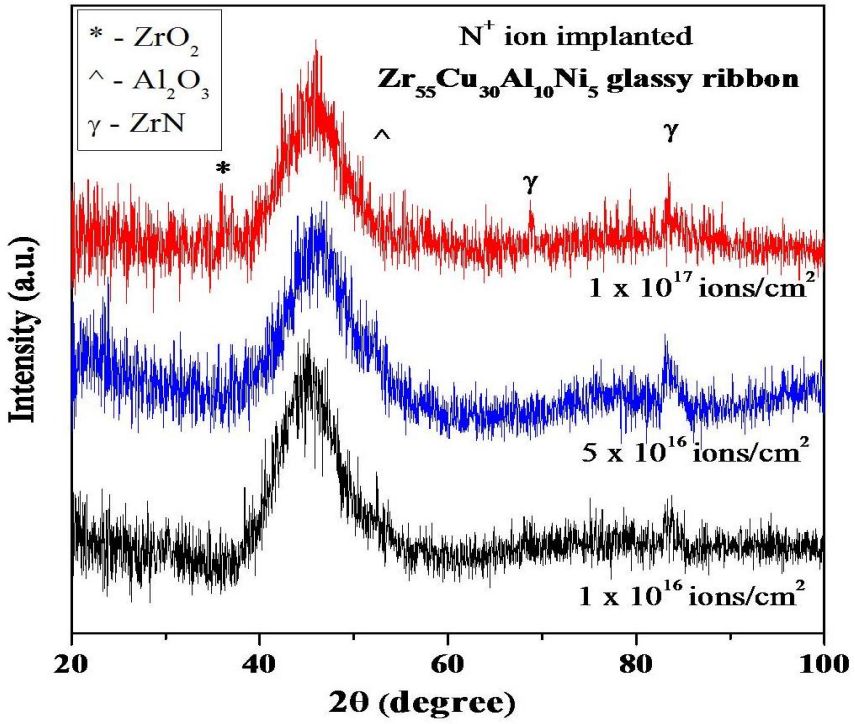

Figure 5.16: GIXRD pattern of N^+ ion implanted $Zr_{55}Cu_{30}Ni_5Al_{10}$ glassy alloys at 1 x 10^{16}, 5 x 10^{16} , 1 x 10^{17} ions/cm^2 fluence

5.2.3.2 N^+ ion implantation simulation by TRIM

The projected range of N^+ ions of 100 keV energy in $Zr_{55}Cu_{30}Ni_5Al_{10}$ amorphous alloy sample was calculated using computer code SRIM (stopping and ranges of ions in metals) [177]. The value of electronic energy loss (S_e), nuclear energy loss (S_n) and projected range are calculated to be 39.96 eV/Å, 9.523 eV/Å and 1401 Å, respectively. The ion range profile was also calculated using TRIM (transport of ions in matters), which is part of the SRIM

software package. A pictorial presentation on the simulated trajectory of implant N^+ ions in the amorphous alloy substrate and ion range profile is shown in figure 5.17 (a) and 5.17 (b), respectively. The projected range calculated by SRIM is nearly equal to the projected range calculated from the ion range profile. In figure 5.17 (a), the distribution of N^+ ions after implantation is shown with white color and red dots show the vacancies created due to the collision of ions to the target atom.

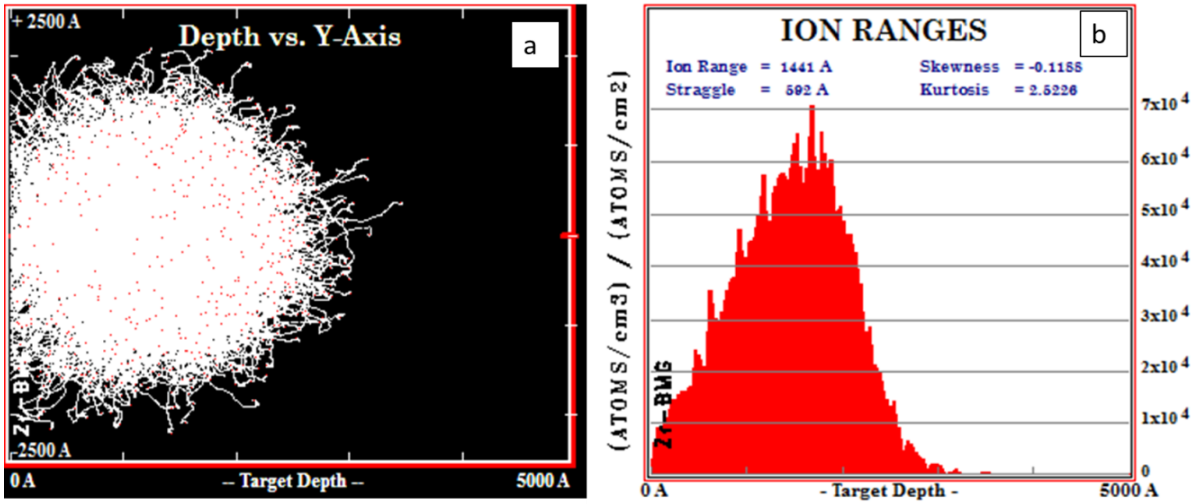

Figure 5.17: Structural simulation of $Zr_{55}Cu_{30}Ni_5Al_{10}$ amorphous alloy after N^+ ion implantation, (a) N^+ ion concentration distribution and (b) ion range profile.

5.2.3.3 Surface morphology after N^+ ion implantation

Figure 5.18 shows the surface morphology of as spun and nitrogen ion implanted $Zr_{55}Cu_{30}Ni_5Al_{10}$ amorphous alloy at 1 x 10^{16}, 5 x 10^{16} and 1 x 10^{17} ions/cm^2 fluences. Figure 5.18 (a) showed that as-spun ribbon sample has clean and smooth surface whereas figure 5.18 (b) shows the presence of oxides or nitrides in the form of some small pockets on the implanted surface of specimen. As the fluence increases during implantation, the formation of contaminated carbon layer took place and also the sample has shown the presence of carbon layer along with implanted area (figure 5.18 (c)). In case of 1 x 10^{17} ions/cm^2 fluence, inhomogeneous layer has been formed on the surface of implanted sample (Fig. 5.18 (d)).

This layer is formed due to carbon contamination and the surface was almost covered with blue color contaminated layer. The FESEM micrographs of implanted sample could not reveal the proper information of changes in surface morphology due to ion implantation so XPS has been carried out for further detailed studies.

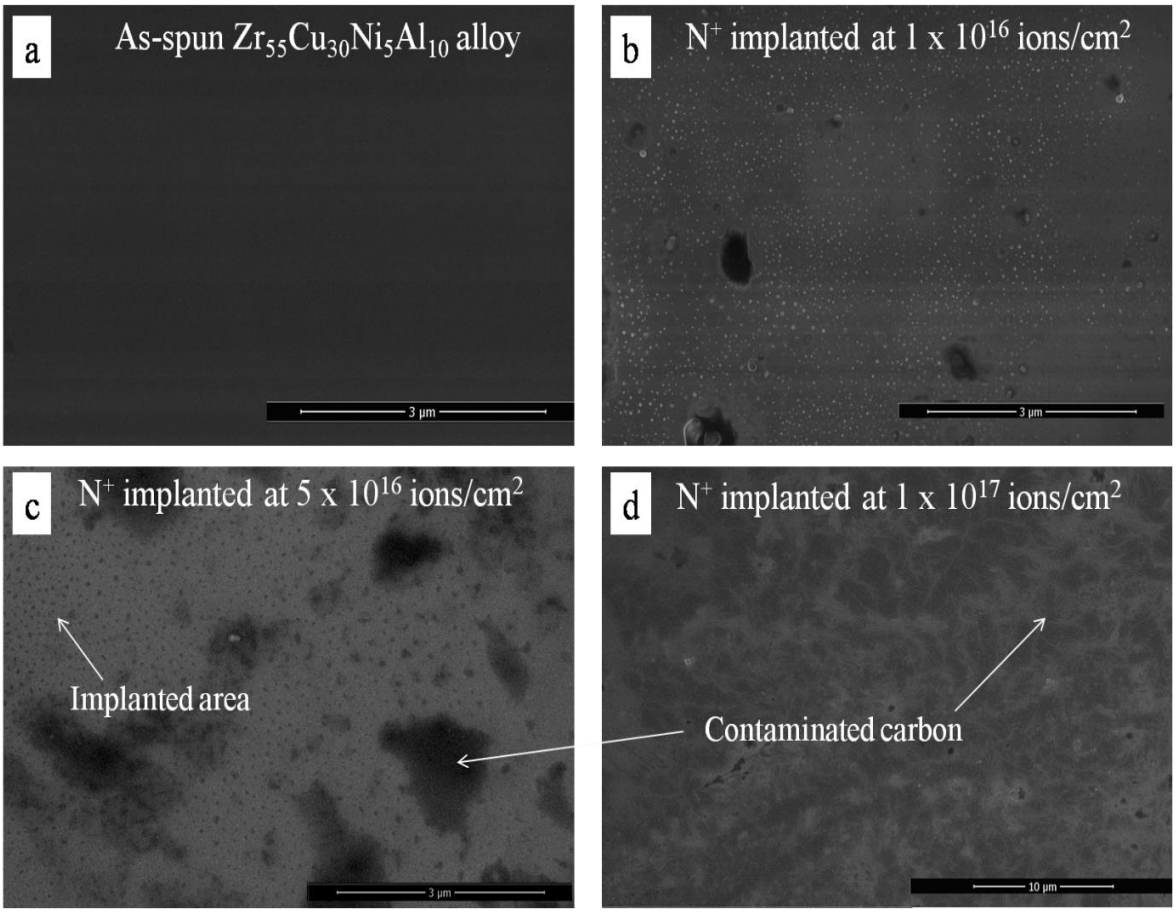

Figure 5.18: FESEM images of (a) as-spun and N^+ ion implanted $Zr_{55}Cu_{30}Ni_5Al_{10}$ amorphous alloy ion fluences (b) at 1 x 10^{16} ions/cm^2, (c) at 5 x 10^{16} ions/cm^2 and (d) at 1 x 10^{17} ions/cm^2

5.2.3.4 EDS study

To verify the quantitative composition of as-spun $Zr_{55}Cu_{30}Ni_5Al_{10}$ amorphous alloy as well as to evaluate the surface changes due to N^+ ion implantation on the surface of $Zr_{55}Cu_{30}Ni_5Al_{10}$ amorphous alloy, EDS measurements were carried out. Figure 5.19 (a) shows the analysis of the EDS spectrum, which indicates that the composition of as-spun alloy is nearly equal to

the targeted composition. The presence of oxygen peak in the EDS spectrum of as-spun alloy indicates the formation of native oxide layer on the surface of as-spun $Zr_{55}Cu_{30}Ni_5Al_{10}$ amorphous alloy in the presence of air. The presence of C peak was also observed due to contamination of surface. On the other hand, EDS spectrum of N^+ ion implanted $Zr_{55}Cu_{30}Ni_5Al_{10}$ amorphous alloy at 1 x 10^{16} ions/cm^2 fluence (figure 5.19 (b)) shows that the atomic concentration of Zr is significantly decreased than that of as-spun alloy and the presence of N peak was obtained due to the formation of ZrN after N^+ ion implantation. The presence of O peak indicates the formation of ZrO_2. This is worth mentioning here that the concentration of Cu was also significantly decreased because it does not take part in formation of oxide layer so it could not be observed on the surface of the alloy. The atomic concentration of Al has been also decreased in EDS spectrum of N^+ ion implanted sample due to the formation of Al_2O_3, which was also observed in GIXRD pattern. These EDS results are in good agreement with GIXRD and FESEM results. The qualitative analysis cannot be carried out by EDS, so XPS is used for detailed investigation.

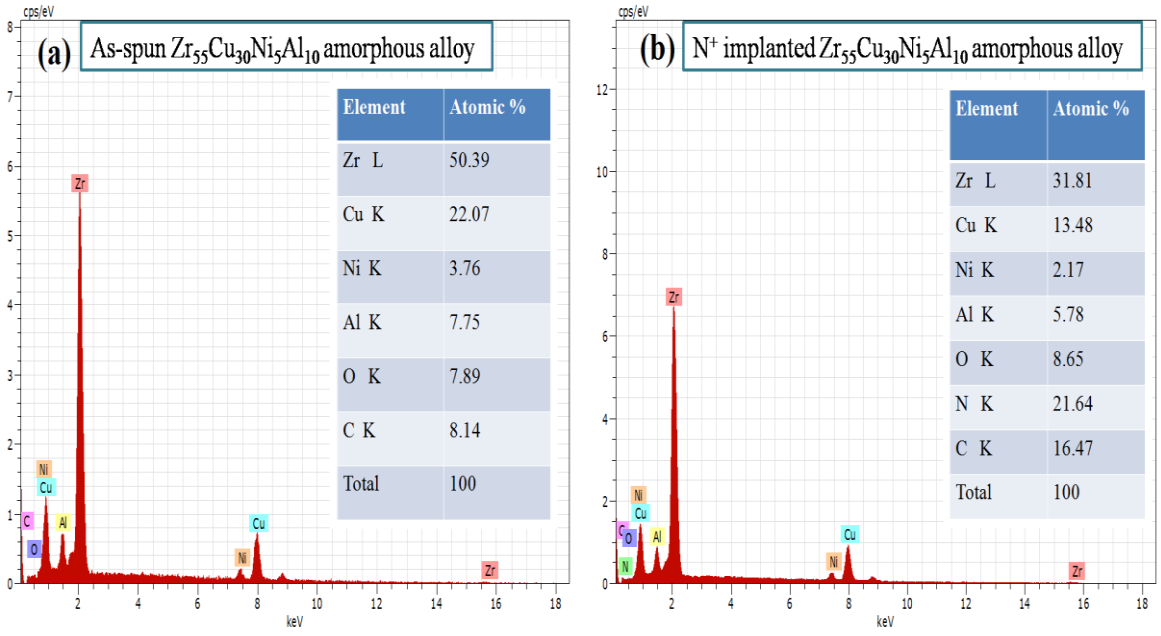

Figure 5.19: EDS spectrum of (a) as-spun $Zr_{55}Cu_{30}Ni_5Al_{10}$ amorphous alloy (b) N^+ implanted $Zr_{55}Cu_{30}Ni_5Al_{10}$ amorphous alloy at 1 x 10^{16} ions/cm^2 fluence

5.2.3.5 XPS study

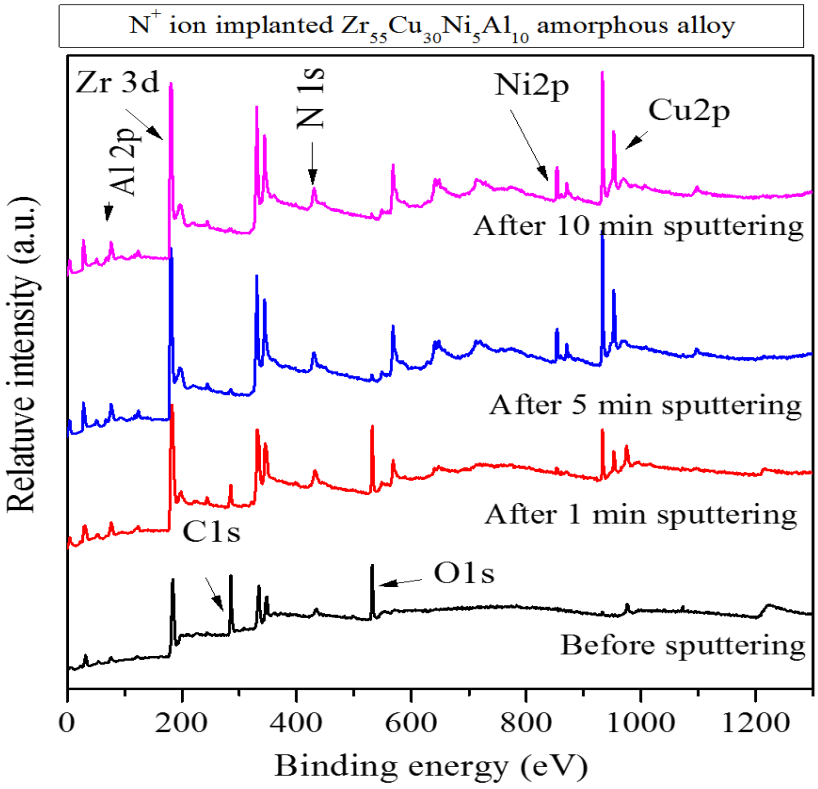

Figure 5.20: XPS survey spectra of N^+ implanted $Zr_{55}Cu_{30}Ni_5Al_{10}$ amorphous alloy at 1 x 10^{16} ions/cm^2 fluence

The elemental composition and chemical state of elements on the implanted surface of the $Zr_{55}Cu_{30}Ni_5Al_{10}$ amorphous alloy was examined by XPS analysis. Figure 5.20 shows the XPS survey spectrum of the N^+ ion implanted sample at 1 x 10^{16} ions/cm^2 fluence. The peaks of Zr 3d, Al 2p, Cu 2p, O 1s and C 1s are predominantly detected on the implanted surface of the alloy at 1 x 10^{16} ions/cm^2 fluence and the peaks corresponding to Ni 2p, N 1s were also detected after the sputtering of the surface. The presence of C 1s peak at 284.8 eV is due to the contamination on the sample surface. The intensity of carbon peak was maximum on the surface of as-implanted sample and it has dropped continuously with the depth as shown in figure 5.20. The XPS peak of O 1s was also obtained on the surface of implanted alloy due to the presence of residual oxygen in vacuum chamber, which is activated during implantation.

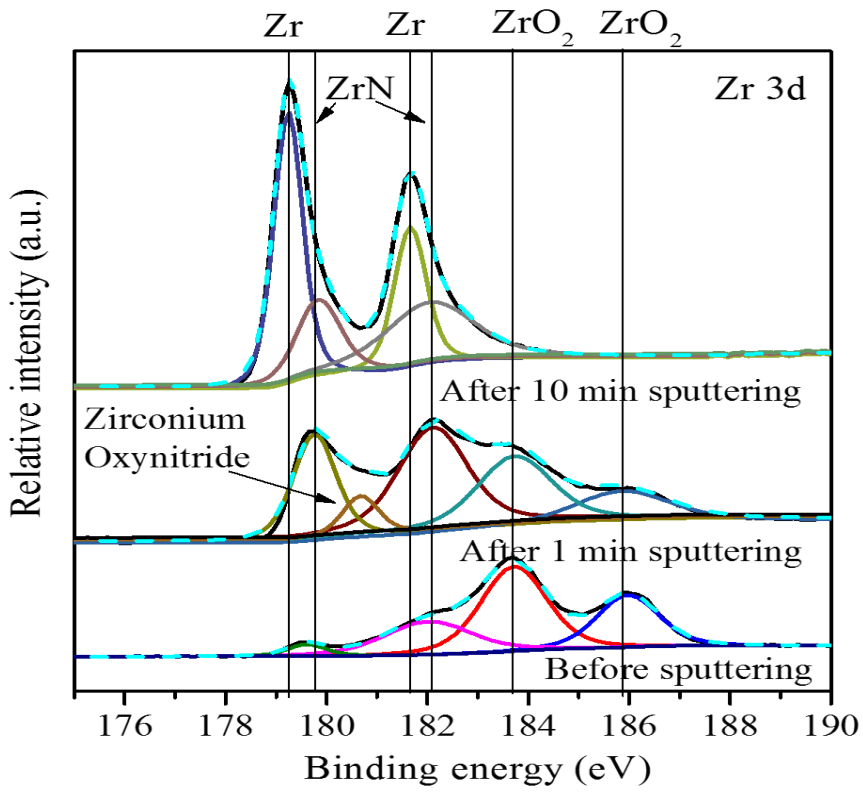

Figure 5.21: High resolution XPS peaks of N^+ implanted $Zr_{55}Cu_{30}Ni_5Al_{10}$ glassy alloy at 1 x 10^{16} ions/cm^2 fluence for Zr

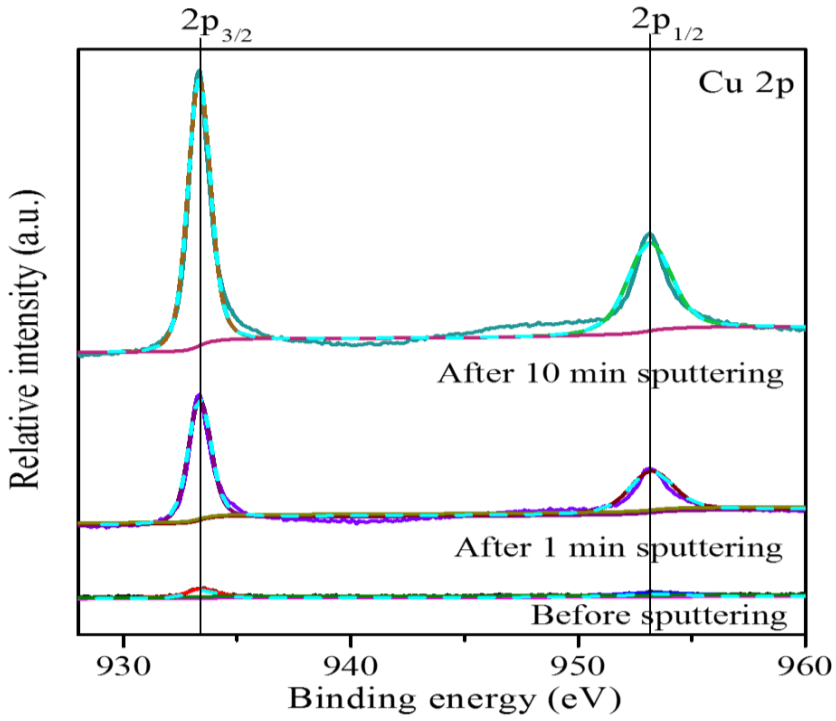

Figure 5.22: High resolution XPS peaks of N^+ implanted $Zr_{55}Cu_{30}Ni_5Al_{10}$ glassy alloy at 1 x 10^{16} ions/cm^2 fluence for Cu

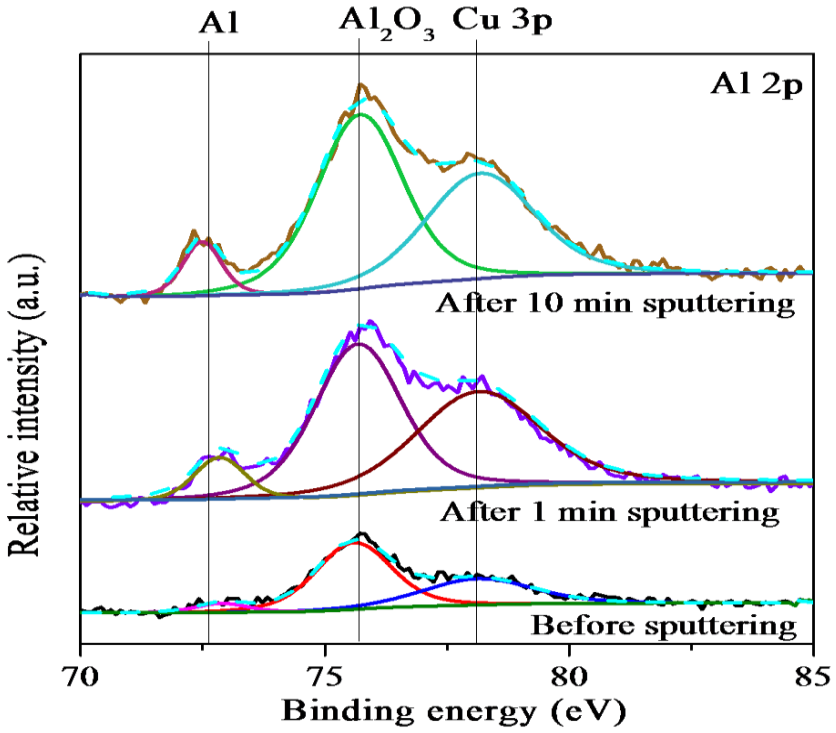

Figure 5.23: High resolution XPS peaks of N^+ implanted $Zr_{55}Cu_{30}Ni_5Al_{10}$ glassy alloy at 1 x 10^{16} ions/cm^2 fluence for Al

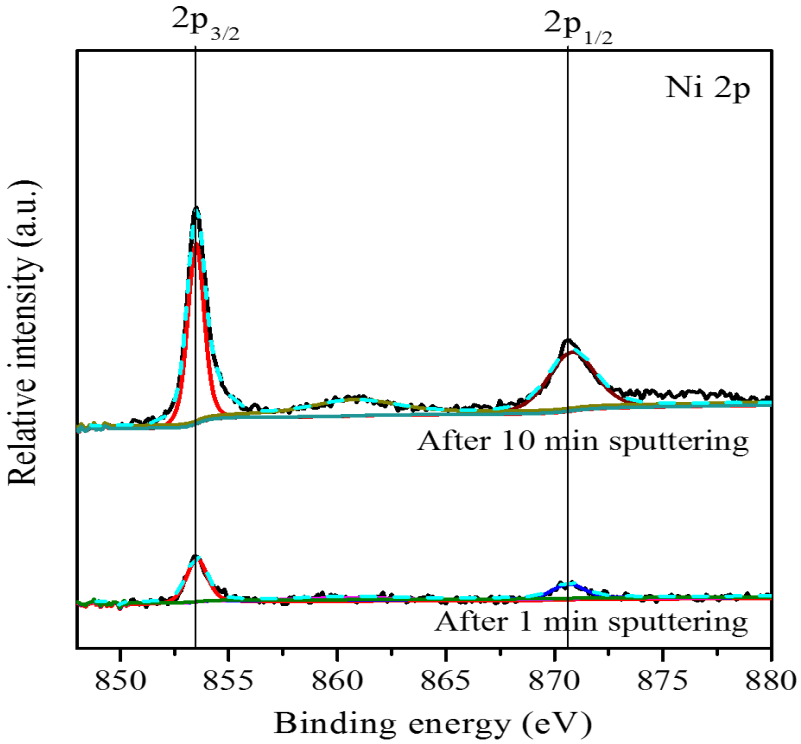

Figure 5.24: High resolution XPS peaks of N^+ implanted $Zr_{55}Cu_{30}Ni_5Al_{10}$ glassy alloy at 1 x 10^{16} ions/cm^2 fluence for Ni

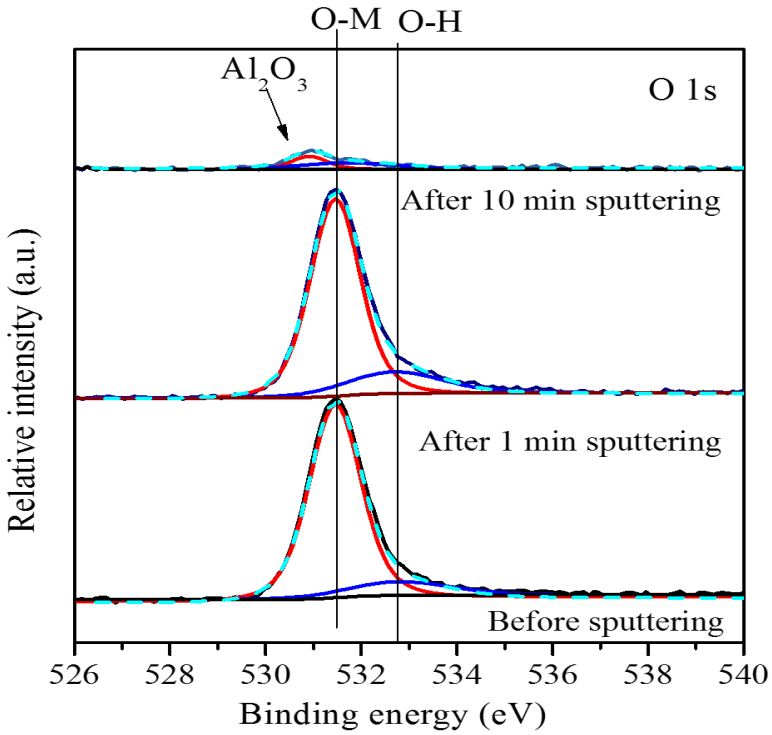

Figure 5.25: High resolution XPS peaks of N^+ implanted $Zr_{55}Cu_{30}Ni_5Al_{10}$ glassy alloy at 1 x 10^{16} ions/cm^2 fluence for O

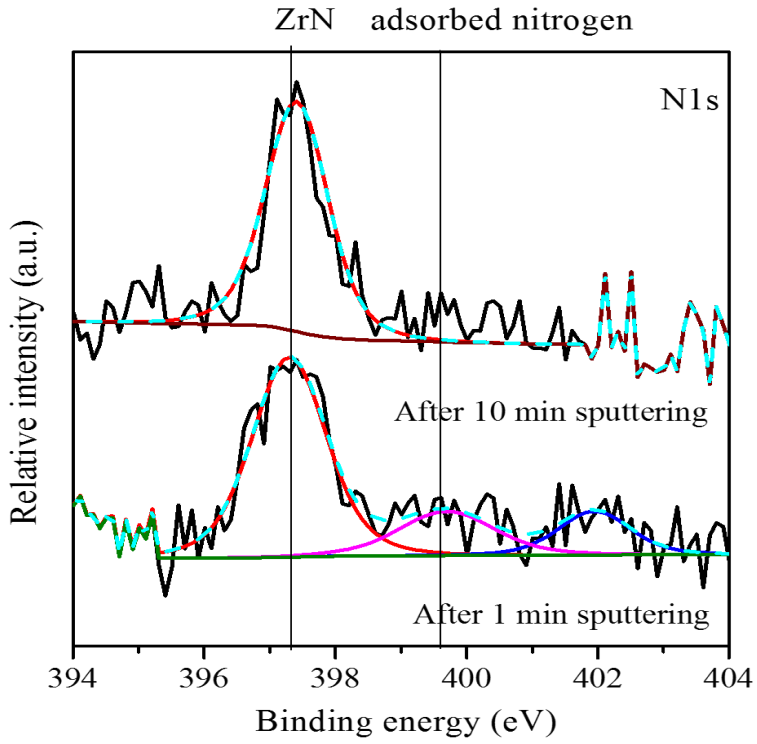

Figure 5.26: High resolution XPS peaks of N^+ implanted $Zr_{55}Cu_{30}Ni_5Al_{10}$ glassy alloy at 1 x 10^{16} ions/cm^2 fluence for N

The high resolution XPS spectra of each element Zr, Cu, Al, Ni, O and N in case of 1 x 10^{16} ions/cm^2 fluence are shown in figure 5.21, 5.22, 5.23, 5.24, 5.25 and 5.26, respectively. The Zr 3d spectra (figure 5.21) from the surface of as-implanted alloy are characterized by doublet terms Zr $3d_{3/2}$ and Zr $3d_{5/2}$ due to spin–orbit coupling. The dominant features in the Zr 3d spectra is the formation of ZrO_2, observed at the binding energy 183.6 eV for Zr $3d_{5/2}$ and 185.8 eV for Zr $3d_{3/2}$ [162,189]. These peaks originated from the Zr^{4+} indicating formation ZrO_2. The deconvolution of Zr 3d spectra also shows the presence of weaker doublet at 179.9 eV and 182 eV binding energy corresponding to ZrN on the surface [190-191]. The intensity of XPS peak corresponding to ZrN has increased after 1 min sputtering and overlapping XPS peak was observed at 179.3 eV and 181.7 eV assigned to metallic Zr [45,152]. One another XPS peak at 180.6 eV was assigned to zirconium oxynitride [179]. The intensities of XPS peaks corresponding to ZrN and metallic Zr has increased with sputtering time. Cu 2p doublet (figure 5.22) was observed at 933.3 eV for Cu $2p_{3/2}$ and 953.1 eV for $Cu2p_{1/2}$ corresponding to metallic Cu [75,161]. The intensities of these XPS peaks corresponding to metallic Cu were increased after sputtering of the surface with no shift in binding energy. The XPS peak at 75.6 eV (figure 5.23) was due to Al 2p having oxidizing state (Al^{3+}) indicating Al_2O_3 on the as-implanted surface [192]. The Al 2p spectrum is overlapped with the Cu 3p spectrum peak at 77.9 eV due to Cu $3p_{1/2}$ electrons [75,193]. The weak XPS peak present at 72.9 eV indicated the presence of the metallic form of Al [154,194] on the surface of implanted sample. The intensity of metallic Al peak was increased with sputtering time. The relative intensity of Al spectrum was very low in comparison to the Zr XPS spectrum. The Ni 2p spectrum (figure 5.24) shows the Ni $2p_{3/2}$ and $2p_{1/2}$ peaks at 853.4 eV and 870.4eV respectively, which are originating from Ni^0 corresponding to metallic Ni. The presence of this Ni 2p spectrum was obtained only after sputtering (as shown in figure 5.20). In the Ni 2p spectrum (figure 5.24), a satellite peak at 860 eV is also appeared due to sputter damaged crystallite [195]. The O 1s spectrum (figure

5.25) was composed of two peaks, one high intensity peak at 531.4 eV, which is assigned to OM oxygen corresponds to O^{+2} ions in oxides [151] and a weaker peak at 532.7 eV, assigned to OH oxygen linked to bound water or hydrogen [75]. The XPS peak of O 1s was shifted towards lower binding energy at 530.5 eV after sputtering of the sample which is assigned to Al_2O_3 [192]. Figure 5.26 illustrates the N 1s spectrum, in which the XPS peaks were located at 397.3 eV and 399 eV corresponding to ZrN [190,196-197] and adsorbed nitrogen, respectively [179,194].

XPS results revealed the formation of ZrO_2 and ZrN after N^+ ion implantation on $Zr_{55}Cu_{30}Ni_5Al_{10}$ amorphous alloy. Due to higher atomic concentration of Zr in the $Zr_{55}Cu_{30}Ni_5Al_{10}$ alloy, its low electronegativity (Zr- 1.33, Cu-1.9, Ni-1.91 and Al-1.61) and relatively low heat of formation, it is preferentially oxidized in the presence of residual gas in vacuum chamber and form ZrO_2 [191]. On the other side, the formation of ZrN due to N^+ ion implantation on Zr metal [185, 196] has already been reported. The formation of ZrO_2 and ZrN was obtained in nitrogen implantation of Zircaloy [52,103] and Zr-Sn-Nb [188]. In the present study, the formation of ZrO_2, ZrN and oxynitride has been observed due to N^+ ion implantation on $Zr_{55}Cu_{30}Ni_5Al_{10}$ amorphous alloy at 1 x 10^{16} ions/cm^2 fluence. In the present work, N ion implantation at 3 x 10^{17} ions/cm^2 fluence on $Zr_{55}Cu_{30}Ni_5Al_{10}$ amorphous alloy was also carried out, but XPS analysis of this sample exhibited the presence of abundant carbon on the surface of sample (as shown in XPS survey spectrum in figure 5.27) and for the same reason the sample has not been taken for further studies. The appearance of carbo-nitrides formed during high fluence N ion implantation on Ti-6Al-7Nb has already reported by Thair et al. [198] and found detrimental effect on corrosion resistance of alloy.

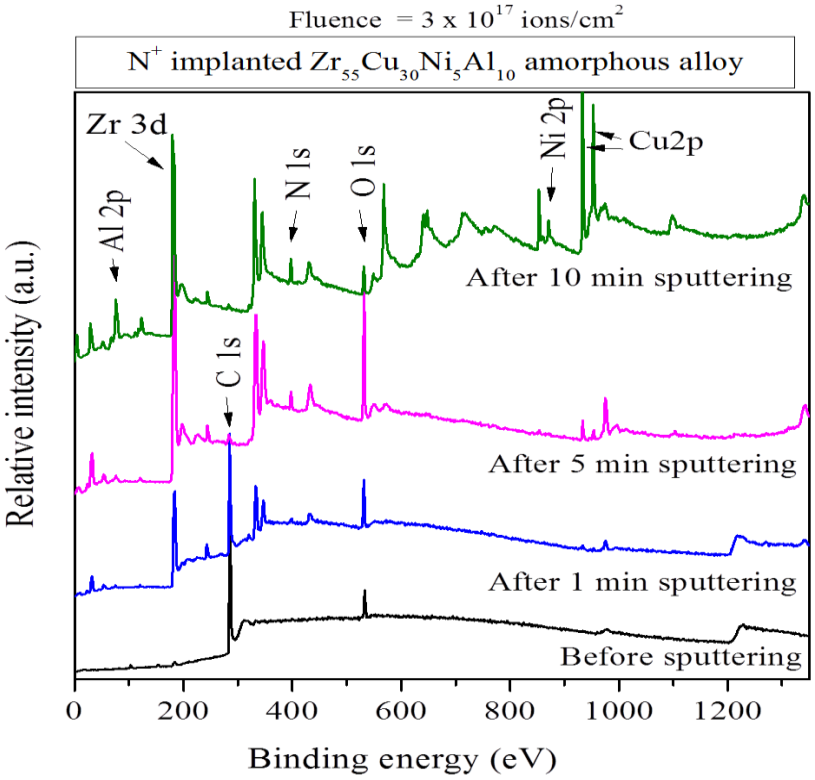

Figure 5.27: XPS survey scan of N^+ implanted $Zr_{55}Cu_{30}Ni_5Al_{10}$ glassy alloy at 3 x 10^{17} ions/cm^2 fluence

5.2.3.6 Potentiodynamic polarization study

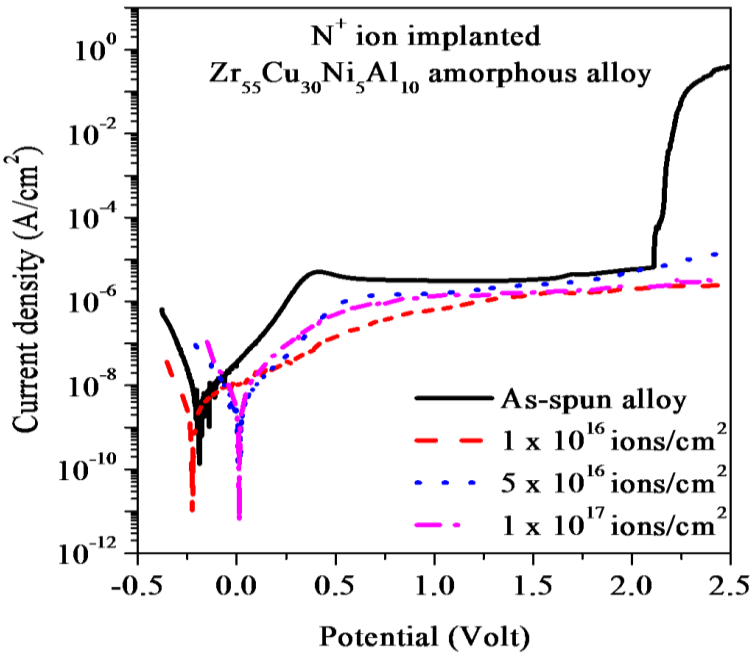

Figure 5.28: Potentiodynamic polarization curve of as spun and N^+ implanted $Zr_{55}Cu_{30}Ni_5Al_{10}$ amorphous alloys at different fluences in 1 M HNO_3 medium

The corrosion behavior of the as-spun and N^+ ion implanted $Zr_{55}Cu_{30}Ni_5Al_{10}$ ribbon samples at different fluences were investigated in 1 M HNO_3 medium. The potentiodynamic polarization curve is shown in figure 5.28. The corrosion potentials (E_{corr}), the corrosion current densities (I_{corr}) and the passive current densities (I_{pass}) for all the samples are shown in Table 5.2. The corrosion current densities were derived using Tafel extrapolation method. The value of E_{corr} is comparable with that of as spun ribbon sample after N^+ ion implantation at 1x 10^{16} ions/cm^2 and the other implanted samples at higher fluences has shown slight increase in E_{corr} value. The increase in E_{corr} value was attributed to the origination of passive layer of ZrN and ZrO_2, which is protective in nature. Padhy et al. [106] have studied the corrosion behavior of N^+ implanted 304L stainless steel in 1 M HNO_3 medium and reported the increase in E_{corr} value due to the combined effect of implanted nitrogen and formation of chromium nitride. In the present work, the value of I_{corr} was slightly increased after N^+ ion implantation at a fluence of 5 x 10^{16} and 1 x 10^{17} ions/cm^2, whereas low I_{corr} value was observed for 1 x 10^{16} ions/cm^2 fluence. However, the value of I_{pass} for all implanted samples was lower than that of virgin sample, which indicated the formation of stable passive film on the surface of implanted samples [184]. The as-spun $Zr_{55}Cu_{30}Ni_5Al_{10}$ amorphous ribbon alloy shows the active-passive transition and exhibited high corrosion current density before passivation region, which is referred as active dissolution current peak. After that, the sample was passivated spontaneously. The formation of protective passive layer on the surface of sample is responsible for this spontaneous passivation. The as-spun $Zr_{55}Cu_{30}Ni_5Al_{10}$ amorphous ribbon alloy exhibited active dissolution-passivation transition whereas, the active dissolution current peak was not observed in the potentiodynamic polarization curve of all N^+ ion implanted $Zr_{55}Cu_{30}Ni_5Al_{10}$ ribbon samples. All these results indicate that the corrosion resistance of $Zr_{55}Cu_{30}Ni_5Al_{10}$ amorphous ribbon is improved after N^+ ion implantation. It was attributed due to the formation of ZrN, ZrO_2 and oxynitrides. Corrosion resistance of nitrogen ion implanted samples for higher fluences was not found to be improved in comparison to the

lower fluence in aqueous HNO_3 media. It is possibly due to appearance of small crystalline phases which were out of detection limit of GIXRD. Infact the corrosion resistance of all N^+ implanted samples was better than virgin sample due to the formation of ZrN and ZrO_2 in the implanted sample. It works as a stable protective passive film in nitric acid medium. It has been reported that corrosion resistance of Zircaloy-4 is improved in NaCl [52] and H_2SO_4 solution [187] after N^+ ion implantation due to the formation of ZrN and ZrO_2 layer. Cubillos et al. [199] have also evaluated the corrosion resistance of a zirconium oxynitride thin film deposited on 304 and 316 stainless steels and concluded that layer provides good resistance to corrosion in chloride-containing media. Furthermore, Roman et al. [200] have reported the improved corrosion resistance of a zirconium nitride coated titanium due to the formation of a ZrO_xN_y-ZrO_2 amorphous mixture. In the present study, the improved corrosion resistance of $Zr_{55}Cu_{30}Ni_5Al_{10}$ amorphous alloy is attributed to the formation of ZrN, zirconium oxynitride and ZrO_2. It is worth mentioning that the transpassive potential of the alloy has been also increased after N^+ ion implantation which refers to the better corrosion resistance [76].

Table 5.2: Polarization parameters for as-spun and N^+ ion implanted $Zr_{55}Cu_{30}Ni_5Al_{10}$ amorphous alloy at different fluences in 1 M HNO_3 medium.

N^+ ion implanted $Zr_{55}Cu_{30}Ni_5Al_{10}$ alloy	E_{corr} (V)	I_{corr} (A/cm^2)	I_{pass} (A/cm^2)
As spun amorphous alloy	-0.190	7.71×10^{-9}	3.175×10^{-6}
1×10^{16} ions/cm^2	-0.233	2.13×10^{-9}	1.257×10^{-6}
5×10^{16} ions/cm^2	0.011	4.16×10^{-9}	1.672×10^{-6}
1×10^{17} ions/cm^2	0.013	4.11×10^{-9}	1.434×10^{-6}

5.2.3.7 Surface morphology after electrochemical measurements

Figure 5.29 (a-c) shows the surface morphology of polarized sample of as-spun and N^+ ion implanted $Zr_{55}Cu_{30}Ni_5Al_{10}$ amorphous ribbon at different fluence in 1 M HNO_3 media. As shown in figure 5.29 (a), electrochemically treated as-spun $Zr_{55}Cu_{30}Ni_5Al_{10}$ amorphous alloy in HNO_3 medium exhibited the corrosion affected area along with honeycomb structure. The presence of honeycomb structure is attributed to the preferential dissolution of Cu in nitric acid environment [71]. Homazava et al. [72] have also reported the preferential dissolution of Cu and Al from $Zr_{58.5}Cu_{15.6}Ni_{12.8}Al_{10.3}Nb_{2.8}$ bulk amorphous alloy in 1 M HNO_3 solution. In the present work, the $Zr_{55}Cu_{30}Ni_5Al_{10}$ amorphous alloy has significantly higher atomic concentration of Cu than Ni and Al, so it has more tendencies to dissolve in nitric acid medium. The N^+ ion implanted surface of the amorphous ribbon sample (figure 5.29 (b)) was mainly covered with smooth passive film. No severe corrosion attack could be observed on the implanted surface at lower fluence. This result shows that the formation of passive film of ZrN and ZrO_2 has protected the alloy from corrosion in nitric acid environment. The N^+ ion implanted surface at a fluence of 1 x 10^{17} ions/cm^2 (figure 5.29 (c)) is comparatively more corroded as compared to the sample implanted at a fluence of 1 x 10^{16} ions/cm^2. It is probably due to the appearance of crystalline phases after implantation at higher fluence. These results are in good agreement with potentiodynamic polarization results. It is revealed from FE-SEM morphology of polarized samples that the corrosion resistance of $Zr_{55}Cu_{30}Ni_5Al_{10}$ amorphous ribbon is improved by N^+ ion implantation at lower fluence.

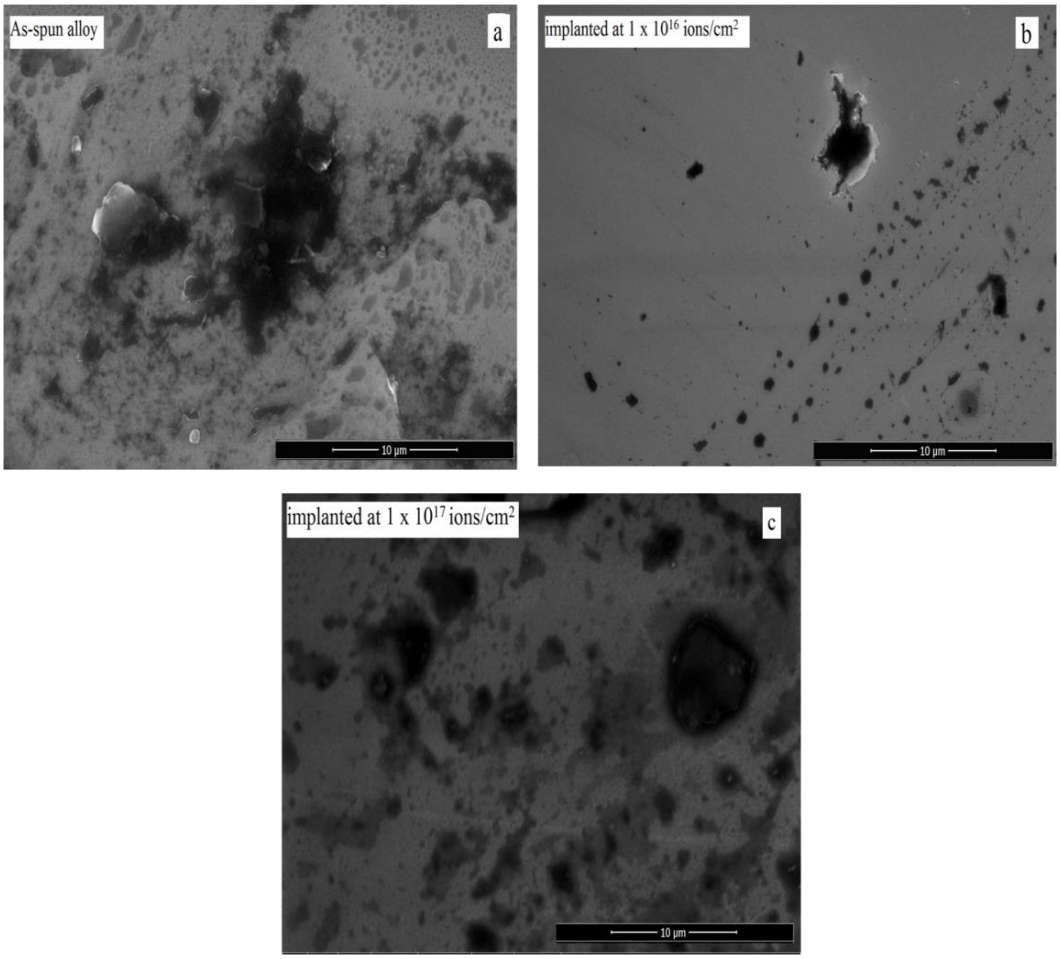

Figure 5.29: FESEM images of (a) as-spun and polarized N^+ ion implanted $Zr_{55}Cu_{30}Ni_5Al_{10}$ amorphous alloy (b) at 1 x 10^{16} ions/cm^2 and (c) at 1 x 10^{17} ions/cm^2 fluence in 1 M HNO_3 medium

5.2.3.8 XPS study after electrochemical measurements

Figure 5.30 shows the XPS survey spectrum obtained from potentiodynamic polarized N^+ ion implanted sample at 1 x 10^{16} ions/cm^2 fluence in 1 M HNO_3 medium. XPS spectra over the wide binding energy region exhibited the peaks of Zr 3d, Al 2p, O 1s, C 1s on surface of polarized sample. The peaks corresponding to Cu 2p, Ni 2p, N 1s were detected after the 1 min sputtering. The presence of C 1s peak at 286 eV was obtained on the surface of polarized sample corresponding to the originally adsorbed hydrocarbons [152]. The peak position is shifted to a lower binding energy (284.8 eV) after 1 min sputtering of the sample and reduced up to negligible intensity.

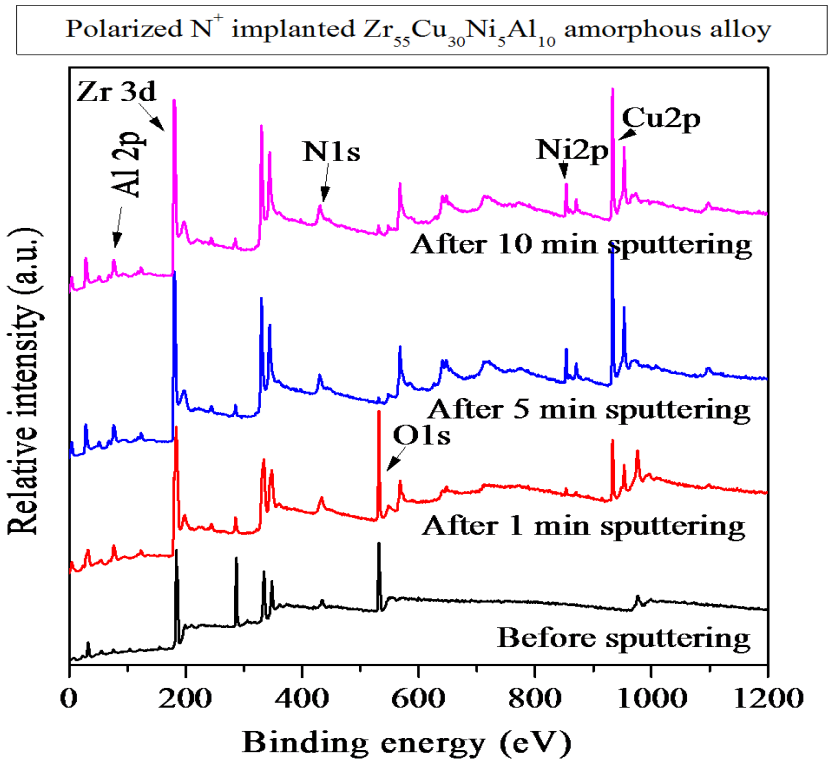

Figure 5.30: XPS survey scan of polarized N^+ implanted $Zr_{55}Cu_{30}Ni_5Al_{10}$ amorphous alloy at 1 x 10^{16} ions/cm^2 fluence in 1 M HNO_3 medium

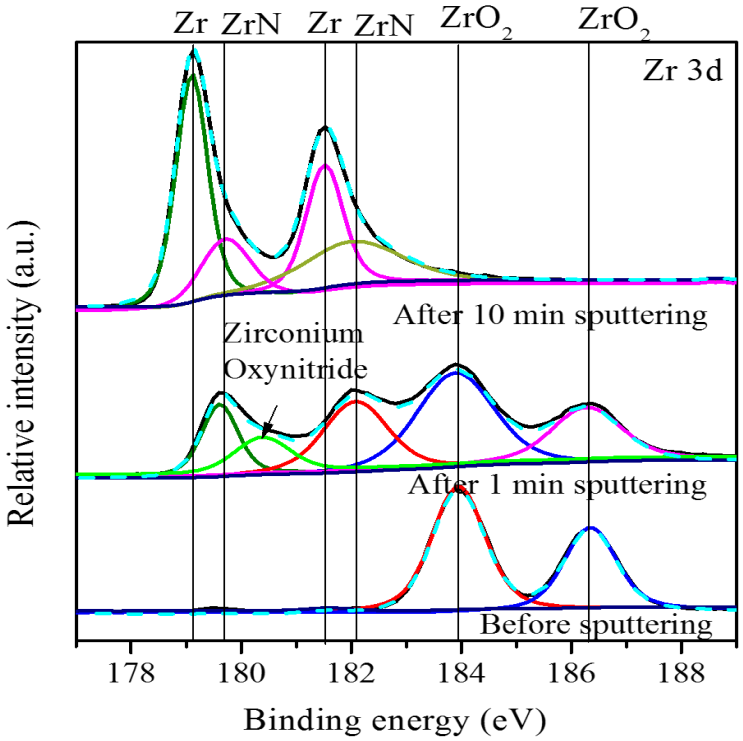

Figure 5.31: High resolution XPS peaks of polarized N^+ implanted $Zr_{55}Cu_{30}Ni_5Al_{10}$ amorphous alloy at 1 x 10^{16} ions/cm^2 fluence for Zr

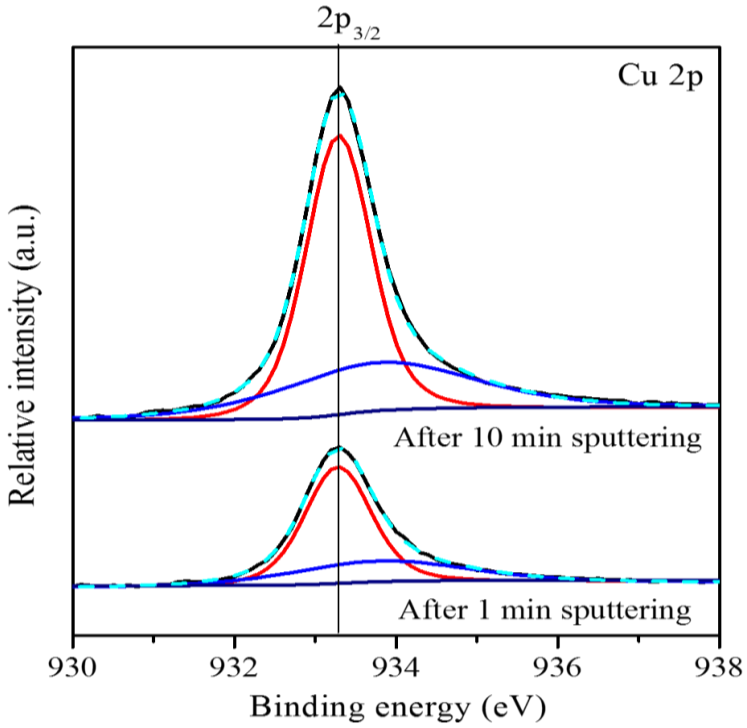

Figure 5.32: High resolution XPS peaks of polarized N^+ implanted $Zr_{55}Cu_{30}Ni_5Al_{10}$ amorphous alloy at 1 x 10^{16} ions/cm^2 fluence for Cu

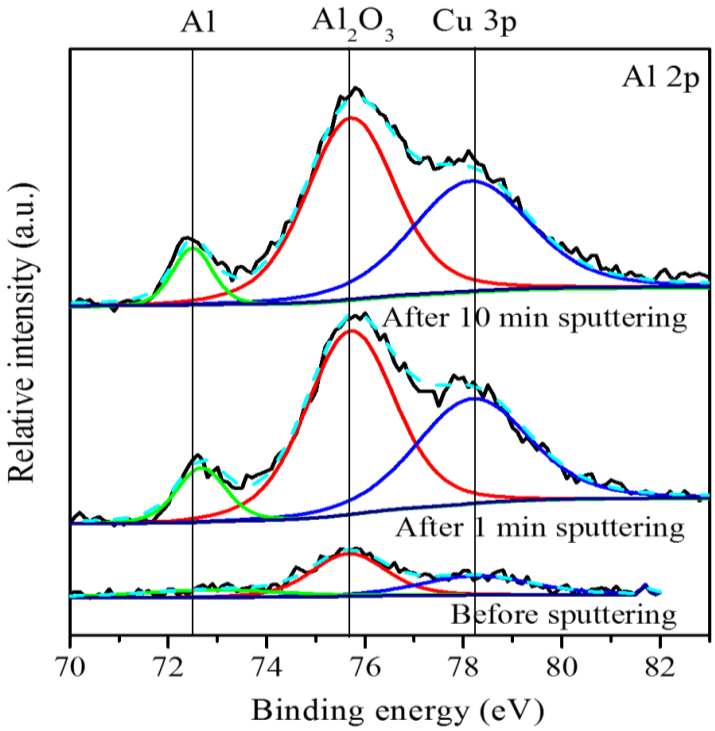

Figure 5.33: High resolution XPS peaks of polarized N^+ implanted $Zr_{55}Cu_{30}Ni_5Al_{10}$ amorphous alloy at 1 x 10^{16} ions/cm^2 fluence for Al

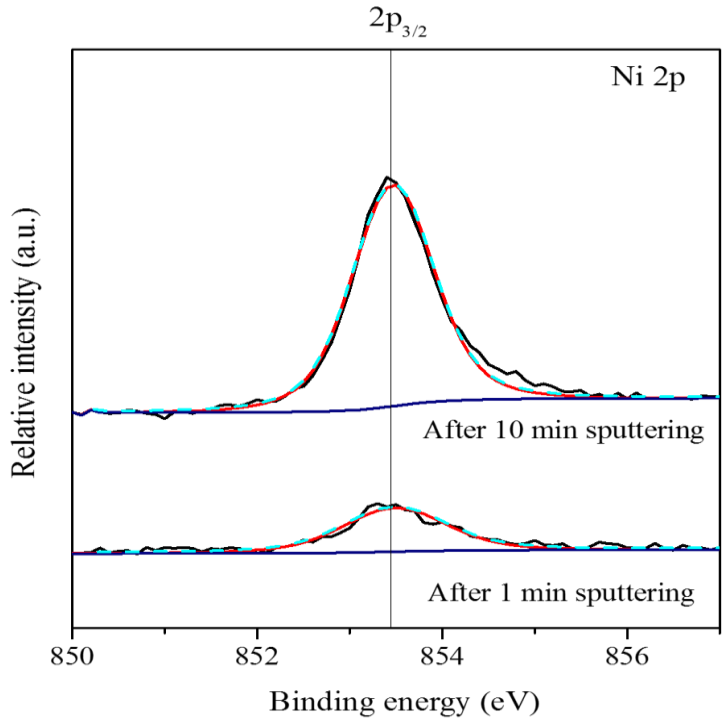

Figure 5.34: High resolution XPS peaks of polarized N^+ implanted $Zr_{55}Cu_{30}Ni_5Al_{10}$ amorphous alloy at 1 x 10^{16} ions/cm^2 fluence for Ni

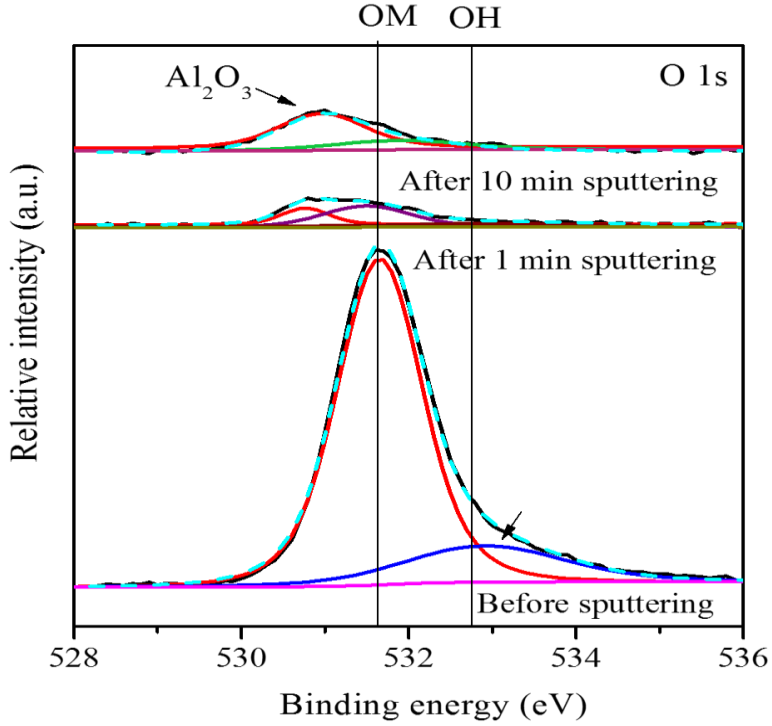

Figure 5.35: High resolution XPS peaks of polarized N^+ implanted $Zr_{55}Cu_{30}Ni_5Al_{10}$ amorphous alloy at 1 x 10^{16} ions/cm_2 fluence for O

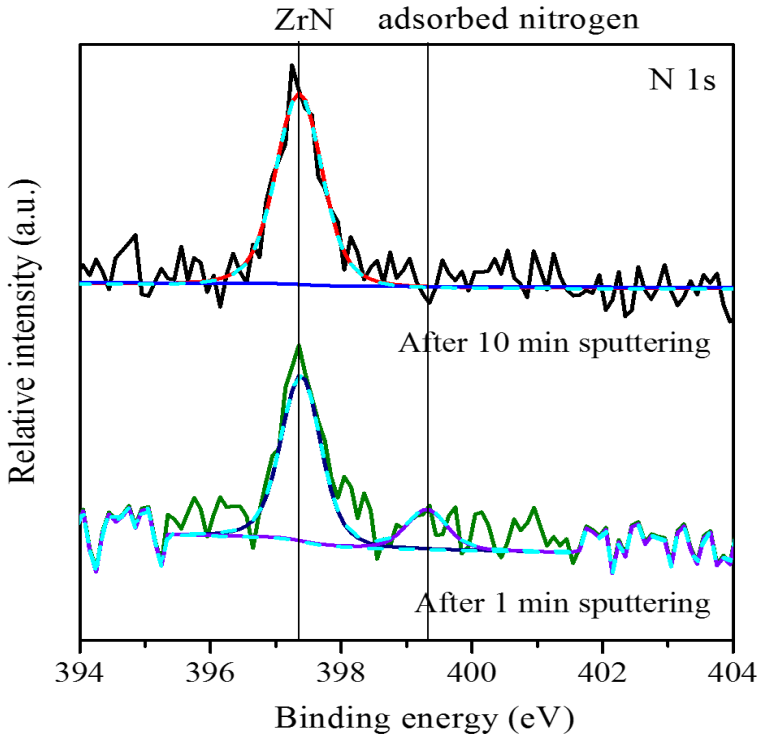

Figure 5.36: High resolution XPS peaks of polarized N^+ implanted $Zr_{55}Cu_{30}Ni_5Al_{10}$ amorphous alloy at 1 x 10^{16} ions/cm^2 fluence for N

The high resolution XPS spectra of each element Zr, Cu, Al, Ni, O and N are shown in figure 5.31, 5.32, 5.33, 5.34, 5.35 and 5.36, respectively. The XPS peak of Zr 3d doublet (figure 5.31) are observed at the binding energy 183.6 eV for Zr $3d_{5/2}$ and 185.8 eV for Zr $3d_{3/2}$ corresponding to ZrO_2 on the surface of the polarized sample. It is revealed that the N^+ ion implanted sample has been found to passivated in HNO_3 medium and formed ZrO_2 layer. After 1 min of sputtering, XPS spectra exhibited the presence of peak corresponding to ZrN and zircoinium oxynitride (at 180.6 eV binding energy) [179] along with ZrO_2. The Cu 2p peak (as shown in figure 5.32) was observed at 933.3 eV for Cu $2p_{3/2}$ corresponding to metallic Cu. The intensity of Cu 2p XPS peak was increased with sputtering time. The Al 2p spectrum (figure 5.33) of the surface of the polarized sample exhibited the presence of XPS peak at 75.6 eV corresponding to Al_2O_3 overlapped with the Cu 3p spectrum peak at 77.9 eV due to Cu $3p_{1/2}$ electrons. The presence of Al metallic peak was observed at 72.9 eV binding

energy after sputtering of the sample. The XPS peak of Ni 2p (figure 5.34) was not appeared on the surface of polarized sample due to minimum atomic concentration of Ni ion in the sample and the sample surface was mainly covered with the passive film of ZrO_2.. After sputtering for 1 min, Ni $2p_{3/2}$ peak was appeared at 853.4 eV binding energy indicating the presence of metallic Ni. The O 1s spectrum (figure 5.35), recorded for the surface of polarized sample, consisted of overlapping peaks originating from oxygen in metal-O-metal bond (at 531.4 eV), metal-OH bond and/or bound water (532.7 eV). One another XPS peak of O 1s corresponding to Al_2O_3 was located at 530.5 eV which was appeared after the sputtering of the sample. The peak corresponding to N 1s (figure 5.36) located at 397.3 eV corresponding to ZrN was appeared only after 1 min sputtering.

The XPS results recorded from the surface of polarized sample in 1 M HNO_3 medium revealed that the surface was mainly covered with the passive layer of ZrO_2. The presence of Al_2O_3 was also obtained on the surface of polarized sample. The heat of formation of CuO, ZrO_2, Al_2O_3 and NiO is -157.3 kJ/mol, -1100.6 kJ/mol, -1675.7 kJ/mol [201] and -314.8 kJ/mol [151], respectively. Hence, the formation of Al_2O_3 is energetically favored over that of ZrO_2, NiO and CuO. However, the formation of Al_2O_3 layer is difficult due to low surface binding energy and low atomic concentration of Al, hence Zr is preferentially oxidized instead of Al. The formation of ZrO_2 layer improves the corrosion resistance of the $Zr_{55}Cu_{30}Ni_5Al_{10}$ amorphous alloy in nitric acid medium, since it is a protective passive layer in acidic, alkaline and chloride solutions [51]. It has already been reported by many researchers that the formation of ZrN and ZrO_2 passive film during nitrogen implantation improves the corrosion resistance of Zr-Sn-Nb alloy in alkaline solution [188] as well as zircaloy-4 in NaCl medium [52,103,187]. The formation of oxynitrides during passivation also significantly enhances the stability of passive film [198]. Hence, in the present work, the formation of ZrN and ZrO_2 is attributed to the better corrosion resistance of nitrogen implanted samples in nitric acid medium.

5.2.4 Conclusion

The influence of N^+ ion implantation at 1 x 10^{16}, 5 x 10^{16} and 3 x 10^{17} ions/cm^2 fluences on the corrosion behavior of $Zr_{55}Cu_{30}Ni_5Al_{10}$ amorphous alloy in 1 M HNO_3 has been studied by potentiodynamic polarization tests. The following results have been obtained:

1. The nitrogen ion implantation on the $Zr_{55}Cu_{30}Ni_5Al_{10}$ amorphous alloy results in the formation of ZrN and ZrO_2 which was confirmed by GIXRD and XPS measurements and schematic representation of these results are shown in figure 5.37.
2. The improvement in corrosion resistance of the nitrogen implanted $Zr_{55}Cu_{30}Ni_5Al_{10}$ amorphous alloy in 1 M HNO_3 is attributed to the formation of ZrN, zirconium oxynitride and ZrO_2.
3. The enhancement in corrosion resistance of the $Zr_{55}Cu_{30}Ni_5Al_{10}$ amorphous alloy is obtained at lower fluence of nitrogen implantation.

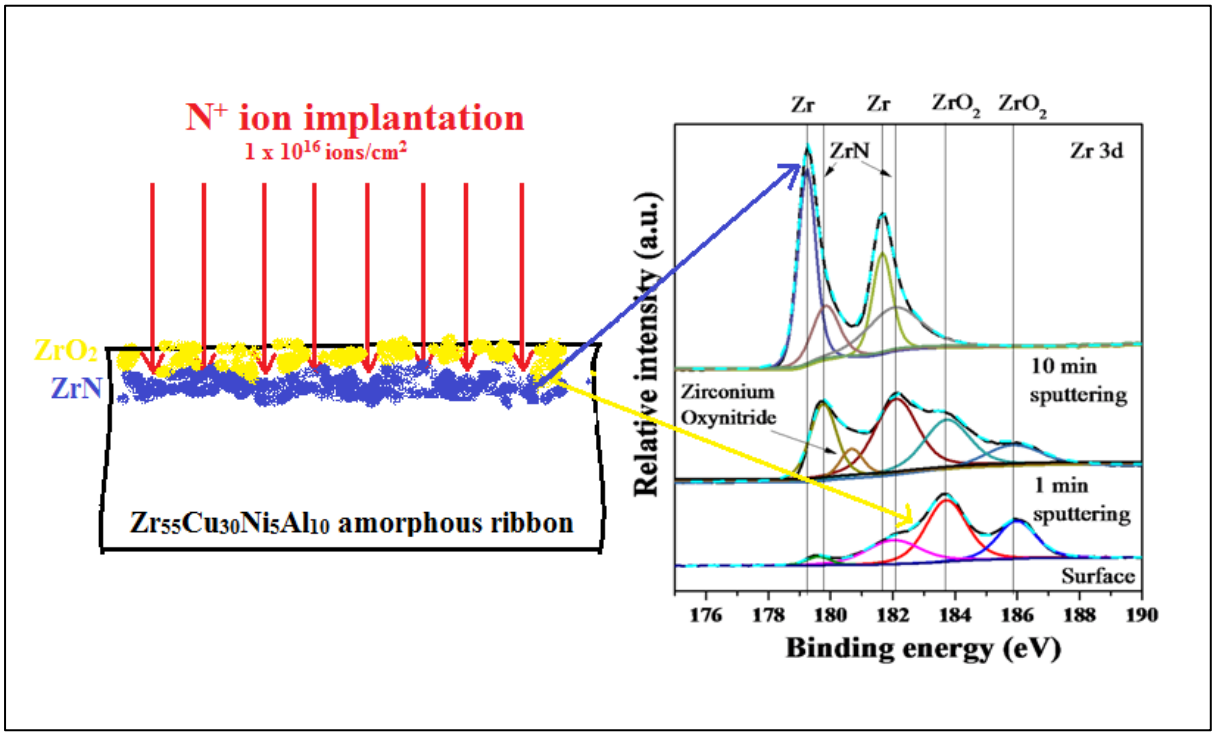

Figure 5.37: Schematic representation of chemical changes in the surface of $Zr_{55}Cu_{30}Ni_5Al_{10}$ amorphous alloy due to N^+ ion implantation

CHAPTER-6

Conclusions and Scope of Future Work

6.1 Conclusions

The work presented in the thesis deal with the study of corrosion behavior of some Zr-based bulk amorphous alloys and its surface modification using ion implantation technique. The potentiodynamic polarization and weight loss analysis methods were used to study the corrosion behavior of as-prepared and ion implanted Zr-based bulk amorphous alloys at room temperature. The high temperature corrosion studies were also carried out by weight loss analysis method. The bulk amorphous $Zr_{55}Cu_{30}Ni_5Al_{10}$ alloys were prepared in strip shape of dimensions 27 mm x 5 mm x 2 mm by copper mold casting system and ribbon shape of thickness of about 30 μm and width of about 7 mm by melt spinning system

The major conclusions of the research work carried out are divided into three parts:

6.1.1 Development of Zr-based amorphous alloys

The amorphous $Zr_{55}Cu_{30}Ni_5Al_{10}$ alloys were prepared in strip shape of dimensions 27 mm x 5 mm x 2 mm by copper mold casting system and ribbon shape of thickness about 30 μm and width about 7 mm by melt spinning system. The XRD pattern of these alloys exhibited the presence of broad hallow peak indicating the amorphous nature of the amorphous alloys.

6.1.2 Corrosion studies on as-prepared Zr-based amorphous alloys

The corrosion behavior of some Zr-based bulk amorphous alloys: $Zr_{55}Cu_{30}Ni_5Al_{10}$, $Zr_{60}Nb_2Cu_{20}Ni_8Al_{10}$, $Zr_{59}Nb_3Cu_{20}Ni_8Al_{10}$, $Zr_{57}Nb_5Cu_{20}Ni_8Al_{10}$, $Zr_{59}Ti_3Cu_{20}Ni_8Al_{10}$, $Zr_{57}Nb_5Cu_{15.4}Ni_{12.6}Al_{10}$ and $Zr_{60}Pd_5Cu_{15}Ni_{10}Al_{10}$ in 1 M, 6 M and 11.5 M HNO_3

media has been investigated by potentiodynamic polarization method at room temperature. To compare the corrosion behavior of strip and ribbon shape, the corrosion investigation on ribbon $Zr_{55}Cu_{30}Ni_5Al_{10}$, $Zr_{60}Nb_2Cu_{20}Ni_8Al_{10}$, $Zr_{59}Nb_3Cu_{20}Ni_8Al_{10}$, $Zr_{57}Nb_5Cu_{20}Ni_8Al_{10}$ and $Zr_{60}Pd_5Cu_{15}Ni_{10}Al_{10}$ amorphous alloys were also carried out in 1 M, 6 M and 11.5 M HNO_3 media at room temperature. The high temperature corrosion investigation on $Zr_{60}Pd_5Cu_{15}Ni_{10}Al_{10}$ and $Zr_{59}Nb_3Cu_{20}Ni_8Al_{10}$ amorphous alloys was carried out in boiling 11.5 M HNO_3 medium. The major findings of these investigations are listed below:

A. Corrosion investigations at room temperature

i. The results of electrochemical investigations revealed that Nb-containing Zr-based bulk amorphous alloy exhibits low value of corrosion current density among all investigated Zr-based bulk amorphous alloys in lower (1 M HNO_3), moderate (6 M HNO_3) and higher (11.5 M HNO_3) concentration of nitric acid media at room temperature. These results indicate that Nb-containing Zr-based bulk amorphous alloys possess better corrosion resistance among all the investigated alloys.

ii. The results of weight loss analysis also exhibited that Nb-containing Zr-based amorphous alloys show least corrosion rate among all investigated alloys in lower (1 M HNO_3), moderate (6 M HNO_3) and higher (11.5 M HNO_3) concentration of nitric acid media at room temperature.

iii. The comparison of bulk and ribbon shaped amorphous alloys in terms of their corrosion behavior revealed that the ribbon shaped amorphous alloys possess better corrosion resistance than bulk amorphous alloys.

iv. The optical micrographs and SEM micrographs of potentiodynamic polarized and immersed alloys in nitric acid medium exhibited the formation of oxide

pockets on the surface of treated alloys, which indicates the formation of inhomogenous passive film in nitric acid medium.

v. The XPS results confirmed the presence of ZrO_2, Al_2O_3 and Nb_2O_5 on the surface of immersed Nb-containing Zr-based amorphous alloy in nitric acid medium.

vi. The improved corrosion resistance of Nb-containing Zr-based bulk amorphous alloys was attributed to the formation of ZrO_2 and Nb_2O_5, which results in corrosion resistant property in nitric acid medium for these alloys.

B. Corrosion investigations at higher temperature

i. The corrosion resistance of Zr based amorphous alloys in boiling nitric acid environment was also investigated by weight loss analysis and results revealed that $Zr_{59}Nb_3Cu_{20}Ni_8Al_{10}$ amorphous alloy possess better corrosion resistance than Pd-containing $Zr_{60}Pd_5Cu_{15}Ni_{10}Al_{10}$ amorphous alloy.

ii. FE-SEM micrographs of $Zr_{59}Nb_3Cu_{20}Ni_8Al_{10}$ amorphous alloy, immersed in 11.5 M HNO_3 medium at boiling temperature, exhibited the origination of inhomogenous passive film in boiling nitric acid medium.

iii. XPS analysis of immersed sample in boiling HNO_3 medium exhibited the presence of ZrO_2, Al_2O_3 and Nb_2O_5 in the surface layer of immersed $Zr_{59}Nb_3Cu_{20}Ni_8Al_{10}$ amorphous alloy, which results in the better corrosion resistance of the alloy.

6.1.3 Corrosion studies on ion-implanted Zr-based amorphous alloys

The influence of O^+ ion implantation at the fluences of 1 x 10^{16}, 1 x 10^{17} and 3 x 10^{17} ions/cm^2 on the corrosion behavior of the bulk $Zr_{55}Cu_{30}Ni_5Al_{10}$ amorphous alloy in 0.5 M H_2SO_4, 1.0 M HNO_3 and in the mixture of 0.1 M NaCl and 0.5 M H_2SO_4 solution has been studied in the present research work. The influence of N^+ ion implantation at 1 x 10^{16}, 5 x 10^{16} and 3 x 10^{17} ions/cm^2 fluences on the corrosion

behavior of $Zr_{55}Cu_{30}Ni_5Al_{10}$ amorphous alloy in 1 M HNO_3 has been studied by potentiodynamic polarization tests.

A. Oxygen ion implantation

i. The GIXRD patterns showed the formation of $Cu_{10}Zr_7$ and ZrO_2 crystalline phases on the surface of O^+ implanted $Zr_{55}Cu_{30}Ni_5Al_{10}$ amorphous alloy.

ii. The formation of ZrO_2 layer on the surface of implanted alloy was confirmed by FE-SEM and XPS.

iii. The potentiodynamic polarization results revealed that corrosion resistance of the bulk $Zr_{55}Cu_{30}Ni_5Al_{10}$ amorphous alloy is improved in H_2SO_4 and H_2SO_4 + NaCl media after O^+ ion implantation due to the formation of the protective ZrO_2 layer. However, no improvement in corrosion resistance was observed in HNO_3 solution due the formation of $Cu_{10}Zr_7$ after O^+ ion implantation.

iv. Surface morphology of corroded specimen surface has also indicated the improvement in corrosion resistance of the as-cast $Zr_{55}Cu_{30}Ni_5Al_{10}$ amorphous alloy in H_2SO_4 and H_2SO_4 + NaCl solution after O^+ ion implantation.

v. The pitting resistance of bulk $Zr_{55}Cu_{30}Ni_5Al_{10}$ amorphous alloy was increased in H_2SO_4 + NaCl medium after O^+ ion implantation.

B. Nitrogen ion implantation

i. The nitrogen ion implantation on the $Zr_{55}Cu_{30}Ni_5Al_{10}$ amorphous alloy results into the formation of ZrN and ZrO_2 which was confirmed by GIXRD and XPS measurements.

ii. The improved corrosion resistance of the nitrogen implanted $Zr_{55}Cu_{30}Ni_5Al_{10}$ amorphous alloy in 1 M HNO_3 is attributed to the formation of ZrN, zirconium oxynitride and ZrO_2.

iii. The enhancement in corrosion resistance of the $Zr_{55}Cu_{30}Ni_5Al_{10}$ amorphous alloy is obtained at lower fluence of nitrogen implantation.

6.2 Scope of the future work

Based on the experimental work and the results obtained in the present investigations, there is a wide scope for doing future studies on related topics:

- GFA of any glassy system plays important role in development of glassy alloys. So identification and addition of different elements can be made by checking them for improved GFA and critical diameter of alloys.
- Fabrication of glassy alloys of a large critical diameter is very difficult and welding of BMG with different materials such as stainless steel (SS), Ti etc. also creates crystalline phases in welded zone, so coating of BMGs could be proposed as an option for making bigger instruments or samples for engineering applications.
- A detailed comparative study may be useful on ribbon and rod shaped Zr-based bulk amorphous alloys to enhance the database and their uses for different applications.
- In the present investigation, the ion implantation was carried out only on $Zr_{55}Cu_{30}Ni_5Al_{10}$ amorphous alloy due to high GFA of this Zr-based amorphous alloy, it will be interesting to study the effect of ion beam implantation on corrosion behavior of some other important Zr-based amorphous alloys having potential applications.
- In the present investigation, the corrosion behaviour of N^+ ion implanted $Zr_{55}Cu_{30}Ni_5Al_{10}$ amorphous alloy in HNO_3 medium has been studied. It may worth finding the corrosion behaviour of this alloy in other different aqueous media as well, which has not been studied so far, such as HCl, H_2SO_4, H_2SO_4 + NaCl, Na_2SO_4 etc.
- The corrosion investigation on ion implanted Zr-based bulk amorphous alloys at high temperature will be useful to find out the suitability of the material for withstanding

the severe conditions of high temperature and its sustainability in these conditions for applications in nuclear industries.

REFERENCES

[1] H. Vogel, “The Law of the Relationship between Viscosity of Liquids and the Temperature,” Phys. Z., 22, 645–646, (1921).

[2] D. R. Uhlmann and H. Yinnon, “Glass Science and Technology” Vol. 1, ‘Glass Forming Systems’, Academic Press, New York, (1983).

[3] C. S. Ray, S. T. Reis, R. K. Brow, W. Holand and V. Rheinberger, ‘A New DTA Method for Measuring Critical Cooling Rate for Glass Formation’, J. Non-Cryst. Solids, 351, 1350-1358, (2005).

[4] C. V. Thompson and F. Spaepen, “On the Approximation of Free Energy Change on Crystallization”, Acta Metall., 27, 1855–1859, (1979).

[5] D. Turnbull, “Metastable Structures in Metallurgy”, Metall. Trans. B, 12, 217-230, (1981).

[6] W.H. Wang, C. Dong and C.H. Shek, “Bulk metallic glasses” Mater. Sci. Eng. R, 44, 45-89, (2004).

[7] A. T. Patel, H. R. Shevde and A. Pratap, “Thermodynamics of $Zr_{52.5}Cu_{17.9}Ni_{14.6}Al_{10}Ti_5$ Bulk Metallic Glass Forming Alloy”, J. Therm. Anal. Calorim., 107, 167-170, (2012).

[8] A. T. Patel, H. R. Shevde and A. Pratap, “Thermodynamic Study of Bulk Metallic Glass: $Zr_{57}Cu_{15.4}Ni_{12.6}Al_{10}Nb_5$”, J. Sci. Technol. Manag., 3, 9-12, (2011).

[9] R. Busch, J. Schroers, and W.H. Wang, “Thermodynamics and Kinetics of Bulk Metallic Glass”, MRS Bull., 32, 620-623 (2007).

[10] D.R. Uhlmann, “A Kinetic Treatment of Glass Formation”, J. Non-Cryst. Solids, 7, 337-348, (1972).

[11] C. A. Angell, “Formation of Glasses From Liquids and Biopolymers”, Science, 267, 1924-1935, (1995).

[12] D. Turnbull, “Under What Conditions Can A Glass Be Formed?”, Contemp. Phys., 10, 473-488, (1969).

[13] Z. P. Lu, Y. Li and S. C. Ng, “Reduced Glass Transition Temperature and Glass Forming Ability of Bulk Glass Forming Alloys”, J. Non-Cryst. Solids, 270, 103-114, (2000).

[14] W. Chen, Y. Wang , J. Qiang and C. Dong, “Bulk Metallic Glasses in The Zr-Al-Ni-Cu System”, Acta Mater., 51, 1899–1907, (2003).

[15] A. Inoue, “Bulk Amorphous Alloys”, Switzerland: Trans. Tech. Publication Ltd. Zurich (1998).

[16] S. R. Nagel and J. Taue, “Nearly-Free-Electron Approach to the Theory of Metallic Glass Alloys”, Phys Rev Lett., 35, 380-383, (1975).

[17] P. Haussler, “Interrelations Between Atomic and Electronic Structures—Liquid And Amorphous Metals as Model Systems”, Phys. Rep., 222, 65-143, (1992).

[18] C. H. Shek, Y. M. Wang and C. Dong, “The E/A-Constant Hume- Rothery Phases in An As-Cast $Zr_{65}Al_{7.5}Ni_{10}Cu_{17.5}$ Alloy”. Mater. Sci. Eng. A, 291, 78–85, (2000).

[19] Y. M. Wang, C. H. Shek, J. B. Qiang, C. H. Wong, Q. Wang, X. Zhang and C. Dong, “The e/a Criterion for the Largest Glass-Forming Abilities of the Zr-Al-Ni(Co) Alloys”, Mater. Trans., 45, 1180-1183, (2004).

[20] L. Greer, “Metallic glasses” Fifth Edition, Elsevier B.V. Publication UK , (2014).

[21] J. D. Bernal, “Geometry of The Structure of Monatomic Liquids”, Nature, 185, 68-70, (1960).

[22] J. D. Bernal, “The Bakerian Lecture, 1962 The Structure of Liquids”, Proc. R. Soc. A, 280, 299-322, (1964).

[23] P. H. Gaskell, “A New Structural Model for Amorphous Transition Metal Silicides, Borides, Phosphides and Carbides”, J. Non Cryst. Solids, 32, 207–224, (1979).

[24] D. B. Miracle, “A Structural Model for Metallic Glasses”, Nat. Mater., 3, 697–702, (2004).

[25] H. W. Sheng, W. K. Luo, F. M. Alamgir, J. M. Bai and E. Ma, “Atomic Packing and Short-To-Medium- Range Order in Metallic Glasses”, Nature, 439, 419-425 (2006).

[26] B. J. Yang, J. H. Yao, J. Zhang, H. W. Yang, J. Q. Wang and E. Ma, “Al-rich bulk metallic glasses with plasticity and ultrahigh specific strength”, Scripta Mater., 61, 423–426, (2009).

[27] B. J. Yang, J. H. Yao, Y. S. Chao, J. Q. Wang and E. Ma, “Developing aluminum-based bulk metallic glasses”, Philosophical Magazine, 90, 3215–3231, (2010).

[28] W. Klement, R. H. Willens and P. Duwez, “Non-Crystalline Structure in Solidified Gold-Silicon Alloys”, Nature, 187, 869-870, (1960).

[29] H. S. Chen, “Thermodynamic Considerations on the Formation and Stability of Metallic Glasses”, Acta Metall., 22, 1505–1511, (1974).

[30] H. Libermann and C. Graham,“Production of Amorphous Alloy Ribbons and Effects of Apparatus Parameters on Ribbon Dimensions”, IEEE Trans. Magn., 12, 921-923, (1976).

[31] H.W. Kui, A. L. Greer and D. Turnbull, “Formation of Bulk Metallic Glass by Fluxing”, Appl. Phys. Lett., 45, 615-616, (1984).

[32] A. Inoue, T. Zhang and T. Masumoto, “Al-La-Ni Amorphous Alloys with a Wide Supercooled Liquid Region”, Mater. Trans. JIM, 30, 965-972, (1989).

[33] A. Inoue, A. Kato, T. Zhang, S.G. Kim and T. Masumoto, “Mg–Cu–Y Amorphous Alloys with High Mechanical Strengths Produced by a Metallic Mold Casting Method”, Mater Trans JIM., 32, 609-616, (1991).

[34] T. Zhang, A. Inoue and T. Masumoto, “Amorphous Zr-Al-TM (TM=Co,Ni,Cu) Alloys with Significant Supercooled Liquid Region of Over 100 K”, Mater Trans JIM., 32, 1005-1010, (1991).

[35] Eugen Axinte, “Metallic Glasses From ‘Alchemy’ To Pure Science. Present and Future of Design, Processing and Applications of Glassy Metals”, Mater. Des., 35, 518–556, (2012).

[36] A. Inoue, “Stabilization of Metallic Supercooled Liquid and Bulk Amorphous Alloys”, Acta Mater., 48, 279-306, (2000).

[37] A. Inoue and A. Takeuchi, “Recent Progress in Bulk Glassy, Nanoquasicrystalline and Nanocrystalline Alloys”, Mater. Sci. Eng. A, 375–377, 16-30, (2004).

[38] J. F. Loffler, Bulk Metallic Glasses”, Intermetallics, 11, 529-540, (2003).

[39] M.L. Morrisona, R.A. Buchanan, A. Peker, W.H. Peter, J.A. Horton and P.K. Liaw, “Cyclic-Anodic-Polarization Studies of A $Zr_{41.2}Ti_{13.8}Ni_{10}Cu_{12.5}Be_{22.5}$ Bulk Metallic Glass” Intermetallics, 12, 1177–1181, (2004).

[40] W. L. Johnson, “Bulk Glass-Forming Metallic Alloys: Science and Technology”, MRS Bull., 24, 42-56, (1999).

[41] A. H. Brothers and D. C. Dunand, “Syntactic bulk metallic glass foam”, Appl. Phys. Lett., 84, 1108-1110, (2004).

[42] J. B. Park, “Biomaterials: Introduction. In The Biomedical Engineering” Handbook; CRC Press: Boca Raton, FL, USA, Vol. 1, (2000).

[43] J. Jayaraj, D. N. G. Krishna, C. Mallica and U. K. Mudali, “Passive Film Properties and Corrosion Behavior of Ni-Nb and Ni-Nb-Ta Amorphous Ribbons in Nitric Acid and Fluorinated Nitric Acid Environments”, Mater. Chem. Phys., 151, 318-329, (2015).

[44] C. Qin, K. Asami, H. Kimura, W. Zhang, D. Louzguine, and A. Inoue, “High Corrosion Resistant Ni-Based Glassy Alloys in Boiling Nitric Acid Solutions”, Mater. Trans., 50, 1304-1307, (2009).

[45] J. Jayaraj, A. Ravishankar and U. K. Mudali, “Electrochemical and Passive Characterization of A Beta Type $Ti_{45}Zr_{38}Al_{17}$ Cast Rod in Nitric Acid Medium” J. Electrochimica Acta, 85, 210-219, (2012).

[45] A.T. Motta, F. Lefebvre and C. Lemaignan, Proc. 9th Int. Symp. on “Zirconium in Nuclear Industry”, ASTM-STP 1132, eds. C.M. Eucken and A.M. Garde (ASTM, Philadelphia) 718-739, (1991).

[47] Y. Li, W. Zhang, F. Qin and A. Makino, “Mechanical Properties and Corrosion Resistance of A New $Zr_{56}Ni_{20}Al_{15}Nb_4Cu_5$ Bulk Metallic Glass with A Diameter up to 25 mm”, J. Alloy Compd., 615, S71-S74, (2014).

[48] T. C. Chieh, J. Chu, C. T. Liu and J. K. Wu, “Corrosion of $Zr_{52.5}Cu_{17.9}Ni_{14.6}Al_{10}Ti_5$ Bulk Metallic Glasses in Aqueous Solutions”, Mater. Lett., 57, 3022-3025, (2003).

[49] A. Dhawan, S. Roychowdhury, P. K. De and S. K. Sharma, “Potentiodynamic Polarization Studies on Bulk Amorphous Alloys and $Zr_{46.75}Ti_{8.25}Cu_{7.5}Ni_{10}Be_{27.5}$ and $Zr_{65}Cu_{17.5}Ni_{10}Al_{7.5}$”, J. Non-Cryst. Solids, 351, 951-955, (2005).

[50] B. Raj, and U. K. Mudali, “Materials Development and Corrosion Problems in Nuclear Fuel Reprocessing Plants”, Prog.Nucl. Energy, 48, 283–313, (2006).

[51] B. Lustman and F. Kerze, “The Metallurgy of Zirconium”, Jr. (eds.) Mc Graw Hill Book Co., New York, USA (1955).

[52] W. Kim, K. S. Jung, B. H. Choi, H. S. Kwon, N. J. Lee, J.G. Han, M. I. Guseva and M. V. Atamanov, “Corrosion Behavior of Nitrogen-Implanted Zircaloy”, Surf. Coat. Tech., 76-77, 595-599, (1995).

[53] A. Inoue, T. Zhang and T. Masumoto, “Zr–Al–Ni Amorphous Alloys with High Glass Transition Temperature and Significant Supercooled Liquid Region”, Mater. Trans. JIM, 31, 177-183, (1990).

[54] A. Peker and W. L. Johnson, “A Highly Processable Metallic Glass: $Zr_{41.2}Ti_{13.8}Cu_{12.5}Ni_{10.0}Be_{22.5}$”, Appl Phys Lett., 63, 2342-2344, (1993).

[55] A. Inoue, T. Shibata and T. Zhang, “Effect of Additional Elements on Glass Transition Behavior and Glass Formation Tendency of Zr-Al-Cu-Ni Alloys”, Mater. Trans. JIM, 36, 1420–1426, (1995).

[56] K. Jin and J. F. Loffler, “Bulk Metallic Glass Formation in Zr–Cu–Fe–Al Alloys”, Appl. Phys. Lett., 86, 241909:1-3, (2005).

[57] Q. S. Zhang, W. Zhang and A. Inoue, “Preparation of $Cu_{36}Zr_{48}Ag_8Al_8$ Bulk Metallic Glass with a Diameter of 25 mm by Copper Mold Casting”, Mater. Trans. JIM, 48, 629–631, (2007).

[58] A. Inoue and A. Takeuchi, “Recent Development and Application Products of Bulk Glassy Alloys”, Acta Mater., 59, 2243-2267, (2011).

[59] A Inoue and T Zhang, “Fabrication of Bulk Glassy $Zr_{55}Al_{10}Ni_5Cu_{30}$ Alloy of 30 mm in Diameter by A Suction Casting Method”, Mater. Trans., 37, 185-187, (1996).

[60] A. Inoue, T. Zhang, N. Nishiyama, K. Ohba and T. Masumoto, “Preparation of 16 mm Diameter Rod of Amorphous $Zr_{65}Al_{7.5}Ni_{10}Cu_{17.5}$ Alloy”, Mater. Trans., 34, 1234-1237, (1993).

[61] Y. J. Sun, D. D. Qu, Y. J. Huang, K. D. Liss, X. S. Wei, D. W. Xing and J. Shen, “Zr–Cu–Ni–Al Bulk Metallic Glasses with Superhigh Glass-Forming Ability”, Acta Mater., 57, 1290–1299, (2009).

[62] M. Telford, “The case of bulk metallic glasses”, Materials Today, 7, 36-43, (2004).

[63] N. Hua and W. Chen, “Enhancement of Glass-Forming Ability and Mechanical Property of Zr Based Zr-Al-Ni Bulk Metallic Glasses with Addition of Pd”, J. Alloys Compd., 693, 816-824, (2017).

[64] A. Gebert, K. Buchholz, A. Leonhard, K. Mummert, J. Eckert and L. Schultz, “Investigations on The Electrochemical Behaviour of Zr-Based Bulk Metallic Glasses”, Mater. Sci. Eng. A, 267, 294-300, (1999).

[65] S. Pang, T. Zhang, H. Kimura, K. Asami and A. Inoue, “Corrosion Behaviour of Zr-(Nb)-Al-Ni-Cu Glassy Alloy”, Mater. Trans. JIM, 41, 1490-1494, (2000).

[66] W. H. Peter, R. A. Buchanan, C. T. Liu, P. K. Liaw, M.L. Morrison, J. A. Horton, C. A. Carmichael Jr. and J. L. Wright, “Localized Corrosion Behavior of A Zirconium-Based Bulk Metallic Glass Relative to its Crystalline State”, Intermetallics, 10, 1157-1162, (2002).

[67] V. R. Raju, U. Kuhn, U. Wolff, F. Schneider, J. Eckert, R. Reiche and A. Gebert, "Corrosion Behaviour of Zr-Based Bulk Glass-Forming Alloys Containing Nb or Ti", Mater. Lett., 57, 173-177, (2002).

[68] F. X. Qin, H. F. Zhang, P. Chen, F. F. Chen, D. C. Qiao and Z. Q. Hu, "Corrosion Behavior of Bulk Amorphous $Zr_{55}Al_{10}Cu_{30}Ni_{5-X}Pd_x$ Alloys", Mater. Lett., 58, 1246-1250, (2004).

[69] U. K. Mudali , S. Scudino, U. Kuhn , J. Eckert and A. Gebert, "Polarisation Behaviour of The $Zr_{57}Ti_8Nb_{2.5}Cu_{13.9}Ni_{11.1}Al_{7.5}$ Alloy in Different Microstructural States in Acid Solutions", Scripta Mater., 50, 1379-1384, (2004).

[70] U. K. Mudali, S. Baunack , J. Eckert , L. Schultz and A. Gebert, "Pitting Corrosion of Bulk Glass-Forming Zirconium-Based Alloys", J. Alloys Compds., 377, 290-297, (2004).

[71] K. Mondal, B. S. Murty and U. K. Chatterjee, "Electrochemical Behavior of Multicomponent Amorphous and Nanocrystalline Zr-Based Alloys in Different Environments", Corros. Sci., 48, 2212-2225, (2006).

[72] N. Homazava, A. Shkabko, D. Logvinovich, U. Krahenbuhl and A. Ulrich, "Element-Specific in Situ Corrosion Behavior of Zr–Cu–Ni–Al–Nb Bulk Metallic Glass in Acidic Media Studied using A Novel Microcapillary Flow Injection Inductively Coupled Plasma Mass Spectrometry Technique", Intermetallics, 16, 1066-1072, (2008).

[73] N. Padhy, S. Ningshen and U. K. Mudali, "Electrochemical and Surface Investigation of Zirconium Based Metallic Glass $Zr_{59}Ti_3Cu_{20}Al_{10}Ni_8$ Alloy in Nitric Acid and Sodium Chloride Media", J. Alloys Compd., 503, 50-56, (2010).

[74] M. H. Pourgashti, E. Marzbanrad and E. Ahmadi, "Corrosion Behavior of $Zr_{41.2}Ti_{13.8}Ni_{10}Cu_{12.5}Be_{22.5}$ Bulk Metallic Glass in Various Aqueous Solutions", Mater. Des., 31, 2676-2679, (2010).

[75] A. Kawashima, K. Ohmura, Y. Yokoyama and A. Inoue, "The Corrosion Behaviour of Zr-based Bulk Metallic Glasses in 0.5 M NaCl Solution", Corros. Sci., 53, 2778-2784, (2011).

[76] S. Ningshen, U. K. Mudali, R. Krishnan and B. Raj, “Corrosion Behavior of Zr-based Metallic Glass Coating on Type 304L Stainless Steel by Pulsed Laser Deposition Method”, Surf. Coat. Technol., 205, 3961–3966, (2011).

[77] L. Mihaylov, L. Lyubenova, Ts. Gerdjikov, D. Nihtianova and T. Spassov, “Selective Dissolution of Amorphous Zr–Cu–Ni–Al Alloys”, Corros. Sci., 94, 350–358, (2015).

[78] H. F. Tian, J. W. Qiao, H. J. Yang, Y. S. Wang, , P. K. Liaw and A. D. Lan, “The Corrosion Behavior of In-Situ Zr-Based Metallic Glass Matrix Composites in Different Corrosive Media”, Appl. Surf. Sci., 363, 37–43, (2016).

[79] L. Yu, J. Tang, J. Qiao, H. Wang, Y. Wang, M. Apreutesei, M. Chamas and M. Duan, “Effect of Yttrium Addition on Corrosion Resistance of Zr-Based Bulk Metallic Glasses in Nacl Solution”, Int. J. Electrochem. Sci., 12, 6506 – 6519, (2017).

[80] U. K. Mudali, R. K. Dayal and J. B. Gnanamoorthy, “Corrosion Studies on Materials of Construction for Spent Nuclear Fuel Reprocessing Plant Equipment”, J. Nucl. Mater., 203, 73-82, (1993).

[81] T. Yamamoto, S. Tsukui, S. Okamoto, T. Nagai, M. Takeuchi, S. Takeda and Y. Tanaka, “Gamma-Ray Irradiation Effect on Corrosion Rates of Stainless Steel, Ti and Ti-5Ta in Boiling 9N Nitric Acid”, J. Nucl. Mater., 228, 162-167, (1996).

[82] A. Ravishankar, V. R. Raju, M. N. Rao, U. K. Mudali, H. S. Khatak and B. Raj, “Corrosion Of Zircaloy-4 And its Welds in Nitric Acid Medium”, Corros. Sci., 47, 3527-3538, (2007).

[83] C. Qin, K. Asami, H. Kimura, W. Zhang and A. Inoue, “Surface Characteristics of High Corrosion Resistant Ni–Nb–Zr–Ti–Ta Glassy Alloys for Nuclear Fuel Reprocessing Applications”, Electrochem. Commun., 10, 1408–1410, (2008).

[84] C. Qin, K. Asami, H. Kimura, W. Zhang and A. Inoue, “Electrochemical and XPS Studies of Ni-Based Metallic Glasses in Boiling Nitric Acid Solutions”, Electrochimica Acta., 54, 1612-1617, (2009).

[85] R. Mythili, S. Saroja and M. Vijayalakshmi, “Characterization of Passive Oxide Film on a Ti–5%Ta–1.8%Nb Alloy on Exposure to Severe Oxidizing Conditions”, Mater Charact., 61, 1326 – 1334, (2010).

[86] J. Jayaraj, K. Thyagarajan, C. Mallika, and U. K. Mudali, “Corrosion Behavior of Zirconium, Titanium, and their Alloys in Simulated Dissolver Solution of Fast Breeder Reactor Spent Nuclear Fuel using Zircaloy-4 Mock-Up Dissolver Vessel”, Nucl. Technol., 191, 58-70, (2015).

[87] J. Zhang, Y. Hu, L. Tu, F. Sun, M. Yao and B. Zhou, “Corrosion Behavior and Oxide Microstructure of Zr-1Nb-xGe Alloys Corroded in 360◦C/18.6 MPa Deionized Water”, Corros. Sci., 102, 161-167, (2016).

[88] J. Jayaraj, P. Krishnaveni, D. Nanda Gopala Krishna, C. Mallika and U. K. Mudali, “Corrosion Investigations on Zircaloy-4 and Titanium Dissolver Materials for MOX Fuel Dissolution in Concentrated Nitric Acid Containing Fluoride Ions”, J. Nucl. Mater., 473, 157-166, (2016).

[89] N. Kawasegi, N. Morito, S. Yamada, N. Takano, T. Oyama, K. Ashida, J. Taniguchi, I. Miyamotu, S. Momoto and H. O fune, “Rapid Nanopatterning of A Zr Based Metallic Glass Surface Utilizing Focused Ion Beam Induced Selective Etching”, Appl. Phy. Lett., 89, 143115 1-3, (2006).

[90] S. Nagata, S. Higashi, B. Tsuchiya, K. Toh, T. Shikama, K. Takahiro, K. Ozaki, K. Kawatusra, S. Yamamoto and A. Inouye, “Ion Irradiation Effects on Amorphization and Thermal Crystallization in Zr–Al–Ni–Cu Alloys”. Nucl. Instr. Meth. Phys. Res. B, 257, 420-423, (2007).

[91] M Iqbal, J. I. Akhter, Z. Q. Hu, H. F. Zhang, A. Qayyum and W. S. Sun, “Mechanical Properties and Ion Irradiation of Bulk Amorphous $Zr_{55}Cu_{30}Al_{10}Ni_5$ Alloy”, J. Non-Cryst. Solids, 353, 2452-2458, (2007).

[92] P. Tao, Y.Z.Yang, X. J. Bai, Z. X. mu, G. Q. Li, Z. W. Xie and X. C. Chen, “Study on Implantation of Co Ions in ZrCuNiAl Bulk Metallic Glass”, Surf. Coat. Tech., 203, 1656-1659, (2009).

[93] P. J. Tao, Y. Z. Yang, Z. X. Mu, X. C. Chen and Z. W. Xie, “Influences of Ion Implantation on Non-Isothermal Crystallization Behaviors of Bulk Metallic Glass”, J. Alloy Compd., 479, 736-740, (2009).

[94] J. Carter, E.G. Fu, M. Martin, G. Xie, X. Zhang, Y.Q. Wang, D. Wijesundera, X.M. Wang, W.K. Chu, S. M. McDeavitt and L. Shao, “Ion Irradiation Induced Nanocrystal Formation in Amorphous $Zr_{55}Cu_{30}Al_{10}Ni_5$ Alloy”, Nucl. Instr. Meth. Phys. Res B, 267, 2827-2831, (2009).

[95] J. Cao, H.Y. Chen, X.G. Song, J.K. Liu and J.C. Feng, “Effects of Ar Ion Irradiation on The Diffusion Bonding Joints of $Zr_{55}Cu_{30}Ni_5Al_{10}$ Bulk Metallic Glass to Aluminum Alloy”, J. Non-Cryst. Solids, 364, 53-56, (2013).

[96] H. Chen, J. Cao, X.Song, J. Qi and J. Feng, “Effect of Ion Beam Irradiation Surface Treatment on Solid State Bonding of Zr-Based Bulk Metallic Glass to Pure Copper”, Indian J. Pure Appl. Phy. 52, 162-165 (2014).

[97] D. Krupa, J. Baszkiewicz, J. Kozubowski, A. Barcz, G. Gawlik, J. Jagielski and B. Larisch, “Effect of Oxygen Implantation upon the Corrosion Resistance of the OT-4-0 Titanium Alloy”, Surf. Coat. Tech., 96, 223-229, (1997).

[98] S. Ningsen, U. K. Mudali, P. Mukherjee, A. Sarkar, P. Barat, N. Padhy and B. Raj, “Influence of Oxygen Ion Irradiation on The Corrosion Aspects of Ti-5%Ta-2%Nb Alloy and Oxide Coated Titanium”, Corros. Sci., 50, 2124-2134, (2008).

[99] S. Ningsen, U. K. Mudali, P. Mukherjee, P. Barat and B. Raj, “Oxygen Ion Irradiation Effect on Corrosion Behavior of Titanium in Nitric Acid Medium”, J. Nucl. Mater., 408, 1-6, (2011).

[100] S. Venkatraman, M. R. Nair, D. C. Kothari and K. B. Lal, R. Raman, "Anodic Polarization Behaviour of Ion Implanted Aluminium in 3.5 Wt.% NaCl Electrolyte", NIM Phy. Res. B, 19/20, 241-246, (1987).

[101] T. D. Radjabov, "Improvement of the Corrosion Properties of Metals by Ion Implantation", Vacuum, 38, 979-985, (1988).

[102] D. Krupa, E. Jezierska, J. Baszkiewicz, M. Kamifiski, T. Wierzchofi and A. Barcz, "Effect of Nitrogen Ion Implantation on the Structure and Corrosion Resistance of OT-4-0 Titanium Alloy", Surf. Coat. Tech., 79, 240-245, (1996).

[103] G. Tang, B. H. Choi, W. Kim, K. S. Jung, H.S. Kwon , S. J. Lee, J. H. Lee, T. Y. Song, D. H. Shon and J. G. Han, "The Characteristics of Surface Oxidation and Corrosion Resistance Of Nitrogen Implanted Zircaloy-4", Surf. Coat. Tech., 89, 252-257, (1997).

[104] U. K. Mudali, T. Sundararajan, K.G.M. Nair, R. K. Dayal, "Pitting and Intergranular Corrosion Resistance of Nitrogen Ion Implanted Type 304 Stainless Steel", Mater. Sci. Forum, 318-320, 531-538, (1999).

[105] S. J. Lee, C. J. Park, H. S. Kwon and B. H. Choi, "Corrosion Resistance of Nitrogen-Implanted Zircaloy-4 in High-Temperature Water", J. Nucl. Mater., 282, 223-231, (2000).

[106] N. Padhy, S. Ningshen, B.K. Panigrahi and U. K. Mudali, "Corrosion Behaviour of Nitrogen Ion Implanted AISI Type 304L Stainless Steel in Nitric Acid Medium", Corros. Sci., 52, 104-112, (2010).

[107] H. Savaloni, K. Khojier, S. Torabi, "Influence of N^+ Ion Implantation on the Corrosion and Nano-Structure of Ti Samples", Corros. Sci., 52, 1263–1267, (2010).

[108] S. Mathur, R. Vyas, R. Jain, P. Kumar, K. Sachdev, S. K. Sharma "Effect of Ion Beam Irradiation on The Corrosion Behavior of the Melt-Spun Ribbon $Ti_{60}Ni_{40}$", J. Non-Cryst. Solids, 357, 966-969, (2011).

[109] M.G Fontana, “Corrosion Testing”, 3rd Edn., ‘Corrosion Engineering’, Tata Mc. Graw-Hill, New York, NY, (2005).

[110] E. Protopopoff and P. Marcus, “Potential Measurements with Reference Electrodes”, ‘Corrosion: Fundamentals, Testing, and Protection’, Vol. 13A, ASM Handbook, ASM International, 13-16, (2003).

[111] J. R. Scully and R. G. Kelly, “Methods for Determining Aqueous Corrosion Reaction Rates, Corrosion: Fundamentals, Testing, and Protection”, Vol 13A, ASM Handbook, ASM International, USA ISBN: 0-87170-705-5, 68–86, (2003).

[112] ASM Metals Handbook: Volume 13, “Corrosion” ASM International 584, USA ISBN 0-87170-007-7 (v.1) (1987).

[113] G. K. Robert, J. R. Scully, D. W. Shoesmith and R. G. Buchheit, “Electrochemical Techniques in Corrosion Science and Engineering”, Marcel Dekker, Inc., New York, ISBN: 0-8247-9917-8, (2003).

[114] H. Ryssel and I. Ruge, “Ion Implantation”, John Wiley & Sons, Chichester, ISBN 0471-10311 X, (1986).

[115] G. Dearnaley, “Ion Beam Modification of Metals” Nucl. Instr. Meth. Phys. Res B, 50, 358-367, (1990).

[116] S.T. Picraux, “Ion Implantation in Metals”, Ann. Rev. Mater. Sci., 14, 335-72, (1984).

[117] G. S. Was, “Ion Beam Modification of Metals: Compositional and Microstructural Changes”, Prog. Surf. Sci., 32, 211-332, (1990)

[118] G. S. Was, “Fundamentals of Radiation Materials Science: Metals and Alloys”, Springer, Verlag Berlin Heidelberg, (2007).

[119] W. L. Johnson, “Thermodynamic and Kinetic Aspects of the Crystal to Glass Transformation in Metallic Materials”, Prog. Mater. Sci., 30, 81-134, (1986).

[120] M. H. Cohen and D. Turnbull, “Molecular Transport in Liquids and Glasses”, J. Chem. Phys., 31, 1164-1169, (1959).

[121] F. Spaepen, “A Microscopic Mechanism for Steady State Inhomogeneous Flow in Metallic Glasses, Acta Metall., 25, 407-415, (1977).

[122] T. Sundararajan, U. K. Mudali, K. G. M. Nair, S. Rajeswari and M. Subbaiyan, “Electrochemical Studies on Nitrogen Ion Implanted Ti6Al4V Alloy”, Anti-Corros. Methods Mater., 45, 162–166, (1998).

[123] T. Sundararajan and Z. Praunseis, “The Effect of Nitrogen-Ion Implantation on The Corrosion Resistance of Titanium in Comparison with Oxygen- and Argon-Ion Implantations”, Mater. Tehnol., 38, 19-24, (2004).

[124] T. Sundararajan, U. K. Mudali, K. G. M. Nair and M. Subbaiyan, “Effect of nitrogen ion implantation on the corrosion resistance of Titanium modified type 316L stainless steel in comparison with Argon and Oxygen ion implantation”, Mater. Sci. Forum, 318-320, 553-560, (1999).

[125] S. Amelinckx, “Diffraction and Imaging Techniques in Material Science” Volume I: Electron Microscopy, Elsevier, North Holland, (2012).

[126] B. A. Van Brussel and J. Th. M. De Hosson, “Glancing Angle Xray Diffraction: A Different Approach”, Appl. Phy. Lett., 64, 1585-1587, (1994).

[127] R. D. Tarey, R. S. Rastogi and K. L. Chopra, “Characterization of Thin Films by Glancing Incidence X-Ray Diffraction”, The Rigaku Journal, 4, 11-15, (1987).

[128] L. Reimer, “Scanning Electron Microscopy: Physics of Image Formation and Microanalysis”, Second Edition, Vol. 45, Springer-Verlag Berlin Heidelberg, ISBN 978-3-540-38967-5, (1998).

[129] J. Goldstein, D.E. Newbury, D.C. Joy, C.E. Lyman, P. Echlin, E. Lifshin, L. Sawyer and J. R. Michael, "Scanning Electron Microscopy and X-Ray Microanalysis" Third Edition, Springer US, ISBN 978-0-306-47292-3, (2003).

[130] K. Kalantar-Zadeh and B. Fry "Nanotechnology-Enabled Sensors" First Edition, Springer US, ISBN 978-0-387-68023-1, (2008).

[131] M. D. Nazzal, W. Mogawer, S. Kaya and T. Bennert, "Multiscale Evaluation of the Composite Asphalt Binder in High–Reclaimed Asphalt Pavement Mixtures", J. Mater. Civ. Eng. 26, 04014019:1-8, (2014).

[132] G. Haugstad, "Atomic Force Microscopy: Understanding Basic Modes and Advanced Applications", John Wiley & Sons. INC, New Gersey ISBN:9781118360668, (2012).

[133] J. F. Watts, "X-Ray Photoelectron Spectroscopy", Vacuum, 45, 653-671, (1994).

[134] C. R. Brundle and A. D. Baker, "Electron Spectroscopy: Theory, Techniques and Applications", Academia Press, New York, (1978).

[135] K. Asami and K. Hashimoto, "X-Ray Photoelectron Spectroscopy for Corrosion Studies" Langmuir, 3, 897–904, (1987).

[136] C.S. Fadley, "X-Ray Photoelectron Spectroscopy: Progress And Perspectives", J. Electron. Spectros. Relat. Phenomena, 178–179, 2–32, (2010).

[137] A. Inoue, "Bulk Amorphous and Nanocrystalline Alloys with High Functional Properties", Mater. Sci. Eng., A304–306, 1–10, (2001).

[138] A. Inoue, T. Nakamura, T. Sugita, T. Zhang and T. Masumoto, "Bulky La-Al-TM (TM=Transition Metal) Amorphous Alloys with High Tensile Strength Produced by a High-Pressure Die Casting Method", Mater. Trans., JIM 34, 351-358, (1993).

[139] A. Inoue, C. Fan, and A. Takenchi, "High-Strength Bulk Nanocrystalline Alloys in a Zr-Based System Containing Compound and Glassy Phases", J. Non-Cryst. Solids, 250/251, 724– 28, (1999).

[140] Y. Kawamura, T. Shibata, A. Inoue, and T. Masumoto, “Workability of The Supercooled Liquid in The $Zr_{65}Al_{10}Ni_{10}Cu_{15}$ Bulk Metallic Glass”, Acta Mater., 46, 253–263, (1998).

[141] F. X. Qin, H. F. Zhang, Y. F. Deng, B. Z. Ding, and , Z. Q. Hu, “Corrosion Resistance of Zr-Based Bulk Amorphous Alloys Containing Pd”, J. Alloys Compd., 375, 318-323, (2004).

[142] A. Dhawan, K. Sachdev, S. Roychowdhury, P. K. De, and S. K. Sharma, “Potentiodynamic Polarization Studies in Amorphous $Zr_{46.75}Ti_{8.25}Cu_{7.5}Ni_{10}Be_{27.5}$, $Zr_{65}Ni_{10}Cu_{17.5}Al_{7.5}$, $Zr_{67}Ni_{33}$ And $Ti_{60}Ni_{40}$ in Aqueous HNO_3 Solution”, J. Non-Cryst. Solids, 353, 2619-2623, (2007).

[143] Z. Fang-Quin, C. Zhi-Hao, T. Jin-Jue, L. Lan-Jun, Y. Jin, and X. Yun, “Corrosion Resistance of Zr-Al-Ni-Cu(Nb) Bulk Amorphous Alloys”, Trans. Nonferrous Met. Soc. China, 14, 961-965, (2004).

[144] Y. F. Sun, C.H. Shek, B. C. Wei, W. H. Li and Y. R. Wang, “Effect of Nb Content on the Microstructure and Mechanical Properties of Zr-Cu-Ni-Al-Nb Glass Forming Alloys”, J. Alloys Compd., 403, 239-244, (2005).

[145] C. M. A. Brett and A. M. Oliviera Brett. “Electrochemistry: Principles, Methods, and Applications” Oxford University Press, UK, ISBN-10:0198553889 (1993).

[146] P. Fauvet, F. Balbaud, R. Robin, Q. T. Tran, A. Mugnier, and D. Espinoux, “Corrosion Mechanisms of Austenitic Stainless Steels in Nitric Media Used in Reprocessing Plants”, J. Nucl. Mater., 375, 52-64, (2008).

[147] K. Hashimoto, K. Osada, T. Masumoto and S. Shimodaira, “Characteristics of Passivity of Extremely Corrosion-Resistant Amorphous Iron Alloys”, Corros. Sci., 16, 71-76, (1976).

[148] J. Jayaraj, A. Gebert, and L. Schultz, “Passivation Behavior of Structurally Relaxed $Zr_{48}Cu_{36}Ag_8Al_8$ Metallic Glass”, J. Alloys Compd., 479, 257-261, (2009).

[149] S. Baunack, U. K. Mudali and A. Gebert "Characterization of Oxide Layers on Amorphous Zr- Based Alloys By Auger Electron Spectroscopy with Sputter Depth Profiling", Appl. Surf. Sci., 252, 162-166, (2005).

[150] A. Takeuchi, and A. Inoue "Classification of Bulk Metallic Glasses by Atomic Size Difference, Heat of Mixing and Period of Constituent Elements and its Application to Characterization of the Main Alloying Element", Mater. Trans., 46, 2817- 2829, (2005).

[151] S. K. Sharma, T. Strunskus, H. Ladebusch, and F. Faupel "Surface Oxidation of Amorphous $Zr_{65}Cu_{17.5}Ni_{10}Al_{7.5}$ and $Zr_{46.75}Ti_{8.25}Cu_{7.5}Ni_{10}Be_{27.5}$", Mater. Sci. Eng. A, 304-306, 747-752, (2001).

[152] R. Kaufmann, H. Klewe-Nebenius, H. Moers, G. Pfennig, H. Jenett and H. J. Ache, "XPS Studies of the Thermal Behaviour of Passivated Zircaloy-4 Surfaces", Surf. Interface. Anal., 11, 502-509, (1988).

[153] X. P. Nie, X. H. Yang, L. Y. Chen, K. B. Yeap, K. Y. Zeng, D. Li, J. S. Pan, X. D. Wang, Q. P. Cao, S. Q. Ding and J. Z. Jiang, "The Effect of Oxidation on the Corrosion Resistance and Mechanical Properties of a Zr-Based Metallic Glass", Corros. Sci., 53, 3557–3565, (2011).

[154] H. K. Sanghera, J. L. Sullivan and S. O. Saied, "A Study of Nitrogen Implantation in Aluminium- A Comparison of Experimental Results and Computer Simulation", Appl. Surf. Sci., 141, 57–76, (1999).

[155] L. Liu, K. C. Chan and T. Zhang, "The Effect of Temperature on the Crystallization of $Zr_{55}Cu_{30}Al_{10}Ni_5$ Bulk Metallic Glass in the Glass Transition Region", J. Alloys Compd., 396, 114-121, (2005).

[156] Te-Lin Yau, "Zirconium for Nitric Acid Solutions", Fourth ASTM Symposium on Titanium and Zirconium in Industrial Applications, Philadelphia, PA, 10–11, 57–68, (1984).

[157] K. Kapoor, V. Kain, T. Gopalkrishna, T. Sanyal, and P. K. De: "High Corrosion Resistant Ti-5%Ta-1.8%Nb Alloy for Fuel Reprocessing Application", J. Nucl. Mater., 322, 36-44, (2003).

[158] P. Sharma, A. Dhawan and S. K. Sharma, "Corrosion Behavior of Amorphous $Zr_{59}Nb_3Al_{10}Ni_8Cu_{20}$ Alloy in Aqueous HNO_3 Media", Anti-Corros. Method Mater., 63, 97-104, (2016).

[159] S. Sohrabi, H. Arabi, A. Beitollahi and R. Gholamipour, "Planar Flow Casting of $Fe_{71}Si_{13.5}B_9Nb_3Cu_1Al_{1.5}Ge_1$ Ribbons", J. Mater. Eng. Perform., 22, 2185-2190, (2013).

[160] A. Dhawan, V. Zaporojtchenko, F. Faupel and S. K. Sharma, "Study of Air Oxidation of Amorphous $Zr_{65}Cu_{17.5}Ni_{10}Al_{7.5}$ by X-Ray Photoelectron Spectroscopy (XPS)", J. Mater. Sci., 42, 9037–9044, (2007).

[161] C.W. Kim, H.G. Jeong and D.B. Lee, "Oxidation of $Zr_{65}Al_{10}Ni_{10}Cu_{15}$ Bulk Metallic Glass", Mater. Lett., 62, 584–586, (2008).

[162] Y. Z.Yang, P. J. Tao, G. Q. Li, Z. X. Mu, X. Ru., Z. W. Xie and X. C. Chen, "Effects of Ion Implantation on Surface Structures and Properties for Bulk Metallic Glass", Intermetallics, 17, 722-726, (2009).

[163] S. Muraishi, H. Naito, T. Aizawa, "Microstructure and Elasticity of Glassy Alloy Surface by Reactive and Inert Ion Implantation", Mater. Trans. JIM, 48, 1859-1863, (2007).

[164] E. Menéndez, A. Hynowska, J. Fornell, S. Suriñach, J. Montserrat, K. Temst, A. Vantomme, M.D. Baró, E. García-Lecina, E. Pellicer and J. Sort "Influence of the Irradiation Temperature on the Surface Structure and Physical/Chemical Properties of Ar Ion-Irradiated Bulk Metallic Glasses", J. Alloys Compd., 610, 118–125, (2014).

[165] P. Tao, Y. Yang, X. Chen, C. Wang and J. Gao, "Study on Crystallization Behaviour in Zirconium-Based Bulk Amorphous Alloy after Cobalt Implantation", Mater. Lett., 121, 177-180, (2014).

[166] N. Kawasegi, N. Morita, S. Yamada, N. Takano, T. Oyama, K. Ashida, S. Momota, J. Taniguchi, I. Miyamoto and H. Ofune, “Sub-Micrometer-Scale Patterning on Zr-Based Metallic Glass using Focused Ion Beam Irradiation and Chemical Etching”, Nanotechnology, 18, 375302:1-8, (2007).

[167] J. He, X. Bai, C. Ma and H. Chen, “The Effect of Ion Implantation of Ar on the Aqueous Corrosion Resistance of Zr-4 Alloy”, Nucl. Instrum. Methods Phys. Res., Sect. B ,100, 59-64, (1995).

[168] J. Xu, X. Bai, F. He, S. Wang, X. He and Y. Fan, “Infuence of Ar Ion Bombardment on The Uniform Corrosion Resistance of Laser-Surface-Melted Zircaloy-4”, J. Nucl. Mater., 265, 240-244, (1999).

[169] J. Xu, X. Bai, J. An and Y. Fan, “Effect of Ar Ion Irradiation on Electrochemical Behaviors of Zircaloy-4”, Appl. Radiat. Isot., 53, 1005-1010, (2000).

[170] W. Pilarczyk and J. Podwórny, “Study of Atoms Arrangement in Zr-Based Bulk Metallic Glass Structure”, Acta Phys. Pol. A, 129, 216-218, (2016).

[171] J. L. Brimhall, L. A. Charlot and R. Wang “Irradiation Effects in Amorphous and Crystalline, Sputter-Deposited Mo-Ni”, Scripta Meter., 13, 217-220, (1979).

[172] E.M. Bringa, R.E. Johnson, “Coulomb Explosion and Thermal Spikes”, Phys. Rev. Lett., 88, 165501, (2002).

[173] Lin Shao, Di Chen, Michael Myers, Jing Wang,Buddhi Tilakaratne, Dharshana Wijesundera, Wei-Kan Chu, Guoqiang Xie, Arezoo Zare, and Don A. Lucca, “Smoothing Metallic Glasses Without Introducing Crystallization by Gas Cluster Ion Beam”, Appl. Phys. Lett., 102, 101604, (2013).

[174] H. Thomas, S. Thomas, R. V. Ramanujan, D.K. Avasthi, I.A. Al- Omari, S. Al-Harthi, M.R. Anantharaman, “Swift Heavy Ion Induced Surface and Microstructural Evolution in Metallic Glass Thin Films”, Nucl. Instr. Meth. Phys. Res.B, 287, 85–90, (2012).

[175] B. Wang, D. Y. Huang, Z. Chen, N. Prudhomme and V. Ji, “Oxidation Kinetics and Diffusion Mechanism Study of a Zr-Based Bulk Metallic Glass Alloy”, Mater. Sci. Forum, 675-677, 193-196, (2011).

[176] B. Wang, D.Y. Huang, N. Prud’homme, Z. Chen, F. Jomard, T. Zhang and V. Ji, “Diffusion Mechanism of Zr-Based Metallic Glass During Oxidation under Dry Air”, Intermetallics 28, 102-107, (2012).

[177] J. F. Ziegler, J. P. Biersack, U. Littmark, “The Stopping and Range of Ions in Solids”, New York, Pergamon Press, (1985).

[178] X.P. Nie, X.H. Yang, Y.Ma, L.Y. Chen, K.B. Yeap, K.Y. Zeng, D. Li, J.S. Pan, X.D. Wang, Q.P. Cao, S.Q. Ding and J.Z. Jiang, “Thermal Oxidation Effect on Corrosion Behavior of $Zr_{46}Cu_{37.6}Ag_{8.4}Al_8$ Bulk Metallic Glass”, Intermetallics, 22, 84-91, (2012).

[179] M. Matsuoka, S. Isotani, W. Sucasaire, N. Kuratani and K. Ogata, “X-Ray Photoelectron Spectroscopy Analysis of Zirconium Nitride-Like Films Prepared on Si(100) Substrates by Ion Beam Assisted Deposition”, Surf. Coat. Technol., 202, 3129-3135, (2008).

[180] U. K. Mudali, U. Kuhn, J. Eckert, L. Schultz and A. Gebert, “Corrosion Behaviour of Zirconium Based Bulk Metallic Glasses”, Trans. Indian Inst. Met., 59, 123-138, (2006).

[181] H. M. Lin, J. K. Wu, C. C. Wang, P. Y. Lee, “The Corrosion Behavior of Mechanically Alloyed Cu–Zr–Ti Bulk Metallic Glasses”, Mater. Lett., 62, 2995–2998, (2008).

[182] C. Li, D. Chen, W. Chen, L. Wang and D. Luo, “Corrosion Behavior of TiZrNiCuBe Metallic Glass Coatings Synthesized by Electrospark Deposition”, Corros. Sci., 84, 96–102, (2014).

[183] T. Sundararajan, U. K. Mudali, K.G.M. Nair, S. Rajeswari and M. Subbaiyan, “Effect of Nitrogen Ion Implantation on the Corrosion Resistance of Titanium Modified Type 316L Stainless Steel in Comparison with Argon and Oxygen Ion Implantation”, J. Mater. Eng. Perform., 8, 252-260, (1999).

[184] L. Thair, U. K. Mudali, S. Rajagopalan, R. Asokamani and B. Raj, “Surface Characterization of Passive Film Formed on Nitrogen Ion Implanted Ti-6Al-4V and Ti-6Al-7Nb Alloys using SIMS”, Corros. Sci., 45, 1951–1967, (2003).

[185] S. Miyagawa, K. Saitoh, M. Ikeyama, G. Massouras and Y. Miyagawa, “Composition and Structure of Zirconium Implanted With Nitrogen at High Fluence”, Nucl. Instr. Meth. Phys. Res. B, 69, 437-442, (1992).

[186] S. Miyagawa, M. Ikeyama, K. Saitoh, S. Nakao, H. Niwa, S. Tanemura and Y. Miyagawa, “Computer Simulation of Dynamic Change of Surface Composition Induced by High-Fluence Nitrogen Implantations”, Surf. Coat. Technol., 66, 235-239, (1994).

[187] S. J. Lee, H. S. Kwon, W. Kim and B. H. Choi, “Effects of Compositional and Structural Change on the Corrosion Behaviour of Nitrogen Implanted Zircaloy-4”, Mater. Sci. Eng. A, 263, 23-31, (1999).

[188] Y. Z. Liu, X. T. Zu, S. Zhu and L. M. Wang, “Phase Formation and Corrosion Behavior of Nitrogen Implanted Zr-Sn-Nb Alloy in Alkaline Environment”, Nucl. Instr. Meth. Phys. Res. B, 246, 345-350, (2006).

[189] A. Roustila, J. Chêne and C. Séverac, “XPS Study of Hydrogen and Oxygen Interactions on the Surface of the NiZr Intermetallic Compound”, Int. J. Hydrogen Energy, 32, 5026-5032, (2007).

[190] S. Calderon, A. Cavaleiro and S. Carvalho, “Chemical and Structural Characterization of Zr-C-N-Ag Coatings: XPS, XRD and Raman Spectroscopy”, Appl. Surf. Sci., 346, 240–247, (2015).

[191] T. L. Cheung and C.H. Shek, “Surface Characteristics of Nitrogen and Argon Plasma Immersion Ion Implantation of Cu-Zr-Al Bulk Metallic Alloy”, Rev. Adv. Mater. Sci., 18, 112-120, (2008).

[192] P. Motamedi and K. Cadien, “XPS Analysis of AlN Thin Films Deposited by Plasma Enhanced Atomic layer Deposition”, Appl. Surf. Sci., 315, 104–109, (2014).

[193] H. H. Huang, H.M. Huang, M.C. Lin, W. Zhang, Y.S. Sun, W. Kai and P.K. Liaw, “Enhancing the Bio-Corrosion Resistance of Ni-Free ZrCuFeAl Bulk Metallic Glass through Nitrogen Plasma Immersion Ion Implantation”, J. Alloys Compd., 615, S660–S665, (2014).

[194] J. Chakraborty, S. Mukherje, P.M. Raol and P.I. John, “Feasibility Study of Aluminium Nitride Formation by Nitrogen Plasma Source Ion Implantation on Aluminium”, Mater. Sci. Eng. A, 304–306, 910–913, (2001).

[195] Y. Fu, H. Du, S. Zhang and W. Huang, “XPS Characterization of Surface and Interfacial Structure of Sputtered TiNi Films on Si Substrate”, Mater. Sci. Eng. A, 403, 25–31, (2005).

[196] J. A. Garcia, A. Guette, A. Medrano, C. Labrugere, M. Rico, M. Lahaye, R. Sanchez, A. Martınez and R. J. Rodriguez, “Nitrogen Ion Implantation on Group IVB Metals: Chemical, Mechanical and Tribological Study”, Vacuum, 64, 343–351, (2002).

[197] I. Milošev, H.H. Strehblow, B. Navinšek and P. Panjan, “Zirconium Nitride by XPS”, Surf. Sci. Spectra, 5, 152-158, (1998).

[198] L. Thair, U. K. Mudali and N. Bhuvaneswaran, “Nitrogen Ion Implantation and in Vitro Corrosion Behavior of As-Cast Ti–6Al–7Nb Alloy”, Corros. Sci., 44, 2439–2457, (2002).

[199] G.I. Cubillos, J.J. Olaya, M. Bethencourt, G. Antorrena and K. El Amrani, “Synthesis and Characterization of Zirconium Oxynitride Zroxny Coatings Deposited via Unbalanced DC Magnetron Sputtering”, Mater. Chem. Phys., 141, 42 -51, (2013).

[200] D. Roman, J. Bernardi, C. de Amorim, F. de Souza, A. Spinelli, C. Giacomellid, C. Figueroa, I. Baumvol and R. Basso, “Effect Of Deposition Temperature On Microstructure and Corrosion Resistance of Zrn Thin Films Deposited by DC Reactive Magnetron Sputtering”, Mater. Chem. Phys., 130, 147-153, (2011).

[201] D. R. Lide, “Standard Thermodynamic Properties of Chemical Substances”, CRC Handbook of Chemistry and Physics, CRC Press LLC , 93rd Ed 4-42, (2007).

LIST OF PUBLICATIONS

In Journals (International/National)

1. **Poonam Sharma**, Anil Dhawan and S.K. Sharma, **"High Temperature Corrosion Study of Zr-based Amorphous Alloys in Aqueous HNO_3 media",** IJMCTR Vol.2, Issue 1 (2014) 1-4.
2. **Poonam Sharma**, Anil Dhawan and S. K. Sharma, **"Corrosion and surface characterization of Zr-based metallic glasses in nitric acid",** J. Advance Microscopy Research Vol. 9, (2014) 262-267.
3. **Poonam Sharma**, Anil Dhawan and S. K. Sharma, **"Corrosion behavior of amorphous $Zr_{59}Nb_3Al_{10}Ni_8Cu_{20}$ alloy in aqueous HNO_3 media"**, Anti-Corrosion Method & Materials, Vol. 63, Issue 2 (2016) 97-104.
4. **Poonam Sharma**, Anil Dhawan and S. K. Sharma, **"Surface morphology study of Zr-based amorphous alloys after immersion in boiling nitric acid medium",** AIP Conf. Proc. 1731, 070021 (2016).
5. **Poonam Sharma**, Anil Dhawan and S. K. Sharma, **"Electrochemical investigation of amorphous $Zr_{60}Pd_5Cu_{15}Ni_{10}Al_{10}$ and $Zr_{57}Nb_5Cu_{20}Ni_8Al_{10}$ alloys in oxidizing medium"** Advanced Science Letters, Vol. 22 (2016) 56-59.
6. Poonam Sharma, Anil Dhawan, S. Faheem Naqvi, S. K. Sharma, "**Effect of Ni ion irradiation on microstructure and corrosion properties of $Zr_{59}Nb_3Cu_{20}Al_{10}Ni_8$ amorphous alloy"** Indian Journal of Pure & Applied Physics, Vol. 56, Accepted 15 May 2018.

International/ National Conferences

7. **Poonam Sharma**, Anil Dhawan and U. K. Mudali, **"Potentiodynamic Polarization Studies of Bulk Amorphous Alloy $Zr_{57}Cu_{15.4}Ni_{12.6}Al_{10}Nb_5$ and $Zr_{59}Cu_{20}Ni_8Al_{10}Ti_3$ in aqueous HNO_3 Media"**, presented at International conference NACE, CORSYM-2013 (28 Feb.-02 March, 2013 at Chennai).
8. **Poonam Sharma**, Anil Dhawan and S. K. Sharma, **"Corrosion behavior of amorphous $Zr_{59}Nb_3Cu_{20}Ni_8Al_{10}$ and $Zr_{60}Pd_5Cu_{15}Ni_{10}Al_{10}$ alloys in aqueous HNO_3 media at boiling temperature",** presented in National Conference "National conference on thermophysical properties, (NCTP-2013)" during October, 17-19, 2013 at Kanpur University (India).
9. Anil Dhawan, **Poonam Sharma,** S. Mathur and S. K. Sharma, **"Comparing the corrosion behavior of the bulk amorphous alloy $Zr_{65}Cu_{17.5}Ni_{10}Al_{7.5}$ with binary alloy $Ti_{60}Ni_{40}$ in aqueous HNO_3 medium before and after irradiation",** presented in a National conference on Perspectives of Physics in Multidisciplinary Research on 12-13 March, 2014 at Department of Physics, University of Rajasthan, Jaipur.

10. **Poonam Sharma**, Anil Dhawan and S. K. Sharma, **"Electrochemical investigation of amorphous $Zr_{60}Pd_5Cu_{15}Ni_{10}Al_{10}$ and $Zr_{57}Nb_5Cu_{20}Ni_8Al_{10}$ alloys in oxidizing medium",** presented at International Conference of Emerging Materials: Characterization and Applications 2014 on 4-6 Dec. 2014 at CSIR-CGCRI, Kolkata.
11. **Poonam Sharma**, Anil Dhawan and S. K. Sharma, **"Surface morphology study of Zr-based amorphous alloys after immersion in boiling nitric acid medium",** accepted for presentation in 60th DAE Solid State Physics Symposium on 21-25 Dec, 2015 at Amity University, Noida. **Got best poster presentation award**)
12. **Poonam Sharma,** J. Jayaraj, A. Dhawan, S. K. Sharma and U. Kamachi Mudali**,"Corrosion behavior of O^+ ion implanted $Zr_{55}Cu_{30}Al_{10}Ni_5$ bulk metallic glassy alloy in nitric acid medium"** presented in International Conference on Frontiers at the Chemistry-Allied Sciences Interface on April 25-26, 2016 at Department of Chemistry, University of Rajasthan, Jaipur.
13. **Poonam Sharma**, J. Jayaraj, A. Dhawan, S. K. Sharma and U. Kamachi Mudali, **"Influence of O+ ion implantation on corrosion behavior of $Zr_{55}Cu_{30}Ni_5Al_{10}$ metallic glassy alloy in different aqueous media"** presented in International Conference CORCON-2016 on 18-21 September 2016 at Leela Ambience Convention Hotel, Delhi.
14. Anil Dhawan, **Poonam Sharma**, S. F. Naqvi and S. K. Sharma, **"Effect of ion irradiation on the structure sensitive properties of the Zr-based amorphous alloy"** presented at IISF, New Delhi on 7-10, Dec. 2016. (**Got best poster presentation award**)

BIO-DATA

Poonam Sharma

E-mail : pnms90@gmail.com

Mob. 9660474999, 7597063935

ACADEMIC QUALIFICATIONS

Ph.D	Corrosion Investigations on As-prepared and Ion-implanted Zr-based Bulk Amorphous Alloys Year of Passing 2018, C.G.P.A. – 8.75/10.00 Malaviya National Institute of Technology, Jaipur (INDIA)
M.Sc.	Physics Year of Passing 2011, C.G.P.A. – 8.1/10.00 Malaviya National Institute of Technology, Jaipur (INDIA)
B.Sc.	Physics, Chemistry, Mathematics Year of Passing 2009, Percentage: 73.78% Maharaja Ganga Singh University, Bikaner (INDIA)
Fellowship:	BRNS/DAE funded Junior/Senior research fellowship (JRF/SRF) from May 2012- March 2016

RESEARCH PROJECTS

- Research Project **"Development of Zr and Ni - based metallic glasses and Surface modification for reprocessing applications"** under the supervision of Prof. Anil Dhawan, Anand International College of Engineering, Jaipur during May, 2012- March, 2016.

- Reseach work carried out at **"Indira Gandhi Center for Atomic Research, Kalpakkam, Tamilnadu"** under **BRNS/DAE Research Project.**

- M.Sc. Project entitled **"Simulation of Ion Beam Irradiation on Ti-based Alloys"** under the supervision of **Prof. S. K. Sharma, Department of Physics, MNIT, Jaipur.**

- Summer research project on **"Chaos (Nonlinear dynamics)"** at **IISER, Muhali** under **Prof. Sudheshna Sinha**

RESEARCH PUBLICATIONS

In Journals (International/National)

1. **Poonam Sharma**, Anil Dhawan and S.K. Sharma, **"High Temperature Corrosion Study of Zr-based Amorphous Alloys in Aqueous HNO_3 media",** IJMCTR Vol.2, Issue 1 (2014) 1-4.
2. **Poonam Sharma**, Anil Dhawan and S. K. Sharma, **"Corrosion and surface characterization of Zr-based metallic glasses in nitric acid",** J. Advance Microscopy Research 9, (2014) 262-267.
3. **Poonam Sharma**, Anil Dhawan and S. K. Sharma, **"Corrosion behavior of amorphous $Zr_{59}Nb_3Al_{10}Ni_8Cu_{20}$ alloy in aqueous HNO_3 media"**, Anti-Corrosion Method & Materials, Vol. 63, Issue 2 (2016) 97-104.
4. **Poonam Sharma**, Anil Dhawan and S. K. Sharma, **"Surface morphology study of Zr-based amorphous alloys after immersion in boiling nitric acid medium",** AIP Conf. Proc. 1731, 070021 (2016).
5. **Poonam Sharma**, Anil Dhawan and S. K. Sharma, **"Electrochemical investigation of amorphous $Zr_{60}Pd_5Cu_{15}Ni_{10}Al_{10}$ and $Zr_{57}Nb_5Cu_{20}Ni_8Al_{10}$ alloys in oxidizing medium"** Advanced Science Letters, 22 (2016) 56-59.
6. Poonam Sharma, Anil Dhawan, S. Faheem Naqvi, S. K. Sharma, "**Effect of Ni ion irradiation on microstructure and corrosion properties of $Zr_{59}Nb_3Cu_{20}Al_{10}Ni_8$ amorphous alloy"** Indian Journal of Pure & Applied Physics, Vol. 56, Accepted 15 May 2018.

International/ National Conferences

7. **Poonam Sharma**, Anil Dhawan and U. K. Mudali, **"Potentiodynamic Polarization Studies of Bulk Amorphous Alloy $Zr_{57}Cu_{15.4}Ni_{12.6}Al_{10}Nb_5$ and $Zr_{59}Cu_{20}Ni_8Al_{10}Ti_3$ in aqueous HNO_3 Media"**, presented at International conference NACE, CORSYM-2013 (28 Feb.-02 March, 2013 at Chennai).
8. **Poonam Sharma**, Anil Dhawan and S. K. Sharma, **"Corrosion behavior of amorphous $Zr_{59}Nb_3Cu_{20}Ni_8Al_{10}$ and $Zr_{60}Pd_5Cu_{15}Ni_{10}Al_{10}$ alloys in aqueous HNO_3 media at boiling temperature",** presented in National Conference "National conference on thermophysical properties, (NCTP-2013)" during October, 17-19, 2013 at Kanpur University (India).
9. Anil Dhawan, **Poonam Sharma,** S. Mathur and S. K. Sharma, **"Comparing the corrosion behavior of the bulk amorphous alloy $Zr_{65}Cu_{17.5}Ni_{10}Al_{7.5}$ with binary alloy $Ti_{60}Ni_{40}$ in aqueous HNO_3 medium before and after irradiation",** presented in a National conference on Perspectives of Physics in Multidisciplinary Research on 12-13 March, 2014 at Department of Physics, University of Rajasthan, Jaipur.

10. **Poonam Sharma**, Anil Dhawan and S. K. Sharma, **"Electrochemical investigation of amorphous $Zr_{60}Pd_5Cu_{15}Ni_{10}Al_{10}$ and $Zr_{57}Nb_5Cu_{20}Ni_8Al_{10}$ alloys in oxidizing medium",** presented at International Conference of Emerging Materials: Characterization and Applications 2014 on 4-6 Dec. 2014 at CSIR-CGCRI, Kolkata.
11. **Poonam Sharma**, Anil Dhawan and S. K. Sharma, **"Surface morphology study of Zr-based amorphous alloys after immersion in boiling nitric acid medium",** accepted for presentation in 60th DAE Solid State Physics Symposium on 21-25 Dec, 2015 at Amity University, Noida. **Got best poster presentation award**)
12. **Poonam Sharma,** J. Jayaraj, A. Dhawan, S. K. Sharma and U. Kamachi Mudali**,"Corrosion behavior of O^+ ion implanted $Zr_{55}Cu_{30}Al_{10}Ni_5$ bulk metallic glassy alloy in nitric acid medium"** presented in International Conference on Frontiers at the Chemistry-Allied Sciences Interface on April 25-26, 2016 at Department of Chemistry, University of Rajasthan Jaipur
13. **Poonam Sharma**, J. Jayaraj, A. Dhawan, S. K. Sharma and U. Kamachi Mudali, **"Influence of O+ ion implantation on corrosion behavior of $Zr_{55}Cu_{30}Ni_5Al_{10}$ metallic glassy alloy in different aqueous media"** presented in International Conference CORCON-2016 on 18-21 September 2016 at Leela Ambience Convention Hotel, Delhi.
14. Anil Dhawan, **Poonam Sharma**, S. F. Naqvi and S. K. Sharma, **"Effect of ion irradiation on the structure sensitive properties of the Zr-based amorphous alloy"** presented at IISF, New Delhi on 7-10, Dec. 2016 (**Got best poster presentation award**)

BOOK PUBLISHED

Sanjiv Class VII Science, Publisher: Sanjiv Prakashan, 2018

WORKSHOP/SEMINAR ATTENDED (Technical)

- 19th National Children's Science Congress during 27-31 Dec, 2011 organized by Jaipur National University, Jaipur.
- National Workshop on "**Ion beams in materials research**" (IBMR-2013) during 22-23March, 2013, organized by Department of Physics, Malaviya National Institute of Technology, Jaipur.
- Short term course on "**Frontier Materials**" during 12-17 August, 2013 at Malaviya National Institute of Technology, Jaipur.
- Short term course on "**Nanotechnology & Its Applications**" during 7-11 October, 2013 at Malaviya National Institute of Technology, Jaipur.
- Attended workshop on "**Workshop on Technical Report writing and authoring of Research Manuscripts with Latex**" Organized by MNIT and EICT Academy at MNIT Jaipur during 14-16 April, 2017.

WORKSHOP/SEMINAR ATTENDED (Non-technical)

- Attended 8 days workshop on "**Universal Human Values**" organised by Anand-ICE, Jaipur in coordination with Value Education Cell AKTU, Lucknow from December 26, 2017 to January 2, 2018.
- Attended Teacher training workshop on "**Induction Programme**" organised by Rajasthan Technical University, Kota under TEQIP-III RTU (ATU) Project at SKIT, Jaipur from 22-24 March, 2018.

TECHNICAL SKILLS

- **Machine Handling**

  Vacuum tubular Furnace
  Hot corrosion testing setup
  Autolab potentiostat
  150 KeV Ion beam accelerator

- **Software Relevance**

  Origin 8.1
  NOVA 1.10- Metrohm Autolab
  CASA Software
  Latex

- **Packages**

  Power Point, MS-Word, MS-Excel, C++

Present Address
Poonam Sharma W/O Anubhav Sharma
5/336, Malaviya Nagar,
Jaipur (Rajasthan) pin- 302017

Permanent Adress
Poonam Sharma W/O Anubhav Sharma
MA. V. Ke Pass, Gothada Bhukaran
Teh- Dhod, Dist-Sikar (Raj.)-332031

Journal of
Advanced Microscopy Research
Vol. 9, 262–267, 2014

RESEARCH ARTICLE

Corrosion and Surface Characterization of Zr-Based Metallic Glasses in Nitric Acid

Poonam Sharma[1], Anil Dhawan[1,*], and S. K. Sharma[2]

[1] Department of Physics, Anand International College of Engineering, Jaipur 303012, India
[2] Department of Physics, Malaviya National Institute of Technology, Jaipur 302017, India

The electrochemical measurement, weight loss analysis and surface investigation were carried out on $Zr_{62-X}Nb_XCu_{20}Ni_8Al_{10}$ ($X = 2$ and 3) glassy alloys in aqueous HNO_3 medium at room temperature to understand the corrosion behavior of Zr-based amorphous alloys. Electrochemical studies were carried out in 1 M, 6 M and 11.5 M HNO_3 medium by recording open circuit potential/time and potentiodynamic polarization characteristics. The scanning electron microscopy and atomic force microscopy was used to investigate the surface morphology of the alloy after weight loss test. The electrochemical measurement results revealed that $Zr_{59}Nb_3Cu_{20}Ni_8Al_{10}$ glassy alloy possess better corrosion resistance than $Zr_{60}Nb_2Cu_{20}Ni_8Al_{10}$ alloy and the weight loss results also support the same. The potentiodynamic polarization curves revealed that E_{corr} values shifted towards nobler sides, as the concentration of nitric acid was increased and it is attributed due to higher oxidizing power of nitric acid. SEM and AFM micrographs indicate the formation of inhomogeneous passive film on surface of the alloy in nitric acid environment.

Keywords: Corrosion, Potentiodynamic Polarization, Weight Loss Measurement, SEM, AFM.

1. INTRODUCTION

Among glass forming systems, Zr-based multicomponent alloys have received increasing attention due to the positive combination of easy castability and high thermal stability against crystallization together with remarkable mechanical properties.[1,2] Among these alloys, the Zr-TM-Al alloys, where TM is transition metal, are particularly interesting because they exhibit an extremely large temperature interval of super-cooled liquid region exceeding 100 K.[3] In the series of Zr-TM-Al alloys, the effect of Nb element addition on glass formation and thermal stability of $Zr_{65}(Cu_{0.4}Al_{0.3}Ni_{0.3})_{35-x}Nb_x$ ($x = 0$, 3, 5, 6, 7) alloys were investigated by Yongjiang et al.[4] It has been reported in this investigation that the addition of Nb element leads to an increased disorder in atomic structure of the alloy and hence increases the thermal stability of the alloy. Major concern for these materials are high pitting susceptibility in chloride containing environment, viability of good mechanical properties and prolonged service in the presence of corrosive environment.[5–7] The significant efforts have been made to evaluate the corrosion resistance of Zr-based bulk metallic glasses so far. Homozava et al.[8] have predicted high corrosion resistance for $Zr_{58.5}Cu_{15.6}Ni_{12.8}Al_{10.3}Nb_{2.8}$ in 1 M HCl and 1 M HNO_3 acidic media due to change in elemental composition in oxide film. Pang et al.[9] have studied the corrosion behaviour of Zr–Nb–Al–Ni–Cu glassy alloys in HCl, NaCl and H_2SO_4 solutions using weight loss and electrochemical measurements. They have reported that the addition of Nb is effective in improving the corrosion resistance of the investigated Zr-based glassy alloys in HCl solution. The Zr–Cu–Ni–Al–(Ti, Nb) alloys were studied to investigate the behaviour of oxide film formed on these alloys in H_2SO_4 medium using Auger electron spectroscopy by Baunack et al.[10]

The motivation for the present study was derived from the need of searching a high corrosion resistant glassy alloy in nitric acid environment for fuel reprocessing applications. Therefore the main purpose of this work is to analyze the corrosion resistance of Zr–Nb–Cu–Ni–Al glassy alloys in aqueous HNO_3 solution. The corrosion behaviour of the resulting glassy alloys in various concentration of nitric acid solution at room temperature has been investigated by electrochemical measurements and weight loss method.

2. EXPERIMENTAL DETAILS

The glassy alloys $Zr_{62-X}Nb_XCu_{20}Ni_8Al_{10}$ ($X = 2$ and 3) has been used for investigations. The amorphous nature

*Author to whom correspondence should be addressed.

 2156-7573/2014/9/262/006 doi:10.1166/jamr.2014.1219

of the samples has been ascertained by X-Ray diffraction using Xpert Pro-Pananalytical system with Cu-Kα radiations. The Electrochemical measurements were carried out using a potentiostat (Autolab-AUT84276) which consist of a three electrode cell; Ag/AgCl reference electrode, Pt counter electrode and glassy alloys as working electrode and open circuit potential (OCP) was monitored for 1800 sec for stabilization prior to all the tests. The potentiostat was interfaced with Nova (version 1.9) software for measuring the change in OCP with immersion time and also performing the polarization experiments. Potentiondynamic polarization test were conducted in 1 M, 6 M and 11.5 HNO_3 at room temperature. The samples were cleaned with acetone and distilled water before inserting them into an electrolyte. The potentiodynamic polarization experiments were carried out at the scanning rate 1 mV/s from 200 mV below OCP to 2200 mV. All the polarization plots were almost reproducible. Prior to corrosion test (weight loss analysis), as spun ribbon specimens of $Zr_{62-X}Nb_XCu_{20}Ni_8Al_{10}$ ($X = 2$ and 3) alloys were cleaned with distilled water, acetone and then dried it in air. The surface area and initial mass of each sample were measured. These samples were finally immersed into the corrosive medium of 1 M, 6 M and 11.5 M HNO_3 solution at room temperature for 480 hours and the corrosion rates were estimated from the weight loss analysis. The microgram balance (Mettler Toledo) used to measure the actual weight loss of the samples has an accuracy of ± 10 μg. The surface morphology of both the alloys after immersion in 1 M and 11.5 M HNO_3 solution was carried out with the help of a ZEISS-EVO 18 scanning electron microscope (SEM) and a Bruker Multimode-8 atomic force microscope (AFM) with a Nanoscope V controller.

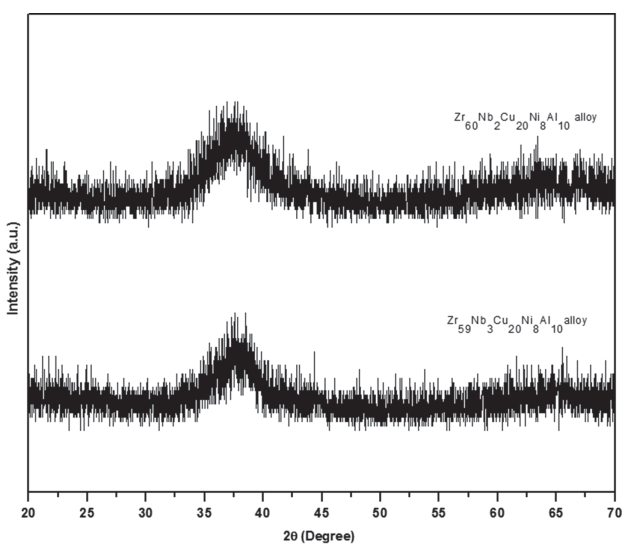

Fig. 1. XRD patterns of the $Zr_{62-X}Nb_XCu_{20}Ni_8Al_{10}$ ($X = 2$ and 3) alloys.

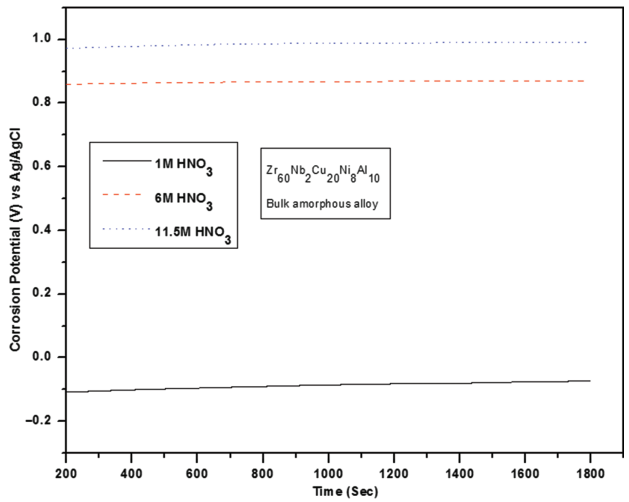

Fig. 2. Open circuit potential of $Zr_{60}Nb_2Cu_{20}Ni_8Al_{10}$ glassy alloy in 1 M, 6 M and 11.5 M aqueous HNO_3 medium at room temperature.

3. RESULTS

Figure 1 shows X-Ray diffraction patterns of $Zr_{62-X}Nb_XCu_{20}Ni_8Al_{10}$ ($X = 2$ and 3) glassy alloys. The XRD patterns of $Zr_{62-X}Nb_XCu_{20}Ni_8Al_{10}$ ($X = 2$ and 3) alloys shows only broad spectrum indicating amorphous nature.

Figure 2 shows the open circuit potential curve of $Zr_{60}Nb_2Cu_{20}Ni_8Al_{10}$ glassy alloy in 1 M, 6 M and 11.5 M aqueous HNO_3 medium at room temperature. It can be seen from the Figure 2 that the value of open circuit potential for the alloy increases as the concentration of HNO_3 increases. Figure 3 shows the potentiodynamic polarization curve of $Zr_{60}Nb_2Cu_{20}Ni_8Al_{10}$ glassy alloy in 1 M, 6 M and 11.5 M aqueous HNO_3 medium at room temperature. The corrosion parameters such as corrosion

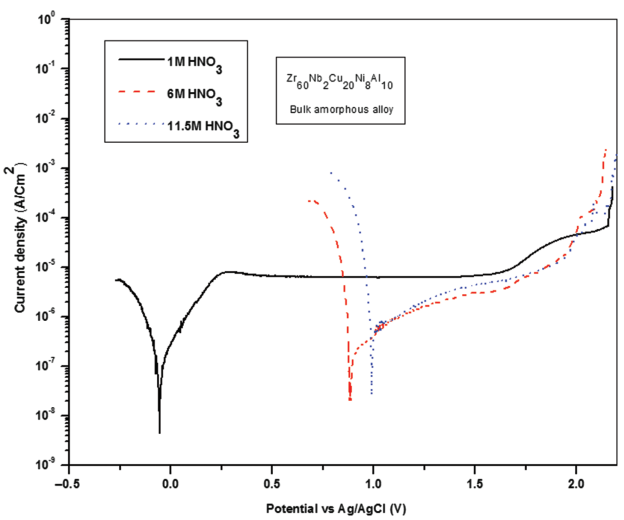

Fig. 3. Potentiodynamic polarization curve of $Zr_{60}Nb_2Cu_{20}Ni_8Al_{10}$ glassy alloy in 1 M, 6 M and 11.5 M aqueous HNO_3 medium at room temperature.

RESEARCH ARTICLE

Table I. Polarization parameter of $Zr_{60}Nb_2Cu_{20}Ni_8Al_{10}$ glassy alloy in 1 M, 6 M, 11.5 M HNO_3 medium at room temperature.

Concentration of HNO_3	E_{corr} (V)	I_{corr} (μA cm^{-2})
1 M	-0.055 ± 0.008	0.201 ± 0.021
6 M	0.884 ± 0.004	0.324 ± 0.015
11.5 M	0.991 ± 0.001	0.711 ± 0.006

potential E_{corr}, corrosion current density I_{corr} obtained from the polarization curve (Fig. 3) are shown in Table I. It can be observed from Figure 3 that the alloy shows a wider passive range in 1 M HNO_3 solution but at higher concentration of HNO_3 a clear passivity could not be observed. The value of passive potential E_{pass} and passive current density I_{pass} is 0.411 V and 6.333 μA/cm^2 respectively for the $Zr_{60}Nb_2Cu_{20}Ni_8Al_{10}$ alloy in 1 M HNO_3 solution. As the concentration of HNO_3 increases the value of corrosion current density for the alloy also increases.

Figure 4 shows the open circuit potential of $Zr_{59}Nb_3Cu_{20}Ni_8Al_{10}$ glassy alloy in 1 M, 6 M and 11.5 M aqueous HNO_3 media at room temperature. It is observed from Figure 4 that the value of open circuit potential for the alloy increases as the concentration of HNO_3 increases. Figure 5 shows the potentiodynamic polarization curve of $Zr_{59}Nb_3Cu_{20}Ni_8Al_{10}$ alloy in 1 M, 6 M and 11.5 M HNO_3 medium at room temperature. The various corrosion parameters obtained from Figure 5 are shown in Table II. It can be seen from Figure 5 and Table II that the alloy shows wider passive region in all concentration of HNO_3 solution. The value of passive potential E_{pass} in 1 M, 6 M and 11.5 M HNO_3 is 0.362 V, 0.744 V and 1.492 V respectively and passive current density I_{pass} in 1 M, 6 M and 11.5 M HNO_3 media is 5.748 μA/cm^2, 5.466 μA/cm^2 and 6.437 μA/cm^2 respectively for the $Zr_{60}Nb_2Cu_{20}Ni_8Al_{10}$ alloy. As the concentration of HNO_3 increases the value of corrosion current density for the alloy also increases.

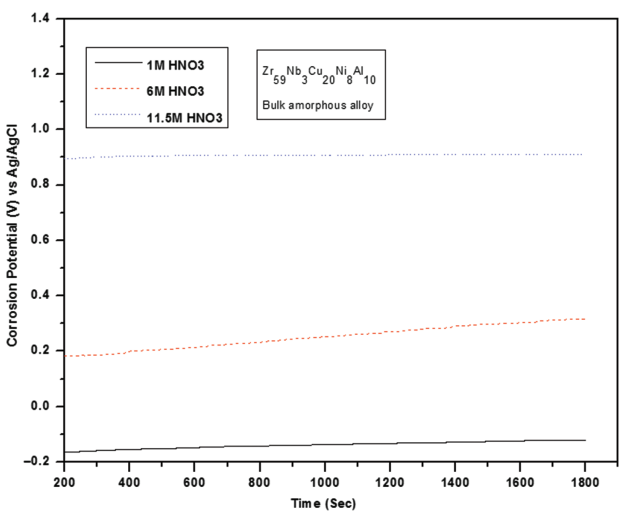

Fig. 4. Open circuit potential of $Zr_{59}Nb_3Cu_{20}Ni_8Al_{10}$ glassy alloy in 1 M, 6 M and 11.5 M aqueous HNO_3 medium at room temperature.

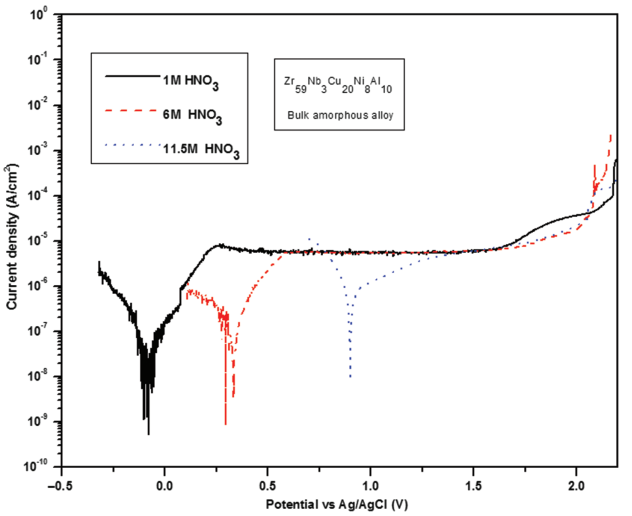

Fig. 5. Potentiodynamic polarization curve of $Zr_{59}Nb_3Cu_{20}Ni_8Al_{10}$ glassy alloy in 1 M, 6 M and 11.5 M aqueous HNO_3 medium at room temperature.

Figure 6 shows the corrosion rate of glassy $Zr_{62-X}Nb_XCu_{20}Ni_8Al_{10}$ ($X = 2$ and 3) alloys in 1 M, 6 M and 11.5 M aqueous HNO_3 medium at room temperature. It can be seen from Figure 6 that the corrosion rates of these alloys are increasing as the concentration of HNO_3 increases. The $Zr_{60}Nb_2Cu_{20}Ni_8Al_{10}$ alloy shows high value of corrosion rate in 1 M HNO_3 solution than $Zr_{59}Nb_3Cu_{20}Ni_8Al_{10}$ alloy. In 6 M HNO_3 solution, a significant change could not be observed in the value of corrosion rate but in 11.5 M HNO_3 solution $Zr_{59}Nb_3Cu_{20}Ni_8Al_{10}$ alloy shows least value of corrosion rate which is significantly less than other alloy.

The surface morphology of the treated samples were examined by SEM. Figures 7 and 8 shows the SEM micrographs of $Zr_{60}Nb_2Cu_{20}Ni_8Al_{10}$ and $Zr_{59}Nb_3Cu_{20}Ni_8Al_{10}$ glassy alloys after immersion in 1 M and 11.5 M aqueous HNO_3 medium for 480 hr at room temperature, respectively. It has been observed from Figures 7(a) and (b) that the $Zr_{60}Nb_2Cu_{20}Ni_8Al_{10}$ glassy alloy in 1 M HNO_3 medium shows clean surface as compared to $Zr_{60}Nb_2Cu_{20}Ni_8Al_{10}$ glassy alloys in 11.5 M HNO_3 medium and similar trends has been followed for $Zr_{59}Nb_3Cu_{20}Ni_8Al_{10}$ alloy as shown in Figures 8(a) and (b).

In order to further elucidate the surface morphology of $Zr_{60}Nb_2Cu_{20}Ni_8Al_{10}$ and $Zr_{59}Nb_3Cu_{20}Ni_8Al_{10}$ glassy alloys, AFM studies were carried out. Figures 9 and 10

Table II. Polarization parameter of $Zr_{59}Nb_3Cu_{20}Ni_8Al_{10}$ glassy alloy in 1 M, 6 M, 11.5 M HNO_3 medium at room temperature.

Concentration of HNO_3	E_{corr} (V)	I_{corr} (μA cm^{-2})
1 M	-0.077 ± 0.016	0.105 ± 0.006
6 M	0.338 ± 0.010	0.232 ± 0.012
11.5 M	0.904 ± 0.004	0.893 ± 0.008

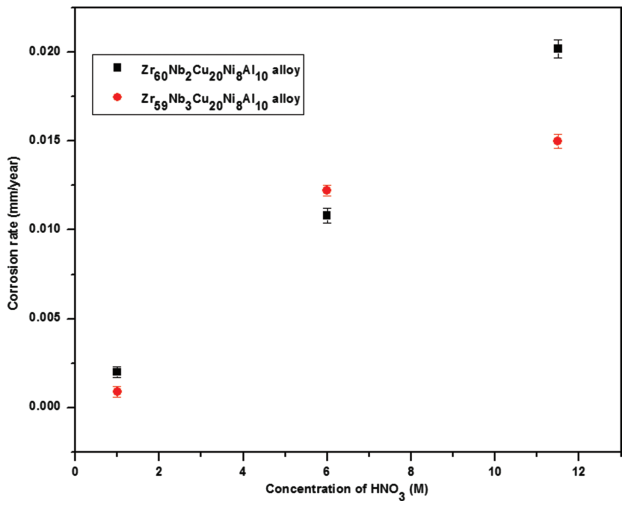

Fig. 6. Corrosion rate of $Zr_{62-X}Nb_XCu_{20}Ni_8Al_{10}$ ($X = 2$ and 3) glassy alloys in 1 M, 6 M and 11.5 M aqueous HNO_3 medium at room temperature for 480 h duration.

shows the AFM micrographs of $Zr_{60}Nb_2Cu_{20}Ni_8Al_{10}$ and $Zr_{59}Nb_3Cu_{20}Ni_8Al_{10}$ glassy alloys after immersion in 1 M and 11.5 M aqueous HNO_3 medium for 480 hr at room temperature. The $Zr_{60}Nb_2Cu_{20}Ni_8Al_{10}$ glassy alloy in 1 M HNO_3 (Fig. 9(a)) shows more rough surface than in 11.5 M HNO_3 (Fig. 9(b)) whereas, the appearance of trench like structure in Figure 10(b) is due to the aggressive dissolution of $Zr_{59}Nb_3Cu_{20}Ni_8Al_{10}$ alloy in 11.5 M HNO_3 medium than 1 M HNO_3 medium (Fig. 10(a)).

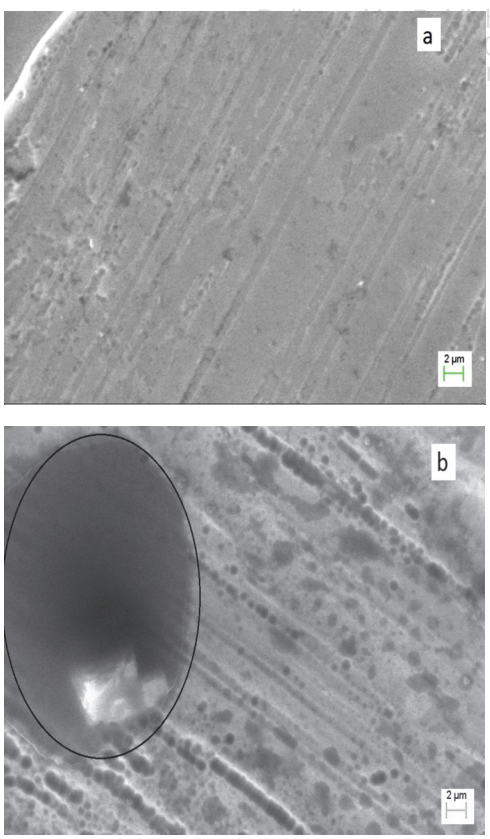

Fig. 7. SEM micrographs of $Zr_{60}Nb_2Cu_{20}Ni_8Al_{10}$ glassy alloy after immersion in (a) 1 M and (b) 11.5 M aqueous HNO_3 medium for 480 hr at room temperature.

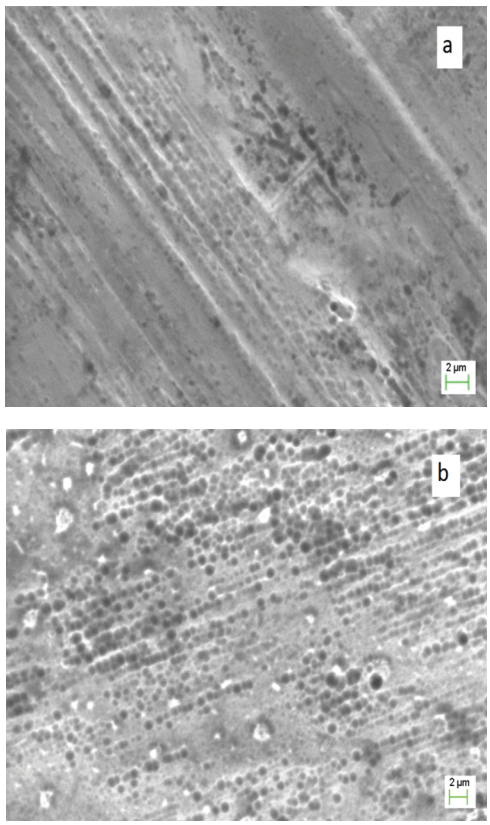

Fig. 8. SEM micrographs of $Zr_{59}Nb_3Cu_{20}Ni_8Al_{10}$ glassy alloy after immersion in (a) 1 M and (b) 11.5 M aqueous HNO_3 medium for 480 hr at room temperature.

4. DISCUSSION

In electrochemical investigations, it is found that the corrosion potential shifts towards more positive values with the increase in the concentration of nitric acid for both amorphous alloys as shown in Figures 2 and 4, which is attributed to the higher oxidizing power of nitric acid.[11] Judging from the potentiodynamic polarization curve shown in Figures 3 and 5, the $Zr_{60}Nb_2Cu_{20}Ni_8Al_{10}$ glassy alloy shows higher corrosion current density than $Zr_{59}Nb_3Cu_{20}Ni_8Al_{10}$ glassy alloy in 1 M HNO_3 solution with a clear passive range at room temperature. It means in 1 M HNO_3 solution $Zr_{59}Nb_3Cu_{20}Ni_8Al_{10}$ glassy alloy shows better corrosion resistance than $Zr_{60}Nb_2Cu_{20}Ni_8Al_{10}$ glassy alloy. It is well known that amorphous alloys consist of structurally and chemically homogeneous single phase solid solutions, which do not contain crystalline defects, such as grain boundaries or dislocations, acting as nucleation sites for corrosion, and thus the amorphous state provides the formation of a uniform passive

RESEARCH ARTICLE

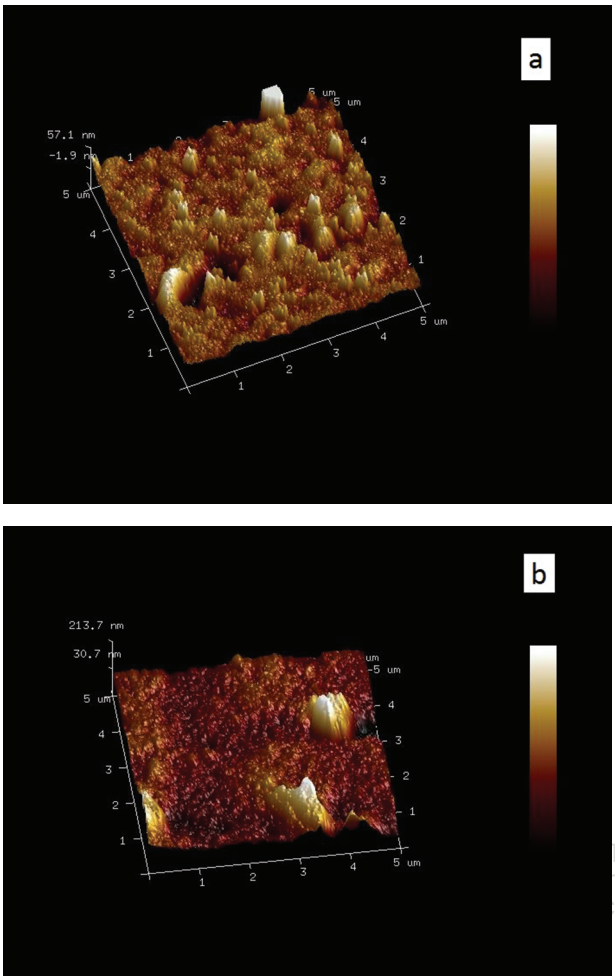

Fig. 9. AFM micrographs of $Zr_{60}Nb_2Cu_{20}Ni_8Al_{10}$ glassy alloy after immersion in (a) 1 M and (b) 11.5 M aqueous HNO_3 medium for 480 hr at room temperature.

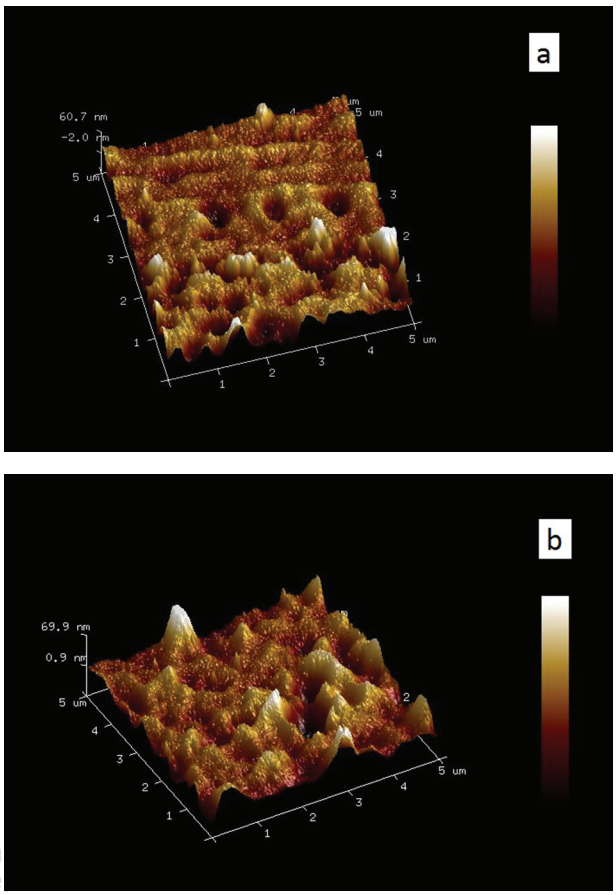

Fig. 10. AFM micrographs of $Zr_{59}Nb_3Cu_{20}Ni_8Al_{10}$ glassy alloy after immersion in (a) 1 M and (b) 11.5 M aqueous HNO_3 medium for 480 hr at room temperature.

film without weak points with respect to corrosion.[12] Potentiodynamic polarization curve in Figure 3 indicates the formation of less protective surface films on the $Zr_{60}Nb_2Cu_{20}Ni_8Al_{10}$ glassy alloy as the concentration of HNO_3 increased whereas $Zr_{59}Nb_3Cu_{20}Ni_8Al_{10}$ glassy alloy shows clear passive range in all 1 M, 6 M and 11.5 M HNO_3 solutions. The potentiodynamic polarization curves reveal the fact that $Zr_{59}Nb_3Cu_{20}Ni_8Al_{10}$ glassy alloy shows better corrosion resistance than $Zr_{60}Nb_2Cu_{20}Ni_8Al_{10}$ glassy alloy. In their study, Homozava et al.[13] has investigated the corrosion behavior of Nb containing Zr based amorphous $Zr_{58.5}Cu_{15.6}Ni_{12.8}Al_{10.3}Nb_{2.8}$ alloy in 1 M HNO_3 and 1 M HCl medium. In this study the detection limits of all elements potentially dissolved from $Zr_{58.5}Cu_{15.6}Ni_{12.8}Al_{10.3}Nb_{2.8}$ alloy were calculated based on a 3σ method. It was found that the dissolution of Ni in nitric acid was below the detection limit and Zr and Nb was described by a very reduced dissolution rate as compared to Al and Cu. This could be possibly due to the oxidizing nature of HNO_3 and it is also applicable in our present study.

The corrosion rate for both $Zr_{62-X}Nb_XCu_{20}Ni_8Al_{10}$ ($X = 2$ and 3) glassy alloys in 1 M, 6 M and 11.5 M aqueous HNO_3 medium at room temperature kept for 480 h has been shown in Figure 6. It can be observed from Figure 6 that $Zr_{59}Nb_3Cu_{20}Ni_8Al_{10}$ glassy alloy has better corrosion resistance than $Zr_{60}Nb_2Cu_{20}Ni_8Al_{10}$ glassy alloy. Pang et al.[9] has reported that the addition of Nb effectively improves the corrosion resistance of the Zr-based glassy alloys in 1 N HCl, 3% NaCl and 1 N H_2SO_4 solution at room temperature. In present investigation, it can be suggested that the addition of Nb improves the corrosion resistance in nitric acid solution, which means that the selection of alloy composition is of great importance in finding its corrosion behaviour in aqueous HNO_3.

In order to further decipher the corrosion behavior of the $Zr_{62-X}Nb_XCu_{20}Ni_8Al_{10}$ ($X = 2$ and 3) glassy alloys, scanning electron microscopy was employed to investigate the morphology of the samples after immersion in 1 M and 11.5 M HNO_3 medium for 480 hour at room temperature. Figures 7(a) and (b) shows the micrographs of $Zr_{60}Nb_2Cu_{20}Ni_8Al_{10}$ glassy alloy after immersion in 1 M and 11.5 M aqueous HNO_3 medium for 480 hr at room temperature respectively. It can be seen that Figure 7(a)

shows clean surface as compare to Figure 7(b) which means $Zr_{60}Nb_2Cu_{20}Ni_8Al_{10}$ alloy in 1 M HNO_3 solution is less corroded than in 11.5 M HNO_3 solution. Similarly, $Zr_{59}Nb_3Cu_{20}Ni_8Al_{10}$ glassy alloy is less corroded in 1 M HNO_3 (Fig. 8(a)) than in 11.5 M HNO_3 media (Fig. 8(b)). It can be further observed from Figures 7 and 8 that the surface of $Zr_{59}Nb_3Cu_{20}Ni_8Al_{10}$ glassy alloy contains more inhomogeneous granular pockets of oxides as compared to $Zr_{60}Nb_2Cu_{20}Ni_8Al_{10}$ alloy. XPS analysis of $Zr_{58.5}Cu_{15.6}Ni_{12.8}Al_{10.3}Nb_{2.8}$ alloy before and after immersion in acidic medium has been carried out by Homazava et al.[13] in which they have reported that the oxide film formed on the surface of alloy was consist mainly of ZrO_2 with smaller fraction of Al oxide and very small amount of Cu-, Nb- and Ni-oxides. The Nb element is present in the form of Nb_2O_5 in oxide film. It is well known that oxides of Zr and Nb possess a high corrosion resistance in a wide range of pHs.[14] It can be suggested from present study that the oxide film formed on the surface of $Zr_{60}Nb_2Cu_{20}Ni_8Al_{10}$ and $Zr_{59}Nb_3Cu_{20}Ni_8Al_{10}$ glassy alloys consist the oxides of Zr and Nb element, which play an important role in improving the corrosion resistance of the alloy in aqueous nitric acid medium. The oxide film present on the surface of $Zr_{59}Nb_3Cu_{20}Ni_8Al_{10}$ glassy alloy has a greater amount of Nb_2O_5 as compare to $Zr_{60}Nb_2Cu_{20}Ni_8Al_{10}$ glassy alloy due to the greater atomic percentage of Nb in $Zr_{59}Nb_3Cu_{20}Ni_8Al_{10}$ alloy and this leads to the better corrosion resistance of $Zr_{59}Nb_3Cu_{20}Ni_8Al_{10}$ glassy alloy in aqueous HNO_3. SEM results indicates the possibility of pilling off of the passive film formed on the $Zr_{60}Nb_2Cu_{20}Ni_8Al_{10}$ alloy at 11.5 M HNO_3 (Fig. 7(b)).

In order to verify this, AFM scans of these samples were recorded as shown in Figures 9 and 10. The dark region in Figure 9(b) shows that the passive film on $Zr_{60}Nb_2Cu_{20}Ni_8Al_{10}$ alloy at 11.5 M HNO_3 has been pilled off which can also be seen in SEM micrograph by circled region (Fig. 7(b)), whereas the trench like structure in AFM micrographs (Fig. 10(b)) of $Zr_{59}Nb_3Cu_{20}Ni_8Al_{10}$ glassy alloy in 11.5 M HNO_3 shows the inhomogeneous dissolution of passive film thereby forming a non-uniform film on the surface of the alloy, which is also supported by the SEM micrograph (Fig. 8(b)).

5. CONCLUSIONS

(1) The value of corrosion current density of $Zr_{62-X}Nb_XCu_{20}Ni_8Al_{10}$ ($X = 2$ and 3) glassy alloys were found to be comparable in aqueous HNO_3 solution, though the formation of passive film on the surface of $Zr_{59}Nb_3Cu_{20}Ni_8Al_{10}$ alloy was found more protective than the $Zr_{60}Nb_2Cu_{20}Ni_8Al_{10}$ alloy, thereby increasing the corrosion resistance of $Zr_{59}Nb_3Cu_{20}Ni_8Al_{10}$ alloy.
(2) It can be concluded from weight loss measurement that the corrosion rate of these glassy alloys increases with increasing concentration of nitric acid. The overall corrosion resistance of $Zr_{59}Nb_3Cu_{20}Ni_8Al_{10}$ glassy alloy was found to be better than $Zr_{60}Nb_2Cu_{20}Ni_8Al_{10}$ alloy in 1 M and 11.5 M HNO_3 solution.
(3) SEM and AFM micrographs also support the result of corrosion studies and shows the presence of inhomogeneous passive film on the surface of $Zr_{62-X}Nb_XCu_{20}Ni_8Al_{10}$ ($X = 2$ and 3) glassy alloys.

Acknowledgments: The financial support for this work under BRNS/DAE Research project No. 2011/36/44-BRNS/1974 is gratefully acknowledged. Thanks are due to Dr. U. Kamachi Mudali, CSTG, IGCAR-Kalpakkam, for providing the Zr-based metallic glass alloy for this investigation and we are also thankful to Dr. J. Jayaraj, CSTG, IGCAR-Kalpakkam, for his help and support in this work.

References and Notes

1. A. Inoue, *Acta Mater.* 48, 277 (**2000**).
2. J. F. Loeffler, *Intermet.* 11, 529 (**2003**).
3. T. Zhang, A. Inoue, and T. Masumoto, *Mater. Trans. JIM* 32, 1005 (**1991**).
4. H. Yongjiang, S. Jianfei, Y. Xin, and S. Jun, *Rare Metal Mat. Eng.* 37, 391 (**2008**).
5. U. K. Mudali, S. Baunack, J. Eckert, L. Schultz, and A. Gebert, *J. Alloys Compd.* 377, 297 (**2004**).
6. V. Schroeder and R. O. Ritchie, *Acta. Mater.* 54, 1785 (**2004**).
7. S. Buzzi, K. Jin, Peter J. Uggowitzer, S. Tosatti, I. Gerber, and J. F. Loffler, *Intermet.* 14, 729 (**2006**).
8. N. Homozava, A. Shkabko, D. Longvinovich, V. Krahenbuhl, and A. Ulrich, *Intermet.* 16, 1066 (**2008**).
9. S. Pang, T. Zhang, H. Kimura, K. Asami, and A. Inoue, *Mater. Trans. JIM* 41, 1490 (**2000**).
10. S. Baunack, U. K. Mudali, and A. Gebert, *Appl. Surf. Sci.* 252, 162 (**2005**).
11. P. Fauvet, F. Balbaud, R. Robin, Q.-T. Tran, A. Mugnier, and D. Espinoux, *J. Nucl. Mater.* 375, 52 (**2008**).
12. K. Hashimoto, K. Osada, T. Masumoto, and S. Shimodaira, *Corros. Sci.* 16, 71 (**1976**).
13. N. Homazava, A. Shkabko, D. Logvinovish, U. Krahenbuhl, and A. Ulrich, *Intermat.* 16, 1066 (**2008**).
14. M. Pourbaix, Atlas of electrochemical equilibria in aqueous solutions, National Association of Corrosion Engineers, Brussels (**1974**).

Received: 26 September 2014. Accepted: 11 November 2014.

Anti-Corrosion Methods and Materials

Corrosion behavior of amorphous $Zr_{59}Nb_3Al_{10}Ni_8Cu_{20}$ alloy in aqueous HNO_3 media

Poonam Sharma Anil Dhawan S. K. Sharma

Corrosion behavior of amorphous $Zr_{59}Nb_3Al_{10}Ni_8Cu_{20}$ alloy in aqueous HNO_3 media

Poonam Sharma
Department of Physics, Malaviya National Institute of Technology, Jaipur, India and
Department of Physics, Anand International College of Engineering, Jaipur, India
Anil Dhawan
Department of Physics, Anand International College of Engineering, Jaipur, India, and
S.K. Sharma
Department of Physics, Malaviya National Institute of Technology, Jaipur, India

Abstract

Purpose – The purpose of this paper was to investigate the corrosion behavior of the $Zr_{59}Nb_3Al_{10}Ni_8Cu_{20}$ amorphous alloy in aqueous 1M, 6M and 11.5M HNO_3 media using potentiodynamic polarization and weight loss determinations.

Design/methodology/approach – The electrochemical study, weight loss analysis and surface investigation were carried out on amorphous $Zr_{59}Nb_3Al_{10}Ni_8Cu_{20}$ alloy that had been immersed in aqueous HNO_3 medium at room temperature to understand the corrosion behavior of Zr-based amorphous $Zr_{59}Nb_3Al_{10}Ni_8Cu_{20}$ alloy. The amorphous state of the alloy was investigated using X-ray diffraction. Electrochemical studies were carried out in aqueous 1M, 6M and 11.5M HNO_3 media by recording open circuit potential/time and potentiodynamic polarization characteristics. Optical microscopy and scanning electron microscopy were used to examine the surface morphology of the alloy after the electrochemical tests and weight loss determinations.

Findings – The electrochemical results revealed that E_{corr} values shifted toward more noble values, as the concentration of the nitric acid was increased, and this was attributed to the higher oxidizing power of the nitric acid. The higher value of corrosion current density was obtained for the $Zr_{59}Nb_3Al_{10}Ni_8Cu_{20}$ amorphous alloy in aqueous 11.5M HNO_3 medium at room temperature. The optical microscopy and scanning electron microscopy examinations revealed that the formation of protective oxide layer on the surface of amorphous $Zr_{59}Nb_3Al_{10}Ni_8Cu_{20}$ alloy leads to the improvement in the corrosion behavior in nitric acid medium at room temperature.

Originality/value – The results can be helpful in finding the suitable material for fuel reprocessing applications.

Keywords Corrosion, Electrochemistry, Microscopy, Materials

Paper type Research paper

1. Introduction

Reprocessing of spent nuclear fuel used in fast breeder reactors involves use of nitric acid at high concentrations and temperatures for the dissolvers and evaporators, which are operated in highly corrosive conditions. To ensure reliable, safe and economic operation of reprocessing plants, the development of highly corrosion resistant materials with high reliability is necessary. Three criteria are considered for this purpose:

1 stabilizing of the passive film to reduce dissolution;
2 enhancing the passive range by shifting the transpassive conditions to more noble potentials; and
3 the development of improved alloys with better corrosion resistance properties (Raj *et al.*, 2006, 2000).

Austenitic stainless steel (SS) with low carbon content are widely used in spent nuclear fuel reprocessing plants, owing to their good corrosion resistance, but they are sensitive to intergranular attack in such environments (Shaw *et al.*, 1984; Davison *et al.*, 1997; Mudali *et al.*, 1993; Tsuji *et al.*, 1987). Ningshen *et al.* (2009, 2011) has reported that nitric acid grade SS shows good corrosion resistance at higher concentrations of nitric acid, but it is also susceptible to intergranular corrosion. Studies have been carried out to explore Zr, Ti and Ti-based alloys as alternatives to austenitic

The current issue and full text archive of this journal is available on Emerald Insight at: **www.emeraldinsight.com/0003-5599.htm**

Anti-Corrosion Methods and Materials
63/2 (2016) 97–104

[DOI 10.1108/ACMM-04-2014-1370]

The financial support for this work under BRNS/DAE Research project No. 2011/36/44-BRNS/1974 is gratefully acknowledged. Thanks are due to Dr U. Kamachi Mudali, CSTG-IGCAR-Kalpakkam, for providing the Zr-based metallic glass alloy for this investigation. The SEM facility provided by the USIC, Department of Physics, University of Rajasthan, Jaipur, is also gratefully acknowledged.

Received 7 April 2014
Revised 24 July 2014
Accepted 13 July 2015

stainless steels (Mudali *et al.*, 1993; Kapoor *et al.*, 2003; Jayaraj *et al.*, 2012).

The excellent corrosion resistance of zirconium in nitric acid has been known for over 50 years (Yau, 1984). In an investigation, it was found that Zircaloy-4 exhibited superior corrosion resistance in both wrought and welded condition to 11.5 M HNO_3, in comparison to CP-Ti, Ti–5 per cent Ta, and Ti–5 per cent Ta–1.8 per cent Nb alloys(Ravishankar *et al.*, 2007). Zr-based bulk amorphous alloys have been developed and are expected to be used as engineering materials in many potential applications (Heilmaier, 2001; Inoue *et al.*, 1999; Kawamura *et al.*, 1998; Qin *et al.*, 2004). To investigate the performance of highly corrosion resistant amorphous alloy, potentiodynamic polarization studies were carried out by Dhawan *et al.* (2007) on $Zr_{46.75}Ti_{8.25}Cu_{7.5}Ni_{10}Be_{27.5}$, $Zr_{65}Cu_{17.5}Ni_{10}Al_{7.5}$, $Zr_{67}Ni_{33}$ and $Ti_{60}Ni_{40}$ amorphous alloys that were exposed in aqueous HNO_3 solutions of varying concentrations. The higher glass-forming ability (GFA) was also a point of concern, along with evaluation of the improved mechanical and electrochemical properties. Caltech group reported that Nb-containing Zr-based alloys, such as $Zr_{57}Nb_5Cu_{15.4}Ni_{12.6}Al_{10}$ (Vit 106) and $Zr_{58.5}Nb_{2.8}Cu_{15.6}Ni_{12.8}Al_{10.3}$ (Vit 106a), exhibit outstanding GFAs, which allow relatively easy processing to obtain fully amorphous bulk materials (Choi-Yim and Johnson, 1997; Hays *et al.*, 2000). The corrosion properties of the Nb- and Ti-containing alloys were studied in comparison to those of the bulk glass-forming $Zr_{55}Cu_{30}Al_{10}Ni_5$ alloy in aqueous electrolytes of Na_2SO_4 and NaCl. It was found that Nb- and Ti-containing alloys exhibited increased corrosion resistance, especially in chloride solutions, as compared to the $Zr_{55}Cu_{30}Al_{10}Ni_5$ alloy (Raju *et al.*, 2002). In a further investigation, it was found that the resistance to pitting corrosion in HCl solution can be improved by the addition of Nb in the $Zr_{65}Al_{7.5}Ni_{10}Cu_{17.5}$ alloy (Fang-Quin *et al.*, 2004). Nb-containing Ni-based bulk amorphous alloys (Qin *et al.*, 2009a; 2009b) and Nb-containing Ti-based alloys (Mythili *et al.*, 2010) have been studied in nitric acid medium at boiling temperature, but only a limited information is available in the literature on corrosion behavior of Nb-containing Zr-based bulk amorphous alloy in nitric acid media.

The motivation for the present study was derived from the need for a highly corrosion resistant amorphous alloy for service in nitric acid environments for fuel reprocessing applications. The interest for the present investigation resulted primarily from the lack of sufficient data in the literature on the corrosion behavior of the amorphous $Zr_{59}Nb_3Al_{10}Ni_8Cu_{20}$ alloy in nitric acid environments. In consequence, during the present investigation, the corrosion behavior of amorphous $Zr_{59}Nb_3Al_{10}Ni_8Cu_{20}$ alloy in aqueous HNO_3 medium was studied using potentiodynamic polarization and weight loss determinations.

2. Experimental

2.1 Materials and microstructural characterization

As-received glassy ribbons of $Zr_{59}Nb_3Al_{10}Ni_8Cu_{20}$ alloy, 0.03 mm in thickness and 3 mm in width, were used for the investigation. The specimens were cleaned with distilled water and acetone and dried in air. The microstructural characterization of the specimen was performed using X-ray diffraction (Bruker XRD) with monochromatic CuKα radiations.

2.2 Electrochemical measurement

The corrosion behavior of the glassy $Zr_{59}Nb_3Al_{10}Ni_8Cu_{20}$ alloy was evaluated using potentiodynamic polarization tests. For polarization experiments, a potentiostat (Autolab-AUT84276) was connected to a three-electrode cell which used a saturated calomel reference electrode, Pt counter electrode and $Zr_{59}Nb_3Al_{10}Ni_8Cu_{20}$ glassy alloy as the working electrode. The open circuit potential (OCP) was monitored for 1,800 s prior to all the tests. The potentiostat was interfaced with Nova (version 1.9) software for measuring the change in OCP with immersion time and to conduct the polarization experiments. Potentio-dynamic polarization tests were conducted in 1 M, 6 M and 11.5 M HNO_3 at room temperature. Both sides of the glassy ribbon samples were cleaned with acetone and distilled water prior insertion into the test solution. The exposed surface area of the sample was 1.5 × 0.3 cm. The potentiodynamic polarization experiments were carried out at a scanning rate 1 mV/s from 200 mV below OCP to 2,200 mV above it. All of the electrode potentials were measured against the Ag/AgCl (saturated KCl) reference electrode. All the polarization plots were almost reproducible.

2.3 Weight loss exposures

As-spun ribbon specimens of $Zr_{59}Nb_3Al_{10}Ni_8Cu_{20}$ alloy were cut in same size and were cleaned with distilled water, acetone and dried in air. The surface area and initial mass of each sample were measured, and the samples then were immersed into the corrosive media of 1 M, 6 M and 11.5 M HNO_3 at room temperature. Each sample was weighed after immersion in the 1 M, 6 M and 11.5 M HNO_3 media for 120, 240 and 360 h. The corrosion rates were determined by using formula (Fontana, 2005):

$$CorrosionRate(mm/year) = \frac{87.6(W)}{DAT}$$

Where,

W = Weight loss in milligram
D = Density in gm/cm^3
A = Surface area in cm^2
T = Time in hours

2.4 Corroded surface examination

To study the surface morphology of the amorphous $Zr_{59}Nb_3Al_{10}Ni_8Cu_{20}$ alloy after exposure in the polarization tests in 1 M, 6 M and 11.5 M HNO_3 aqueous media, an optical microscope (METZER-M) and scanning electron microscope (Mini SEM SNE-3000M Model) were used. The optical microscopic view of a virgin $Zr_{59}Nb_3Al_{10}Ni_8Cu_{20}$ alloy and after its immersion in 1 M, 6 M and 11.5 M HNO_3 media was carried out with the help of METZER-M Microscope. SEM images of similar samples were undertaken using a ZEISS- EVO 18 SEM.

3. Results

To evaluate the condition of the $Zr_{59}Nb_3Al_{10}Ni_8Cu_{20}$ alloy, XRD of the specimen was performed, and the result is shown in Figure 1.

3.1 Corrosion analysis

The corrosion parameters shown in Table I such as corrosion potential E_{corr}, corrosion current density I_{corr}, passive potential E_{pass} and transpassive potential E_{TP} were obtained from the polarization curve and are shown in Figure 2. Similar data were recorded for $Zr_{59}Nb_3Al_{10}Ni_8Cu_{20}$ alloy exposed in 1 M, 6 M and 11.5 M HNO_3 media. It can be observed from the potentiodynamic polarization curve (Figure 2) that the alloy $Zr_{59}Nb_3Al_{10}Ni_8Cu_{20}$ showed active, passive and transpassive behavior in the aqueous 1 M, 6 M and 11.5 M HNO_3 media and that the passive regions lie in the potential ranges 1.119 to 2.072 V, 1.263 to 2.024 V and 1.341 to 2.110 V, respectively. It also was observed that for $Zr_{59}Nb_3Al_{10}Ni_8Cu_{20}$ alloy, the value of the corrosion current density (I_{corr}) increased with increase in the concentration of nitric acid. In 1 M HNO_3 concentration, the polarization curve exhibited a wider passive range with low passive current density, while at higher concentrations of nitric acid, the passive range became narrower.

The corrosion rate of amorphous $Zr_{59}Nb_3Al_{10}Ni_8Cu_{20}$ alloy was calculated using weight loss determinations in 1 M, 6 M and 11.5 M nitric acid. The plot of the corrosion rate in different concentrations of HNO_3 at room temperature is shown in Figure 3. The corrosion rate is very low in 1 M and 6 M HNO_3 medium in comparison to 11.5 M HNO_3. The corrosion rate increased slightly with time at lower concentrations of nitric acid, but at 11.5 M HNO_3, the corrosion rate decreased with the increase in time.

Figure 1 XRD pattern of the $Zr_{59}Nb_3Al_{10}Ni_8Cu_{20}$ alloy

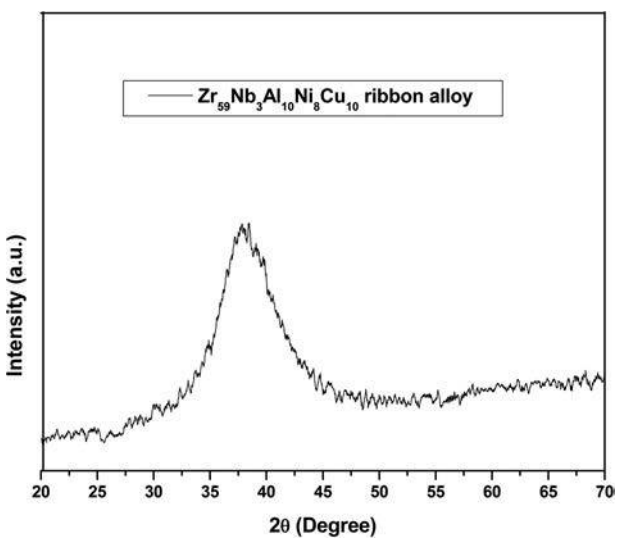

Table I Polarization parameter of amorphous $Zr_{59}Nb_3Al_{10}Ni_8Cu_{20}$ alloy in 1 M, 6 M, 11.5 M HNO_3 media at room temperature

Concentration of HNO_3	E_{corr}/V	I_{corr}/nA cm^{-2}	E_{pass}/V	E_{TP} /V
1 M	0.014 ± 0.005	0.936 ± 0.33	1.119 ± 0.013	2.072 ± 0.023
6 M	0.322 ± 0.031	6.942 ± 1.70	1.264 ± 0.017	2.024 ± 0.006
11.5 M	0.885 ± 0.003	65.351 ± 1.80	1.349 ± 0.025	2.110 ± 0.010

Figure 2 Potentiodynamic polarization curve of bulk amorphous $Zr_{59}Nb_3Al_{10}Ni_8Cu_{20}$ alloy in 1M, 6M and 11.5M HNO_3 medium at room temperature

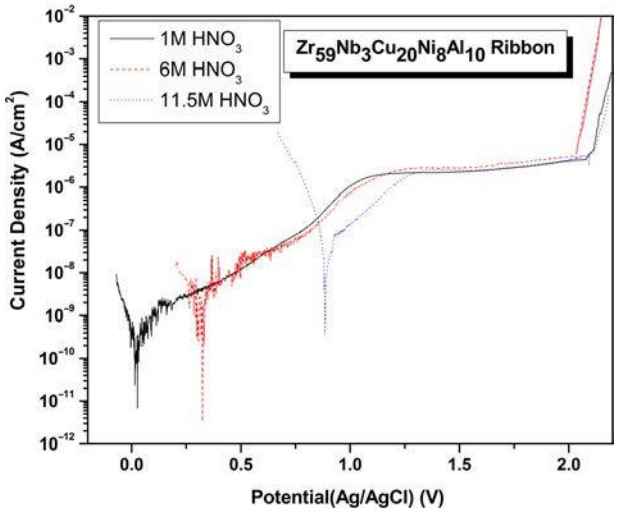

Figure 3 Corrosion rate of $Zr_{59}Nb_3Al_{10}Ni_8Cu_{20}$ alloy in different concentration of HNO_3 at room temperature

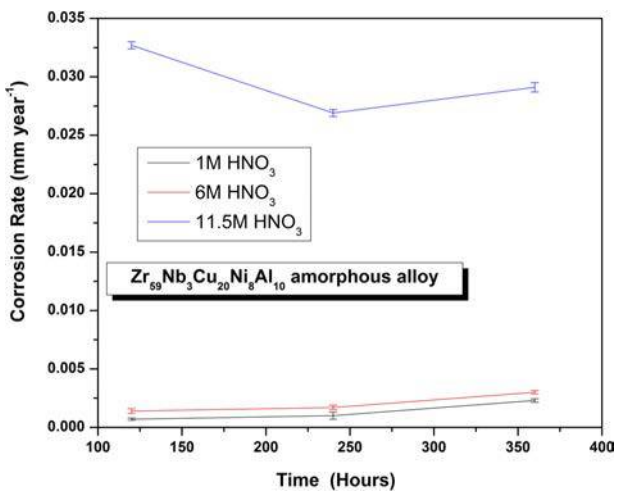

3.2 Surface morphology

The optical micrographs and SEM images of the $Zr_{59}Nb_3Al_{10}Ni_8Cu_{20}$ alloy after potentiodynamic polarization studies in 1 M, 6 M and 11.5 M HNO_3 at room temperature are shown in Figures 4 and 5, respectively. Some significant changes were observed on the surface condition of the samples that had been exposed in 11.5 M HNO_3 after the electrochemical measurements. The optical microstructure of amorphous $Zr_{59}Nb_3Al_{10}Ni_8Cu_{20}$ alloy before exposure and after immersion in 1 M, 6 M and 11.5 M HNO_3 at room temperature for 360 h are shown in Figure 6. The effect of

Figure 4 Optical micrographs of $Zr_{59}Nb_3Al_{10}Ni_8Cu_{20}$ alloy after potentiodynamic polarization studies in (a) 1M aqueous HNO_3 (b) 6M aqueous HNO_3 and (c) 11.5M aqueous HNO_3 medium at room temperature

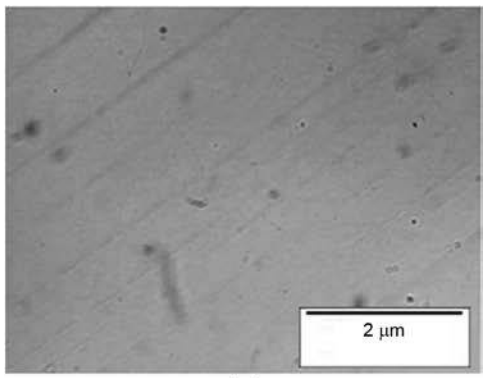

(a)

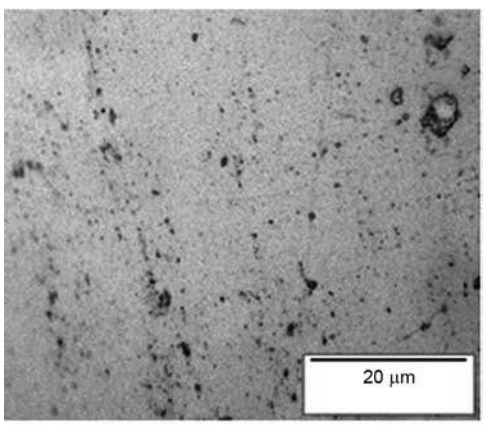

(b)

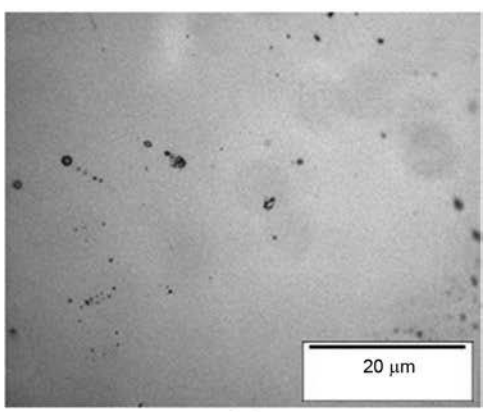

(c)

aqueous HNO_3 medium on the surface of the alloy can be seen in the given microstructures. As the concentration of HNO_3 was increased, the alloy $Zr_{59}Nb_3Al_{10}Ni_8Cu_{20}$ exhibited peeling of the surface at some places. The optical microstructure of $Zr_{59}Nb_3Al_{10}Ni_8Cu_{20}$ alloy after exposure in 11.5 M HNO_3 shows [Figure 6(d)] significant changes on the surface of the alloy in the form of small pockets and patches at various places on the surface. To better understand the corrosion behavior of the $Zr_{59}Nb_3Al_{10}Ni_8Cu_{20}$ alloy, SEM

Figure 5 SEM micrographs of $Zr_{59}Nb_3Al_{10}Ni_8Cu_{20}$ alloy after potentiodynamic polarization studies in (a) 1M aqueous HNO_3 (b) 6M aqueous HNO_3 and (c) 11.5M aqueous HNO_3 medium at room temperature

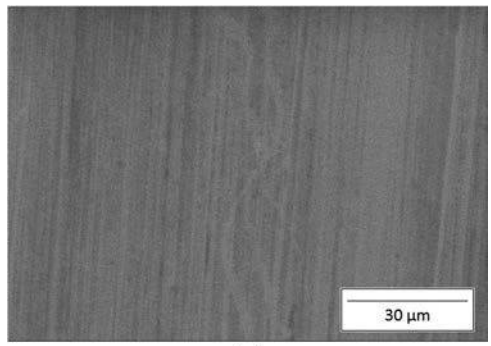

(a)

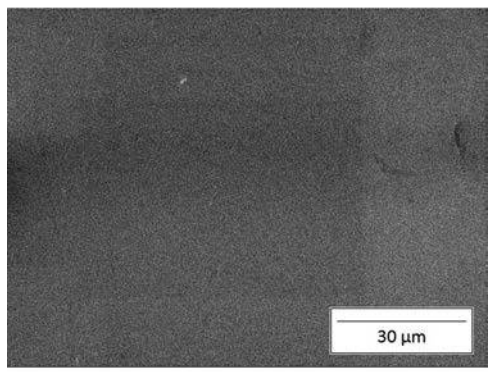

(b)

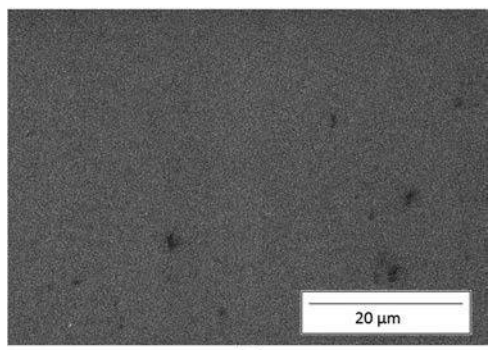

(c)

was used to investigate the morphologies of the samples after immersion in 1 M, 6 M and 11.5 M HNO_3 medium for 360 h at room temperature. Figure 7 shows SEM micrographs of $Zr_{59}Nb_3Al_{10}Ni_8Cu_{20}$ alloy after immersion in the nitric acid environments.

4. Discussion

The XRD pattern of the specimen shown in Figure 1 indicates that the typical broad maxima were especially pronounced in the range from 31° to 45°, suggesting that the $Zr_{59}Nb_3Al_{10}Ni_8Cu_{20}$ alloy is predominantly amorphous. No significant peaks corresponding to crystalline phases were identified.

Figure 6 Optical micrographs of $Zr_{59}Nb_3Al_{10}Ni_8Cu_{20}$ alloy

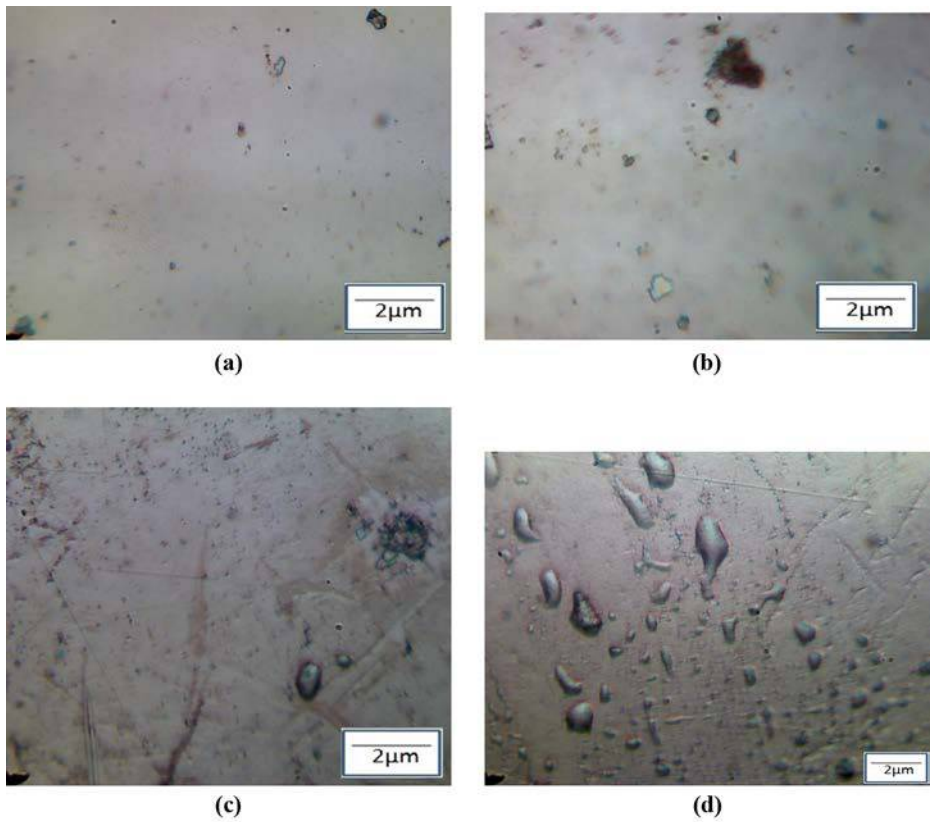

Notes: (a) As spun ribbon and after exposure in; (b) 1M aqueous HNO_3; (c) 6M aqueous HNO_3; (d) 11.5M aqueous HNO_3 medium for 360 h at room temperature

As regards the electrochemical investigation, the amorphous $Zr_{59}Nb_3Al_{10}Ni_8Cu_{20}$ alloy was passivated spontaneously with low passive current density in 1 M, 6 M and 11.5 M concentrations of HNO_3 at room temperature, as can be seen in Figure 2. It is suggested that the alloy probably undergoes general corrosion and may tend to form a protective oxide film on the surface of the alloy in the aqueous HNO_3 medium. However, in the present study, the potentiodynamic polarization test was conducted up till transpassive region (Figure 2), so dissolution of the passive film that formed on the surface of the alloy was initiated. It was further observed that the corrosion potential shifted toward more positive values with increasing concentration of nitric acid, which was attributed to the higher oxidizing power of the acid (Fauvet *et al.*, 2008). The increase in the I_{corr} values with the increase in the concentration of nitric acid is indicative of the severity of the environment, but the passive current densities for 1 M, 6 M and 11.5 M concentration of HNO_3 were quite similar, as is evident from Figure 2. It was revealed by the potentiodynamic polarization curve (Figure 2) that $Zr_{59}Nb_3Al_{10}Ni_8Cu_{20}$ alloy with a low OCP initially dissolved in 1M HNO_3 solution and soon reached a very stable condition with increasing applied potential. Similar behavior was observed for the same alloy in 6 M HNO_3 solution, but at the highest concentration of HNO_3, the alloy showed a high corrosion current density. Raju *et al.* (2002) observed that thin passive layer films are formed on bulk amorphous $Zr_{59}Nb_3Al_{10}Ni_8Cu_{20}$ alloy in Na_2SO_4 solution that are significantly more enriched in copper and nickel species close to the interface oxide/alloy. In the present study, dissolution of Cu and Ni appears to occur possibly due to the smaller Goldschmidt's radii of Cu and Ni among the other elements. For example, the Goldschmidt's radii of Zr, Cu, Al, Ni and Nb are 0.160, 0.128, 0.143, 0.125, and 0.147, respectively, and therefore the mobility of these atoms is quite high. Thus, the Cu and Ni atoms that are underlying the native oxide film may reach the surface by a tunneling process due to applied potential during electrochemical corrosion, and they are dissolved at the interface with the test environment (Jayaraj *et al.*, 2009). Baunack *et al.* (2005) reported that electrochemically treated Nb-containing Zr-based alloys show a distinct enrichment of metallic copper at the oxide/metal interface. Aluminum has a strong chemical affinity with Zr, for which the mixing enthalpy is −44 kJ/mol, and this value is very similar to that of the Zr–Ni bimetallic (i.e. −49kJ/mol), whereas the mixing enthalpy of Zr–Cu is −23kJ/mol. This means that the Zr–Cu bond is not stronger than the Zr–Al or Zr–Ni bonds (Takeuchi *et al.*, 2005), which may lead to the dissolution of Cu; this being weaker in bonding with the Zr. It has also been reported that the virgin surface of the $Zr_{65}Cu_{17.5}Ni_{10}Al_{7.5}$ had oxides of Zr and Al present on it, whereas Ni and Cu were present in the metallic forms (Sharma *et al.*, 2001).

The weight loss results show (Figure 3) that the higher corrosion rate of the amorphous $Zr_{59}Nb_3Al_{10}Ni_8Cu_{20}$ alloy in 11.5 M HNO_3 medium in comparison to 1 M and 6 M HNO_3 was due to the severity of environment. Figure 3 shows that in 11.5 M HNO_3, the corrosion rate decreased with the increase in time. It has been reported that the passivation speed of the Nb-containing Zr-based BMG sample was quickened with an increase in the concentration of the HNO_3 solution over a certain range and that its corrosion resistance also became stronger (Fang-Quin *et al.*, 2004). In the present study, at the higher concentration of the HNO_3 medium, a significant decrease in corrosion rate was observed over a limited concentration range, possibly due to the formation of a passive layer of niobium oxide.

The SEM results (Figure 5) clearly show that as the concentration of nitric acid increases, the oxidation layer formed on the surface of alloys improved. It can be seen that Nb-containing bulk amorphous alloy has a relatively smooth surface when exposed in an oxidizing medium. Figure 5 shows that, after potentiodynamic polarization studies in 1 M HNO_3 medium, an oxide layer had formed on the surface of alloy, as can be observed from Figures 7(a) and 5(a), comparing the SEM micrographs of virgin and electrochemically treated $Zr_{59}Nb_3Al_{10}Ni_8Cu_{20}$ alloy specimens in 1 M HNO_3. However, as the concentration of the oxidizing acid increased, the formation of the oxide layer also was enhanced. Both optical and SEM micrographs (Figures 4 and 5) confirmed that an oxidation layer was formed on the surface of the alloy in the nitric acid media, and that some dissolution of the oxidation layer was observed in 11.5 M HNO_3 [Figure 5(c)] due to the severity of the environment.

SEM micrographs obtained after the weight loss exposures show that as concentration of the nitric acid increased, the passive layer formation on the surface of alloy also increased. Figure 7(c) shows that the oxidation layer was not uniform in 6 M HNO_3, and in 11.5 M HNO_3, some granular inhomogeneous distribution of the oxide layer could be observed, as illustrated in Figure 7(d). It is possible that the passive layer of niobium oxide protects the alloy from corrosion because the Nb_2O_5 exhibits good corrosion resistance (Mythili *et al.*, 2010). The good corrosion behavior of $Zr_{59}Nb_3Al_{10}Ni_8Cu_{20}$ alloy in Na_2SO_4 solution was studied by Raju *et al.* (2002). In that study, niobium species were detected in the oxide layer region by Auger electron spectroscopy (AES) analysis, and the oxidized species of niobium which, as a valve metal in its pure state, tends to form spontaneously a very thin barrier-type oxide layer when exposed to air or humid environments. This participates in the passive layer formation on the amorphous alloys. In the present study, possibly this could be a reason of passive layer formation on surface of $Zr_{59}Nb_3Al_{10}Ni_8Cu_{20}$ alloy in nitric acid media. However, this requires further surface analytical studies by more sensitive methods, such as X-ray photoelectron spectroscopy (XPS).

Figure 7 SEM micrographs of $Zr_{59}Nb_3Al_{10}Ni_8Cu_{20}$ alloy

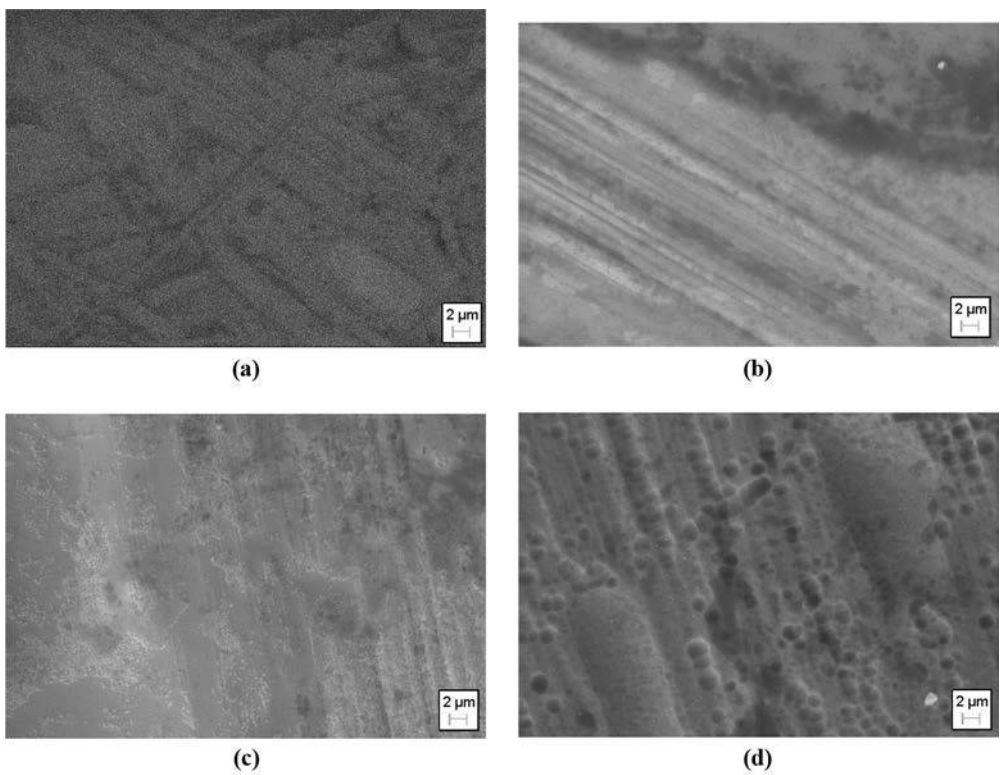

Notes: (a) As spun ribbon and after exposure in; (b) 1M aqueous HNO_3; (c) 6M aqueous HNO_3; (d) 11.5M aqueous HNO_3 medium for 360 h at room temperature

5. Conclusions

1 A comparison of the potentiodynamic polarization behavior of $Zr_{59}Nb_3Al_{10}Ni_8Cu_{20}$ alloy in 1 M, 6 M and 11.5 M HNO_3 at room temperature shows a clear passivity, but the alloy exhibited higher corrosion current density with the increase in the concentration of HNO_3.

2 The effect of passive layer formation at higher concentrations of aqueous HNO_3 during the potentiodynamic polarization studies were well-explained from the SEM micrographs, which showed a uniform oxide layer that formed on the surface of the alloy at higher acid concentrations.

3 The development of an oxide film was observed on the surface of $Zr_{59}Nb_3Al_{10}Ni_8Cu_{20}$ alloy, as illustrated by the SEM micrographs. The maximum oxide growth was found in 11.5 M HNO_3 and showed a granular morphology, possibly due to the formation of strong protective passive layer of Nb_2O_5, which is corrosion resistant in nitric acid media.

References

Baunack, S., Mudali, U.K. and Gebert, A. (2005), "Characterization of oxide layers on amorphous Zr- based alloys by Auger electron spectroscopy with sputter depth profiling", *Applied Surface Science*, Vol. 252 No. 1, pp. 162-166.

Choi-Yim, H. and Johnson, W.L. (1997), "Bulk metallic glass matrix composites", *Applied Physics Letters*, Vol. 71 No. 1, pp. 3808-3811.

Davison, R.M., DeBold, T. and Johnson, M.J. (1997), "Corrosion of stainless steel in corrosion", 9th edn, *ASM Handbook*, ASM International, Amsterdam, Vol. 13 No. 1, pp. 546-565.

Dhawan, A., Sachdev, K., Roychowdhury, S., De, P.K. and Sharma, S.K. (2007), "Potentiodynamic polarization studies in amorphous $Zr_{46.75}Ti_{8.25}Cu_{7.5}Ni_{10}Be_{27.5}$, $Zr_{65}Ni_{10}Cu_{17.5}Al_{7.5}$, $Zr_{67}Ni_{33}$ and $Ti_{60}Ni_{40}$ in aqueous HNO_3 solution", *Journal of Non-Crystalline Solids*, Vol. 353 No. 2, pp. 2619-2623.

Fang-Quin, Z., Zhi-Hao, C., Jin-Jue, T., Lan-Jun, L., Jin, Y. and Yun, X. (2004), "Corrosion resistance of Zr-Al-Ni-Cu(Nb) bulk amorphous alloys", *Transactions of Nonferrous Metals Society of China*, Vol. 14 No. 1, pp. 961-965.

Fauvet, P., Balbaud, F., Robin, R., Tran, Q.T., Mugnier, A. and Espinoux, D. (2008), "Corrosion mechanisms of austenitic stainless steels in nitric media used in reprocessing plants", *Journal of Nuclear Materials*, Vol. 375 No. 1, pp. 52-64.

Fontana, M.G. (2005), "Corrosion testing, 3rd edn", *Corrosion Engineering*, Tata Mcgraw-Hill, New York, NY, pp. 171-172.

Hays, C.C., Schroers, J., Geyer, U., Bossuyt, S., Stein, N. and Johnson, W.L. (2000), "Glass forming ability in the Zr-Nb-Ni-Cu-Al bulk metallic glasses", *Materials Science Forum*, Vols 343/346 No. 1, pp. 103-108.

Heilmaier, M. (2001), "Deformation behaviour Zr-based metallic glasses", *Journal of Materials Processing Technology*, Vol. 117 No. 1, pp. 374-380.

Inoue, A., Fan, C. and Takenchi, A. (1999), "High-strength bulk nanocrystalline alloys in a Zr-based system containing compound and glassy phases", *Journal of Non-Crystalline Solids*, Vols 250/251 No. 1, pp. 724-728.

Jayaraj, J., Gebert, A. and Schultz, L. (2009), "Passivation behavior of structurally relaxed $Zr_{48}Cu_{36}Ag_8Al_8$ metallic glass", *Journal of Alloys and Compounds*, Vol. 479 No. 1, pp. 257-261.

Jayaraj, J., Ravishankar, A. and Mudali, U.K. (2012), "Electrochemical and passive characterization of a beta type Zr45Zr38Al17 cast rod in nitric acid medium", *Electrochimica Acta*, Vol. 85 No. 1, pp. 210-219.

Kapoor, K., Kain, V., Gopalkrishna, T., Sanyal, T. and De, P.K. (2003), "High corrosion resistant Ti-5%Ta-1.8%Nb alloy for fuel reprocessing application", *Journal of Nuclear Materials*, Vol. 322 No. 1, pp. 36-44.

Kawamura, Y., Shibata, T., Inoue, A. and Masumoto, T. (1998), "Workability of the supercooled liquid in the $Zr_{65}Al_{10}Ni_{10}Cu_{15}$ bulk metallic glass", *Acta Materialia*, Vol. 46 No. 1, pp. 253-263.

Mudali, U.K., Dayal, R.K. and Gnanamoorthy, J.B. (1993), "Corrosion studies on materials of construction for spent nuclear fuel reprocessing plant equipment", *Journal of Nuclear Materials*, Vol. 203 No. 1, pp. 73-82.

Mythili, R., Saroja, S. and Vijayalakshmi, M. (2010), "Characterization of passive oxide film on a Ti–5%Ta–1.8%Nb alloy on exposure to severe oxidizing conditions", *Materials Characterization*, Vol. 61 No. 1, pp. 1326-1334.

Ningshen, S., Mudali, U.K., Amarendra, G. and Raj, B. (2009), "Corrosion assessment of nitric acid grade austenitic stainless steel", *Corrosion Science*, Vol. 51 No. 1, pp. 322-329.

Ningshen, S., Mudali, U.K., Ramya, S. and Raj, B. (2011), "Corrosion behavior of AISI type 304L stainless steel in nitric acid media containing oxidizing species", *Corrosion Science*, Vol. 53 No. 1, pp. 64-70.

Qin, C., Asami, K., Kimura, H., Zhang, W. and Inoue, A. (2009a), "Electrochemical and XPS studies of Ni-based metallic glasses in boiling nitric acid solutions", *Electrochimica Acta*, Vol. 54 No. 1, pp. 1612-1617.

Qin, C.L., Asami, K., Kimura, H., Zhang, W., Louzguine, D.V. and Inoue, A. (2009b), "High corrosion resistant Ni-based glassy alloys in boiling nitric acid solutions", *Materials Transactions*, Vol. 50 No. 6, pp. 1304-1307.

Qin, F.X., Zhang, H.F., Deng, Y.F., Ding, B.Z. and Hu, Z.Q. (2004), "Corrosion resistance of Zr-based bulk amorphous alloys containing Pd", *Journal of Alloys and Compounds*, Vol. 375 No. 1, pp. 318-323.

Raj, B. and Mudali, U.K. (2006), "Materials development and corrosion problems in nuclear fuel reprocessing plants", *Progress in Nuclear Energy*, Vol. 48 No. 1, pp. 283-313.

Raj, B., Mudali, U.K., Jayakumar, T., Kasiviswanathan, K.V. and Natarajan, R. (2000), "Meeting the challenges related to material issues in chemical industries", *Sadhana*, Vol. 25 No. 1, pp. 519-559.

Raju, V.R., Kuhn, U., Wolff, U., Schneider, F., Eckert, J., Reiche, R. and Gebert, A. (2002), "Corrosion behavior of Zr-based bulk glass forming alloys containing Nb or Ti", *Materials Letters*, Vol. 57 No. 1, pp. 173-177.

Ravishankar, A., Raju, V.R., Rao, M.N., Mudali, U.K., Khatak, H.S. and Raj, B. (2007), "Corrosion of Zircaloy-4 and its welds in nitric acid medium", *Corrosion Science*, Vol. 49 No. 9, pp. 3527-3538.

Sharma, S.K., Strunskus, T., Ladebusch, H. and Faupel, F. (2001), "Surface oxidation of amorphous $Zr_{65}Cu_{17.5}Ni_{10}Al_{7.5}$ and $Zr_{46.75}Ti_{8.25}Cu_{7.5}Ni_{10}Be_{27.5}$", *Materials Science and Engineering: A*, Vols 304/306 No. 1, pp. 747-752.

Shaw, R.D. and Elliott, D. (1984), "Stainless steel in UK nuclear fuel reprocessing plants", *Proceedings of Conference in Stainless Steels'1984*, *Gothenburg*, pp. 395-402.

Takeuchi, A. and Inoue, A. (2005), "Classification of bulk metallic glasses by atomic size difference, heat of mixing and period of constituent elements and its application to characterization of the main alloying element", *Materials Transactions*, Vol. 46 No. 12, pp. 2817-2829.

Tsuji, N., Ishikawa, K., Kishimoto, Y. and Hayashi, S. (1987), "Nuclear fuel reprocessing and waste management", *Nuclear Fuel Reprocessing and Waste Management Proceeding of International Conference, Society of French Nuclear Energy*, *Paris*, *23-27 August*, Vol. 3, p. 1203.

Yau, T.L. (1984), "Zirconium for nitric acid solutions", *Titanium and Zirconium in Industrial Applications Proceeding of Fourth ASTM Symposium*, Philadelphia, PA, 10-11 October, pp. 57-68.

About the authors

Poonam Sharma is pursuing her PhD from Department of Physics, Malaviya National Institute of Technology, Jaipur, India, under the supervision of Prof S.K. Sharma and co-supervision of Dr Anil Dhawan. She has received her MSc degree from Department of Physics at Malaviya National Institute of Technology, Jaipur. Her research interest includes the area of corrosion and oxidation study of bulk metallic glasses. She is working as a SRF under BRNS/DAE Research Project Grants No. 2011/36/44-BRNS/1974 under the guidance of Dr Anil Dhawan at Anand International College of Engineering, Jaipur. She has two international publication in her hand and presented research papers in National and International conferences. She has also completed her one project on Chaos at IISER, Mohali, India. In addition to this, she has attended a workshop on frontier materials at MNIT, Jaipur and completed a short-term course on "Nanotechnology and its applications" at MNIT, Jaipur.

Dr Anil Dhawan is a Professor and Head of Department of Physics at Anand International College of Engineering, Jaipur. He has received his PhD in physics (materials science) from University of Rajasthan, Jaipur (India) and carried out his PhD work at Malaviya National Institute of Technology, Jaipur. He has received his MSc (physics), COSIST specialization in Microwave Electronics from University of Rajasthan, Jaipur (India). His specific area of discipline is oxidation and corrosion studies of bulk metallic glasses. Recently, he received a research project entitled "Development of Zr and Ni - based metallic glasses and Surface modification for reprocessing applications" from BRNS/Department of Atomic Energy, Government of India. He has 15 years experience in the teaching field. In addition to this, he has the membership of Material Research Society of India. He has 30 national and international publications in hand and also is the author of *Engineering Physics-II* (B. Tech. II semester, RTU, Kota), 2011 edition; Publisher: Vayu Education of India, New Delhi, India. He is also a reviewer of *Journal of Non-crystalline solids* (North Holland, Amsterdam). He has attended and presented research papers in various conferences, and also one research paper has been presented by him for young achiever award in DAE solid state physics symposium at Thapar University, Patiala, Punjab, during 17-21 December, 2013. Anil Dhawan is the corresponding author and can be contacted at: dr.anildhawan11@gmail.com

Prof S.K. Sharma is a Professor at Malaviya National Institute of Technology, Jaipur. Formerly, he was a Senior Scientist at Bhabha atomic research centre, Mumbai, India, during 1978-1992 and a Scientist (CSIR Pool Scheme) at Rajasthan University during 1992-1995 and a Research scientist (DST India) at Rajasthan University during 1995-1996. He has been awarded by many international fellowship such as Max-Planck-Fellow (Germany, 1989), Humboldt fellow (Germany, 1990-1991), Research Scientist (Germany, 1992), Visiting Scientist (Germany, 1998-1999 and 2001-2002). He has received his PhD degree from Aligarh Muslim University, Aligarh, India, and carried out the work for PhD at BARC, India. He has completed his MPhil and MSc from Aligarh Muslim University, Aligarh, India. He also has good knowledge of English, Russian, German and Hindi. Prof S.K. Sharma has 96 national and international publications. He is also a reviewer for some international journal like *Journal of Materials Research* (Material Research Society, USA) and *Journal of Non-Crystalline Solids* (North Holland, Amsterdam). He has a life membership of IPA, IIM, IVS, MRSI, IPTA, ILA, ISTA, BARCOA, ISCA, IXS and IGS. He has been a Principal Investigator of research project funded by BRNS/DAE. At present, he is Principal Investigator of BRNS/DAE Research project entitled "SnO2 based microwave sintered combustible gas sensor: study of grain size effects in enhancing the gas sensing behavior ". Four students have been already awarded PhD degree under his supervision, and currently, four students are pursuing PhD under his supervision. His research interest area is diffusion and oxidation study of amorphous alloys and surface study using XPS and AES. Many key invited lectures have been delivered by him in national and international conferences.

Surface morphology study of Zr-based amorphous alloys after immersion in boiling nitric acid medium

Poonam Sharma, Anil Dhawan, and S. K. Sharma

Citation: AIP Conference Proceedings **1731**, 070021 (2016); doi: 10.1063/1.4947853
View online: http://dx.doi.org/10.1063/1.4947853
View Table of Contents: http://scitation.aip.org/content/aip/proceeding/aipcp/1731?ver=pdfcov
Published by the AIP Publishing

Surface Morphology Study Of Zr-Based Amorphous Alloys After Immersion In Boiling Nitric Acid Medium

Poonam Sharma[a,b], Anil Dhawan[a,*] and S. K. Sharma[b]

[a]*Department of Physics, Anand International College of Engineering, Jaipur 303012, India E-mail address:* *dr.anildhawan11@gmail.com

[b]*Department of Physics, Malaviya National Institute of Technology, Jaipur 302017, India*

Abstract. Weight loss studies have been performed to determine the corrosion resistance of amorphous $Zr_{60}Nb_2Al_{10}Ni_8Cu_{20}$ and $Zr_{59}Nb_3Al_{10}Ni_8Cu_{20}$ alloys in aqueous HNO_3 media at boiling temperature. The FESEM micrographs has been obtained to know the surface morphology of specimens after immersion in 11.5M boiling aqueous HNO_3 media. $Zr_{59}Nb_3Al_{10}Ni_8Cu_{20}$ alloy shows better corrosion resistance in nitric acid media than $Zr_{60}Nb_2Al_{10}Ni_8Cu_{20}$ alloy.

Keywords: Bulk amorphous alloys, Weight loss, FESEM, Corrosion Rates
PACS: 82.45.Bb, 81.05.Kf, 68.37.Hk

INTRODUCTION

Reprocessing of spent nuclear fuel used in Fast Breeder Reactors (FBRs) involves use of nitric acid of high concentrations and temperatures for dissolvers and evaporators which are highly corrosive. The materials chosen for the fabrication of such reprocessing plant equipment should possess excellent corrosion resistance, ease of fabricability and reliability [1,2]. An excellent corrosion resistant material is required for the fabrication of dissolver components. Zirconium and its alloys are highly resistant to nitric acid environments and are chosen for the construction of the most critical equipments in term of corrosion such as fuel dissolvers [3-6]. On the other hand, it is well known that bulk metallic glass (BMG) materials possess remarkable physical, chemical and mechanical properties [7,8]. Caltech group reported Nb containing Zr-based alloys, exhibiting outstanding GFA which allows relatively easy processing to obtain fully amorphous bulk material [9-10]. Nb containing Zr-based alloys [11] in nitric acid medium at room temperature, Nb containing Ni-based [12-13] and Ti-based alloys [14] in nitric acid medium at boiling temperature have been studied by the researcher but limited corrosion studies on Nb containing Zr based bulk amorphous alloy has been conducted in boiling nitric acid medium.

So, the aim of the present work is to investigate the corrosion behavior of the $Zr_{60}Nb_2Al_{10}Ni_8Cu_{20}$ and $Zr_{59}Nb_3Al_{10}Ni_8Cu_{20}$ alloys using weight loss study in boiling nitric acid environment. The Field Emission Scanning Electron Microscope is used to elucidate the origin of corrosion resistance by observing the surface morphology.

EXPERIMENTAL

The as spun ribbon specimens of $Zr_{60}Nb_2Al_{10}Ni_8Cu_{20}$ and $Zr_{59}Nb_3Al_{10}Ni_8Cu_{20}$ amorphous alloys were cleaned with acetone and distilled water and dried in air. The specimens were weighed before immersing them into the test solution of concentrated nitric acid in boiling condition. The experimental setup used for the experiment is discussed by Kamachi et al. [15]. In this setup a cold finger condenser was used to reflux the vapours of nitric acid into the solution. The specimens were suspended into boiling 11.5 M HNO_3 through the Teflon thread for the period of 24 h, 48 h and 72 h. The change in the weight of specimen was observed after the each test and corrosion rate of the both alloys was calculated for each concentration using the corrosion rate formula [16].

$$CorrosionRate(mm/y) = 87.6W/DAT$$

DAE Solid State Physics Symposium 2015
AIP Conf. Proc. 1731, 070021-1–070021-3; doi: 10.1063/1.4947853
Published by AIP Publishing. 978-0-7354-1378-8/$30.00

Where W = Weight loss in milligram; D = Density in gm/cm^3; A = Surface area in cm^2; T = Time in hours

Surface morphology of $Zr_{60}Nb_2Al_{10}Ni_8Cu_{20}$ and $Zr_{59}Nb_3Al_{10}Ni_8Cu_{20}$ amorphous alloys after immersion in boiling 11.5 HNO_3 was examined by Field Emission Scanning Electron Microscope NOVA-NANO-FESEM 450.

RESULTS AND DISCUSSION

Fig.1 shows the corrosion rate values obtained for the $Zr_{60}Nb_2Al_{10}Ni_8Cu_{20}$ and $Zr_{59}Nb_3Al_{10}Ni_8Cu_{20}$ amorphous alloys in boiling 11.5M HNO_3 for 24 h, 48 h and 72 hours. The $Zr_{59}Nb_3Al_{10}Ni_8Cu_{20}$ alloy shows low corrosion rate in boiling nitric acid medium in comparison to $Zr_{60}Nb_2Al_{10}Ni_8Cu_{20}$ alloy. A slight decrease in corrosion rate has been observed after 48 hours for both the alloys. It has been reported [17] that the passivation speed of Nb containing Zr based BMG sample is quickened with the increase of HNO_3 solution concentration in a certain range and its corrosion resistance becomes stronger as well. So, in the present study after 48 hours, alloy shows a decrease in value of corrosion rate due to better passivation in a certain range. These results were further confirmed by studying the surface morphology of these treated samples using FESEM. Figure 2 and 3 shows the FESEM images of Virgin $Zr_{60}Nb_2Al_{10}Ni_8Cu_{20}$ and $Zr_{59}Nb_3Al_{10}Ni_8Cu_{20}$ amorphous alloys and after immersion in boiling 11.5M HNO_3 for 24 h, 48 h and 72 hours respectively.

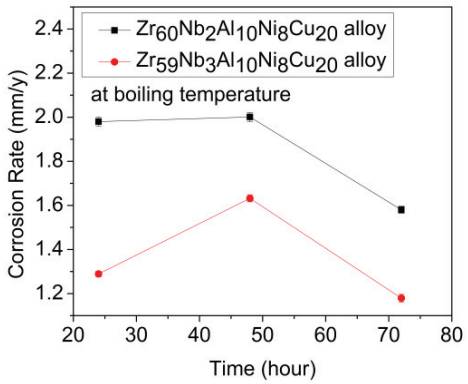

FIGURE 1. Corrosion rate of $Zr_{60}Nb_2Al_{10}Ni_8Cu_{20}$ and $Zr_{59}Nb_3Al_{10}Ni_8Cu_{20}$ amorphous alloys in boiling 11.5M HNO_3.

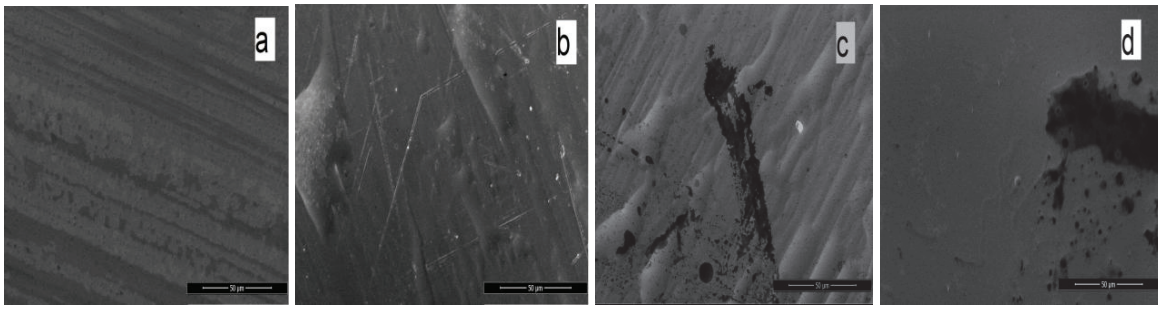

FIGURE 2. FESEM micrographs of virgin $Zr_{60}Nb_2Al_{10}Ni_8Cu_{20}$ amorphous alloy (a) and after immersion in boiling 11.5 M HNO_3 for (b) 24 h (c) 48 h and (d) 72 h.

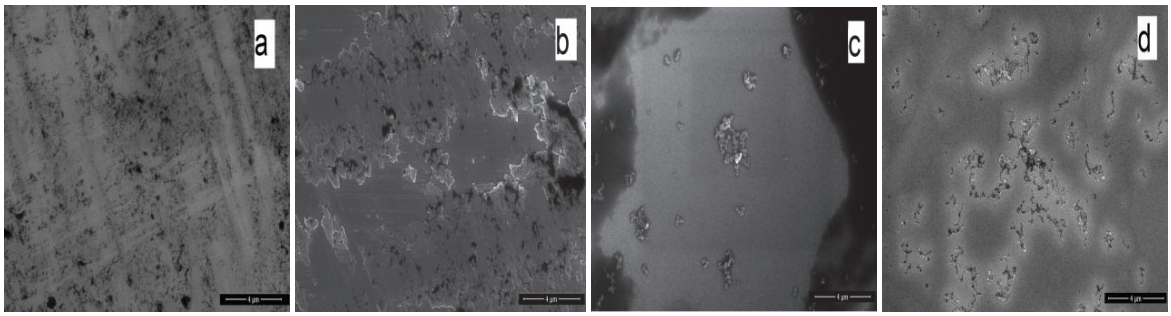

FIGURE 3. FESEM micrographs of virgin $Zr_{59}Nb_3Al_{10}Ni_8Cu_{20}$ amorphous alloy (a) and after immersion in boiling 11.5 M HNO_3 for (b) 24 h (c) 48 h and (d) 72 h.

Figure 2(b) and 2(c) shows typical air pocket morphology is due to the entrapment of air at the wheel-melt interface [18]. Figure 2 (c) and 2(d) shows that some dissolution has taken place on the surface of

$Zr_{60}Nb_2Al_{10}Ni_8Cu_{20}$ amorphous alloy, whereas Figure 3 shows no such dissolution except Figure 3(c). It means that $Zr_{60}Nb_2Al_{10}Ni_8Cu_{20}$ amorphous alloy shows poor corrosion resistance than $Zr_{59}Nb_3Al_{10}Ni_8Cu_{20}$ alloy and it confirms the results of weight loss analysis. Also, Figure 3(c) shows that some dissolution has occurred on the surface of the $Zr_{59}Nb_3Al_{10}Ni_8Cu_{20}$ alloy due to which the value of corrosion rate is high after immersion in boiling nitric acid for 48 hrs (Figure(1)). Figure 3(b) is showing that the film formed on the surface of alloy after 24 hours is non-uniform. Figure 3(c) and 3(d) are the interesting micrographs in which some cluster structure formation has been observed. These structures were initiated in 48 hour duration and further grew up in 72 hours. The nanoscopic view (Figure 4) of $Zr_{59}Nb_3Al_{10}Ni_8Cu_{20}$ amorphous alloy after immersion in boiling 11.5 M HNO_3 for 72 h has been taken. This figure clearly shows a growth of cluster formation on surface of the alloy, which protects the alloy from further corrosion. It is well known that the oxide layer of Nb is more corrosion resistant in acidic medium [14] which the possible reason of better corrosion resistance of $Zr_{59}Nb_3Al_{10}Ni_8Cu_{20}$ alloy in nitric acid medium.

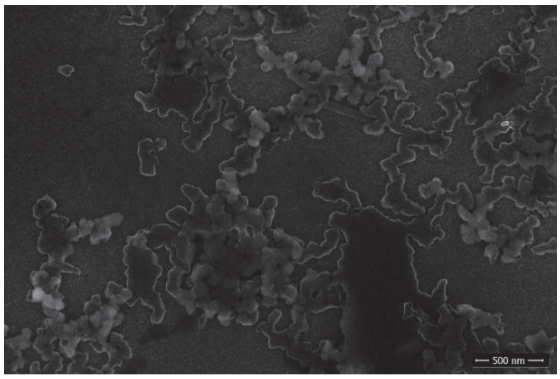

FIGURE 4. FESEM micrographs of $Zr_{59}Nb_3Al_{10}Ni_8Cu_{20}$ amorphous alloy after immersion in boiling 11.5 M HNO_3 for 72 h.

CONCLUSION

The $Zr_{59}Nb_3Al_{10}Ni_8Cu_{20}$ alloy shows a better corrosion resistance in boiling nitric acid medium in comparison to $Zr_{60}Nb_2Al_{10}Ni_8Cu_{20}$ alloy. The surface morphology of these Zr-based alloys shows the passive film formation on the surface of the alloy in acidic medium which protects them from further corrosion.

ACKNOWLEDGMENTS

The financial support for this work under DAE/BRNS Research project (Grants No. 2011/36/44-BRNS/1974) is gratefully acknowledged. Thanks are due to Dr. U. K. Mudali, CSTG- IGCAR, Kalpakkam for providing the samples. MRC-MNIT, Jaipur is acknowledged for FESEM facility.

REFERENCES

1. B. Raj and U. K. Mudali, *Progress in Nuclear Energy* 48, 283–313 (2006).
2. B. Raj, U. K. Mudali, T. Jayakumar, K.V. Kasiviswanathan and R. Natarajan, Meeting the challenges related to material issues in chemical industries, *Sadhana* 25 (2000) 519–559.
3. T. L. Yau, *Zirconium for nitric acid solutions*, Fourth ASTM symposium on Titanium and Zirconium in Industrial applications, Philadelphia, PA, 10–11 October, 1984, pp. 57–68.
4. H. Chauve, J. Decours, R. Demay, M. Pelras, J. Simonnet and G. Turluer, *Zirconium use for large process components*, IAEA-TECDOC-421 165–192 (1987).
5. A. Inoue, T. Nakamura, T. Sugita, T. Zhang and T. Masumoto: *Mater. Trans. JIM.,* 34, 351-358 (1993).
6. Y. J. Sun , D. D. Qu , Y. J. Huang , K.-D. Liss , X. S. Wei, D. W. Xing and J. Shen, *Acta Mater.* 57, 1290–1299 (2009).
7. A. Inoue, *Acta Mater*. 48, 279-306 (2000).
8. W. L. Johnson, *MRS Bull.* 24, 42-56 (1999).
9. H. Choi-Yim and W. L. Johnson, *Appl. Phys. Lett.* 71, 3808- 3811 (1997).
10. C. C. Hays, J. Schroers, U. Geyer, S. Bossuyt, N. Stein and W. L. Johnson, *Mater. Sci. Forum* 343 – 346, 103- 108 (2000).
11. P. Sharma, A. Dhawan and S. K. Sharma, Adv. Microscopic Research, 6, 262-267 (2014)
12. C. L. Qin, K. Asami, H. Kimura, W. Zhang, D. V. Louzguine and A. Inoue, *Mater. Trans.* 50, 1304-1307 (2009).
13. C. Qin, K. Asami, H. Kimura, W. Zhang and A. Inoue, *Electrochimica Acta.* 54, 1612-1617 (2009).
14. R. Mythili, S. Saroja and M. Vijayalakshmi, *Mater Charact*. 61, 1326 – 1334 (2010).
15. U. Kamachi Mudali, R. K. Dyal and J. B. Ganamoorthy, *J. Nucl. Mater.* 203, 73-82 (1993).
16. Mars G. Fontana, "Corrosion Testing" in *"Corrosion Engineering"* Tata McGraw-Hill 2005, pp. 171-172.
17. Z. Fang-quin, C. Zhi-hao, T. Jin-Jue, L. lan-Jun, Y. Jin and X. Yun, *Trans. Nonferrous Met. Soc. China*, 14, 961-965 (2004).
18. S. Sohrabi, H. Arabi, A. Beitollahi, R. Gholamipour, *J. Mater. Eng. Perform.* 22, 2185-2190 (2013).

AMERICAN SCIENTIFIC PUBLISHERS

Advanced Science Letters
Vol. 22, 56–59, 2016

Electrochemical Investigation of Amorphous $Zr_{60}Pd_5Cu_{15}Ni_{10}Al_{10}$ and $Zr_{57}Nb_5Cu_{20}Ni_8Al_{10}$ Alloys in Oxidizing Medium

Poonam Sharma[1,2], Anil Dhawan[2,*], and S. K. Sharma[1]

[1]*Department of Physics, Malaviya National Institute of Technology, Jaipur 302017, India*
[2]*Department of Physics, Anand International College of Engineering, Jaipur 303012, India*

The electrochemical measurements were carried out on $Zr_{60}Pd_5Cu_{15}Ni_{10}Al_{10}$ and $Zr_{57}Nb_5Cu_{20}Ni_8Al_{10}$ bulk amorphous alloys in 1 M, 6 M and 11.5 M aqueous HNO_3 at room temperature. The corrosion potential shifts towards more positive values with the increase in the concentration of nitric acid for both amorphous alloys, which is attributed to the higher oxidizing power of nitric acid and may also be an indicative of high passivating ability. The $Zr_{57}Nb_5Cu_{20}Ni_8Al_{10}$ alloy possesses better corrosion resistance than $Zr_{60}Pd_5Cu_{15}Ni_{10}Al_{10}$ in aqueous HNO_3 medium because $Zr_{60}Pd_5Cu_{15}Ni_{10}Al_{10}$ alloy shows higher value of corrosion current density possibly due to protective oxide film of niobium oxide. The lower value of passive current density I_{pass} also indicates that $Zr_{57}Nb_5Cu_{20}Ni_8Al_{10}$ amorphous alloy shows better corrosion resistance in nitric acid environment than $Zr_{60}Pd_5Cu_{15}Ni_{10}Al_{10}$ alloy.

Keywords: Bulk Amorphous Alloys, Potentiodynamic Polarization, Corrosion.

1. INTRODUCTION

Bulk metallic glasses generally exhibit outstanding mechanical properties such as high mechanical strength, high fracture toughness and good corrosion resistance which cannot be obtained for conventional materials.[1] Environmental degradation pertains to the study of oxidation and corrosion behavior of the amorphous alloy in terms of its utility and various engineering applications. In particular, electrochemical study is required to better understand the behavior of the amorphous alloys in corrosive environment and also suggest the possible corrosion rate in terms of corrosion current density with which that alloy will corrode in stipulated time interval. So far many studies have been carried out on corrosion properties of Fe-based[2], Ni-based[3], Zr-based[4] and Mg-based[5] bulk amorphous alloys in different media, expecting good corrosion resistance because of chemical and structural homogeneity of bulk amorphous alloys. In most of the alloy systems, the amorphous state presents better corrosion properties than the crystalline counterparts with the same component.[3,4] Among glass forming systems, Zr based multicomponent alloys have received increasing attention due to the positive combination of easy castability and high thermal stability against crystallization together with remarkable mechanical properties.[6,7] Among these alloys, the Zr–TM–Al alloys, where TM is transition metal, are particularly interesting because they exhibit an extremely large temperature interval of super-cooled liquid region exceeding 100 K.[8] Bulk amorphous Zr–Al–Ni–Cu alloys belongs to the best glass forming systems known and can be cast at relatively low cooling rates in order to solidify as a glass.[9] Small amount of alloying element significantly influences the corrosion behavior of amorphous alloys. Zr–Al–Ni–Cu alloys containing small amounts of Nb and Ti increases the corrosion resistance in chloride solution.[10,11] Qin et al. has studied the corrosion behavior of Pd containing Zr based amorphous alloys in NaCl medium and found that Pd containing alloy shows poor corrosion resistance in NaCl medium because the surface film formed on the alloy surface is not resistant to the chloride containing solution.[12] Bulk amorphous $Zr_{55}Al_{10}Cu_{30}Ni_{5-x}Pd_x$ ($x = 0$, 5 at.%) alloys have been studied in NaOH medium and these alloys were found to showed excellent corrosion resistance in NaOH medium.[13]

Not many studies has been carried out on Pd and Nb containing Zr-based amorphous alloys in oxidizing media and also the effect of concentration of nitric acid on the corrosion behavior of these alloys has not been reported. So, the objective for the present work is to investigate the corrosion behavior of $Zr_{60}Pd_5Cu_{15}Ni_{10}Al_{10}$ and $Zr_{57}Nb_5Cu_{20}Ni_8Al_{10}$ bulk amorphous alloys using potentiodynamic polarization method in 1 M, 6 M and 11.5 M HNO_3 media at room temperature. This study will also be helpful in selecting the Zr-based amorphous alloy as one of the candidate material to be used for fuel reprocessing applications.

*Author to whom correspondence should be addressed.

 1936-6612/2016/22/056/004 doi:10.1166/asl.2016.6783

2. EXPERIMENTAL DETAILS

As received specimen of $Zr_{60}Pd_5Cu_{15}Ni_{10}Al_{10}$ (3 mm diameter) and $Zr_{57}Nb_5Cu_{20}Ni_8Al_{10}$ (3 mm diameter) have been used for investigations, were received from CSTG, IGCAR-Kalpakkam. The amorphous nature of the samples has been ascertained by X-ray diffraction using Xpert Pro-Panalytical system with Cu–Kα radiations. The Electrochemical measurements were carried out using a potentiostat (Autolab-AUT84276) consisting of a three electrode cell; Ag/AgCl reference electrode, Pt counter electrode and glassy alloys as working electrode. Before potentiodynamic polarization testing, the open circuit potential (OCP) of the working electrode was monitored until it became almost steady in the tested environment. The time taken for the stable OCP was 1800 sec. The potentiostat was interfaced with Nova (version 1.9) software for measuring the change in OCP with immersion time and also performing the polarization experiments. Potentiodynamic polarization tests were conducted in 1 M, 6 M and 11.5 HNO_3 at room temperature. The specimens for electrochemical studies were cut from the 3 mm diameter rod of Zr based bulk metallic glass sample with the help of diamond cutter and further these specimens were cold mounted using Epoxy resin and hardener. The mounted specimens were polished with 1200 grit SiC papers and were then washed with distilled water and cleaned with ethanol. The Potentiodynamic polarization experiments were carried out at the scanning rate 1 mV/s from 200 mV below OCP to 2200 mV. All the polarization plots were almost reproducible.

3. RESULTS

Figure 1 shows X-ray diffraction patterns of $Zr_{60}Pd_5Cu_{15}Ni_{10}Al_{10}$ and $Zr_{57}Nb_5Cu_{20}Ni_8Al_{10}$ glassy alloys. The XRD pattern of the both alloys shows only broad spectrum indicating amorphous nature. A fit to the experimental polarization curves (E vs. I plots) was obtained using the Bulter-Volmer equation,[14], which yielded the values of the corrosion current density (I_{corr}): where s_1 = slope of the anodic branch = $2.303/b_a$; s_2 = slope of the cathodic branch = $2.3037/b_c$; E_{corr} = the corrosion potential or open circuit potential (OCP); I_{corr} = corrosion current density in A/cm^2.

The observed corrosion potential, i.e., the potential where $I = 0$, is taken as the corrosion potential (E_{corr}) or the open-circuit potential and b_a and b_c are Tafel constants.

A fit to the experimental polarization plot was performed using the software Autolab-NOVA supplied by the manufacturer (Metrohm B. V. Netherlands) according to the non-linear least square fit method with the values obtained from selected Tafel lines as starting parameters. After some iterations, a fit with the number of iterations and the goodness of fit parameter chi-square was obtained. The best fit was obtained for both the cathodic and the anodic regions of the polarization plot using this procedure, which yielded the values of I_{corr} and E_{corr}. Prior to carrying out the polarization experiment, the above method has been used for conditioning of the working electrode and for the stabilization of the OCP resulted in the maximum reproducibility of open circuit potential E_{corr} and the corrosion current I_{corr} values.

Figures 2 and 3 shows the open circuit potential curve of $Zr_{60}Pd_5Cu_{15}Ni_{10}Al_{10}$ and $Zr_{57}Nb_5Cu_{20}Ni_8Al_{10}$ glassy alloys in

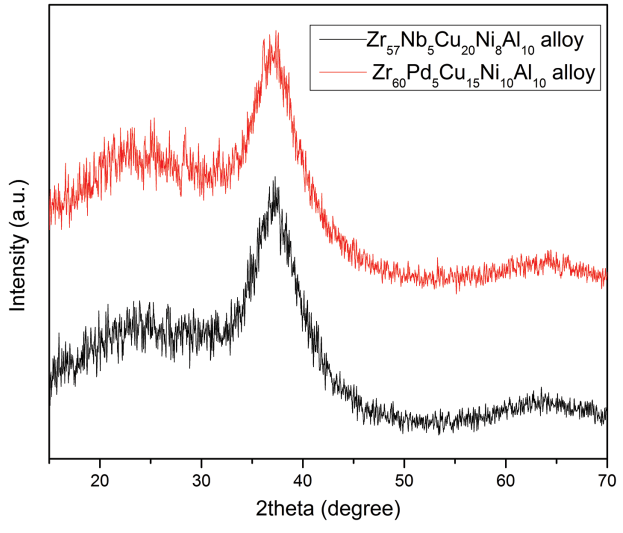

Fig. 1. XRD patterns of the $Zr_{60}Pd_5Cu_{15}Ni_{10}Al_{10}$ and $Zr_{57}Nb_5Cu_{20}Ni_8Al_{10}$ alloy.

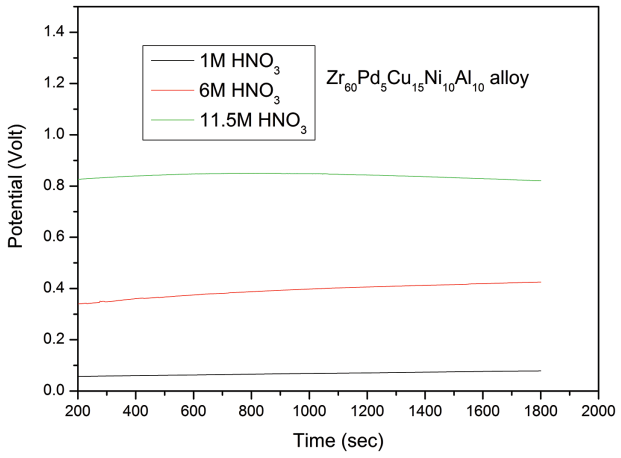

Fig. 2. Open circuit potential plot for $Zr_{60}Pd_5Cu_{15}Ni_{10}Al_{10}$ in 1 M, 6 M, 11.5 M HNO_3 medium at room temperature.

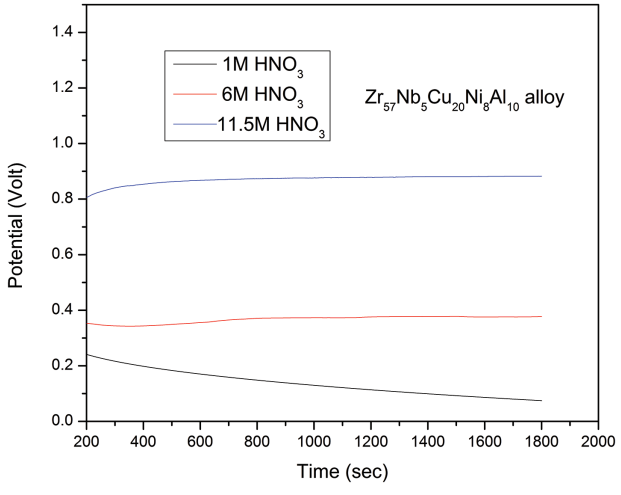

Fig. 3. Open circuit potential plot for $Zr_{57}Nb_5Cu_{20}Ni_8Al_{10}$ in 1 M, 6 M, 11.5 M HNO_3 medium at room temperature.

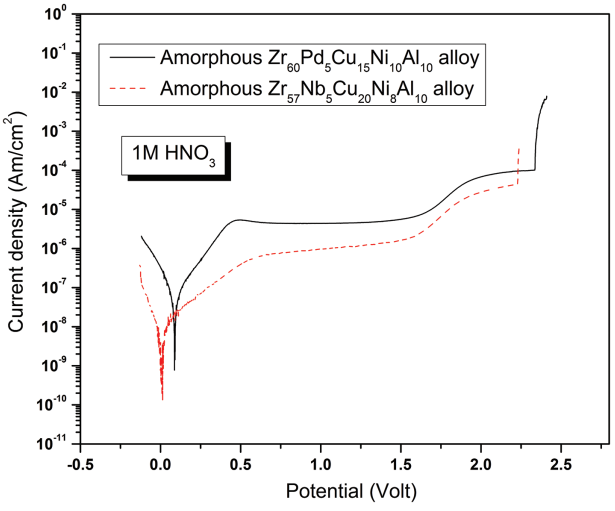

Fig. 4. Potentiodynamic polarization curve of $Zr_{60}Pd_5Cu_{15}Ni_{10}Al_{10}$ and $Zr_{57}Nb_5Cu_{20}Ni_8Al_{10}$ alloy in 1 M HNO_3 at room temperature.

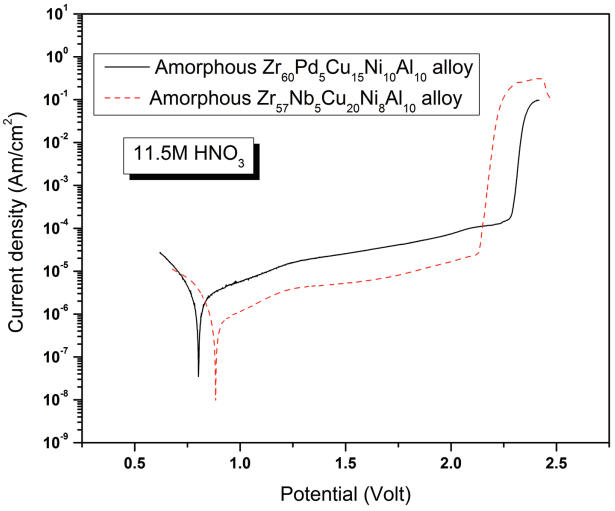

Fig. 6. Potentiodynamic polarization curve of $Zr_{60}Pd_5Cu_{15}Ni_{10}Al_{10}$ and $Zr_{57}Nb_5Cu_{20}Ni_8Al_{10}$ alloy in 11.5 M HNO_3 at room temperature.

1 M, 6 M and 11.5 M aqueous HNO_3 medium at room temperature, respectively. It can be seen from the Figures 2 and 3 that the value of open circuit potential (OCP) for both the alloys increases as the concentration of HNO_3 increases. Figures 4–6 shows the potentiodynamic polarization curve of $Zr_{60}Pd_5Cu_{15}Ni_{10}Al_{10}$ and $Zr_{57}Nb_5Cu_{20}Ni_8Al_{10}$ glassy alloys in 1 M, 6 M and 11.5 M aqueous HNO_3 medium at room temperature, respectively. The corrosion parameters such as corrosion potential E_{corr}, corrosion current density I_{corr} and passive current density I_{pass} obtained from the polarization curve (Figs. 3–5) are shown in Tables I and II. Electrochemical result (Fig. 3) reveals that the value of corrosion current density for $Zr_{60}Pd_5Cu_{15}Ni_{10}Al_{10}$ alloy is higher than $Zr_{57}Nb_5Cu_{20}Ni_8Al_{10}$ bulk amorphous alloy in 1 M HNO_3. Similarly $Zr_{60}Pd_5Cu_{15}Ni_{10}Al_{10}$ alloy shows higher value of corrosion current density in 6 M and 11.5 M HNO_3.

Table I. Polarization parameter of $Zr_{60}Pd_5Cu_{15}Ni_{10}Al_{10}$ alloy in 1 M, 6 M, 11.5 M HNO_3 medium at room temperature.

Concentration of nitric acid	E_{corr} (V)	I_{corr} (A/cm^2)	I_{pass} (A/cm^2)
1 M HNO_3	0.0938	1.362×10^{-7}	4.674×10^{-6}
6 M HNO_3	0.4751	1.130×10^{-7}	4.975×10^{-6}
11.5 M HNO_3	0.7993	2.190×10^{-6}	2.780×10^{-5}

Table II. Polarization parameter of $Zr_{57}Nb_5Cu_{20}Ni_8Al_{10}$ alloy in 1 M, 6 M, 11.5 M HNO_3 medium at room temperature.

Concentration of nitric acid	E_{corr} (V)	I_{corr} (A/cm^2)	I_{pass} (A/cm^2)
1 M HNO_3	0.0146	1.552×10^{-8}	9.325×10^{-7}
6 M HNO_3	0.3269	2.554×10^{-8}	5.996×10^{-6}
11.5 M HNO_3	0.8843	6.715×10^{-7}	4.839×10^{-5}

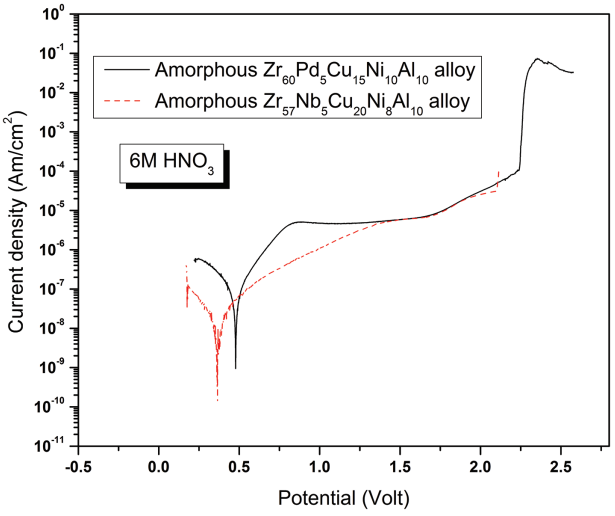

Fig. 5. Potentiodynamic polarization curve of $Zr_{60}Pd_5Cu_{15}Ni_{10}Al_{10}$ and $Zr_{57}Nb_5Cu_{20}Ni_8Al_{10}$ alloy in 6 M HNO_3 at room temperature.

4. DISCUSSION

In electrochemical investigations, it is found that the corrosion potential (OCP) shifts towards more positive values with the increase in the concentration of nitric acid for both amorphous alloys as shown in Figures 2 and 3 which indicates that the metal surfaces are being spontaneously passivated in nitric acid medium due to the formation of oxide film and also this is attributed to the higher oxidizing power of nitric acid.[15] The shift of OCP values to more noble potential in nitric acid may also be an indicative of high passivating ability. Furthermore, the shifting towards more noble OCP in these alloys have been attributed due to the thickening of oxide film formed on the metal surface and less noble values implying that the thickness of all the film was being reduced.[16, 17] In the present study Nb containing Zr based alloy shows slight lower OCP value in 1 M and 6 M HNO_3 medium which means that the thickness of oxide film is not more than Pd containing Zr based alloy, but this do not indicate that the film formed on the surface of $Zr_{57}Nb_5Cu_{20}Ni_8Al_{10}$ alloy is less corrosion resistant.

The change of the polarization curve reflects the different corrosion reactions. The potentiodynamic polarization curve (Fig. 4) shows that the value of corrosion current density I_{corr} for $Zr_{60}Pd_5Cu_{15}Ni_{10}Al_{10}$ alloy is higher than $Zr_{57}Nb_5Cu_{20}Ni_8Al_{10}$ bulk amorphous alloy in 1 M HNO_3 medium. The $Zr_{57}Nb_5Cu_{20}Ni_8Al_{10}$ alloy shows less value of corrosion current density possibly due to the formation of Nb_2O_5 which is strong and corrosion resistant in nitric acid medium[18] and oxides of Zr and Nb possess a high corrosion resistance in a wide range of pHs.[19] Similar results were also observed for both Pd and Nb containing Zr based amorphous alloys in 6 M and 11.5 M HNO_3 aqueous medium. It means that $Zr_{57}Nb_5Cu_{20}Ni_8Al_{10}$ alloy shows better corrosion resistance in nitric acid media than $Zr_{60}Pd_5Cu_{15}Ni_{10}Al_{10}$ alloy in similar conditions. The value of corrosion current density I_{corr} (Tables I and II) obtained from the polarization curve increases as the concentration of HNO_3 increases for both the alloys, which indicates that corrosion resistance of both alloys in nitric acid medium is decreasing with increase in concentration of nitric acid. The polarization curves for both alloys shows clear passivity region, which is indication of passive film formed on the surface of alloy. Homozava et al. has investigated the corrosion behavior of Nb containing Zr based amorphous $Zr_{58.5}Cu_{15.6}Ni_{12.8}Al_{10.3}Nb_{2.8}$ alloy in 1 M HNO_3 and 1 M HCl medium and it was found that the dissolution of Ni in nitric acid was below the detection limit and Zr and Nb was described by a very reduced dissolution rate as compared to Al and Cu. The reason of high Al release in nitric acid is probably related to the oxidizing nature of HNO_3.[20] Similarly, in the present study of $Zr_{57}Nb_5Cu_{20}Ni_8Al_{10}$ alloy Zr and Nb would play the important role for good corrosion resistant behavior in nitric acid medium. The I_{pass} value also gives an indication of the resistance of the specimen against corrosion. A lower I_{pass} indicates a high corrosion resistance of the material in the environment. The low value of passive current I_{pass} at lower concentration of nitric acid reveals the lower metal dissolution due to the uniform and more protective film formation with low electronic conductivity, which is a typical behavior of valve metals e.g., Zr, Ti, Al, Hf, Nb and Ta.[21, 22] The I_{pass} value for both the alloys increases with the increase in the concentration of nitric acid (Tables I and II). This is possibly due to the reason that in the higher nitric acid concentration, increased redox potential of HNO_3/HNO_2 system with relatively high rate of autocatalytic reaction is expected, which also aid faster transpassive dissolution.[23, 24] Hence, the lower I_{pass} value for $Zr_{57}Nb_5Cu_{20}Ni_8Al_{10}$ alloy than $Zr_{60}Pd_5Cu_{15}Ni_{10}Al_{10}$ also indicates that Nb containing Zr-based alloy shows better corrosion resistance than Pd containing Zr-based amorphous alloy.

5. CONCLUSIONS

The conclusion from the electrochemical study of $Zr_{60}Pd_5Cu_{15}Ni_{10}Al_{10}$ and $Zr_{57}Nb_5Cu_{20}Ni_8Al_{10}$ bulk amorphous alloys in 1 M, 6 M, 11.5 M HNO_3 at room temperature is that the value of corrosion current density for amorphous $Zr_{60}Pd_5Cu_{15}Ni_{10}Al_{10}$ alloy is found higher than $Zr_{57}Nb_5Cu_{20}Ni_8Al_{10}$ alloy in nitric acid medium (1 M, 6 M, 11.5 M HNO_3) by an order of a magnitude, thereby indicating that the bulk amorphous alloy $Zr_{57}Nb_5Cu_{20}Ni_8Al_{10}$ possesses better corrosion resistance than $Zr_{60}Pd_5Cu_{15}Ni_{10}Al_{10}$ alloy in aqueous HNO_3 medium.

Acknowledgments: The financial support for this work under BRNS/DAE Research project No. 2011/36/44-BRNS/1974 is gratefully acknowledged. Thanks are due to Dr. U. Kamachi Mudali, CSTG-IGCAR-Kalpakkam, for providing the Zr-based metallic glass alloy for this investigations.

References and Notes

1. A. Inoue, Bulk Amorphous Alloys, Trans. Tech. Publications, Zurich **(1998)**.
2. S. J. Pang, T. Zhang, K. Asami, and A. Inoue, *J. Mater. Res.* 17, 701 **(2002)**.
3. A. Kawashima, H. Habazaki, and K. Hashimoto, *Mater. Sci. Eng. A* 304, 753 **(2001)**.
4. A. Gebert, K. Buchholz, A. Leonhard, K. Mummert, J. Eckert, and L. Schultz, *Mater. Sci. Eng. A* 267, 294 **(1999)**.
5. R. V. S. Rao, U. Wolff, S. Baunack, J. Eckert, and A. Gebert, *Corr. Sci.* 45, 817 **(2003)**.
6. A. Inoue, *Acta Mater.* 48, 277 **(2000)**.
7. J. F. Loeffler, *Intermet.* 11, 529 **(2003)**.
8. T. Zhang, A. Inoue, and T. Masumoto, *Mater. Trans. JIM* 32, 1005 **(1991)**.
9. A. Inoue, T. Nakamura, T. Sugita, T. Zhang, and T. Masumoto, *Mater. Trans., JIM* 34, 351 **(1993)**.
10. S. Pang, T. Zhang, H. Kimura, K. Asami, and A. Inoue, *Mater. Trans. JIM* 41, 1490 **(2000)**.
11. V. R. Raju, U. Kuhn, U. Wolff, F. Schneider, J. Eckert, R. Reiche, and A. Gebert, *Mater. Lett.* 57, 173 **(2002)**.
12. F. X. Qin, H. F. Zhang, Y. F. Deng, B. Z. Ding, and Z. Q. Hu, *J. Alloys Compd.* 375, 318 **(2004)**.
13. F. X. Qin, H. F. Zhang, P. Chen, F. F. Chen, D. C. Qiao, and Z. Q. Hu, *Mater. Letters* 58, 1246 **(2004)**.
14. M. Stern and A. L. Geary, *J. Electrochem. Soc.* 104, 56 **(1957)**.
15. P. Fauvet, F. Balbaud, R. Robin, Q.-T. Tran, A. Mugnier, and D. Espinoux, *J. Nucl. Mater.* 375, 52 **(2008)**.
16. A. Robin, H. R. Z. Sandim, and J. L. Rosa, *Corros. Sci.* 41, 1333 **(1999)**.
17. R. D. Armstrong, R. E. Firman, and H. R. Thirsk, *Corros. Sci.* 13, 409 **(1973)**.
18. R. Mythili, S. Saroja, and M. Vijayalakshmi, *Mater. Charact.* 61, 1326 **(2010)**.
19. M. Pourbaix, Altas of electrochemical equilibria in aqueous solutions, National Association of Corrosion Engineers, 1974, Brussels **(2007)**.
20. N. Homazava, A. Shkabko, D. Logvinovish, U. Krahenbuhl, and A. Ulrich, *Intermat.* 16, 1066 **(2008)**.
21. U. Kamachi Mudali, S. Baunack, J. Eckert, L. Schultz, and A. Gebert, *J. Alloys Compd.* 377, 290 **(2004)**.
22. S. Baunack, U. K. Mudali, and A. Gebert, *Appl. Surf. Sci.* 252, 162 **(2005)**.
23. N. Padhy, S. Ningshen, U. K. Mudali, and B. Raj, *J. Alloys Compd.* 503, 50 **(2010)**.
24. S. Ningshen, U. K. Mudali, G. Amarendra, and B. Raj, *Corros. Sci.* 51, 322 **(2009)**.

Received: 3 August 2015. Accepted: 31 December 2015.